THESE EN COTUTELLE

Présentée à L'UNIVERSITE DE LILLE

Ecole Doctorale Régionale Sciences Pour l'Ingénieur Lille Nord-de-France

Et

L'UNIVERSITE LIBANAISE

Ecole Doctorale des Sciences et Technologie Liban-Hadath

Pour obtenir le grade de

DOCTEUR EN NANOTECHNOLOGIE

Dans la spécialité

Micro et Nano Technologies, Acoustique et Télécommunications Par

Abir SWAIDAN

10 Décembre 2019

Preparation of nanostructured materials and their application as enzyme-mimics for sensing and bacterial fighting

Membres du Jury

Dr. Rabah Boukherroub	Directeur de thèse	CNRS & Université de Lille
Prof. Salah Hamieh	Co-Directeur de thèse	Université Libanaise
Prof. Antoine Gedeon	Rapporteur	Université de La Sagesse
Prof. Valérie Keller	Rapporteuse	Université de Strasbourg
Prof. Tayssir Hamieh	Examinateur	Université Libanaise
Prof. Souhir Boujday	Examinatrice	Université Sorbonne
Prof. Joumana Toufaily	Invitée	Université Libanaise

DEDICATIONS

This dissertation is dedicated to the memory of my mother. Without her endless love, encouragement and support I would never have been able to complete this task. Her soul urges me to strive for achieving my goals in life. I appreciate everything she has done for me.

ACKNOWLEDGEMENTS

My PhD gave me the opportunity to gain an overwhelming experience to explore new directions in the field of research.

*First and foremost, I would like to thank my PhD supervisor in France, **Dr. Rabah Boukherroub**, who gave me the opportunity to work in his laboratory for an extended period of time, and the permission to use all the required equipment and the necessary materials to complete this task. I am very thankful for his warm welcome every time I asked for his help, his constant supervision, support, guidance, encouragement, and discussions during the past three years, as well as for providing me with the necessary scientific information regarding the project and for his kindness, and patience. The valuable meetings with **Dr. Rabah Boukherroub** have brightened my PhD. I am very grateful for the time he provided and the patience he had to correct the thesis and responding directly to my emails even during weekends. His professional attitude and knowledge in multi-disciplinary areas, being a great mentor and not giving up on me throughout these three years and the friendly environment, had encouraged me to move forward, and made my PhD thoughtful and fruitful. Whatever I say, words can't express my warm gratitude to him. It's my honor to have worked under his supervision.*

*I place on record, my special and sincere gratitude to **Prof. Tayssir HAMIEH**, **Prof. Salah Hamieh**, and **Prof. Joumana Toufaily**, for their constant encouragement, guidance, sympathy, advices, the confidence they granted me, and the friendly environment and indispensable help during my thesis. I want to thank them for giving me the opportunity to complete this work, and believing in my capabilities. Without their passionate participation, interest and support, my PhD would not have been successfully accomplished. The deep insights of **Prof. Joumana Toufaily** helped me at certain stages in my work. I would like to thank her for encouraging my research and allowing me to grow as a research scholar. Her valuable suggestions, comments and guidance encourage me to learn more day-by-day. Her deep insights as well helped me at various stages of my research. I am also indebted towards her generosity, selfless support and especially for patience during the last three years. Big thanks once again go to her.*

*My special thanks go to **Prof. Sabine Szunerits**, for her help and support over the past three years. I have obtained a lot of scientific knowledge from her. Her wide knowledge in*

*multidisciplinary field and her sweet welcome and help had brightened my way during my thesis. I am also indebted to **Dr. Alexandre Barras**, for his complete guidance, encouragement, and the valuable advices he provided me during my PhD. I greatly appreciate his generosity and kindness, and I am forever grateful for his help and support.*

*Many thanks go in return to the members of the jury for taking the time to read and correct this manuscript: **Prof. Antoine Gedeon**, **Prof. Valerie Keller**, **Prof. Souhir Boujday,** and **Prof. Tayssir HAMIEH**.*

My warmest thanks go to the colleagues in the NanoBioInterfaces group at IEMN in France and the MCEMA group in Lebanon, and to all my friends who encouraged, helped, and supported me to continue this task and motivated me to move forward and overshoot all the hurdles. To all my friends, thank you for being part of my life.

I would like also to express my deepest appreciation to all those who provided me the possibility to complete this thesis especially their support and motivation from long distances. I was really surrounded with great people and friends who have contributed in one way or another to the accomplishment of this doctoral dissertation.

Most important, I am more than grateful to my family for the unconditional support and affection.

Finally, I would like to express my gratitude to the ''Lebanese University'' for the financial support during my PhD.

ABSTRACT

Copper sulfide (CuS)-based nanomaterials have gained enormous attention due to their intrinsic outstanding properties that warranted their use in various applications. CuS-based nanomaterials exhibit enzyme-like activity, referred to as "nanozymes". They are considered as alternatives to natural peroxidase enzymes in their catalytic behavior toward oxidizing the reaction of 3,3′,5,5′-tetramethylbenzidine (TMB) substrate in the presence of H_2O_2. This merit makes them ideal candidates for the development of extremely sensitive and selective colorimetric sensing platforms for the quantitative and qualitative identification of various chemical and biological species.

This manuscript consists of **5 chapters**. **Chapter 1** presents the state of the art that summarizes a literature overview about enzyme mimics as alternatives to natural enzymes, their applications and properties. It focuses on the use of nanomaterials as peroxidase mimics and their utilization as colorimetric sensors with multifunctional properties.

Chapter 2 describes the synthesis of copper sulfide nanoparticles stabilized with bovine serum albumin protein (CuS-BSA) *via* a simple chemical route and their investigation as nanozymes for the decomposition of H_2O_2 into hydroxyl radicals ($HO^•$) for the oxidation of TMB. The catalytic reaction is manifested through the production of a blue colored charge transferred oxidized product (oxTMB) that can be easily observed by the naked eye, or quantitatively assessed by an increase in the UV/vis absorption intensity at 654 nm.

The detection capabilities and sensing properties were subsequently applied for identifying hexavalent toxic form of chromium ion [Cr(VI)], which generates excessive amounts of $HO^•$ from H_2O_2, that represents the key components in the catalytic mechanism. A detection limit of 50 nM was achieved under our optimized experimental conditions, which is below the permissible limit determined by the United States Environmental Protection Agency (U.S. EPA). The practical performance of this sensor is successfully demonstrated using various environmental water samples spiked with different concentrations of Cr(VI).

Decoration of CuS-BSA nanocomposite with copper phosphate nanoparticles ($Cu_3(PO_4)_2$) resulted in the formation of small sized nanoparticles with enhanced catalytic behavior towards non-enzymatic glucose and H_2O_2 sensing, as the final outcome of glucose oxidation. The

nanozyme displayed detection limits as low as 7.4 nM, and 27.6 nM over wide linear range of 10-100 µM and 0-1000 µM for H_2O_2 and glucose, respectively. The small-sized CuS-BSA-$Cu_3(PO_4)_2$ nanoparticles provide access to an enormous number of active sites on the catalyst surface, which accelerates the catalytic reaction by enhancing the production of reactive $HO^{\bullet}$ radicals. The practical applicability of this sensor was investigated by detecting glucose in human blood samples and H_2O_2 in lens care solution **(chapter 3, part A)**.

CuS-BSA-$Cu_3(PO_4)_2$ nanoparticles were also applied for dopamine sensing in beef meat. This colorimetric assay showed an inhibition of the catalytic activity after adding increasing concentrations of dopamine, confirmed by the reduction in oxTMB color and absorbance intensity. The developed nanosensor displayed high sensitivity towards dopamine in the presence of interfering biological molecules and reducing agents and achieved an ultralow detection limit down to 5.2 nM over a wide linear range 0-100 µM. The applicability of the nanosensor proves to be promising for colorimetric studies and further diagnostic and biomedical applications without the requirement of complex and expensive instrumentations **(chapter 3, part B)**.

Encouraged by the promising optical properties of CuS-BSA nanoparticles, we then expanded their applications for biomedical purposes. Thus, we investigated their use as photothermal candidates and drug carriers for the on-demand release of lysozyme antibiotic as an antibacterial drug model for bacterial elimination under a 980 nm NIR laser irradiation. The fabricated nanoparticles were loaded with lysozyme under physiological conditions and showed intrinsic antibacterial action against two bacterial strains, gram negative *E. coli* and gram positive *B. subtilis* under the influence of low laser irradiation power density (0.7 W.cm^{-2}) for a short period of time (3 min). The use of NIR light causes a temperature rise in the bacterial medium mediated by CuS NPs with a controlled release of the loaded antibiotic to achieve a dual therapeutic model **(chapter 4)**.

Finally, the last part summarizes the main results obtained in this thesis and provides perspectives for future research approaches.

The annex presents the experimental section, mainly the synthetic approaches and the various characterization techniques used to confirm the successful synthesis and surface modification of our nanoparticles.

RÉSUMÉ

Les nanomatériaux à base de CuS ont suscité une attention particulière en raison de leurs propriétés intrinsèques exceptionnelles qui justifient leur utilisation dans diverses applications. Les nanomatériaux à base de CuS présentent une activité enzymatique, appelée "nanozymes". Ils sont considérés comme des alternatives aux enzymes peroxydases naturelles dans leur comportement catalytique envers l'oxydation du 3,3′,5,5′-tétraméthylbenzidine (TMB) en présence de H_2O_2. Ce mérite en fait des candidats idéaux pour le développement de plates-formes de détection colorimétrique extrêmement sensibles et sélectives pour l'identification quantitative et qualitative de diverses espèces chimiques et biologiques.

Ce manuscrit de thèse comporte **5 chapitres.** Le **chapitre 1** présente l'état de l'art qui donne un aperçu de la littérature sur les imitations enzymatiques comme alternatives aux enzymes naturelles, leurs applications et propriétés. En particulier, il est concentré sur l'utilisation des nanomatériaux comme imitateurs de peroxydase et leur utilisation comme capteurs colorimétriques aux propriétés multifonctionnelles.

Le **chapitre 2** décrit la synthèse de nanoparticules de sulfure de cuivre stabilisées par la protéine d'albumine sérique bovine (CuS-BSA) par une voie chimique simple, et leur étude comme nanozymes pour la décomposition de H_2O_2 en radicaux hydroxyle ($HO^{\bullet}$) pour l'oxydation du TMB. La réaction catalytique est caractérisée par la production d'un produit oxydé par transfert de charge de couleur bleue (oxTMB) qui peut être facilement observé à l'œil nu, ou évalué quantitativement par une augmentation de l'intensité d'absorption UV/vis à 654 nm.

Les capacités de détection et les propriétés de détection ont ensuite été appliquées pour identifier la forme toxique hexavalente de l'ion chrome [Cr(VI)] qui génère des quantités élevées de $HO^{\bullet}$ à partir de H_2O_2, qui représente les composants clés dans le mécanisme catalytique. Une limite de détection de 50 nM a été atteinte dans nos conditions expérimentales optimisées, ce qui est inférieur à la limite permise par l'Environmental Protection Agency des États-Unis (U.S. EPA). La performance pratique de ce capteur est démontrée avec succès sur divers échantillons d'eau enrichis avec différentes concentrations de Cr(VI).

La décoration du nanocomposite CuS-BSA avec des nanoparticules de phosphate de cuivre ($Cu_3(PO_4)_2$) a conduit à la formation de nanoparticules de petite taille avec un comportement catalytique amélioré pour le glucose et la détection de H_2O_2, comme produit final issu de l'oxydation du glucose. Le nanozyme affichait des limites de détection aussi faibles que 7,4 nM et 27,6 nM sur une large plage linéaire de 10-100 µM et 0-1000 µM pour H_2O_2 et le glucose, respectivement. Les nanoparticules de petite taille CuS-BSA-$Cu_3(PO_4)_2$ présentent un nombre élevé de sites actifs à leur surface qui accélère la réaction catalytique en augmentant la production de radicaux HO réactifs. L'application de ce capteur a été démontrée pour la détection de glucose dans des échantillons de sang humain et de H_2O_2 dans une solution d'entretien des lentilles (**chapitre 3, partie A**).

Les CuS-BSA-$Cu_3(PO_4)_2$ nanoparticules ont également été utilisés pour la détection de dopamine dans la viande bovine. Ce test colorimétrique a montré une inhibition de l'activité catalytique après addition de concentrations croissantes de dopamine, confirmée par la réduction de la couleur et de l'intensité d'absorbance de l'oxTMB. Le nanocapteur mis au point présentait une sensibilité élevée à la dopamine en présence de molécules biologiques interférentes et d'agents réducteurs avec une limite de détection ultra-faible de 5,2 nM dans une large plage linéaire de 0-100 µM. L'applicabilité du nanocapteur s'avère prometteuse pour les études colorimétriques et autres applications diagnostiques et biomédicales sans avoir besoin d'instruments complexes et coûteux (**chapitre 3, partie B**).

Encouragés par les propriétés optiques prometteuses des nanoparticules de CuS-BSA, nous avons ensuite étendu leurs applications à des fins biomédicales. Ainsi, nous avons étudié leur utilisation comme candidats photothermiques et porteurs de médicaments pour la libération à la demande de l'antibiotique « lysozyme » comme modèle de médicament antibactérien pour l'élimination bactérienne sous un laser NIR à 980 nm. Les nanoparticules fabriquées ont été chargées de lysozyme dans des conditions physiologiques et ont montré une action antibactérienne intrinsèque contre deux souches bactériennes, Gram négatif *E. coli* et Gram positif *B. subtilis*, sous l'influence d'une faible densité de puissance d'un rayonnement laser (0,7 W.cm^{-2}) pendant une courte période (3 minutes). L'utilisation de la lumière NIR provoque une élévation de température dans le milieu bactérien médiée par les nanoparticules de CuS avec une libération contrôlée de l'antibiotique chargé pour obtenir un modèle thérapeutique double (**chapitre 4**).

Enfin, la dernière partie résume les principaux résultats obtenus dans le cadre de cette thèse et fournit des perspectives pour les approches de recherche futures.

L'annexe présente la partie expérimentale, principalement les approches synthétiques et les différentes techniques de caractérisation utilisées pour confirmer le succès de la synthèse et de la modification de surface de nos nanoparticules.

Mots clés: Nanoparticules; CuS-BSA; CuS-BSA-Cu$_3$(PO$_4$)$_2$; Nanozymes; Cr(VI); Glucose ; Peroxyde d'hydrogène; HO$^{\bullet}$; Dopamine; Inhibition ; Colorimétrie; Détection; TMB; oxTMB; Peroxidase mimétique; Bactéries; NIR; Lysozyme.

TABLE OF CONTENTS

ABBREVIATIONS

CuS	Copper sulfide
BSA	Bovine serum albumin
Cr(VI)	Hexavalent chromium
H_2O_2	Hydrogen peroxide
$HO^\bullet$	Hydroxyl radicals
FTIR	Fourier transform infrared spectroscopy
EDX	Energy dispersive X-ray spectroscopy
XPS	X-ray photoelectron spectroscopy
UV-vis	Ultraviolet-visible spectroscopy
DLS	Dynamic light-scattering
XRD	X-ray diffraction
TEM	Transmission electron microscopy
SEM	Scanning electron microscopy
FL	Fluorescence spectroscopy
HRTEM	High-resolution transmission electron microscopy
TGA	Thermogravimetric analysis
DMEM	Dulbecco's Modified Eagle's Medium
PBS	Phosphate Buffer Saline
DMSO	Dimethyl sulfoxide
EDX	Energy dispersive X-ray spectroscopy
EPD	Electrophoretic deposition
TMB	3,3′,5,5′-tetramethylbenzidine
oxTMB	Oxidized tetramethyl benzidine

HRP	Horseradish peroxidase
TA	Terephthalic acid
HTA	Hydroxyterephthalic acid
OPD	O-phenylenediamine
DAB	Diazoaminobenzene
ABTS	2,2'-azino-bis(3-ethylbenzothiazoline-6-sulphonic acid)
GOx	Glucose oxidase
DA	Dopamine
AA	Ascorbic acid
UA	Uric acid
DM	Diabetes mellitus
LOD	Limit of detection
SD	Standard deviation
K_m	Michaelis constant
V_{max}	Maximum velocity
[S]	Substrate concentration
U.S. EPA	United States Environmental Protection Agency
RT	Room temperature
R.A	Relative activity
ROS	Reactive oxygen species
E. coli	*Escherichia coli*
B. Subtilis	*Bacillus Subtilis*
CFU	Colony forming unit
NIR	Near infrared irradiation
PTT	Photothermal therapy
PDT	Photodynamic therapy

PS	Photosensitizer
L.E	Loading efficiency
MIC	Minimum inhibitory concentration
MBC	Minimum bactericidal concentration
$O.D_{600}$	Optical density at 600 nm
GC	Growth control
LPS	Lipopolysaccharide
LB	Luria-Bertani Broth
MHB	Mueller Hinton Broth
DPBF	1,3-Diphenyl isobenzofuran
U87MG	Uppsala 87 Malignant Glioma cell line
Hela	Human cervical adenocarcinoma cell line
EPR	Electron paramagnetic resonance
FBS	Fetal Bovine Serum

CHAPTER 1

1. INTRODUCTION

1.1. Nanotechnology and the development of nanomaterials

Nanotechnology can be defined as the use of technology for the preparation of tiny materials. It is a multidisciplinary field which focuses on the development of nanomaterials at an atomic scale, and was first introduced by Richard Feynman in 1959 [1]. However, in the late 1980s, nanotechnology did not receive much attention, as scientists and researchers did not possess proper tools to explore materials at the nanoscale [2]. Thereafter, the story was successfully established by the advancement of nanotechnology in the field of research, where the emergence of nanotechnology has advanced tremendously during the first decade of the 21st century, with a focus on the synthesis, characterization, and self-assembly of complex structures with at least one dimension within 100 nm or even less for application in various fields. Soon after, researchers developed multilayer semiconductor nanoparticles in the early 1990s [2].

The field of nanotechnology combines physics, chemistry, and biology for the fabrication and manipulation of nanomaterials with different dimensions and self-dependent properties that offer fundamental advantages in diverse fields.

The European commission research [3] stated that nanomaterials (NMs) can be defined as small particles in an unbound or aggregated state, with significant properties that differ from those of macromolecular scale. Nanomaterials mediate remarkable and unique physicochemical properties that can guide the creation of new structures, systems or devices that have potential applications in a broad range of scientific areas. These nanostructures are made from smart arrangement of atoms in a peculiar and specific manner, which defines their application and properties. They can also come in various shapes such as films, wires, tubes, rods, spheres, particles, cubes etc. and could be natural or synthetic and hold great potentials in in catalysis, biomedical, biotechnology, health care, textiles, electronics, coatings, and pharmaceutical industries [4].

Particularly, nanoparticles (NPs) with various morphologies and structures have received great attention in the past few decades due to their unique properties, and they represented an

effective connection between bulk counterparts and atomic structures. Their small size and large surface area influence their physiochemical properties as well their reactivity, in which these features strengthen their interaction with other materials [5].

Nanoparticles were first explored as single particles, after which scientists developed hybrid nanoparticles with extraordinary or drastically different properties and proved to be more potent than single nanoparticles [6, 7]. The chemical composition and the way these hybrid nanoparticles are fabricated influence their potential applications that greatly depend on their physiochemical properties [8]. In principle, hybrid nanomaterials are dated to the revolution of the industrial era, since then this concept has permeated the field of research.

The fabrication of nanostructured materials can be classified into two groups, depending on whether their assembly follows top-down or bottom-up approach (**Fig. 1**).

The "top-down" method is based on the use of an energy source to break down bulk materials into smaller and finer fragments to fabricate nanostructures. This approach can be classified into mechanical, thermal, high energy, and lithographic methods [9]. The mechanical method represents the simplest and cost-effective technique among all; an example is ball milling that produces nanomaterials by generating kinetic energy through grinding the bulk medium. Thermal methods in turn involve the use of heat for the fabrication of nanomaterials. Whereas, high energy processes mediate the use of an excessive input of energy that can be in the form of solar energy, heat, or electricity. Lithographic methods in particular include numerous fabrication techniques. Generally, these methods require an electron beam or light source to remove large-scale structures from a precursor referred to "resist". It is considered as the most frequently used approach in semiconductor and microelectronics industry [10].

The bottom-up approach in particular works in different direction. It involves the assembly of atoms or molecules onto one another to create nanostructures with uniform size [11] and sub-nanometer dimensions.
Synthesis of nanoparticles *via* this approach can be divided into liquid-phase and gas-phase methods; typical examples are the sol-gel, hydrothermal, solvothermal, microwave heating and chemical vapor deposition (CVD) methods [9].
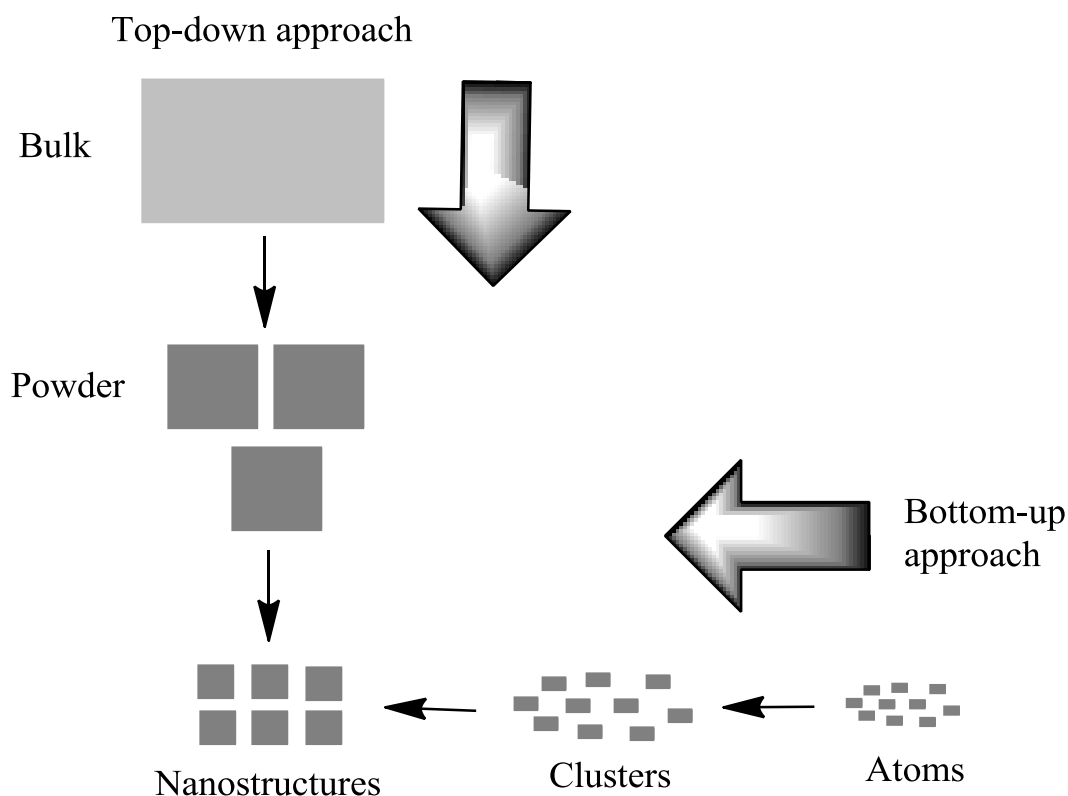
Figure 1: Schematic illustration of top-down and bottom-up approaches for the fabrication of nanostructures [8].

Nanotechnology with its vast majority of applications and the excessive use of nanomaterials in wide range of diverse fields has made huge advances over years. Among different innovative applications of nanotechnology, the use of nanomaterials as nanocatalysts [12] has opened new routes for their application in the field of sensing and showed a fundamental interest in the environmental and industrial fields.

In every aspect of our daily life and in the surrounding environment, there is a demand for information. The growing demand towards measuring the chemical environment had provoked the development of sensors that display real time analysis using cost-effective devices with high accuracy and sensitivity. According to the International Union of Pure and Applied Chemistry (lUPAC) [13], sensors are known as analytical chemicals or biological molecules that transform an analyte or a chemical information into a measurable signal [14, 15]. Traditionally, biological sensors are defined as biosensors [16] that involve the use of natural enzymes, antibodies, nucleic acids, or receptors [17] to interact with an analyte (substrate). Sensors that involve the use of antibodies are often called affinity biosensors. They differ from enzymes in their mode of action, in which antibodies possess no catalytic action, although they

bind to a specific substrate. Unlike antibodies, nucleic acids (NA) biosensors inspired increasing interest due their huge impact in diagnostics and provided a sensitive tool for detection of genetic variations. NA biosensors can be made of a single stranded DNA which hybridizes with its complementary strand to yield a quantified signal of sequence-specific information [18-20]. Moreover, proteins that are anchored in the lipid bilayer of the plasma membrane referred to as receptors are well known biosensors that can work in the same manner as antibodies. In particular, biological elements such as enzymes are called catalytic macromolecules whose roles are based on catalyzing different chemical or biological reactions that take place in living organisms. These are proteins established in the mid of the 19th century, where the first enzyme to be discovered as a protein was urease, in 1926 by James Sumner [21]. Since then, enzymes are classified as proteins or polypeptides that are self-assembled or folded in a 3-dimentional structure with a hydrophobic core confined by a hydrophilic shell, and containing a prosthetic group usually a metal atom, considered as the catalytic center, which gives enzymes their specificity and compatibility to the aqueous environment [22]. Enzymes are also defined as biocatalytic molecules that can catalyze a wide range of biochemical reactions by acting on certain substances known as substrates, with high specificity and efficiency over non-catalyzed reactions in biological systems. Enzymes are large macromolecules of molecular weight ranging from thousands to several millions. Due to the difference in molecular weight between the enzyme and its substrate, only a small fraction of the enzyme is capable for binding to the substrate, which is called the active site. The inherit substrate specificity of natural enzymes and extreme reactivity are attributed to the presence of discrete functional groups in their active sites.

1.2. Enzyme kinetics

Enzymes as discussed above are potent biocatalysts in which their kinetic assay often deals with the factors that influence the rate of an enzyme-catalyzed reaction. Typically, the reactions that are catalyzed by an enzyme follow a Michaelis–Menten kinetic model (1913) [23] that is linked to the formation of a complex enzyme-substrate. Thus, in order to understand the function of enzymes, a description of their kinetic activity has to be taken into consideration.

In the 20th century, Leonor Michaelis and Maud Leonora Menten [24] suggested a simple model under the name "Michaelis-Menten Kinetic" to describe the enzymatic effectivity. The model explains the enhancement of the reaction kinetic rate and describes how this rate is strongly dependent on both the enzyme and substrate concentrations.

Generally, a specific substrate interacts with an enzyme through binding to its active site to generate an enzyme-substrate complex (E.S) with a rate constant k_1. The reaction then proceeds by either decomposing this complex to yield the desired product (P) and regenerate the free enzyme (E) with a rate constant k_2, or dissociating the enzyme-substrate complex to the free enzyme and substrate with the rate constant k_{-1} (**Eq. 1**) [25].
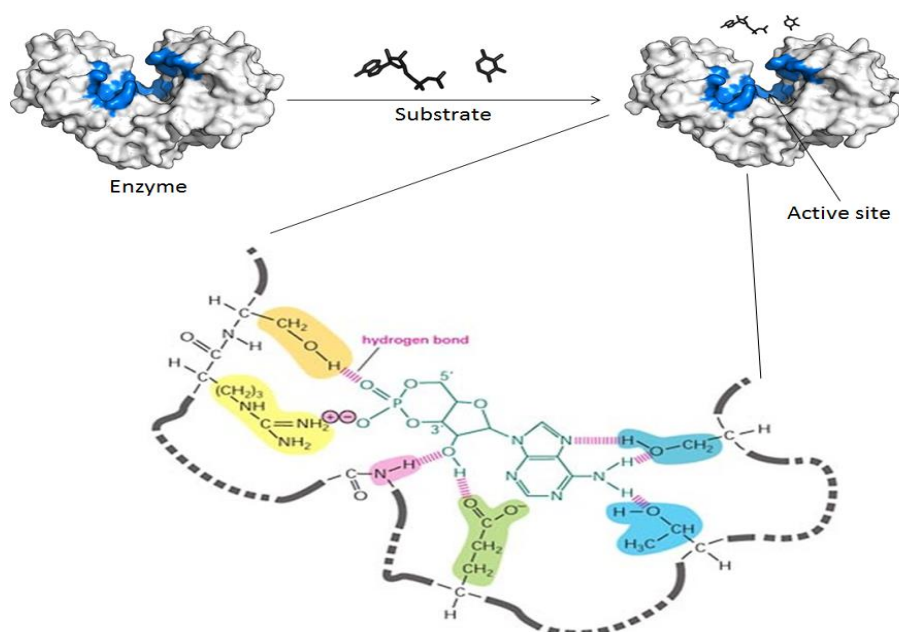
Figure 2: Schematic representation of the reaction between an enzyme and its substrate showing various binding possibilities [26].

$$E + S \underset{k_{-1}}{\overset{k_1}{\rightleftharpoons}} ES \xrightarrow{k_2} E + P \qquad (1)$$
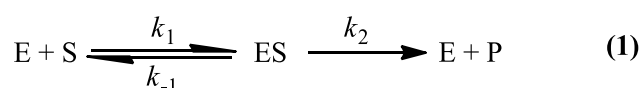
The rate constants for each step are represented as k_1, k_{-1} and k_2 and used to determine the Michaelis-Menten constant (K_m) (**Eq. 2**) [23].

$$k_m = \frac{k_{-1} + k_2}{k_1} \qquad (2)$$

In the enzyme catalyzed process, the rate of reaction which is defined as the number of moles of the product established per second (*V*), is enhanced with the increase of the amount of substrate (S) [24], and approaches a steady state when the concentration of substrate is maximum. At this stage, the rate of the reaction is called V_{max}. This indicates that the catalytic rate is no more dependent on the substrate concentration, and the enzyme is saturated with enough concentration of substrate.

By plotting the initial reaction rate (V_0) *versus* substrate concentration ([S]), a typical Michaelis-Menten curve can be generated **(Fig. 3a)**, and the relation between this rate and the substrate concentration determines the enzyme affinity to this substrate. This is usually referred to as k_m, a Michaelis constant, at which the enzyme reaches half of V_{max} when its active site is half filled. Indeed, a smaller value of k_m reveals that the enzyme is more active and has more affinity to its substrate.
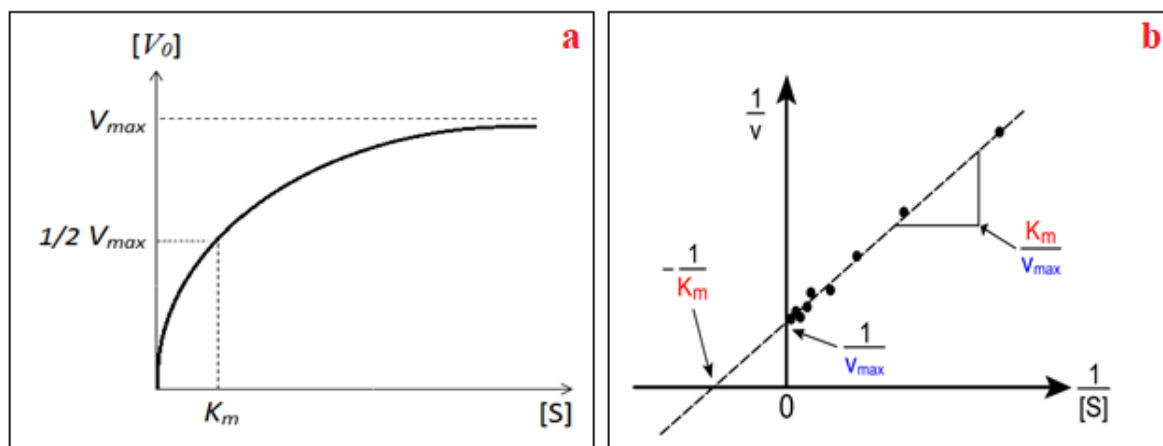
Figure 3: Graphical plot of the enzymatic reaction rate and substrate concentration according to Michaelis-Menten equation (a), and the Lineweaver Burk double reciprocal plot (b) [23].

The Michaelis-Menten equation that describes this aspect is summarized in the following equation **(Eq. 3)**:

$$V_0 = \frac{(V_m \times [S])}{([S] + K_m)} \qquad \textbf{(3)}$$

By inverting the Michaelis-Menten equation, one can get a Lineweaver Burk equation **(Eq. 4)** [27], which is a common way of clarifying the kinetic data:

$$\frac{1}{V} = \frac{K_m}{V_{max}} \times \frac{1}{[S]} + \frac{1}{V_{max}} \qquad \textbf{(4)}$$

The catalytic parameters (K_m and V_{max}) can be determined from a Lineweaver–Burk equation expressed in **Eq. 4**, by plotting the reciprocals of the initial rate *versus* substrate concentration, as shown in **Figure 3b**, where the y-intercept allows determining the V_{max} and the x-intercept gives the K_m value.

The rate at which the enzyme works can be influenced by several parameters such as substrate concentration, pH and temperature. This can be explained by the higher collision and binding affinity as the substrate is more available. Also with the increase of temperature to a certain

limit, the molecular motion between the enzyme and its substrate increases. However, the influence of pH is correlated to its effect on protein conformation, since enzymes are proteins made of amino acids (a.a), thus certain amino acids in the active site of the enzyme become protonated or deprotonated at different pH, which alters the structure of the enzyme, thereby changing the ionization state of a.a, and in turn affects their catalytic behavior.

1.3. Enzyme assay

The enzyme assay is a kinetic method that enables determining the rate of an enzyme-catalyzed reaction. Currently, the assay that determines the rate of enzymatic reactions is based on Kitz and Wilson model [28, 29], also called dilution assay. Dilution assay aims to determine the activity of enzyme in a specified period of time, in which the enzyme is incubated with its substrate and aliquots are then taken during the reaction at specific time intervals. During each time interval, the substrate is transformed into a chromophore or fluorophore product which can be quantified by optical spectroscopy through a spectral signal at a specific wavelength [23]. Furthermore, by plotting the concentration of this product formed against time, and considering the slope of the curve within the linear range, one can determine the initial rate of reaction.

Enzymatic assays are based on fluorogenic or chromogenic substrates whose fluorescence or absorbance properties are altered during the enzymatic reaction, in which upon the reaction between the substrate and the enzyme, a fluorescent or colored product is formed which can be easily monitored by spectrophotometry. However, some products that are formed during the enzyme-catalyzed reaction cannot be detected by optical spectroscopies as they do not absorb light, so the use of indicators can help solve the issue. This assay is referred to an enzyme-coupled model, where the product formed during one reaction can be used as a substrate for the next reaction, until a spectral signal can be obtained.

1.4. Artificial enzyme-mimics

1.4.1. Nanozymes

The development of nanomaterials for solving technological issues through mimicking nature is a general process which is referred to as biomimetic [30]. The incorporation of such biomimetics in monitoring technologies that are able for sensitive, selective and rapid analysis is a steadily growing field of interest for disease diagnosis [31], drug delivery [32] and environmental protection [33], which generally mediates the use of biosensors.

Biosensors were first reported in the 1960s by Lyons and Clark [34], who fabricated a glucose detection system. Thereafter, a rapid evolution has been made in 1967 by Hicks and Updike [15] for the development of enzyme-based sensors. The use of natural enzymes in this field is attributed to their high catalytic action, in which one molecule of the enzyme can transform thousands of specific analytes in a few seconds.

Natural enzymes are commonly used in biosensors to detect specific analytes at a very low level. They are characterized by extreme sensitivity, substrate specificity, and fast reaction response. Despite their advantages in sensing, the high cost associated with their extraction, purification and isolation is still a major challenge. Moreover, natural enzymes work properly under physiological conditions, while they can be easily inactivated under harsh conditions including high temperature, alkaline media, or strong acidic environment [35]. The main reason behind, is due to their 3D structure which exposes the active site and causes a complete loss in their catalytic activity. Scientists proposed that re-engineering of natural enzymes by altering the structure of their active sites could become a straightforward method to recover their catalytic activity [36]. Thereafter, immobilization of enzymes on solid support such bulk materials, nanoparticles, or conjugation with polymers such as polyethylene glycol (PEG), and encapsulation in nano-gels or porous materials [36] were developed as a new approach to improve the properties of natural enzymes such as their thermal stability, and tolerance to different pH or organic solvents to fulfill the needs of practical uses. Despite that enzyme immobilization showed higher catalytic activity than the native ones, their high cost and the unfavorable conformational changes hampered their practical applications [37]. Therefore, scientists made huge efforts for designing highly stable and cost-effective human-made enzymes and alternative materials that are more robust, and differ from physiological enzymes, but possessing same kinetics, mechanisms and characteristics as natural enzymes to overcome the aforementioned drawbacks [38].

The concept of utilizing enzyme mimics was first reported by Breslow in 1970 [39]. Following this, new prospects have inspired the design of alternative enzyme mimics in the field of biomimetic chemistry. This pioneering work has brought scientists and researchers to fabricate materials which imitate the biochemical reactions in natural environment and biological systems, where they established the use of biomolecules and metal complexes having same function and structure as natural enzymes such as cyclodextrin, porphoryin, hemin, etc. as a first attempt [40-42]. Since then, an enormous development has been achieved in the scope of enzyme mimics and accessed the field of analytical chemistry.
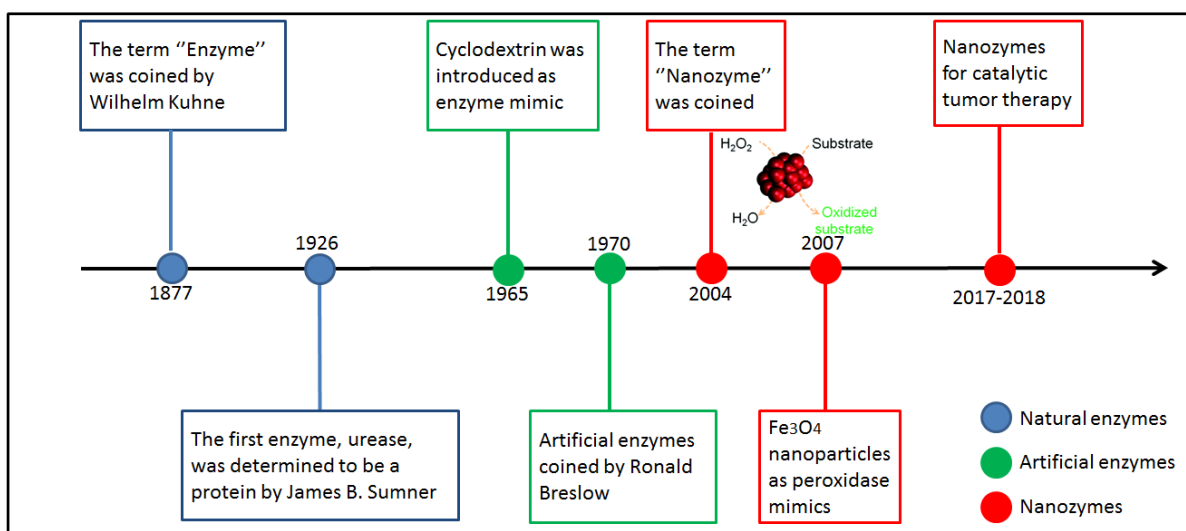
Figure 4: Schematic illustration for the evolution of enzyme mimics.

Tremendous advancement in nanotechnology has prompted the engineering of nanomaterials of various properties and functions as artificial enzyme mimics for industrial applications [43-45]. However, many of these applications were based on the interaction of nanomaterials with enzymes, which alters the physiochemical properties of the nanomaterials and causes conformational changes in the structure of enzymes, which in turn block their catalytic activity [46]. Also, most of the nanomaterials have limited applications due to their cytotoxicity, low selectivity and stability. Therefore, there is a persistent need to discover new enzyme mimics with advanced properties. This issue promoted researchers to utilize nanomaterials as supports for enhancing the enzymatic performance over a broader range of applications, including sensing of biomolecules of interest. An example using glucose oxidase (GOx) enzyme immobilized on gold nanoparticles for sensing of glucose [47], among others. Although gold nanoparticles have been utilized as substituents to native proteins, yet the natural enzyme GOx is still required [48]. Thus, the issue is still unresolved, and the non-enzymatic sensing for glucose in the real meaning is not achieved.

Enzymomimetics are a new generation of artificial enzymes that imitate the catalytic site in natural enzymes "the active site'', and since these agonists are synthetic nanomaterials, they can be used for various applications through altering their structure. Recently, nanomaterials have been fabricated with attached proteins, amino acids or prosthetic metal ions [49], to yield a typical enzyme mimic that is more potent than the enzyme itself. In particular, inorganic materials have been widely utilized to prepare a variety of nanostructured materials in a nano sized range called ''nanoparticles'' and become the forefront scaffolds for developing smart

and bioactive materials. Inorganic nanomaterials ranging from elemental nanoparticles including copper, gold, ferromagnetic, silver, to metal oxide nanoparticles including Fe_3O_4, Cu_2O, Co_3O_4, and allotropes such as graphene, carbon nanotubes, fullerenes, and metal-organic frameworks [50-59] overcome the traditional artificial enzymes which are based on organic materials, and replaced natural enzymes due to their ease of synthesis, low cost, high stability, low molecular weight, less complexed structure and high catalytic action. They gained critical research consideration and enormous interest in a broad range of applications, such as industrial biocatalytic processes, analytical science, therapeutics, biomedical imaging, tissue engineering, energy devices, and sensing [60-65]. Since then, a tremendous amount of efforts has been devoted to the preparation of a plethora of enzyme-like nanomaterials, commonly designed as nanozymes [66].

Nanozymes have been known since 2013, and considered as novel enzyme mimics that differ from immobilized enzymes or native ones. These agonists are characterized by unique properties including superior catalytic conversion efficiency, high stability, simple synthesis method, and ability to tolerate harsh conditions such as high temperature and low pH medium [66, 67]. Their cyclic mode of action and the possibility of recovery without considerable loss of activity makes them distinctive nanomaterials [68]. Their small size also permits their use in biomedical applications due to their ability to easily penetrate cells, in addition to their large surface-to-volume ratio that enables further surface modification and enhanced their catalytic behavior [69, 70]. Meanwhile, the catalytic action of nanozymes can be altered by size, structure and morphology of the nanoparticles, which distinguishes them from natural enzymes. Nanozymes differ from other materials by their catalytic action which is manifested by the nanomaterial itself that follows typical Michaelis-Menten kinetics. These unique features not only supply nanozymes with numerous functionalities, but also extend their use for future applications.

Typically, enzyme mimics can be designed in two different approaches: "functional mimics", which is mimicking the activity of natural enzymes *via* utilizing metal complexes, or ''structural mimics'' that resemble the structure of the active site in an enzyme through functional moieties [49].
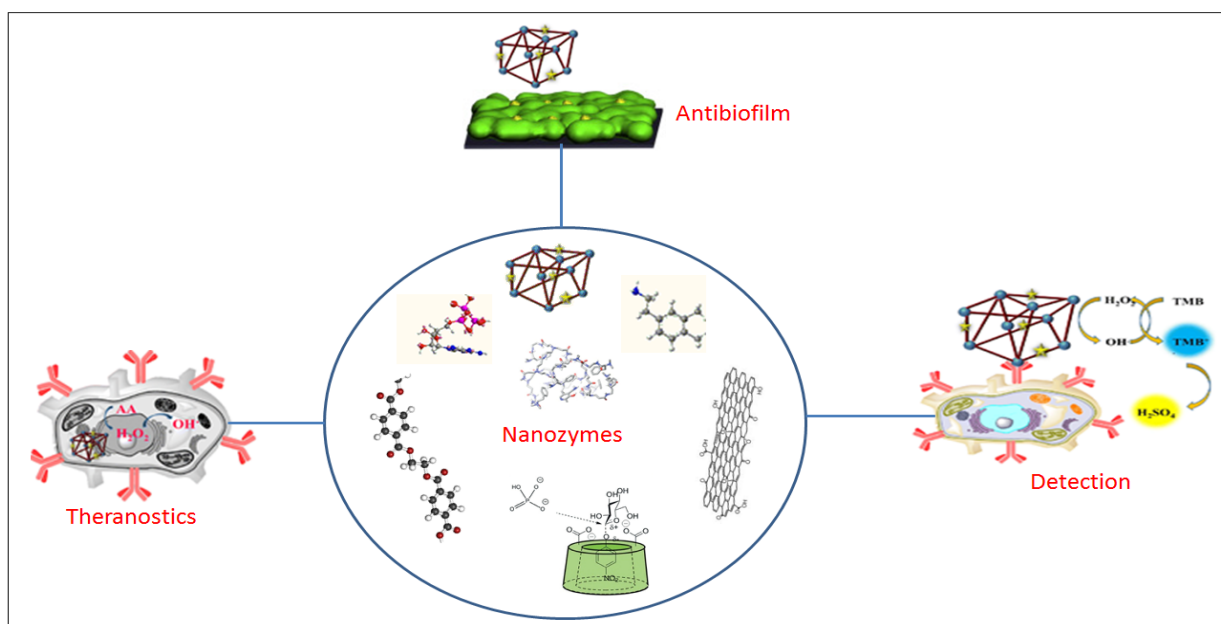
Figure 5: Schematic illustration of different applications of nanozymes.

The first inorganic nanoparticles to be utilized as enzyme mimics were reported by Gao *et al.* in 2007 [71]. They demonstrated that ferromagnetic Fe_3O_4 nanoparticles possess similar catalytic behavior to the natural occurring horseradish peroxidase (HRP) enzyme, in oxidizing organic peroxidase substrates such as 3,3',5,5'-tetramethylbenzidine (TMB), o-phenylenediamine (OPD), diazoaminobenzene (DAB), and 2,2'-azino-bis(3-ethylbenzothiazoline-6-sulphonic acid) (ABTS) in the presence of favorable amount of H_2O_2 under optimal conditions (pH and temperature) and producing a product that can be monitored through color changes. Fe_3O_4 nanoparticles even exhibited better catalytic performance than the native enzyme, which may be due to a plenty of iron ions on the surface of Fe_3O_4 NPs. This assay was developed for colorimetric detection of various analytes and wastewater treatment purposes.

Iron oxide NPs, even called IONzymes [72], opened new prospects to explore different kinds of bioactive nanomaterials and nanoparticles modulated in a way similar to natural enzymes such as catalases, superoxide dismutase (SOD), oxidase mimetics, and particularly peroxidases [73] for sensing assays. Soon afterwards, nanoparticles enter robustly the field of sensing for the determination of biomolecules for environmental protection and disease diagnosis and showed unexpected enzyme-like catalytic activity. Comprehensive studies proposed that the ability of nanomaterials to mimic natural enzymes is related to their adequacy in generating reactive oxygen species (ROS). Although breakthroughs in enzyme mimics have become

abundant in the field of sensing, yet immense efforts have been dedicated to peroxidase-like enzyme mimics.
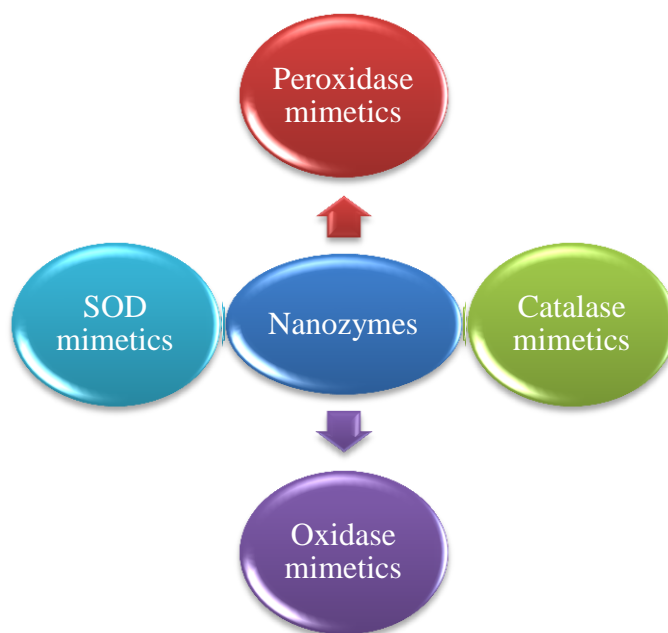
Figure 6: Schematic illustration of different types of nanozymes.

1.4.1.1. Peroxidase enzyme mimics

Peroxidases are a large family of natural enzymes that catalyze the oxidation of various substrates in the presence of hydrogen peroxide (H_2O_2), a naturally occurring by-product of oxygen metabolism. The oxidative nature of these enzymes promoted their use in a wide scope of applications. Peroxidases can be also considered as antioxidant enzymes [74], being found naturally in plants, animals, bacteria, algae and fungi [75]. They are classified based on the presence of a heme group (Iron (III) protoporphyrin IX) as a prosthetic group [76], and they are differentiated by the presence or absence of calcium, disulfide bridges, and N-terminal signal peptide in their structure.
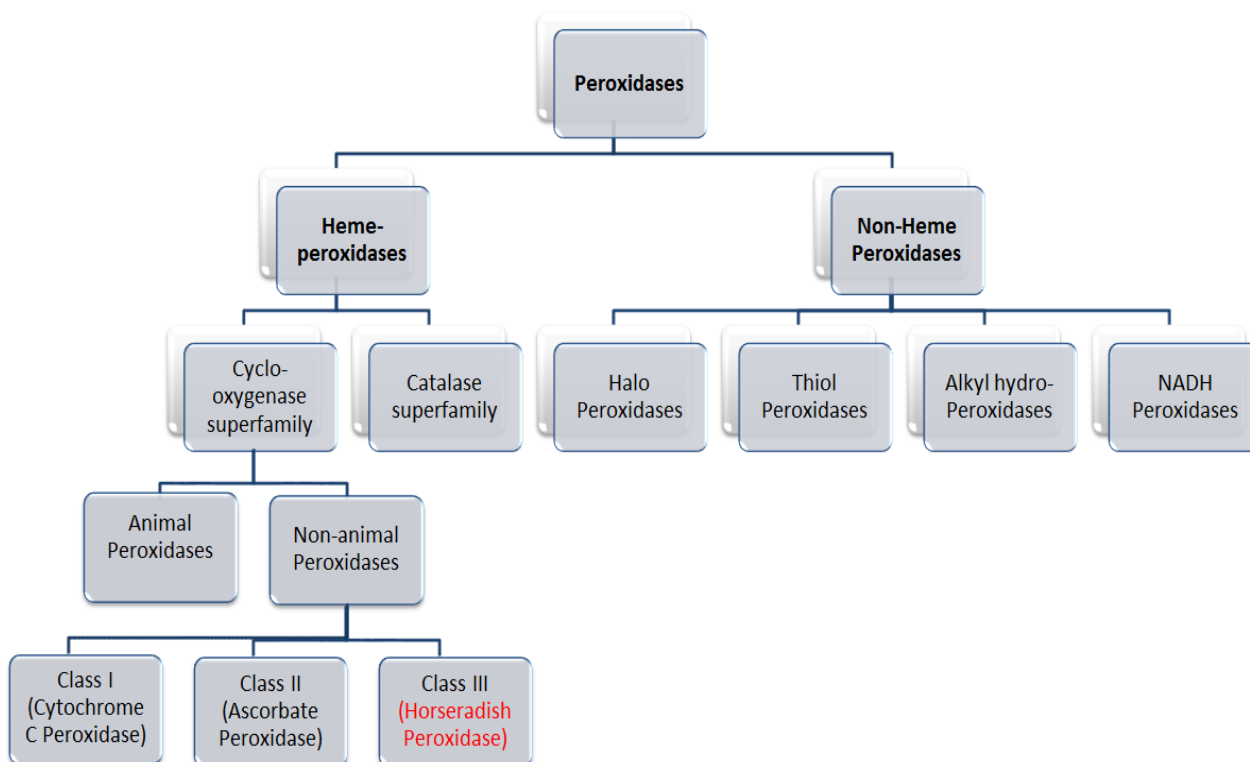
Figure 7: Schematic representation of different classes of peroxidases.

1.4.1.1.1. Mechanism of action of peroxidases

Most classess of peroxidases display a huge role in scavenging reactive oxygen species (ROS), which are defined as reactive molecules or free radicals such as superoxide anions ($O_2^{\bullet -}$), H_2O_2, and organic peroxides, produced during different metabolic processes in aerobic cells, or through oxidation reactions catalyzed by metals [77]. Although ROS participate in various cellular processes, the continuous exposure to high ROS levels can drive the cells through oxidative stress, which leads to cell apoptosis thereby causing serious diseases, with H_2O_2 being the most abundant (its intracellular concentration reaches about 10^{-7} M) [78].

Among various classess of peroxdiases listed in **Figure 7**, class III peroxidases especially HRP enzymes, being the most common example with extremly different specificities to substrates, are adopted in a wide scope of physiological processes such as cell wall metabolism [79] and ROS scavenging [80], and their use in analytical and clinical chemistry applications due to their efficient catalytic activity in converting coloreless substrates into colored oxidized products that can be easily detected through various analytical techniques.

Some of the reactive oxygen species such as H_2O_2 are considered as antibacterial agents. However, under particular conditions, they serve as cytotoxic agents when present in excessive

amounts inside cells ($\geq 50\ \mu M$), thereby altering the physiological state of cells and ultimately leading to oxidative DNA damage thus causing various diseases such as aging, diabetes, and cancer [49]. In this manner, it appears to be likely that most cells are susceptible to the toxic effects of H_2O_2. Thus, the presence of peroxidase inside cells serves as a detoxifying agent to remove excess H_2O_2 and regulate its level. The mechanism behind the interaction between the substrate and peroxidase enzymes is assigned to the partial unfolding configuration of the enzyme, which accelerates the access of H_2O_2 to the enzyme's reaction center, mainly the heme group [81].

Peroxidase enzymes such as HRP with its porphyrin heme group in a trivalent state, present in its active sites, can use H_2O_2 as a substrate to generate free radicals (**Fig. 8**) [75, 82]. HRP enzyme causes decomposition of H_2O_2 to generate $HO^{\bullet}$ and ferryl heme (Fe(VI)=O), where in the presence of an organic chromogenic substrate such as TMB results in the production of an oxidized free radical cation. A number of fluorogenic and chromogenic substrates have been integrated with HRP enzyme and act as hydrogen donors to produce colored products that can be easily observed by the naked eye for sensing of ROS and measuring their concentration.
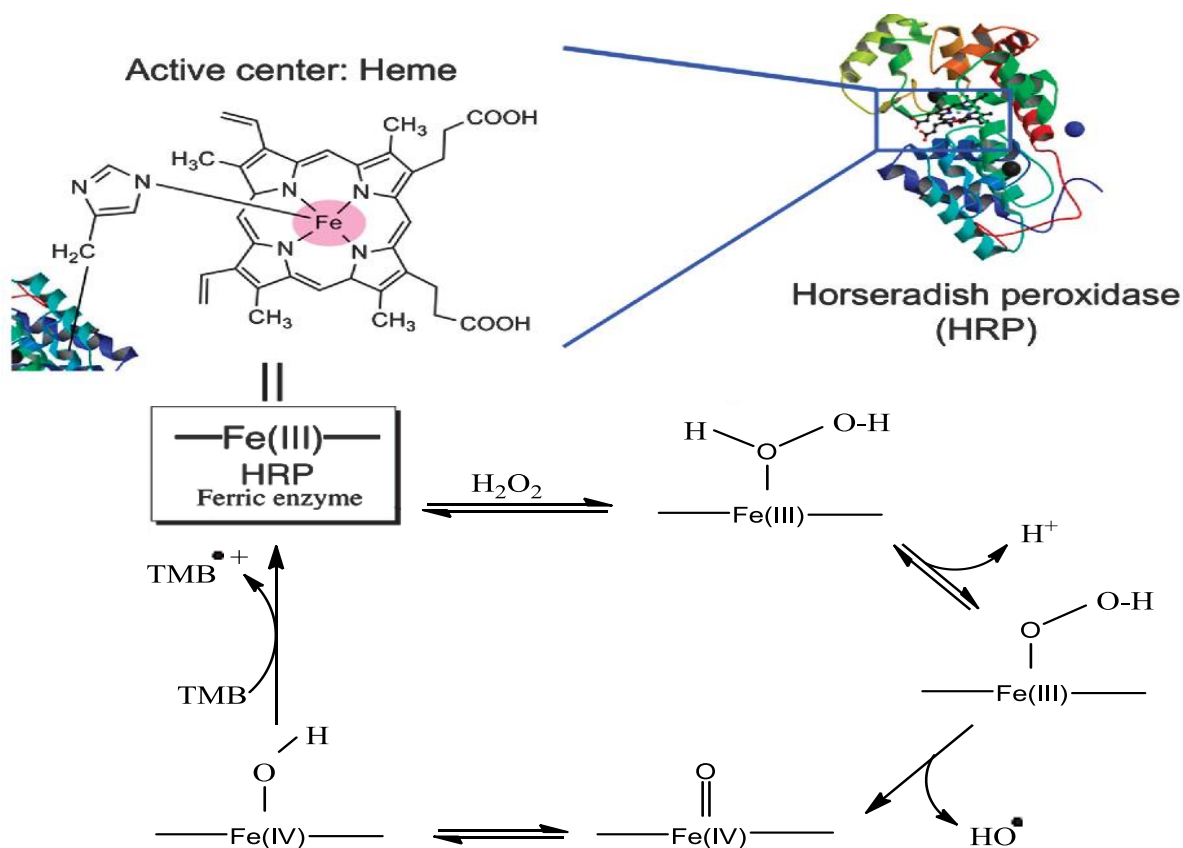
Figure 8: Scheme for the proposed mechanism of the horseradish peroxidase (HRP) for radical formation.

Interested by the expansion of innovative nanomaterials as peroxidase mimics, various chemical probes have been developed as essential tools to monitor intracellular ROS generation [83], where the detection of ROS species is based on the interaction with nanomaterials to construct a measurable data. Thus, to better understand the peroxidase-like catalytic behavior as discussed previously, decomposition of H_2O_2 and oxidation of substrate are essential in this assay. Generally, nanozymes can bind and react with H_2O_2 to produce an intermediate state through generating $HO^\bullet$, after which the presence of a substrate such as TMB, being the most commonly used chromophore, can be oxidized by the generated $HO^\bullet$. The mechanism is based on the abstraction of electrons from the amino function of TMB to generate a colored oxidized product (ox-TMB). In principle, TMB oxidation can either occur on the nanozyme's surface, in which the two molecules (TMB and H_2O_2) can adsorb on the surface *via* Langmuir-Hinshelwood mechanism **(Fig. 9)** or in solution by Eley-Rideal mechanism, where TMB comes from the bulk solution [84].
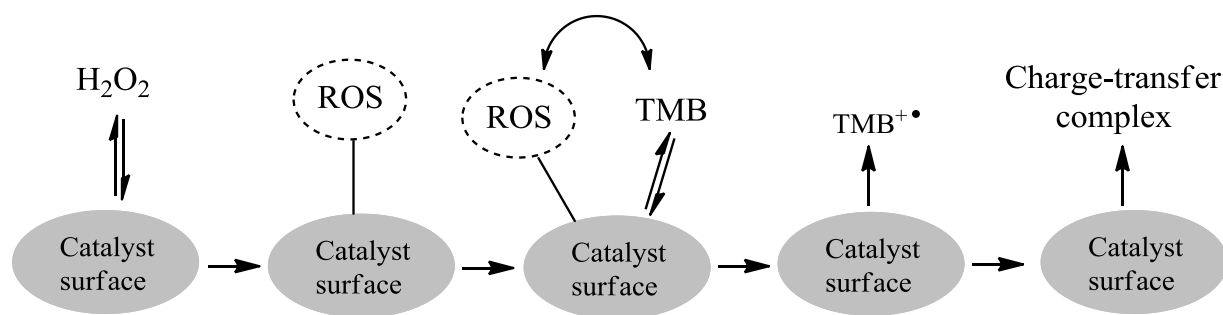
Figure 9: Mechanistic model for TMB oxidation on the surface of nanozymes *via* Langmuir-Hinshelwood kinetics.

This enzymatic mechanism can be also correlated to the Fenton-chemistry, as the existence of transition metal ions such as iron (Fe^{2+}) can cause decomposition of H_2O_2 into powerful oxidizing agents with unpaired electron, hydroxyl radicals ($HO^\bullet$), through a Fenton-mediated reaction in acidic environment [85]. The generated radicals are able to effectively degrade pollutants in the wastewater stream. To evaluate this strategy, EPR (electron paramagnetic resonance) commonly used for determining organic radicals and metal complexes can be also considered as a useful tool to confirm the generation of $HO^\bullet$ at an acidic pH, suggesting that acidic medium is essential for Fenton chemistry [86, 87]. In general, all the reported studies on peroxidase mimics have shown that an acidic medium is one of the principle prerequisites to generate a colorimetric oxidized product for the detection of targeted substrates [88].

1.4.1.1.2. Fenton chemistry

The Fenton chemistry is considered as an advanced oxidation process (AOP), which can be summarized as an approach to produce $HO^{\bullet}$ for the oxidation of majority of organic and chemical contaminants present in the water stream [89]. The oxidation process is based on H_2O_2 as a Fenton reagent which is catalyzed by ferrous salt, and dates back to 1894 when Henry John Horstman Fenton [90] proved that ferrous iron salts robustly promote the oxidation of tartaric acid by H_2O_2 [91]. The discovery of Fenton played a key role in all aspects of our life. Since then, the application of Fenton enters the field of chemistry, biology, and many industrial processes.

The main steps of the Fenton reaction are summarized in the following equations (**Eq. 5-8**), to describe the reaction of ferrous ions with H_2O_2 in acidic condition [87, 92].

$$Fe^{2+} + H_2O_2 \rightarrow Fe^{3+} + OH^- + HO^{\bullet} \qquad \textbf{(5)}$$

$$H_2O_2 + HO^{\bullet} \rightarrow H_2O + HO_2^{\bullet} \qquad \textbf{(6)}$$

$$H_2O_2 + HO_2^{\bullet} \rightarrow H_2O + O_2 + HO^{\bullet} \qquad \textbf{(7)}$$

$$Fe^{2+} + HO^{\bullet} \rightarrow Fe^{3+} + OH^- \qquad \textbf{(8)}$$
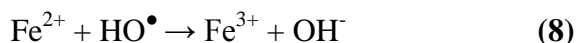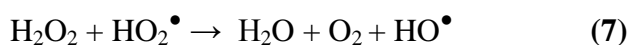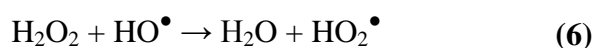
The first step in the Fenton reaction is initiated by the generation of $HO^{\bullet}$ by ferrous ions and is called the classical Fenton reaction, while steps (**6**) and (**7**) propagate the chain reaction, and step (**8**) is a termination reaction in which ferrous iron (Fe^{2+}) is consumed to produce ferric ions (Fe^{3+}).

In 1934, Haber and Weiss [93] suggested that the generation of $HO^{\bullet}$ by iron (II) ions (Fe^{2+}) is a chain reaction. Theoretically, this process is related to the free radical mechanism, and became a potential approach for the generation of oxidized species to eliminate toxic contaminants. Being the most potent free radicals, hydroxyl radicals (E^o=2.33 V) [94] can be used to oxidize a wide range of chemical species at a relatively high rate.

In 1951, Barb and co-workers [95, 96] changed the Haber and Weiss Fenton's classical mechanism showing the regeneration of H_2O_2, where iron is cycled between (+2) and (+3) oxidation states.

$$Fe^{3+} + H_2O_2 \rightarrow Fe^{2+} + H^+ + HO_2^{\bullet} \qquad \textbf{(9)}$$

$$Fe^{3+} + HO_2^{\bullet} \rightarrow Fe^{2+} + H^+ + O_2 \qquad \textbf{(10)}$$

$$Fe^{2+} + HO_2^{\bullet} + H^+ \rightarrow Fe^{3+} + H_2O_2 \qquad \textbf{(11)}$$

$$2HO_2^{\bullet} \rightarrow H_2O_2 + O_2 \qquad \textbf{(12)}$$
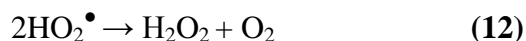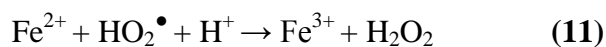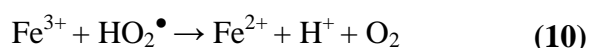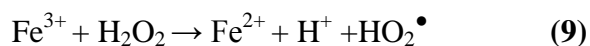
The generated hydroxyl radicals can then oxidize organic compounds (RH or R) through elimination of H-atom or by $HO^{\bullet}$ addition, thus yielding carbon radicals.

$$RH + HO^{\bullet} \rightarrow H_2O + R^{\bullet} \qquad \textbf{(13)}$$

$$R + HO^{\bullet} \rightarrow {}^{\bullet}ROH \qquad \textbf{(14)}$$
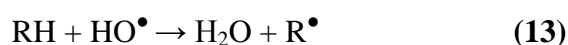
In this mechanism, H_2O_2 can act as an oxidizing or a reducing agent depending on the species present. It can either reduce Fe^{3+} to form Fe^{2+}, which then readily reacts with H_2O_2 to generate $HO^{\bullet}$. Thereafter, Walling et al. (1975) [97] improved the overall Fenton reaction into a more simplified step, where the existence of H^+ is necessary for the decomposition of H_2O_2 and oxidation of ferrous iron. From here, the Fenton process is shown to be pH-dependent.

$$2Fe^{2+} + H_2O_2 + 2H^+ \rightarrow 2Fe^{3+} + 2H_2O \qquad \textbf{(15)}$$
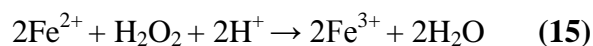
However, a neutral pH medium causes the dismutation of H_2O_2 into water and oxygen [98]:

$$2H_2O_2 \rightarrow O_2 + H_2O \qquad \textbf{(16)}$$
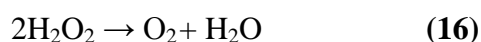
The Fenton process was then cited as a typical model for industrial processes, and promoted the development of new nanomaterials to catalyze the decomposition of H_2O_2 for the degradation of organic contaminants and sensing of biomolecules or metal ions, and becomes the subject of current studies. Numerous Fenton-like transition metal ions such as copper ions (Cu^{2+}) can also initiate the decomposition of H_2O_2. Thereby, researchers have found that the catalytic mechanism associated with nanozymes is quite similar to Fenton process, which is derived from the presence of transition metal ions that play a key role in the peroxidase-like catalytic activity, similar to the coordinated heme iron group, to achieve effective electron transfer in this redox cycle.

Nanomaterials possessing peroxidase-like and Fenton-like behavior can be also integrated with other nanozymes or metal ions to create multifunctional hybrid complexes with enhanced catalytic activity. The main advantages of nanozymes over natural enzymes is their long-term stability even under harsh conditions, such as high temperature, strong acidic or basic environments, and their activity can be tuned based on the application needs. Moreover, their activity can be also affected by surface charge, where nanomaterials with positive surface charge possess higher catalytic activity when a negatively charged substrate is present, and vice versa [72], due to the electrostatic interactions mediated by this process.

1.4.1.2. Superoxide Dismutase (SOD) mimics

Superoxide dismutase (SOD) is another naturally occurring antioxidant enzyme, which catalyzes the dismutation of a superoxide anion ($O_2^{\bullet-}$) into H_2O_2 and molecular oxygen (O_2) (**Eq. 17**). Some SOD enzymes have a transition metal ion in their core, which enhances the activity of the enzyme to mediate an oxidation-reduction reaction [99]. Although the naturally occurring SOD enzyme plays an essential role in superoxide anions scavenging, its huge synthesis cost and low stability inspired the development of alternative nanozymes. The first nanozyme displaying SOD activity was reported by Singh *et al.* [100] using cerium NPs, as cerium can be cycled between Ce^{4+} and Ce^{3+} ions, making it a promising candidate for the development of enzyme mimics. Dugan *et al.* [101] also utilized fullerene-based nanomaterials as SOD enzyme-mimics, among others.

$$2O_2^{\bullet-} + 2H^+ \rightarrow O_2 + H_2O_2 \qquad \textbf{(17)}$$
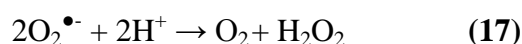
By possessing the ability to change their oxidation states, nanoparticles such as Fe, Ce, Se, Si, Zn, and Mn oxides can constantly neutralize superoxide anionic radicals [68], thus mimicking SOD activity and protecting biological compartments from oxidative stress.

1.4.1.3. Catalase mimics

Catalase is a biological enzyme that catalyzes the decomposition of the final product of superoxide radicals' dismutation, H_2O_2, into water (H_2O) and molecular oxygen (O_2) (**Eq. 18**), to complete the detoxification process which was already initiated by superoxide dismutase. Despite the low reactivity and high stability of H_2O_2, yet there is a possibility to be converted into highly reactive $HO^{\bullet}$ by Fenton-mediated and Haber-Weiss reactions, in the presence of transition metal ions [102]. Thus, it is fundamental for catalase enzyme to neutralize H_2O_2 to H_2O and O_2.

$$H_2O_2 \rightarrow \tfrac{1}{2}\,O_2 + H_2O \qquad\qquad \textbf{(18)}$$

Researchers have utilized different nanoparticles possessing catalase-like activity, such as Fe_2O_3 and Co_3O_4 nanoparticles, among others [103-106], and showed that the use of catalase mimics can enhance the cell defense against excess H_2O_2 concentration. However, other reported studies revealed that some catalase mimic nanoparticles can also exhibit peroxidase-like activity in acidic environment. Thus, pH plays a predominant role in the relative activity of enzyme mimics. This pioneering work incentivized the development of new nanozymes with dual enzyme-mimetic function [107].

With these interesting properties, a promising approach can be achieved by utilizing these nanomaterials in sensing processes along with their use in biomedical applications such as cancer diagnosis and treatment, since it is well known that tumors possess a slightly acidic pH, thus dual model functioning nanomaterials can cause cancer cell death due to their ability to generate hydroxyl radicals in acidic environment, thereby lowering H_2O_2 content in normal cells.
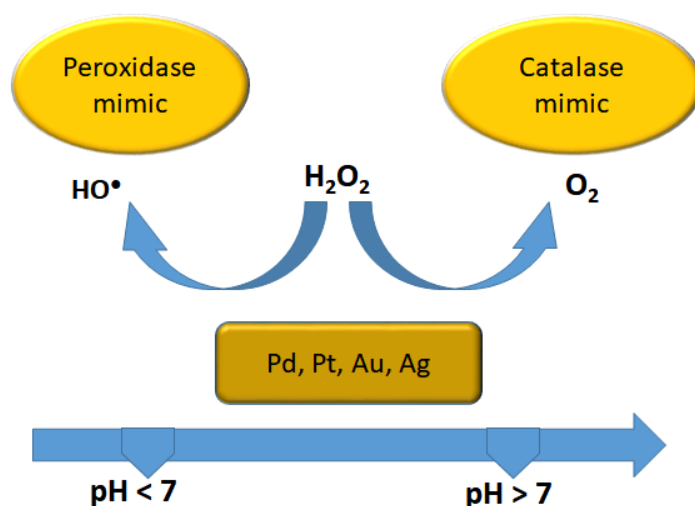
Figure 10: The multifunctional enzyme-mimic behavior of Pd, Pt, Au, and Ag metals at different pH.

1.4.1.4. Oxidase mimics

Nanozymes mimicking oxidases are implicated in the catalytic redox reaction where the oxidation of substrate (RH) occurs in the presence of molecular oxygen as an electron acceptor to generate H_2O_2 or water. Typical models of this category are cytochrome c oxidase and glucose oxidase.

$$2RH + \tfrac{1}{2}\,O_2 \rightarrow 2R + H_2O \qquad \textbf{(19)}$$

$$2RH + 3/2\,O_2 + H_2O \rightarrow 2R + 2H_2O_2 \qquad \textbf{(20)}$$
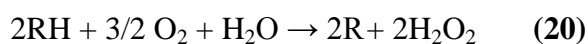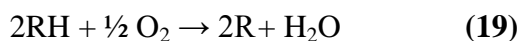
Oxidase mimics such as CeO_2, $CoFe_2O_4$, and $MnFe_2O_4$, are also demonstrated as ideal candidates for sensing of chemical and biological substrates [108-110].

The mechanism of enzyme mimics can be summarized in the figure below (**Fig. 11**).
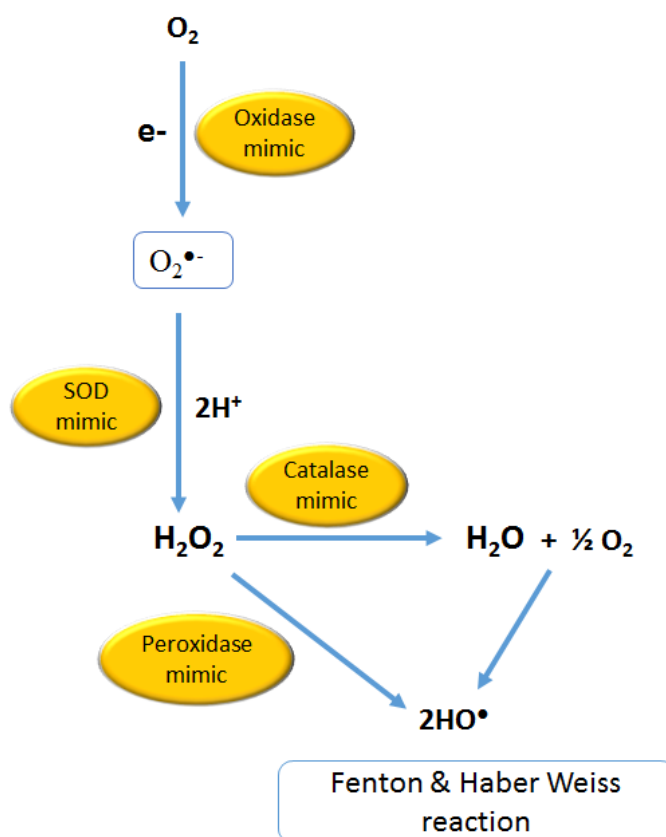
Figure 11: The generation of hydroxyl radicals mediated by different types of enzyme mimics.

1.4.2. Applications and properties of enzyme mimics

There are plentiful applications of nanozymes reported in literature (**Fig. 12**) and it is out of the scope of this thesis to discuss all of them. We will thus focus on the ones applied during this thesis work to give more detailed information about their interest.
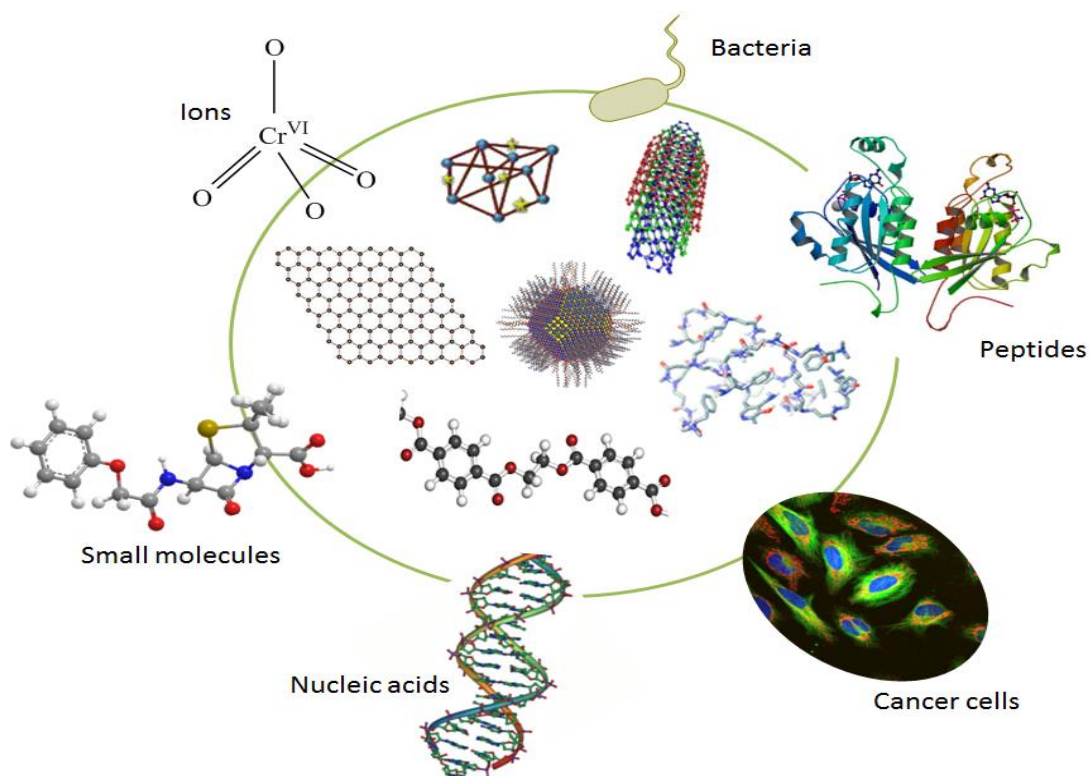
Figure 12: Schematic illustration of various sensing applications of nanozymes.

The development of simple, cost-effective innovative methodology using inorganic nanomaterials as enzyme mimics openned new paradigms for their widespread use in various fields ranging from photovoltaic, photocatalysis, energy conversion devices, biosensors, wastewater treatment and food industry [108, 111, 112]. Moreover, the fabrication of biocompatible nanozymes or coating with biocomaptible nanomaterials being approved by the US Food and Drug Administration enhances their use in biomedical applications for treatment of different diseases [113]. Thus minor alterations in the properties of nanomaterials can lead to major transformation in their applications.

Due to their fascinating properties such as novel magnetic, physical, chemical, electronic and surface properties, as well their facile synthesis, low cost, surface functionalization, small size, high surface area, catalytic specificity [114], high colloidal stability, high catalytic performance and fast reaction response [115], nanozymes replace physiological enzymes and many other traditional analytical methods and became ideal candidates in the development of enzyme-free nanosensors for field-based applications [116].
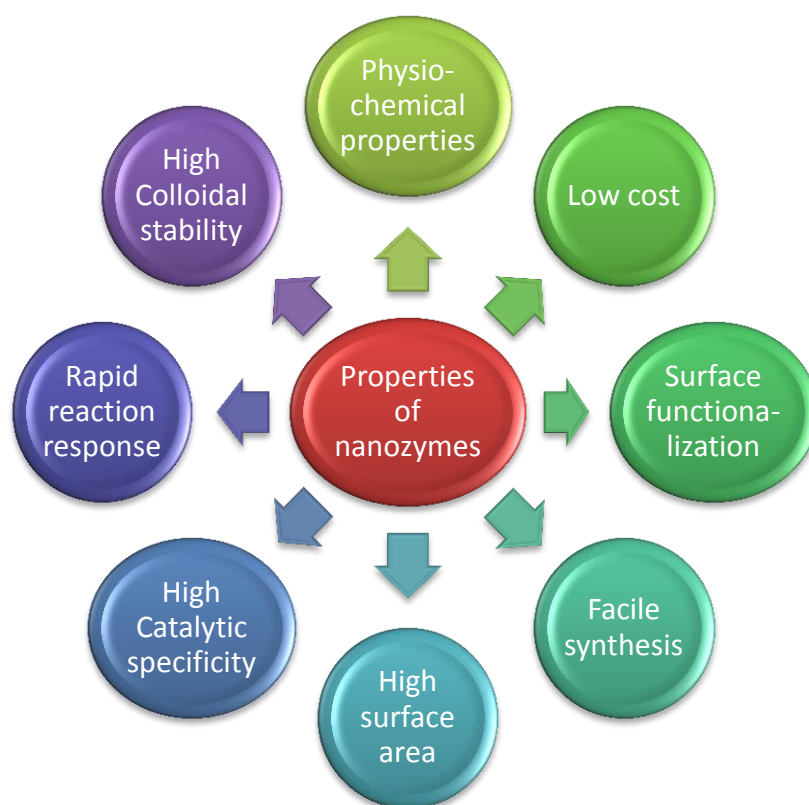
Figure 13: Intrinsic properties of nanozymes.

In general, nanosensors are defined as hybrid nanomaterials which are capable of identifying and quantifying specific chemical species including drugs, pesticides, biological molecules and metal ions [117] in a real-time mode. In order to achieve a robust analytical tool, nanosensors must possess multimodal functioning in terms of selectivity, specificity, stability and reusability, as well the ability to detect analytes at an ultralow concentration. Although nanosensors can fulfill these requirements, yet their catalytic activity can be strongly affected by various parameters including pH, buffer, concentration of salt in buffer, and temperature, where any change in one of these parameters can alter dramatically the catalytic performance of the nanosensor.

1.4.3. Analytical detection methods

Biomolecules and many ions play a vital role in nature. However, when they exceed their normal level, they possess some notion of toxicity, causing various disorders in cells which lead to serious diseases on the long term and huge threat to human health. Detection and speciation of these species attracted researchers' attention and encouraged them to sense their concentrations in different samples using various analytical techniques.

Real-time analytical methodologies for detection of analytes are becoming progressively important. It is not surprising that new techniques for detection exploit the intrinsic features of nanomaterials and became the research area of interest. Over the past few decades, advances in nanotechnology and nano-science propelled the development of new analytical tools to monitor the concentrations of biological molecules and ions [118], and utilize new instruments that can measure the properties of nanomaterials which are sensitive to changes at the molecular level. A wide variety of analytical methods have been utilized for the quantitative determination of ions and biological molecules, such as inductively coupled plasma-mass spectroscopy (ICP-MS), inductively coupled plasma-atomic emission spectroscopy (ICP-AES), X-ray fluorescence spectrometry (XRF), gas chromatography–mass spectrometry, atomic absorption spectrometry (AAS), chemiluminescence, ion chromatography, amperometry, and fluorimetry. However, the direct use of such techniques is limited by their high cost, low specificity, sensitivity, selectivity, response time, and technical expertise.

Apart from the aforementioned analytical techniques available in the field of sensing, recent fundamental interest has been reported where enzyme mimics are investigated to achieve a more reliable determination of targeted analytes at a relatively high scale.

Typically, analytical sensors must possess basic criteria as discussed previously [13]. A set of parameters are listed below to evaluate the performance of analytical sensors.

- ➤ **Sensitivity** indicates the relation between the output of a sensor and the quantity measured.
- ➤ **Selectivity** is a characteristic which indicates the ability of a sensor to respond to a specific analyte. For example, when the detection is applied for water analysis, or in blood samples, there are plenty of ions and molecules which can interfere with the data analysis. Thus, the selectivity of the technique is a crucial aspect to insure the sensitivity of the method.
- ➤ **Stability** determines the ability of a sensor to give numerous results over a specified period of time.
- ➤ **Limit of detection (LOD)** is the lowest concentration of an analyte that can be determined under specific conditions. LOD is an important indication about the validity of the technique [119].
- ➤ **Response time** which is the desirable time for the sensor to respond to concentration changes. The time of analysis for conventional methods is considered to be longer than

the time required for nanomaterials and nanoparticles, which generate rapid color response and facilitate the detection assay.

➤ **Reproducibility** is one of the most noted serious challenges in the sensing assay. It indicates whether the nanomaterial is able to give same results which are not expected to change over time under the same conditions.

1.4.3.1. Spectroscopic methodologies available for sensing

1.4.3.1.1. Optical sensors

The increasing demand for sensing applications has witnessed the development of non-destructive techniques such as optical sensors, which are based on fluorescence and absorption spectroscopies that involve studying absorption, scattering and emission of an electromagnetic radiation that provides a high reliable quantitative determination of small quantities of a specific analyte.

Optical sensors have numerous preferences making detection one of the easiest methodologies in the field of sensing. They are characterized by their simplicity, ability to detect a wide range of analytes with a fast response [120], low detection limit, high sensitivity, selectivity and reproducibility.

1.4.3.1.1.1. Absorption spectroscopy

Absorption spectroscopy is a sensitive tool based on the fundamental interaction between light and matter to experience vibrational, rotational, and translational motion or ionization of molecules. The energy of light will promote the electrons in a molecule to be excited, thus giving off the energy in electromagnetic radiation, where the absorption and emission of light can be then recorded in a spectral form at a specific wavelength.

Among various spectroscopic techniques such as Raman and nuclear magnetic resonance (NMR), the ultraviolet-visible (UV-vis) and fluorescence spectroscopies are ideal tools for desirable quantification of analytes, including metal ions and biological macromolecules [121, 122].

UV-vis is an absorption spectroscopic technique limited to particular functional groups in an analyte, commonly named ''chromophores'' that absorb light either in the near-UV (200–400 nm) or in the visible (400–800 nm) region to create a non-specific spectrum [122]. The Beer-Lambert Law can be coupled with UV-vis absorbance spectroscopy to perform a quantitative analysis.

In 1852, the German chemist August Beer stated that the intensity of absorbance of a colored analyte in the UV-vis region is equivalent to its concentration in solution. Thereafter, Lambert claimed that the absorption of light by a colored solution is directly proportional to the length of the column through which light passes. Combining both laws is known as the Beer-Lambert law, which describes that the absorbance can be converted to an actual concentration using the following equation [123]:

$$A = \varepsilon.c.\ell \qquad\qquad (21)$$

Where A is the absorbance in arbitrary units (a.u), c is the molar concentration (mol.l^{-1}), ℓ represents the path length (cm), and ε corresponds to the molar absorption coefficient (L.mol^{-1}.cm^{-1}).

Herein, UV-vis spectroscopy becomes a useful analytical tool that provides convenient determination of color changes in solution, and since different ions possess different absorption bands at a specific wavelength, the selective determination of analytes can be easily obtained by this technique in the presence of various interfering ions and molecules.

1.4.3.1.1.2. Colorimetric sensing

Various analytical methods and sensors have been explored after the development of instrument technology. However, the previously reported approaches were considered to be complex ones, requiring various needs which delayed the response analysis. Thus, to meet the practical requirements in terms of rapid and real-time analysis for monitoring water quality, disease diagnosis, protect public health and minimize many adverse health problems, nanomaterials have emerged and received considerable interest which become nowadays used frequently in various disciplines, particularly in colorimetric sensing due to the simplicity, low cost and high practicality of the technique, and sometimes, are instrument-free, such as the pregnancy test strip. Since color changes can be easily observed by the naked eye, the utilization of colorimetric sensors does not request the need of complex or expensive instruments.

Recently, nanotechnology showed an important aspect in sensor technology where the design of smart colorimetric sensors that respond to color changes has replaced the use of sophisticated instrumentation. Commonly utilized colorimetric sensors are nanozymes such as metal nanoparticles, metal oxide nanostructures including cerium oxide, and iron oxide as well as metal sulfide nanoparticles, in addition to magnetic nanoparticles, graphene-based

nanomaterials, and conjugated polymers [124]. They are considered as excellent candidates for colorimetric detection due to their robust properties which authorize their use in environmental and biomedical applications. Most of the mentioned nanoparticles displayed peroxidase-like behavior in catalyzing the oxidation of organic substrates in the presence of H_2O_2 as an electron acceptor or an oxidizing agent thus producing color changes which can be read out by the naked eye or through optical spectrophotometry.

A common reported organic substrate that is widely used in colorimetric sensing is the 3,3′,5,5′-tetramethylbenzidine (TMB). TMB is a chromogenic aromatic amine benzidine derivative that is oxidized by heme peroxidases. Saunders et al. [125] proposed that the oxidation products of TMB results from one-electron transfer to produce a cationic free radical that can be detected by UV-vis at ~ 370 and 652 nm or by the naked eyes through the formation of a blue colored solution. According to the ESR quantitative detection for the monitoring of free radical formation, it has been shown that the charge transfer complex is in equilibrium with a radical cation, and this radical cation increases with the increase of the square root of charge transfer complex, thus the mechanism towards TMB oxidation can be illustrated as in **Figure 14**.
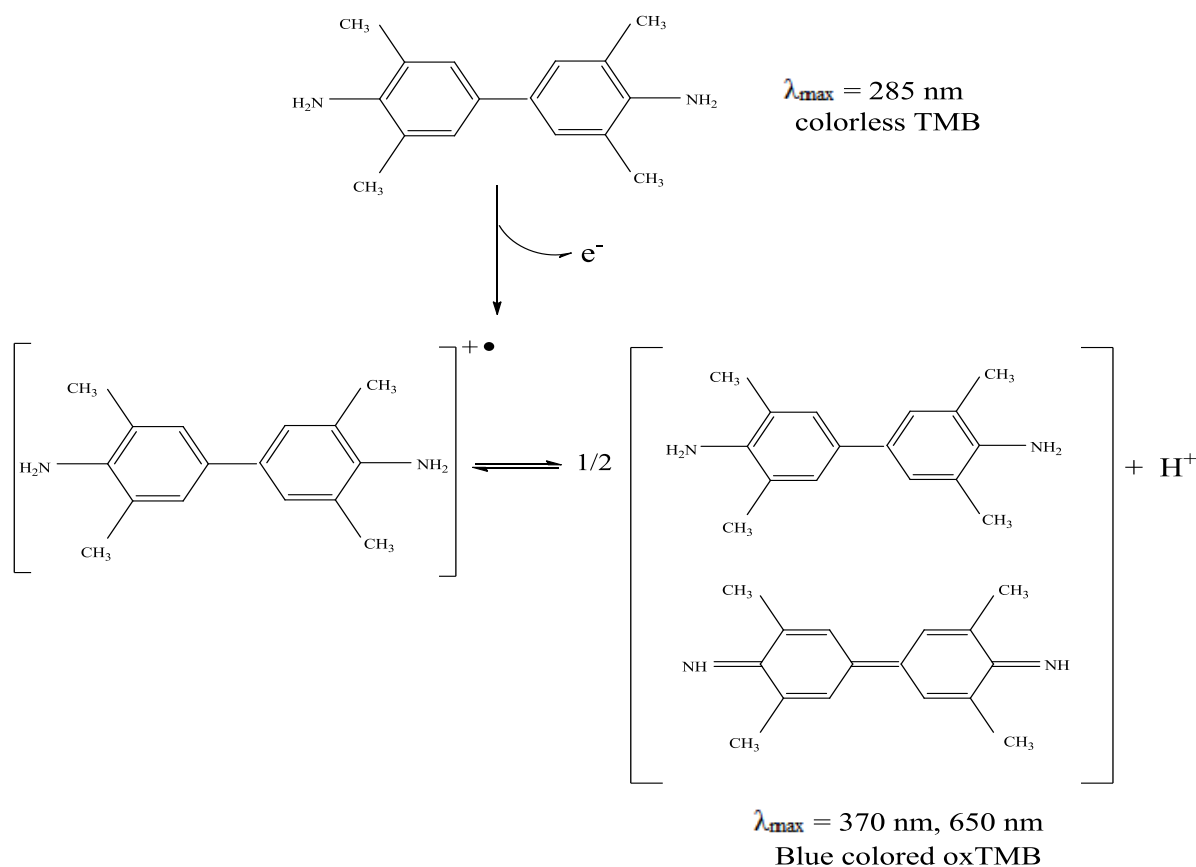
Figure 14: Chemical structure of TMB and its oxidation mechanism.

1.4.3.1.1.3. Fluorescence spectroscopy

Fluorescence spectroscopy is based on the analysis of fluorophores that absorb light within their absorption band and emit this light at a higher wavelength. Generally, a light beam of a specific wavelength traverses a solution containing the analyte of interest. The analyte then absorbs the light energy in the form of photon to reach a higher vibrational level in an excited state, followed by loss of excess vibrational energy to fall in a lower vibrational level of the excited state [126]. Fluorescence emission then occurs at higher wavelength as the fluorophore decays from this excited state to a vibrational level of the electronic ground state, as shown in **Figure 15**. On the basis of this phenomenon, fluorescent probes can be selectively analyzed, by displaying an emission spectrum that can be recorded by fluorescence spectrometer at a specific wavelength, in which the intensity of emission determines the concentration of analyte.
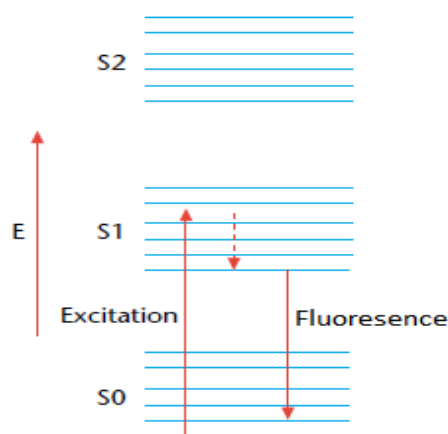
Figure 15: A simplified Jablonski diagram of fluorophore excitation and emission. E is the energy scale; S0 denotes the ground singlet electronic state; S1 and S2 represent the higher energy excited electronic states [127].

Fluorescence spectroscopy can be characterized by specific features [128] that make it ideal analytical tool for sensing. It supplies analysis with high sensitivity and accuracy, as the quantitative determination can be feasible even at low concentrations. Moreover, the fluorescence analysis can be used to monitor rapid chemical changes in an analyte.

Sensing using this technique has been first reported by Nagasawa and Oshima in 1972 [129]. The mechanism is based on using fluorescent dyes or non-fluorescent substances [129] that can be transformed into fluorescent molecules when they react with specific ROS, such as superoxide anions and hydroxyl radicals. A common example is terephthalic acid (TA) which

is widely used due to the absence of isomer interferences. TA is a non-fluorescent organic molecule, which upon reaction with HO$^•$ radicals, is transformed into a fluorescent 2-hydroxterephthalic acid (HTA) product **(Fig. 16)** that can be easily detected by fluorescence spectrometry [130]. The use of fluorescence attracted huge interest to monitor the presence of HO$^•$, as the detection of HO$^•$ radicals is somehow difficult due to their high reactivity.

For this thesis work, fluorescence spectroscopy was utilized to evaluate the generation of hydroxyl radicals, which play a key role in this sensing methodology, as these radicals participate in the catalytic mechanism of nanozymes for the colorimetric determination of various analytes.

Terephthalic acid   2-Hydroxyterephthalic acid
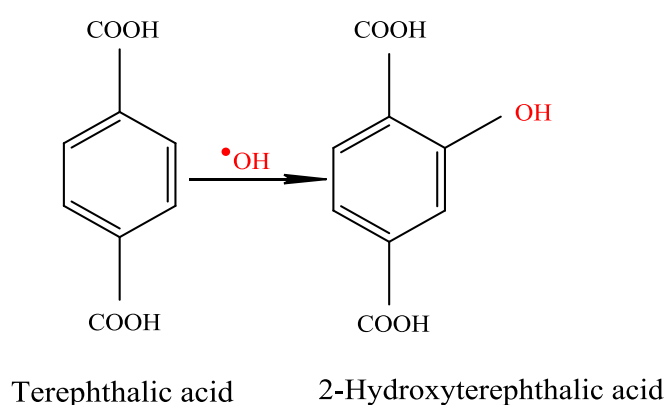
Figure 16: Reaction mechanism of hydroxyl radicals with non-fluorescent TA to form a fluorescent HTA molecule.

1.4.4. Multi-functional nanomaterials

1.4.4.1. Nanomaterials in colorimetric sensing

Materials in nanoscale form have been discovered in a way to cut down expenses and ameliorate their catalytic efficiency, in the meantime when their bulk counterparts were estimated to be catalytically inactive [131]. This provided nanomaterials a property as interesting analytical devices that are capable to sense trace amounts of target analytes through recording their spectral changes with respect to concentration and producing intense color changes.

Based on these advantages, we present the general prospects of copper sulfide (CuS) nanoparticles (NPs) in sensing applications to elicit qualitative and quantitative information with high accuracy, extreme sensitivity and specificity, which overcome many commercial analytical detection methods discussed in the chapter. The excellent surface chemistry of CuS

NPs enabled them to efficiently catalyze the redox process of a wide range of molecules. Most importantly, the unique physical, chemical, and optical properties of CuS NPs make them ideal candidates as colorimetric sensors, which rely on the principle of Fenton chemistry that is restricted to their electron transfer reactions with biomolecules and other substrates.

The choice of the material as a colorimetric enzyme-like sensor represents a crucial factor in determining the practicality of the method which is closely related to their outstanding properties. Thus, CuS NPs as nanozymes offer the potential to accomplish an on-site sensing platform by minimizing time response and achieving low limit of detection with a wide linear range, and become the focus of research interest, and show promising requirements for designing advanced bio-chemical detection platforms. This advancement will facilitate the implementation of using CuS NPs not only in sensing, but also in diverse applications.

1.4.4.2. Nanomaterials in biomedical applications

Nanomaterials are key components in nanotechnology due to their outstanding properties. When focusing on their unique physical properties, the resulting nanomaterials can be fabricated in a way to perform multi-modal functions, which expands their use in different applications.

Among a plethora of successful applications, the biomedical field can remarkably benefit from the fundamental properties of nanomaterials that are designed as nanozymes. For example, nanozymes have been reported for sensing biological molecules with high sensitivity, and their utilization in such field is of crucial importance for early disease diagnosis [132]. Thus, a single nanomaterial can be used for disparate purposes.

Among myriads of nanomaterials, noble and transition-metal based nanoparticles, in particular, represent interesting approaches due to their unique intrinsic optical properties and their wide spread use in diverse fields. The interaction of these inorganic nanomaterials with electromagnetic radiation causes a cohesive oscillation of their conduction band electrons creating a net charge difference [117, 133], a phenomenon referred to localized surface plasmon resonance (LSPR). Commonly, silver, gold, and copper display LSPR, and such metals possess inter-band transition under which electrons in their occupied energy states transit to empty levels as a result of optical energy absorption. This merit makes the absorption and light scattering cross sections of these metals very promising [134]. That is why such nanomaterials absorb and transform the electromagnetic optical energy of absorbed light into kinetic energy and heat. Hence, this property extended their use not only in sensing as

discussed previously in this chapter, but also as photothermal candidates in pharmaceuticals, drug delivery, clinical diagnosis, photoacoustic imaging and many biomedical applications [135].

Nanotechnology has accomplished great achievements in the biomedical field, where a group of novel approaches based on the interaction of nanomaterials and light made a good progress in various therapies. The combination of surgery with radiation therapy represents the classical treatment regime of various diseases, in which laser pulses absorbed by either endogenous substances such as hemoglobin and melanin, or exogenous nanomaterials such as gold-based and copper-based nanoparticles among others, to induce local hyperthermia [136]. Besides the potential reliability of endogenous agents, absorption and scattering of light by tissues in the visible region remained challenging. To address this problem, exogenous NPs commonly named "photothermal nanoagents" that absorb light in the near-infrared region (NIR ~ 650-1100 nm) have emerged as appealing contrast agents in nanomedicine and mediate the use of NIR-wave energy.

The use of NIR light as an external physical stimulus, absorbed by photothermal nanoagents to cause an increase in temperature to 40–50°C provided great opportunity for thermal ablation of tumor tissues through disrupting the integrity of their cell membranes. The mechanism is based on the uptake of photothermal absorbing agents by cells to generate heat from optical energy, prompting photoablation of the tumor cells and leading to cell death. NIR light is a promising strategy in nanomedicine due to deeper tissue penetration provided by NIR laser, since skin, tissues, water and blood do not absorb at this range [137], even human body lacks chromophores that absorb in the NIR region. This strategy, referred to as photothermal therapy (PTT), showed successful evolution in the medicinal field, particularly in transdermal drug delivery.

A variety of photothermal responsive nanomaterials such as noble metals, carbon-based nanomaterials, plasmonic nanoparticles, polymers and semiconductor-based nanoparticles have been explored and their photothermal performances have been examined [138-141]. Particularly, gold-based nanomaterials with their photothermal properties have been fabricated in various morphologies, sizes and shapes such as nanorods, nanocages, nanocrystals, nanospheres, nanoplates and are conventionally utilized as photothermal candidates for molecular imaging and drug delivery [134]. However, their low thermal stability after long time exposure to NIR laser, too high concentrations of gold nanoparticles, high cost and their relative large size (>50 nm) hampered their practical use, and their investigation in PTT did not

ensure progress in this scope. Fortunately, scientists developed copper-containing semiconductor nanomaterials as alternatives to gold-based nanoparticles with superior advantages in terms of high photothermal conversion efficiency and stability, inexpensive production, and low cytotoxicity for biomedical purposes. Commonly, CuS NPs were significantly employed for photothermal ablation of infected tissues, and overwhelmed the use of gold nanostructures, the most significantly used photothermal NPs. Since the photothermal heating performance of CuS NPs is due to the d-d band transition of Cu^{2+} ions which extends the absorption to ~ 900 nm, unlike gold NPs which relies on LSPR only [142, 143] that is influenced by the dielectric constant of the surrounding medium.
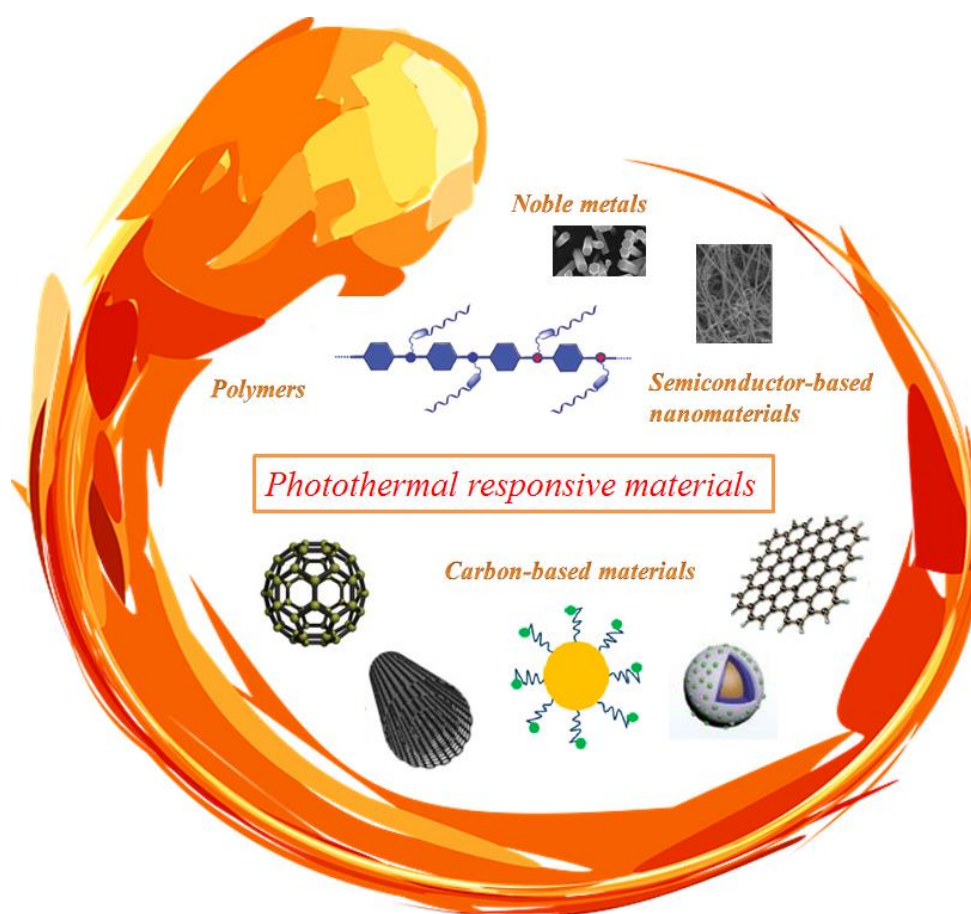
Figure 17: A summary of various photothermal responsive nanomaterials.

Copper sulfide (CuS) has made a noticeable influence in the world of nano-science, and enormous attempts have been coordinated toward the growth of new applications for this fascinating material. To the best of our knowledge, near-infrared light induced photothermal therapy achieved by CuS nanoparticles elicited lots of attention and provided a great opportunity as a minimally-invasive technique to exploit such materials in the medicinal field [135].

Despite all the advantages of PTT, it is impossible to achieve a complete therapeutic approach *via* a single treatment method. Therefore, the development of combinatorial therapeutic methods in one nanomaterial is fascinating to avoid undesirable side effects through a diversity of mechanisms. Researchers nowadays have paid more attention to combination therapies in order to achieve synergistic effects.

To the best of our knowledge, several photothermal nanomaterials have been considered as co-delivery carriers of drugs and showed remarkable tumor cell killing efficiency [144]. Among them, silicon-based nanomaterials have shown to have photothermal effect and used for drug loading and release; however their low drug loading efficiency impeded their clinical success, thereafter mesoporous silica nanoparticles (MSNs) with their large pore volume, tunable size, high surface area, and the presence of silanol groups on the surface of pores and on the outer surfaces of NPs which facilitates their functionalization, make them ideal nanocarriers for drug targeting and delivery, which become promising alternatives for advanced therapies. Despite all the advantages of mesoporous silica nanoparticles, researchers continue to improve the properties of MSNs by their combination with magnetic nanoparticles, metallic nanoparticles and polymers which give rise to composite materials or core/shell nanoparticles [145-147]. Another attempt have been made through synthesis of CuS core shell MSNs for anti-cancer drug delivery [148]. Though, drug delivery by CuS nanoparticles [134] under the influence of NIR light is another approach that holds a promising potential in the field of nanomedicine. The concept is based on immobilizing the drug onto CuS NPs and illuminating the complex by NIR laser to induce temperature rise in the surrounding media; in turn, at high temperature, the drug can be released from the nanocomposite and a dual effect can induce killing of the targeted tissue, by means of local hyperthermia and drug delivery.

Interested by the success of these nanomaterials as drug delivery carriers under NIR region, CuS-based nanoparticles carry many enhanced promising properties and have been broadly used in diverse applications. Although these materials have attracted enormous attention in PTT and drug delivery, yet the *in vivo* applications still a major challenge due to their poor solubility. Thus, suitable surface modification of these nanoparticles represents a good choice to improve their solubility and compatibility, where a variety of surface-coating molecules such as polyethylene glycol (PEG), bovine serum albumin (BSA), citric acid, and cysteine are commonly available materials that enhance the biocompatibility of CuS [140, 149, 150], and reduce its potential toxicity *in vitro* as well *in vivo*. In addition, such NPs should possess size < 50 nm to be non-cytotoxic to normal cells with functionalized surfaces to target specific

cellular moieties and avoid their rapid clearance, because after *in vivo* injection, they can be directly recognized by macrophages which causes their elimination from blood. Thus, functionalization is essential to reduce premature clearance and increase circulation life times. Furthermore, the surface area of inorganic nanoparticles is very critical in the biomedical field, where a high surface area enhances the rapid absorption and dissolution of nanoparticles in blood [151].

Targeting of the drug towards a specific region in the body *via* this approach can achieve high therapeutic efficacy, enhance drug stability, avoid the development of drug-resistance, minimize drug doses and improve patients' life quality [152]. All these advantages can stimulate the future biomedical applications of CuS-based nanomaterials.

In spite of the progress in scientific research that provided a deep understanding of the use of nanomaterials in nanomedicine, and enhanced the development of new clinical trials through combination therapy that made huge revolution in nanotechnology, it is of great interest to emphasis on other current therapeutic approaches.

Based on these observations, nanomaterials can be also used in photodynamic therapy (PDT) [153], and are so-called "photosensitizers" (PS) [154, 155], in which they generate singlet oxygen ($^1O_2$), as ROS from molecular O_2 when illuminated by appropriate light, to disrupt the targeted tissue *via* a series of photo-chemical reactions.

A variety of organic materials such as micelles, liposomes, and polymers [156-158] have been reported as PS carriers or as PDT nanoagents themselves. Although PDT showed successful treatment modality of several diseases, yet most PS that are currently used can only be activated under visible light, which did not show effective treatment for solid tumors due to the huge thickness of tumor tissue. Thereafter, inorganic nanomaterials including gold nanoshells, zinc oxide, copper sulfide, carbon-based nanoparticles and quantum dots [154, 155, 159-161], which are considered as PTT agents and drug carriers showed promising results in PDT due to their extended absorption of light in the NIR region as discussed above.

The above-mentioned therapies, PTT, drug delivery and PDT all act in different mechanisms and their integration into one therapeutic system constitutes an effective approach and shows powerful therapeutic efficacy to treat various diseases.
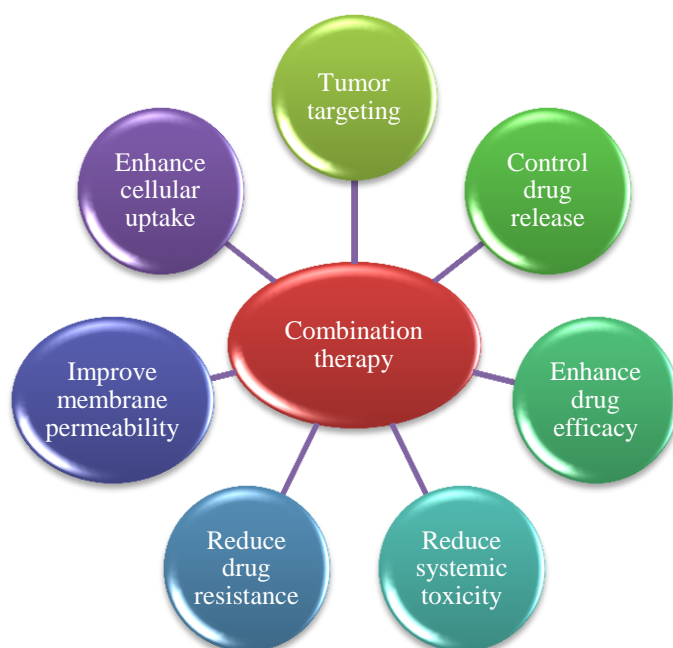
Figure 18: Advantages of combinatorial therapy PTT/PDT/Drug delivery.
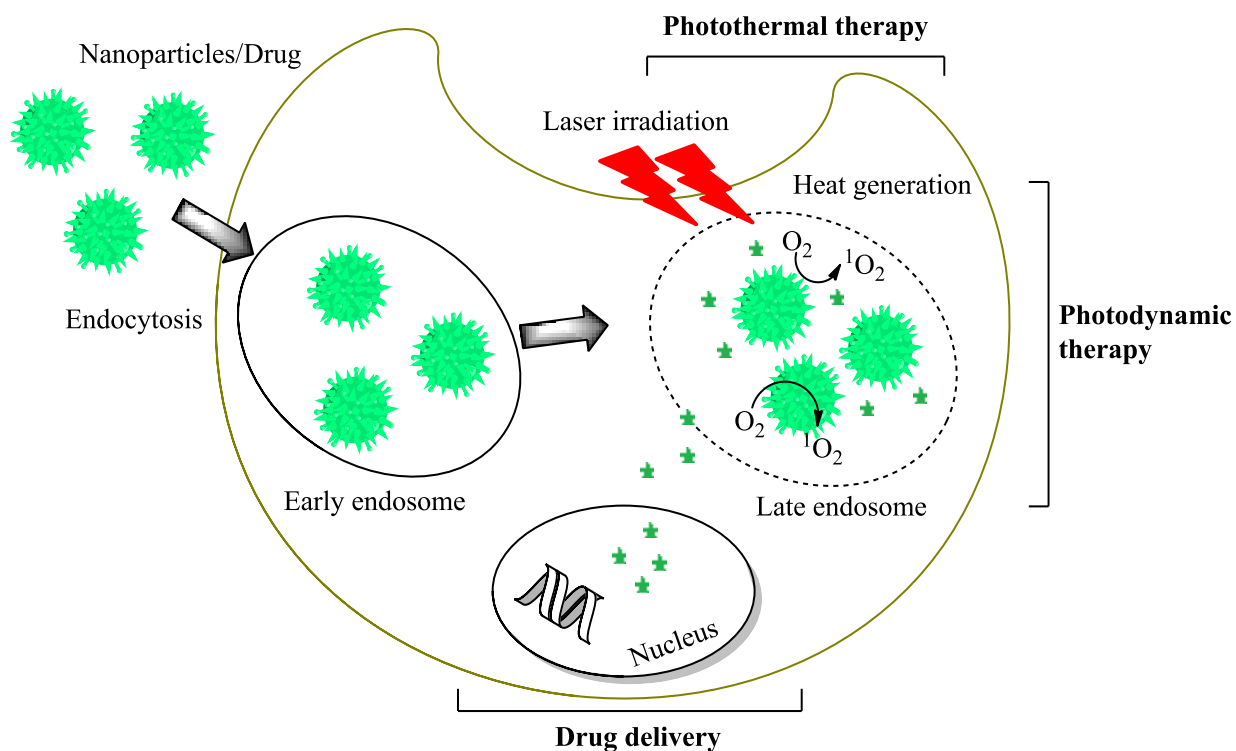
Figure 19: Schematic illustration that summarizes the cellular internalization of nanoparticles loaded with a drug model for the triple combination of PTT, PDT, and Drug delivery.

OBJECTIVES

The objectives of this thesis work are the development of facile, rapid, cost-effective and versatile sensors that possess a peroxidase-like catalytic behavior for sensing various chemical and biological species for environmental and biomedical purposes.

These objectives can be summarized as follows:

1. Elucidate the potency of copper sulfide NPs as enzyme mimics for the colorimetric sensing of toxic metal ions in aqueous system.
   - ❖ Study the effect of surface modification of CuS NPs with BSA protein on their colloidal stability, solubility, as well their catalytic activity.
   - ❖ Determine the influence of variable parameters on the colorimetric properties of CuS-BSA toward Cr(VI) sensing.
   - ❖ Examine the selectivity of the designed nanosensor in the presence of interfering ions.
   - ❖ Confirm the selectivity and sensitivity of the sensing methodology by coupling the designed sensor with UV-vis spectrophotometry.

2. Develop a Cu-based sensor with superior catalytic behavior for the qualitative and quantitative determination of biological molecules including glucose and dopamine.
   - ❖ Select the optimal conditions to obtain a set of sensitive responses for sensing of glucose in human blood serum and dopamine in beef meat.
   - ❖ Generate a selective and sensitive detection assay towards glucose and dopamine in the presence of various interfering molecules.

3. Establish the unique properties of CuS as thermo-responsive nanoparticles that could serve as drug carriers for the encapsulation and release of lysozyme for antibacterial purposes.
   - ❖ Fabricate CuS-based photothermal (PTT) agent for rapid lysozyme release under near infrared irradiation (NIR) as an external physical stimulus.

❖ Examine the cellular toxicity of the developed nanocarrier system on cancer cells.

1.5. References

[1] R. Feynman, There's plenty of room at the bottom, Feynman and computation, CRC Press (2018) 63-76.

[2] E.J. Al Dine, Synthesis and characterization of smart nanoparticles: Université de Lorraine; Université libanaise; 2017.

[3] C. Parisi, M. Vigani, E. Rodríguez-Cerezo, Agricultural nanotechnologies: what are the current possibilities?, Nano Today 10 (2015) 124-127.

[4] R. Nagarajan, T.A. Hatton, Nanoparticles: synthesis, stabilization, passivation, and functionalization: ACS Publications 996 2008. DOI:10.1021/bk-2008-0996.fw001.

[5] V.M. Starov, Nanoscience: colloidal and interfacial aspects: CRC Press 147 2010. ISBN: 9781420065015.

[6] A. Henglein, Small-particle research: physicochemical properties of extremely small colloidal metal and semiconductor particles, Chem. Rev. 89 (1989) 1861-1873.

[7] K. Gregorczyk, M. Knez, Hybrid nanomaterials through molecular and atomic layer deposition: Top down, bottom up, and in-between approaches to new materials, Prog. Mater. Sci. 75 (2016) 1-37.

[8] K. Habiba, V.I. Makarov, B.R. Weiner, G. Morell, Fabrication of nanomaterials by pulsed laser synthesis, Manufacturing Nanostructures, One Central Press, Manchester, UK, (2014) 263-285. ISBN: 9781910086070.

[9] V. Arole, S. Munde, Fabrication of nanomaterials by top-down and bottom-up approaches-an overview, J. Mater. Sci. 1 (2014) 89-93.

[10] P. Colson, C. Henrist, R. Cloots, Nanosphere lithography: a powerful method for the controlled manufacturing of nanomaterials, J. Nanomater. 2013 (2013) 21.

[11] C. Dhand, N. Dwivedi, X.J. Loh, A.N.J. Ying, N.K. Verma, R.W. Beuerman, et al., Methods and strategies for the synthesis of diverse nanoparticles and their applications: a comprehensive overview, RSC Adv. 5 (2015) 105003-105037.

[12] D. Astruc, Transition-metal nanoparticles in catalysis: from historical background to the state-of-the art, Wiley Online Library 2008, pp. 1-48.

[13] S. Nag, Development of Conductive Nanocomposite Sensors for Anticipated Diagnostic of Diseases: Université de Bretagne Sud; 2014.

[14] T. Mehta, N. Patni, S.G. Pillai, NANO TECHNOLOGY IN CHEMICAL SENSORS, (2015).

[15] P. Mehrotra, Biosensors and their applications–A review, J. Oral Biol. Craniofac. Res. 6 (2016) 153-159.

[16] A. Turner, I. Karube, G.S. Wilson, Biosensors: fundamentals and applications: Oxford university press; 1987.

[17] B.R. Eggins, Chemical sensors and biosensors: John Wiley & Sons; 2008.

[18] Y. Du, S. Dong, Nucleic acid biosensors: recent advances and perspectives, Anal. Chem. 89 (2016) 189-215.

[19] J.I.A. Rashid, N.A. Yusof, The strategies of DNA immobilization and hybridization detection mechanism in the construction of electrochemical DNA sensor: A review, Sens. Bio-Sens. Res. 16 (2017) 19-31.

[20] V. Kavita, DNA biosensors—a review, J. Bioeng. Biomed. Sci. 7 (2017) 222.

[21] L. Gao, X. Yan, Nanozymes: an emerging field bridging nanotechnology and biology, Sci. China Life Sci. 59 (2016) 400-402.

[22] Y. Murakami, J.-i. Kikuchi, Y. Hisaeda, O. Hayashida, Artificial enzymes, Chem. Rev. 96 (1996) 721-758.

[23] Q.-Q. Jiang, Discovery of Potent Inhibitors of Human B-tryptase by Protein Surface Recognition, Department of Chemistry, University of Duisburg-Essen, China (2013).

[24] D. Gonze, M. Kaufman, Chemical and enzyme kinetics, (2016).

[25] E. Andersson, Validation of a dispenser machine and enzyme kinetics for alcohol dehydrogenase, Department of Biochemistry, University of Lund (2018).

[26] https://en.wikipedia.org/wiki/Enzyme_catalysis, Enzyme catalysis, https://en.wikipedia.org/wiki2015.

[27] P. Borthakur, G. Darabdhara, M.R. Das, R. Boukherroub, S. Szunerits, Solvothermal synthesis of CoS/reduced porous graphene oxide nanocomposite for selective colorimetric detection of Hg (II) ion in aqueous medium, Sens. Actuators, B 244 (2017) 684-692.

[28] R. Kitz, I.B. Wilson, Esters of methanesulfonic acid as irreversible inhibitors of acetylcholinesterase, J. Biol. Chem. 237 (1962) 3245-3249.

[29] W.X. Tian, C.L. Tsou, Determination of the rate constant of enzyme modification by measuring the substrate reaction in the presence of the modifier, Biochem. 21 (1982) 1028-1032.

[30] K.D. Sattler, Carbon nanomaterials sourcebook: nanoparticles, nanocapsules, nanofibers, nanoporous structures, and nanocomposites: CRC Press; 2016.

[31] S. Barizuddin, S. Bok, S. Gangopadhyay, Plasmonic sensors for disease detection–a review, J. Nanomed. Nanotechnol. 7 (2016) 1000373.

[32] D. Yu, B. Blankert, J.C. Viré, J.M. Kauffmann, Biosensors in drug discovery and drug analysis, Anal. Lett. 38 (2005) 1687-1701.

[33] S. Rodriguez-Mozaz, M.J.L. de Alda, M.-P. Marco, D. Barceló, Biosensors for environmental monitoring: A global perspective, Talanta 65 (2005) 291-297.

[34] L.C. Clark Jr, C. Lyons, Electrode systems for continuous monitoring in cardiovascular surgery, Ann. NY Acad. Sci. 102 (1962) 29-45.

[35] X. Zhu, W. Chen, K. Wu, H. Li, M. Fu, Q. Liu, et al., A colorimetric sensor of H_2O_2 based on Co_3O_4–montmorillonite nanocomposites with peroxidase activity, New J. Chem. 42 (2018) 1501-1509.

[36] Y. Zhang, J. Ge, Z. Liu, Enhanced activity of immobilized or chemically modified enzymes, ACS Catal. 5 (2015) 4503-4513.

[37] Y. Yin, Z. Dong, Q. Luo, J. Liu, Biomimetic catalysts designed on macromolecular scaffolds, Prog. Polym. Sci. 37 (2012) 1476-1509.

[38] K. Korschelt, M.N. Tahir, W. Tremel, A step into the future: Applications of Nanoparticle Enzyme Mimics, Chem. Eur. J. 24 (2018) 9703-9713.

[39] R. Breslow, Artificial enzymes, Science 218 (1982) 532-537.

[40] Z. Liu, R. Cai, L. Mao, H. Huang, W. Ma, Highly sensitive spectrofluorimetric determination of hydrogen peroxide with β-cyclodextrin–hemin as catalyst, Analyst 124 (1999) 173-176.

[41] Y.-X. Ci, Y.-G. Zheng, J.-K. Tie, W.-B. Chang, Chemiluminescence investigation of the interaction of metalloporphyrins with nucleic acids, Anal. Chim. Acta. 282 (1993) 695-701.

[42] G. Zhang, P.K. Dasgupta, Hematin as a peroxidase substitute in hydrogen peroxide determinations, Anal. Chem. 64 (1992) 517-522.

[43] P. Xu, G.M. Zeng, D.L. Huang, C.L. Feng, S. Hu, M.H. Zhao, et al., Use of iron oxide nanomaterials in wastewater treatment: a review, Sci. Total Environ. 424 (2012) 1-10.

[44] C. Lai, M.-M. Wang, G.-M. Zeng, Y.-G. Liu, D.-L. Huang, C. Zhang, et al., Synthesis of surface molecular imprinted TiO_2/graphene photocatalyst and its highly efficient photocatalytic degradation of target pollutant under visible light irradiation, Appl. Surf. Sci. 390 (2016) 368-376.

[45] G. De Crozals, R. Bonnet, C. Farre, C. Chaix, Nanoparticles with multiple properties for biomedical applications: A strategic guide, Nano Today 11 (2016) 435-463.

[46] M. Chen, G. Zeng, P. Xu, C. Lai, L. Tang, How do enzymes 'meet'nanoparticles and nanomaterials?, Trends Biochem. Sci. 42 (2017) 914-930.

[47] Y. Song, J. Chen, H. Liu, Y. Song, F. Xu, H. Tan, et al., Conformation, bioactivity and electrochemical performance of glucose oxidase immobilized on surface of gold nanoparticles, Electrochim. Acta 158 (2015) 56-63.

[48] Y. Hu, H. Cheng, X. Zhao, J. Wu, F. Muhammad, S. Lin, et al., Surface-enhanced raman scattering active gold nanoparticles with enzyme-mimicking activities for measuring glucose and lactate in living tissues, ACS Nano. 11 (2017) 5558-5566.

[49] E. Kuah, S. Toh, J. Yee, Q. Ma, Z. Gao, Enzyme mimics: advances and applications, Chem. Eur. J. 22 (2016) 8404-8430.

[50] L. Gao, J. Zhuang, L. Nie, J. Zhang, Y. Zhang, N. Gu, et al., Intrinsic peroxidase-like activity of ferromagnetic nanoparticles, Nat. Nanotechnol. 2 (2007) 577.

[51] W. Qin, L. Su, C. Yang, Y. Ma, H. Zhang, X. Chen, Colorimetric detection of sulfite in foods by a TMB–O_2–Co_3O_4 nanoparticles detection system, J. Agric. Food Chem. 62 (2014) 5827-5834.

[52] C. Dong, H. Zhong, T. Kou, J. Frenzel, G. Eggeler, Z. Zhang, Three-dimensional Cu foam-supported single crystalline mesoporous Cu_2O nanothorn arrays for ultra-highly sensitive and efficient nonenzymatic detection of glucose, ACS Appl. Mater. Interfaces 7 (2015) 20215-20223.

[53] N. Li, P. Zhao, D. Astruc, Anisotropic gold nanoparticles: synthesis, properties, applications, and toxicity, Angew. Chem. Int. Ed. 53 (2014) 1756-1789.

[54] M. Rycenga, C.M. Cobley, J. Zeng, W. Li, C.H. Moran, Q. Zhang, et al., Controlling the synthesis and assembly of silver nanostructures for plasmonic applications, Chem. Rev. 111 (2011) 3669-3712.

[55] J. Luo, S. Jiang, H. Zhang, J. Jiang, X. Liu, A novel non-enzymatic glucose sensor based on Cu nanoparticle modified graphene sheets electrode, Anal. Chim. Acta. 709 (2012) 47-53.

[56] Y. Lin, J. Ren, X. Qu, Nano-gold as artificial enzymes: hidden talents, Adv. Mater. 26 (2014) 4200-4217.

[57] K. Yang, L. Feng, X. Shi, Z. Liu, Nano-graphene in biomedicine: theranostic applications, Chem. Soc. Rev. 42 (2013) 530-547.

[58] Y. Song, K. Qu, C. Zhao, J. Ren, X. Qu, Graphene oxide: intrinsic peroxidase catalytic activity and its application to glucose detection, Adv. Mater. 22 (2010) 2206-2210.

[59] D. Feng, Z.Y. Gu, J.R. Li, H.L. Jiang, Z. Wei, H.C. Zhou, Zirconium-metalloporphyrin PCN-222: mesoporous metal–organic frameworks with ultrahigh stability as biomimetic catalysts, Angew. Chem. Int. Ed. 51 (2012) 10307-10310.

[60] K. Fan, C. Cao, Y. Pan, D. Lu, D. Yang, J. Feng, et al., Magnetoferritin nanoparticles for targeting and visualizing tumour tissues, Nat. Nanotechnol. 7 (2012) 459.

[61] A.J. Mieszawska, W.J. Mulder, Z.A. Fayad, D.P. Cormode, Multifunctional gold nanoparticles for diagnosis and therapy of disease, Mol. Pharm. 10 (2013) 831-847.

[62] M.-R. Gao, Y.-F. Xu, J. Jiang, S.-H. Yu, Nanostructured metal chalcogenides: synthesis, modification, and applications in energy conversion and storage devices, Chem. Soc. Rev. 42 (2013) 2986-3017.

[63] M. Janani, P. Srikrishnarka, S.V. Nair, A.S. Nair, An in-depth review on the role of carbon nanostructures in dye-sensitized solar cells, J. Mater. Chem. A 3 (2015) 17914-17938.

[64] D.P. Cormode, B.L. Sanchez-Gaytan, A.J. Mieszawska, Z.A. Fayad, W.J. Mulder, Inorganic nanocrystals as contrast agents in MRI: synthesis, coating and introduction of multifunctionality, NMR Biomed. 26 (2013) 766-780.

[65] E. Petryayeva, U.J. Krull, Localized surface plasmon resonance: nanostructures, bioassays and biosensing—a review, Anal. Chim. Acta. 706 (2011) 8-24.

[66] H. Wei, E. Wang, Nanomaterials with enzyme-like characteristics (nanozymes): next-generation artificial enzymes, Chem. Soc. Rev. 42 (2013) 6060-6093.

[67] Q. Wang, H. Wei, Z. Zhang, E. Wang, S. Dong, Nanozyme: An emerging alternative to natural enzyme for biosensing and immunoassay, TrAC, Trends Anal. Chem. 105 (2018) 218-224.

[68] S. Tsekhmistrenko, V. Bityutskyy, O. Tsekhmistrenko, V. Polishchuk, S. Polishchuk, N. Ponomarenko, et al., Enzyme-like activity of nanomaterials, Regul. Mech. Biosyst. 9 (2018) 469-476.

[69] L. Pasquato, F. Rancan, P. Scrimin, F. Mancin, C. Frigeri, N-methylimidazole-functionalized gold nanoparticles as catalysts for cleavage of a carboxylic acid ester, Chem. Commun. (2000) 2253-2254.

[70] L. Wang, H. Zou, Z. Dong, L. Zhou, J. Li, Q. Luo, et al., Temperature-driven switching of the catalytic activity of artificial glutathione peroxidase by the shape transition between the nanotubes and vesicle-like structures, Langmuir, 30 (2014) 4013-4018.

[71] L. Gao, J. Zhuang, L. Nie, J. Zhang, Y. Zhang, N. Gu, et al., Intrinsic peroxidase-like activity of ferromagnetic nanoparticles, Nat. Nanotechnol. 2 (2007) 577.

[72] L. Gao, K. Fan, X. Yan, Iron oxide nanozyme: a multifunctional enzyme mimetic for biomedical applications, Theranostics 7 (2017) 3207.

[73] R. Ragg, M.N. Tahir, W. Tremel, Solids go bio: inorganic nanoparticles as enzyme mimics, Eur. J. Inorg. Chem. 2016 (2016) 1906-1915.

[74] V.P. Pandey, M. Awasthi, S. Singh, S. Tiwari, U.N. Dwivedi, A comprehensive review on function and application of plant peroxidases, Biochem. Anal. Biochem. 6 (2017) 308.

[75] J.N. Rodríguez-López, D.J. Lowe, J. Hernández-Ruiz, A.N. Hiner, F. García-Cánovas, R.N. Thorneley, Mechanism of reaction of hydrogen peroxide with horseradish peroxidase: identification of intermediates in the catalytic cycle, J. Am. Chem. Soc. 123 (2001) 11838-11847.

[76] F. Passardi, G. Theiler, M. Zamocky, C. Cosio, N. Rouhier, F. Teixera, et al., PeroxiBase: the peroxidase database, Phytochem 68 (2007) 1605-1611.

[77] P. Held, An introduction to reactive oxygen species measurement of ROS in cells, BioTek Instruments Inc, Application Guide (2012) 1-2.

[78] M. Giorgio, M. Trinei, E. Migliaccio, P.G. Pelicci, Hydrogen peroxide: a metabolic by-product or a common mediator of ageing signals?, Nat. Rev. Mol. Cell Biol. 8 (2007) 722.

[79] F. Passardi, C. Penel, C. Dunand, Performing the paradoxical: how plant peroxidases modify the cell wall, Trends Plant Sci. 9 (2004) 534-540.

[80] R. Huang, R. Xia, L. Hu, Y. Lu, M. Wang, Antioxidant activity and oxygen-scavenging system in orange pulp during fruit ripening and maturation, Sci. Hortic. 113 (2007) 166-172.

[81] Y.A. Vladimirov, E. Proskurnina, D.Y. Izmailov, A. Novikov, A. Brusnichkin, A. Osipov, et al., Cardiolipin activates cytochrome c peroxidase activity since it facilitates H_2O_2 access to heme, Biochem. 71 (2006) 998-1005.

[82] M. Kohri, Development of HRP-mediated enzymatic polymerization under heterogeneous conditions for the preparation of functional particles, Polym. J. 46 (2014) 373.

[83] D. Lee, S. Khaja, J.C. Velasquez-Castano, M. Dasari, C. Sun, J. Petros, et al., *In vivo* imaging of hydrogen peroxide with chemiluminescent nanoparticles, Nat. Mater. 6 (2007) 765.

[84] S. Gu, Catalytic activity analysis of metallic nanoparticles by model reactions, Faculty of Mathematics and Natural Sciences, University of Humboldt, Berlin (2018). DOI: 10.18452

[85] B. Halliwell, J.M. Gutteridge, Free radicals in biology and medicine: Oxford University Press, USA; 2015.

[86] S. Singh, Nanomaterials exhibiting enzyme-like properties (Nanozymes): Current advances and future perspectives, Front Chem. 7 (2019) 46.

[87] M.I. Litter, M. Slodowicz, An overview on heterogeneous Fenton and photoFenton reactions using zerovalent iron materials, J. Adv. Oxid. Technol. 20 (2017). DOI: 10.1515/jaots-2016-0164.

[88] Y. Li, S. Ouyang, H. Xu, X. Wang, Y. Bi, Y. Zhang, et al., Constructing solid–gas-interfacial fenton reaction over alkalinized-C_3N_4 photocatalyst to achieve apparent quantum yield of 49% at 420 nm, J. Am. Chem. Soc. 138 (2016) 13289-13297.

[89] W.H. Glaze, J.-W. Kang, D.H. Chapin, The chemistry of water treatment processes involving ozone, hydrogen peroxide and ultraviolet radiation, Ozone Sci. Eng. 9 (1987) 335-352.

[90] K. Barbusiński, Henry John Horstman Fenton-short biography and brief history of Fenton reagent discovery, Chemistry-Didactics-Ecology-Metrology, 14 (2009) 101-105.

[91] H. Fenton, LXXIII.—Oxidation of tartaric acid in presence of iron, J. chem. Soc. Trans. 65 (1894) 899-910.

[92] S. Gligorovski, R. Strekowski, S. Barbati, D. Vione, Environmental implications of hydroxyl radicals ($^{\bullet}$OH), Chem. Rev. 115 (2015) 13051-13092.

[93] F. Haber, J. Weiss, The catalytic decomposition of hydrogen peroxide by iron salts, Proc. R. Soc. Lond. A Math Phys. Sci. 147 (1934) 332-351.

[94] C. Huang, C. Dong, Z. Tang, Advanced chemical oxidation: its present role and potential future in hazardous waste treatment, Waste Manage. 13 (1993) 361-377.

[95] W. Barb, J. Baxendale, P. George, K. Hargrave, Reactions of ferrous and ferric ions with hydrogen peroxide. Part I.—The ferrous ion reaction, Trans. Faraday Soc. 47 (1951) 462-500.

[96] A. Naldoni, A. Schiboula, C.L. Bianchi, D.H. Bremner, Mineralisation of surfactants using ultrasound and the advanced Fenton process, Water Air Soil Pollut. 215 (2011) 487-495.

[97] C. Walling, Fenton's reagent revisited, Acc. Chem. Res. 8 (1975) 125-131.

[98] M.L. Kremer, The Fenton reaction. Dependence of the rate on pH, J. Phys. Chem. A 107 (2003) 1734-1741.

[99] M. Vanaporn, M. Wand, S.L. Michell, M. Sarkar-Tyson, P. Ireland, S. Goldman, et al., Superoxide dismutase C is required for intracellular survival and virulence of Burkholderia pseudomallei, Microbiol. 157 (2011) 2392-2400.

[100] S. Singh, Cerium oxide based nanozymes: Redox phenomenon at biointerfaces, Biointerphases, 11 (2016) 04B202.

[101] S.S. Ali, J.I. Hardt, K.L. Quick, J.S. Kim-Han, B.F. Erlanger, T.-t. Huang, et al., A biologically effective fullerene (C60) derivative with superoxide dismutase mimetic properties, Free Radical Biol. Med. 37 (2004) 1191-1202.

[102] A. Rahal, A. Kumar, V. Singh, B. Yadav, R. Tiwari, S. Chakraborty, et al., Oxidative stress, prooxidants, and antioxidants: the interplay, Biomed. Res. Int. 2014 (2014).

[103] J. Mu, L. Zhang, M. Zhao, Y. Wang, Catalase mimic property of Co_3O_4 nanomaterials with different morphology and its application as a calcium sensor, ACS Appl. Mater. Interfaces 6 (2014) 7090-7098.

[104] X. Wang, Q. Yang, Y. Cao, H. Hao, J. Zhou, J. Hao, Metallosurfactant Ionogels in Imidazolium and Protic Ionic Liquids as Precursors To Synthesize Nanoceria as Catalase Mimetics for the Catalytic Decomposition of H_2O_2, Chem. Eur. J. 22 (2016) 17857-17865.

[105] W. Zhang, J. Dong, Y. Wu, P. Cao, L. Song, M. Ma, et al., Shape-dependent enzyme-like activity of Co_3O_4 nanoparticles and their conjugation with his-tagged EGFR single-domain antibody, Colloids Surf. B 154 (2017) 55-62.

[106] S. Bhagat, N.S. Vallabani, V. Shutthanandan, M. Bowden, A.S. Karakoti, S. Singh, Gold core/ceria shell-based redox active nanozyme mimicking the biological multienzyme complex phenomenon, J. Colloid Interface Sci. 513 (2018) 831-842.

[107] J. Li, W. Liu, X. Wu, X. Gao, Mechanism of pH-switchable peroxidase and catalase-like activities of gold, silver, platinum and palladium, Biomaterials 48 (2015) 37-44.

[108] X. Wang, Y. Hu, H. Wei, Nanozymes in bionanotechnology: from sensing to therapeutics and beyond, Inorg. Chem. Front. 3 (2016) 41-60.

[109] A.A. Vernekar, T. Das, S. Ghosh, G. Mugesh, A remarkably efficient $MnFe_2O_4$-based oxidase nanozyme, Asian J. Chem. 11 (2016) 72-76.

[110] A. Asati, S. Santra, C. Kaittanis, S. Nath, J.M. Perez, Oxidase-like activity of polymer-coated cerium oxide nanoparticles, Angew. Chem. Int. Ed. 48 (2009) 2308-2312.

[111] Y. Wang, Z. Li, J. Wang, J. Li, Y. Lin, Graphene and graphene oxide: biofunctionalization and applications in biotechnology, Trends Biotechnol. 29 (2011) 205-212.

[112] C. Coughlan, M. Ibanez, O. Dobrozhan, A. Singh, A. Cabot, K.M. Ryan, Compound copper chalcogenide nanocrystals, Chem. Rev. 117 (2017) 5865-6109.

[113] S. Xu, X. Bai, L. Wang, Exploration of photothermal sensors based on photothermally responsive materials: a brief review, Inorg. Chem. Front. 5 (2018) 751-759.

[114] M. Saranya, C. Santhosh, S.P. Augustine, A.N. Grace, Synthesis and characterisation of CuS nanomaterials using hydrothermal route, J. Exp. Nanosci. 9 (2014) 329-336.

[115] A. Hayat, G. Catanante, J. Marty, Current trends in nanomaterial-based amperometric biosensors, Sensors 14 (2014) 23439-23461.

[116] M. Nasir, M.H. Nawaz, U. Latif, M. Yaqub, A. Hayat, A. Rahim, An overview on enzyme-mimicking nanomaterials for use in electrochemical and optical assays, Microchim. Acta 184 (2017) 323-342.

[117] S.K. Kailasa, J.R. Koduru, M.L. Desai, T.J. Park, R.K. Singhal, H. Basu, Recent progress on surface chemistry of plasmonic metal nanoparticles for colorimetric assay of drugs in pharmaceutical and biological samples, TrAC, Trends Anal. Chem. 105 (2018) 106-120.

[118] L. Yu, Y. Qiao, L. Miao, Y. He, Y. Zhou, Recent progress in fluorescent and colorimetric sensors for the detection of ions and biomolecules, Chin. Chem. Lett. 29 (2018) 1545-1559.

[119] L.N. Suvarapu, S.-O. Baek, Recent studies on the speciation and determination of mercury in different environmental matrices using various analytical techniques, Int. J. Anal. Chem. 2017 (2017).

[120] G. Luka, A. Ahmadi, H. Najjaran, E. Alocilja, M. DeRosa, K. Wolthers, et al., Microfluidics integrated biosensors: A leading technology towards lab-on-a-chip and sensing applications, Sensors 15 (2015) 30011-30031.

[121] F.X. Schmid, Biological macromolecules: UV-visible spectrophotometry, e LS, (2001). DOI: 10.1038/npg.els.0003142.

[122] J. Roberts, A. Power, J. Chapman, S. Chandra, D. Cozzolino, The Use of UV-Vis Spectroscopy in Bioprocess and Fermentation Monitoring, Fermentation 4 (2018) 18.

[123] C.H. Tan, Determination of Pb (II), Cu (II) and Ni (II) in Water by Direct Measurement Using UV/VIS Spectrophotometer: Universiti Sains Malaysia; 2015.

[124] Y. Song, W. Wei, X. Qu, Colorimetric biosensing using smart materials, Adv. Mater. 23 (2011) 4215-4236.

[125] P.D. Josephy, T. Eling, R.P. Mason, The horseradish peroxidase-catalyzed oxidation of 3, 5, 3', 5'-tetramethylbenzidine. Free radical and charge-transfer complex intermediates, J. Biol. Chem. 257 (1982) 3669-3675.

[126] A. Sharma, S.G. Schulman, Introduction to fluorescence spectroscopy: Wiley-interscience; 1999.

[127] P.T. So, C.Y. Dong, Fluorescence spectrophotometry, e LS, (2001). DOI: 10.1038/npg.els.0002978.

[128] X.F. Wang, A. Periasamy, B. Herman, D.M. Coleman, Fluorescence lifetime imaging microscopy (FLIM): instrumentation and applications, Crit. Rev. Anal. Chem. 23 (1992) 369-395.

[129] Z. Yilong, Z. Dean, L. Daoliang, Electrochemical and other methods for detection and determination of dissolved nitrite: A review, Int. J. Electrochem. Sci. 10 (2015) 1144-1168.

[130] K. Bubacz, E. Kusiak-Nejman, B. Tryba, A. Morawski, Investigation of OH radicals formation on the surface of TiO_2/N photocatalyst at the presence of terephthalic acid solution. Estimation of optimal conditions, J. Photochem. Photobiol. A 261 (2013) 7-11.

[131] R.R. Arvizo, S. Bhattacharyya, R.A. Kudgus, K. Giri, R. Bhattacharya, P. Mukherjee, Intrinsic therapeutic applications of noble metal nanoparticles: past, present and future, Chem. Soc. Rev. 41 (2012) 2943-2970.

[132] R. De La Rica, D. Aili, M.M. Stevens, Enzyme-responsive nanoparticles for drug release and diagnostics, Adv. Drug Deliv. Rev. 64 (2012) 967-978.

[133] S. Link, M.A. El-Sayed, Optical properties and ultrafast dynamics of metallic nanocrystals, Annu. Rev. Phys. Chem. 54 (2003) 331-366.

[134] L. Wang, Synthetic methods of CuS nanoparticles and their applications for imaging and cancer therapy, RSC Adv. 6 (2016) 82596-82615.

[135] X. Huang, I.H. El-Sayed, W. Qian, M.A. El-Sayed, Cancer cell imaging and photothermal therapy in the near-infrared region by using gold nanorods, J. Am. Chem. Soc. 128 (2006) 2115-2120.

[136] S. Wang, J. Lin, P. Huang, Advances on the Use of Biodegradable Proteins/Peptides in Photothermal Theranostics, J. Nanomater. 2016 (2016) 13.

[137] V. Shanmugam, S. Selvakumar, C.-S. Yeh, Near-infrared light-responsive nanomaterials in cancer therapeutics, Chem. Soc. Rev. 43 (2014) 6254-6287.

[138] Y. Zhao, L. Tong, Z. Li, N. Yang, H. Fu, L. Wu, et al., Stable and multifunctional dye-modified black phosphorus nanosheets for near-infrared imaging-guided photothermal therapy, Chem. Mater. 29 (2017) 7131-7139.

[139] T. Liu, Y. Chao, M. Gao, C. Liang, Q. Chen, G. Song, et al., Ultra-small MoS_2 nanodots with rapid body clearance for photothermal cancer therapy, Nano Res. 9 (2016) 3003-3017.

[140] M. Zhou, R. Zhang, M. Huang, W. Lu, S. Song, M.P. Melancon, et al., A chelator-free multifunctional [64Cu] CuS nanoparticle platform for simultaneous micro-PET/CT imaging and photothermal ablation therapy, J. Am. Chem. Soc. 132 (2010) 15351-15358.

[141] B.P. Jiang, L. Zhang, X.L. Guo, X.C. Shen, Y. Wang, Y. Zhu, et al., Poly (N-phenylglycine)-Based nanoparticles as highly effective and targeted near-infrared photothermal therapy/photodynamic therapeutic agents for malignant melanoma, Small 13 (2017) 1602496.

[142] H. Lee, S.W. Yoon, E.J. Kim, J. Park, In-situ growth of copper sulfide nanocrystals on multiwalled carbon nanotubes and their application as novel solar cell and amperometric glucose sensor materials, Nano Lett. 7 (2007) 778-784.

[143] Y. Li, W. Lu, Q. Huang, C. Li, W. Chen, Copper sulfide nanoparticles for photothermal ablation of tumor cells, Nanomed. 5 (2010) 1161-1171.

[144] J. Bai, Y. Liu, X. Jiang, Multifunctional PEG-GO/CuS nanocomposites for near-infrared chemo-photothermal therapy, Biomaterials 35 (2014) 5805-5813.

[145] C.D. Liu H, Li L, Liu T, Tan L, Wu X, et al., Multifunctional gold nanoshells on silica nanorattles: a platform for the combination of photothermal therapy and chemotherapy with low systemic toxicity., Angew. Chem. Int. Ed. 50 (2011) 891-895.

[146] T.S. Fang W, Liu P, Fang X, Gong J, Zheng N., Pd nanosheet-covered hollow mesoporous silica nanoparticles as a platform for the chemo-photothermal treatment of cancer cells, Small 8 (2012) 3816-3822.

[147] M. Vallet-Regí, M. Colilla, I. Izquierdo-Barba, M. Manzano, Mesoporous silica nanoparticles for drug delivery: current insights, Molecules 23 (2018) 47.

[148] X. Liu, Q. Ren, F. Fu, R. Zou, Q. Wang, G. Xin, et al., CuS@ $mSiO_2$-PEG core–shell nanoparticles as a NIR light responsive drug delivery nanoplatform for efficient chemo-photothermal therapy, Dalton Trans. 44 (2015) 10343-10351.

[149] X. Liu, B. Li, F. Fu, K. Xu, R. Zou, Q. Wang, et al., Facile synthesis of biocompatible cysteine-coated CuS nanoparticles with high photothermal conversion efficiency for cancer therapy, Dalton Trans. 43 (2014) 11709-11715.

[150] Y. Huang, Y. Lai, S. Shi, S. Hao, J. Wei, X. Chen, Copper Sulfide Nanoparticles with Phospholipid-PEG Coating for In Vivo Near-Infrared Photothermal Cancer Therapy, Chem. Asian J. 10 (2015) 370-376.

[151] J. Ong, M.R. Appleford, G. Mani, Introduction to biomaterials: basic theory with engineering applications: Cambridge University Press; 2014.

[152] P. Parhi, C. Mohanty, S.K. Sahoo, Nanotechnology-based combinational drug delivery: an emerging approach for cancer therapy, Drug Discovery Today 17 (2012) 1044-1052.

[153] J. Cao, Z. Chen, J. Chi, Y. Sun, Y. Sun, Recent progress in synergistic chemotherapy and phototherapy by targeted drug delivery systems for cancer treatment, Artif. Cells Nanomed. Biotechnol. 46 (2018) 817-830.

[154] F. Zhou, S. Wu, B. Wu, W.R. Chen, D. Xing, Mitochondria-targeting single-walled carbon nanotubes for cancer photothermal therapy, Small 7 (2011) 2727-2735.

[155] G.N. Makhadmeh, A. Abdul Aziz, K. Abdul Razak, The efficacy of methylene blue encapsulated in silica nanoparticles compared to naked methylene blue for photodynamic applications, Artif. Cells Nanomed. Biotechnol. 44 (2016) 1018-1022.

[156] L. Fan, S. Zhao, X. Jin, Y. Zhang, C. Song, H. Wu, Synergistic chemo-photodynamic therapy by "big & small combo nanoparticles" sequential release system, Nanomed. Nanotechnol. Biol. Med. 14 (2018) 109-121.

[157] L. Fan, B. Jin, S. Zhang, C. Song, Q. Li, Stimuli-free programmable drug release for combination chemo-therapy, Nanoscale 8 (2016) 12553-12559.

[158] X. Feng, D. Jiang, T. Kang, J. Yao, Y. Jing, T. Jiang, et al., Tumor-homing and penetrating peptide-functionalized photosensitizer-conjugated PEG-PLA nanoparticles for chemo-photodynamic combination therapy of drug-resistant cancer, ACS Appl. Mater. Interfaces 8 (2016) 17817-17832.

[159] J.C.Y. Kah, R.C.Y. Wan, K.Y. Wong, S. Mhaisalkar, C.J.R. Sheppard, M. Olivo, Combinatorial treatment of photothermal therapy using gold nanoshells with conventional photodynamic therapy to improve treatment efficacy: an in vitro study, Lasers Surg. Med. 40 (2008) 584-589.

[160] J.L. Vivero-Escoto, R.C. Huxford-Phillips, W. Lin, Silica-based nanoprobes for biomedical imaging and theranostic applications, Chem. Soc. Rev. 41 (2012) 2673-2685.

[161] L. Li, L.H. Rashidi, M. Yao, L. Ma, L. Chen, J. Zhang, et al., CuS nanoagents for photodynamic and photothermal therapies: Phenomena and possible mechanisms, Photodiagn. Photodyn. Ther. 19 (2017) 5-14.

CHAPTER 2

A facile preparation of CuS-BSA nanocomposites as enzyme mimics: Application for selective and sensitive sensing of Cr(VI) ions

2.1. Introduction

Contaminated water by heavy metal ions represents a major risk to human health. Although most of heavy metal ions are essential to human body, when their concentration exceeds the normal level, they cause chronic toxicities. Thus, the detection of metal ions in water is a persistent need for environmental protection.

Chromium generally occurs in the environment in two main forms: Cr(VI) and Cr(III). Cr(III) is considered as an essential element for carbohydrate, protein and lipid metabolism, as well as insulin efficiency [1] due to its enhancement in transporting glucose through the cell membrane. Indeed, supplemental Cr(III) as chromium picolinate enhances the blood glucose, insulin, hemoglobin and cholesterol in a concentration dependent way in Type 2 diabetes mellitus. In contrast, deficiency in Cr(III) can result in nerve and brain damage. The first report to highlight chromium deficiency was in 1977 [2], when a patient suffered from low insulin levels due to glucose intolerance, where it has been observed that Cr requirement is closely related to the level of glucose metabolism. Unlike Cr(III), Cr(VI) is highly toxic and considered to be carcinogen [3]. This form of chromium compound can be found in the earth's crust and used in many industrial processes such as chrome plating, manufacturing of pigments and dyes, paints, plastics, wood preservation, and leather tanning [4]. Therefore, the risk of Cr(VI) disposal to water, air, and soil is restricted to means of industrial facilities. The high solubility and mobility of anionic forms of Cr(VI) ($HCrO_4^-$ or CrO_4^{2-}) raised concern on the hazardous effect of these species. Indeed, Cr(VI) ions can be also transported through cellular membranes by sulphate/phosphate anion channels due to their similarity in structure, since at physiological pH, hexavalent chromium exists as oxyanion with an overall -2 charge [5]; once inside the cells, they can interact with biological species (ex. DNA) [6], causing extensive damage and leading to serious deficiencies.

On the other hand, H_2O_2, a naturally occurring by-product of oxygen metabolism, is of biological interest, due to its ability to transform into harmful free radicals that can readily interact with biological molecules. Recently, it has been found that H_2O_2 can form an intermediate with thiol-group containing species in the cellular membrane for the activation of Cr(VI) ions to enhance their toxicity and mutagenicity [7]. The interaction between H_2O_2 and Cr(VI) ions is demonstrated to be pH-dependent. Joaquin *et al.* [7] reported that at low pH, Cr(VI) acts as an oxidizing agent towards the generation of hydroxyl radicals.

The U.S. EPA (Environmental Protection Agency) Guidelines for Carcinogen Risk Assessment [8, 9], stated that Cr(VI) concentration in drinking water exceeding 0.1 mg/L is considered to be carcinogen through mutagenic mode of action. Thus, people residing near sources of industrial waste of Cr(VI) compounds and consuming Cr(VI) in drinking water are more susceptible to cancer. Therefore, it is mandatory to develop a highly efficient technique for Cr(VI) detection.

Many methods have been reported for efficient sensing of heavy metal ions, such as atomic absorption [10], emission [11], and mass spectroscopies [12]. Although these methods are highly selective and sensitive for detecting heavy metal ions, they do not fulfill all the requirements for sensing. Thereby, the colorimetric detection holds interest due to its simplicity, low cost, fast response, and low detection limit.

With the emergence of nanotechnology, the development of enzyme mimics as colorimetric biosensors offers great advantages in the environmental and biomedical fields. Thus, interested by the innovative technology of nanozymes, semiconductor chalcogenides and particularly copper sulfide (CuS) nanostructures proved to be promising for sensing approaches. These materials have found widespread use in various fields like photovoltaics, photocatalysis, energy conversion devices, biosensors, etc. [13]. However, in absence of appropriate surface coating, these nanostructures tend to agglomerate in aqueous media, hampering their applications [14].

Many studies reported that biomolecules such as proteins can be used to prevent nanomaterial's aggregation [15]. Therefore, great efforts have been made to develop peroxidase mimics with excellent stability. The high water solubility and stability of bovine serum albumin (BSA) protein, as well the presence of various binding sites in its structure, makes it a key factor to stabilize CuS NPs and prevent their aggregation to enhance their sensing performance.

Herein, BSA was used as a template to synthesize water dispersible copper sulfide nanoparticles (CuS NPs) *via* a facile method. The obtained CuS-BSA nanocomposite was applied for selective Cr(VI) colorimetric sensing. The as-synthesized CuS-BSA nanocomposite exhibited good stability and dispersibility in various aqueous media and displayed intrinsic peroxidase-mimic for efficient catalytic TMB substrate in the presence of H_2O_2. This property was further exploited for the detection of Cr(VI) in acidic aqueous medium, as confirmed by a naked eye detection of the color change of the solution from transparent to blue. Additionally, UV/vis absorbance spectroscopy was used for the quantitative determination of the oxidized TMB (oxTMB) at 654 nm. The mechanism of TMB oxidation was enhanced by H_2O_2 decomposition by Cr(VI) to generate $HO^{\bullet}$ in the presence of CuS-BSA. The experimental parameters for colorimetric Cr(VI) detection including temperature, pH and incubation time were also assessed. A detection limit of Cr(VI) as low as 50 nM was achieved under optimized conditions.

2.2. Experimental section

2.2.1. Preparation of the CuS-BSA nanocomposite with 0.1:1 CuS/BSA Molar ratio

The CuS-BSA nanocomposite was prepared *via* bio-mineralization process. In short, an aqueous solution of BSA was prepared by dissolving 250 mg of BSA in 9 mL MQ-water. Then 1 mL of $Cu(Ac)_2$ (0.1 M) was added dropwise to the above solution under magnetic stirring, resulting in a blue cloudy mixture, after which a light green color was observed. 0.5 mL of an aqueous NaOH (2 M) solution was used to adjust the pH at 12, after which the mixture turned directly to purple. Then 52 mg of Na_2S (0.4 M) were added under stirring; the color of the solution turned to brown immediately. The mixture was further processed at 55 °C for 5 h to give a green solution. The resulting CuS-BSA nanocomposite was purified by dialysis against a 12-14 kDa molecular mass cut off dialysis membrane in MQ-water for 24 h to remove excess copper ions (to exclude their contribution in the catalytic process), then stored at 4 °C for later use. A fluffy-like dark green powder of CuS-BSA was collected by lyophilization for further characterization, which can be re-dispersed easily in MQ-water.

2.3. Results and discussion

2.3.1. Synthesis and characterization of CuS-BSA nanocomposite

The synthesis of CuS-BSA nanocomposite was carried out in two steps, first by forming Cu^{2+}-BSA complex through the addition of $Cu(Ac)_2$ into BSA solution, where Cu^{2+} cations can

bind with BSA through exposing the binding sites of BSA to copper ions in alkaline pH medium (pH 12), followed by the release of S^{2-} by adding Na_2S. The presence of free -SH in cysteine amino acid of BSA [16] enhances the conjugation of metal sulfides to BSA, and acts as a nucleating agent for the formation of CuS-BSA. The formation of CuS-BSA can also be easily visualized by color change, as clearly observed in **Fig. 1**.

Figure 1: Colour changes at different stages during the synthesis of CuS-BSA nanocomposite. 1: BSA aqueous solution, 2: BSA-Cu^{2+} metal ion complex formation, 3: growth of BSA-Cu^{2+} at pH 12, 4: Nucleation of Cu^{2+}-S^{2-} on BSA, 5: Growth of CuS-BSA.

The chemical composition of CuS-BSA nanocomposite was evaluated by X-ray photoelectron spectroscopy (XPS) analysis. The XPS survey spectrum of CuS-BSA **(Fig. 2a)** comprises bands attributed to C_{1s} (285 eV), N_{1s} (400 eV), O_{1s} (532 eV), Cu_{2p} (932 eV) and S_{2p} (163 eV) with atomic concentrations of 62.97%, 15.44%, 19.69%, 0.77% and 1.12%, respectively. The atomic ratio of Cu/S is calculated to be 0.68:1; the deviation from 1 is due to the presence of S groups in BSA.
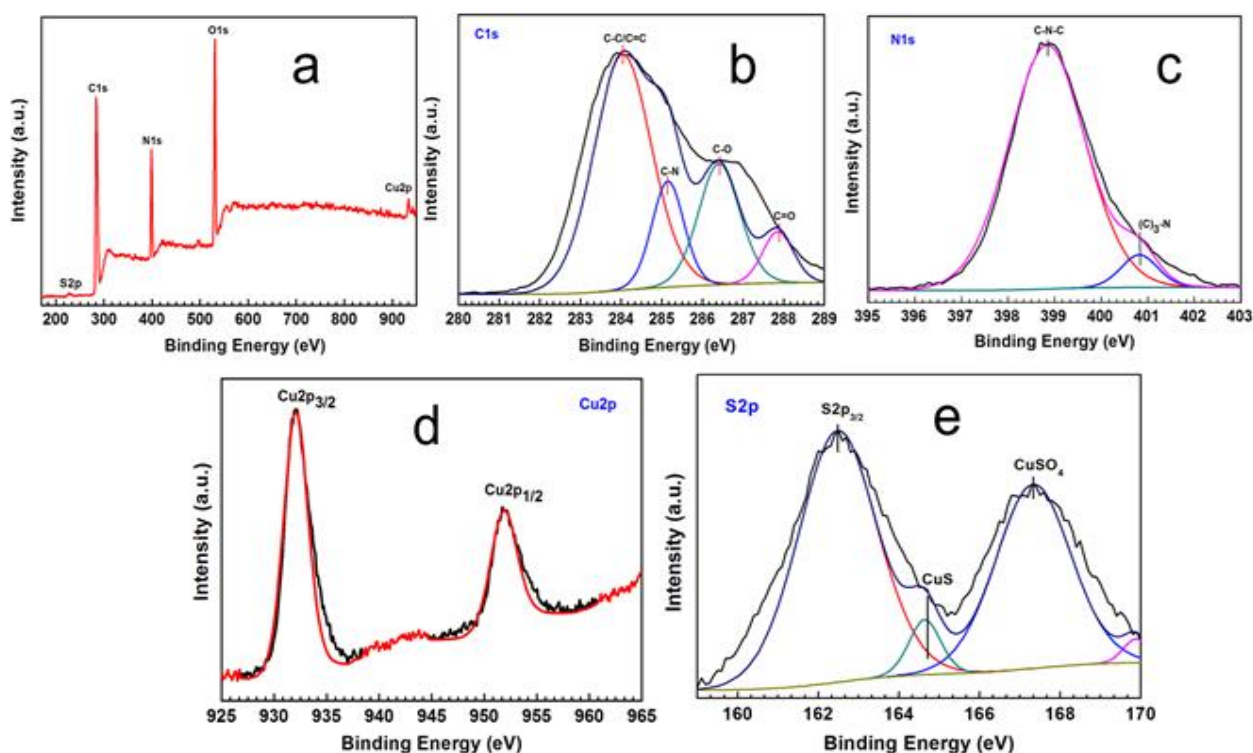
Figure 2: XPS survey spectrum (a), and high resolution XPS spectra of C_{1s} (b), N_{1s} (c), Cu_{2p} (d) and S_{2p} (e) of CuS-BSA nanocomposite.

The C_{1s} high resolution XPS spectrum of CuS-BSA **(Fig. 2b)** can be fitted with several components at binding energies of 284.04, 285.25, 286.41 and 287.86 eV corresponding to C-C/C=C, C-N, C-O and C=O groups, respectively [17, 18]. The C–S bond is not clearly observed because the binding energy of C–S at 285.3 eV is very close to that of sp^3 C–C [19]. Similarly, the N_{1s} high resolution XPS spectrum of CuS-BSA **(Fig. 2c)** can be deconvoluted into C-N-C (398.84 eV) and $(C)_3$-N (400.82 eV) of BSA [20, 21]. This is not surprising since nitrogen contribution originates from BSA only. **Figure 2d** represents the deconvoluted spectrum of Cu_{2p} with peaks at 932.06 and 951.82 eV assigned to $Cu_{2p3/2}$ and $Cu_{2p1/2}$, respectively. A characteristic satellite peak is observed at around 943 eV, indicating the presence of paramagnetic Cu^{2+} ions of CuS [22].

In the S_{2p} high resolution XPS spectrum of CuS-BSA (**Fig. 2e**), the peaks at 164.64 and 167.88 eV are attributed to CuS and $CuSO_4$, respectively [23-25] even though one cannot rule out a contribution of oxidized sulfur in BSA. The peak at ~163 eV originates from S_{2p} in BSA.

The morphology, structure and particle size of CuS-BSA nanocomposite were characterized by TEM analysis (**Fig. 3**). TEM images **(Fig. 3a, b)** indicate that CuS-BSA nanocomposite consists of nanoparticles with an average size of 9.7 ± 0.6 nm, as shown in **Figure 3d** (the size of the NPs was calculated by using Image J software). HRTEM and SAED pattern of the synthesized CuS-BSA nanocomposite revealed good crystallinity of the NPs (**Fig. 3c**). The lattice fringe spacing of CuS-BSA NPs is about 0.15 nm, which corresponds to the (116) plane of CuS nanoparticles. The SAED pattern in the inset of **Figure 3c** displays the (101) and (102) crystalline planes of CuS, confirming the formation of crystalline CuS-BSA NPs. The elemental mapping confirmed the coexistence of C, N, O, Cu and S elements in CuS-BSA nanocomposite (**Fig. 3 f-j**), in full accordance with the XPS analysis data.
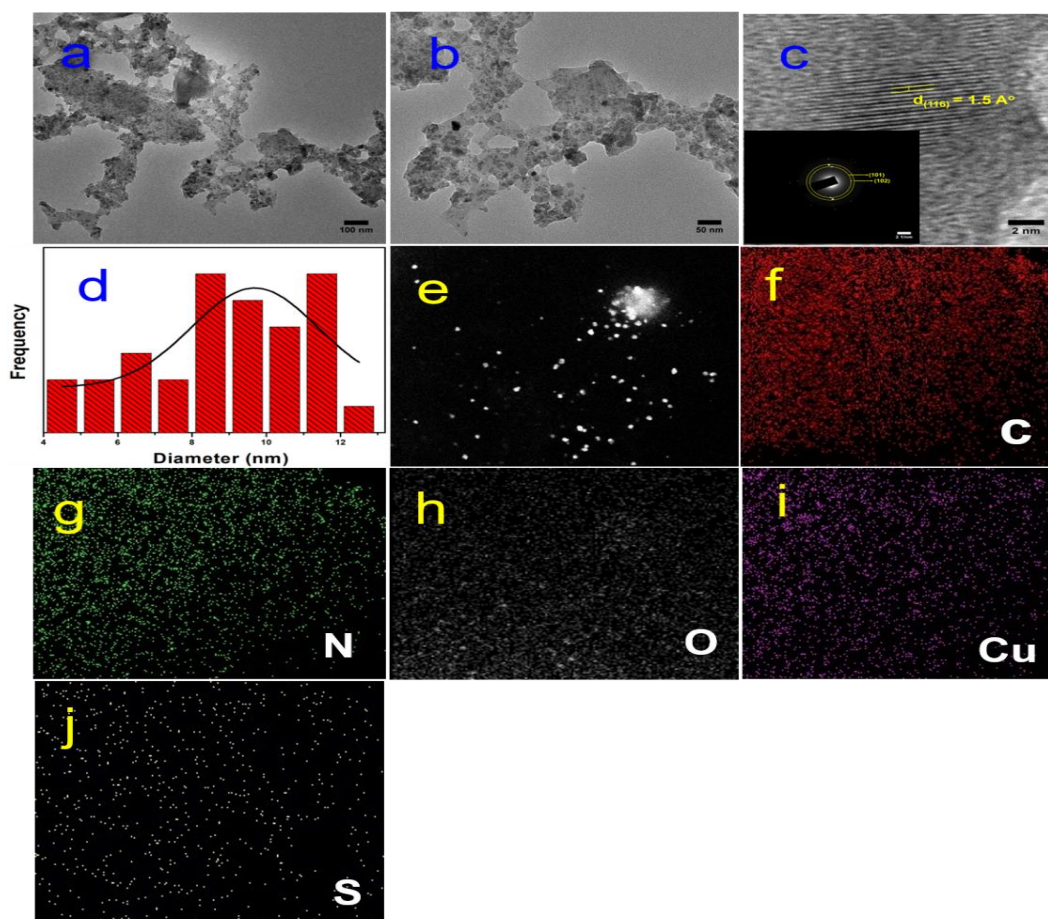
Figure 3: (a, b) TEM images, (c) HRTEM image and SAED pattern (inset), (d) particle size distribution, (e) HAADF-STEM image, elemental mapping for (f) carbon, (g) nitrogen, (h) oxygen, (i) copper, (j) sulfur of CuS-BSA nanocomposite.

Dynamic light-scattering and zeta potential were used to determine the hydrodynamic size and surface charge of CuS-BSA nanocomposite, respectively. The mean hydrodynamic average diameter of the CuS-BSA was determined to be as 53.8 ± 12.3 nm **(Fig. 4a),** which is slightly higher than the mean diameter obtained by TEM due to the hydrodynamic water molecules on the surface of the nanocomposite. The zeta potential of CuS-BSA was recorded by dispersing of CuS-BSA (30 µg/mL) solution in 1 mL MQ-water at different pH values adjusted by using NaOH (0.1 M) or HCl (0.1 M). As depicted in **Figure 4b**, CuS-BSA bears a negative charge value of -31.1 ± 5.7 mV due to the presence of -COOH groups in BSA, with an isoelectric point (IEP) of 5.3 at which the surface zeta potential is zero **(Fig. 4c)**.
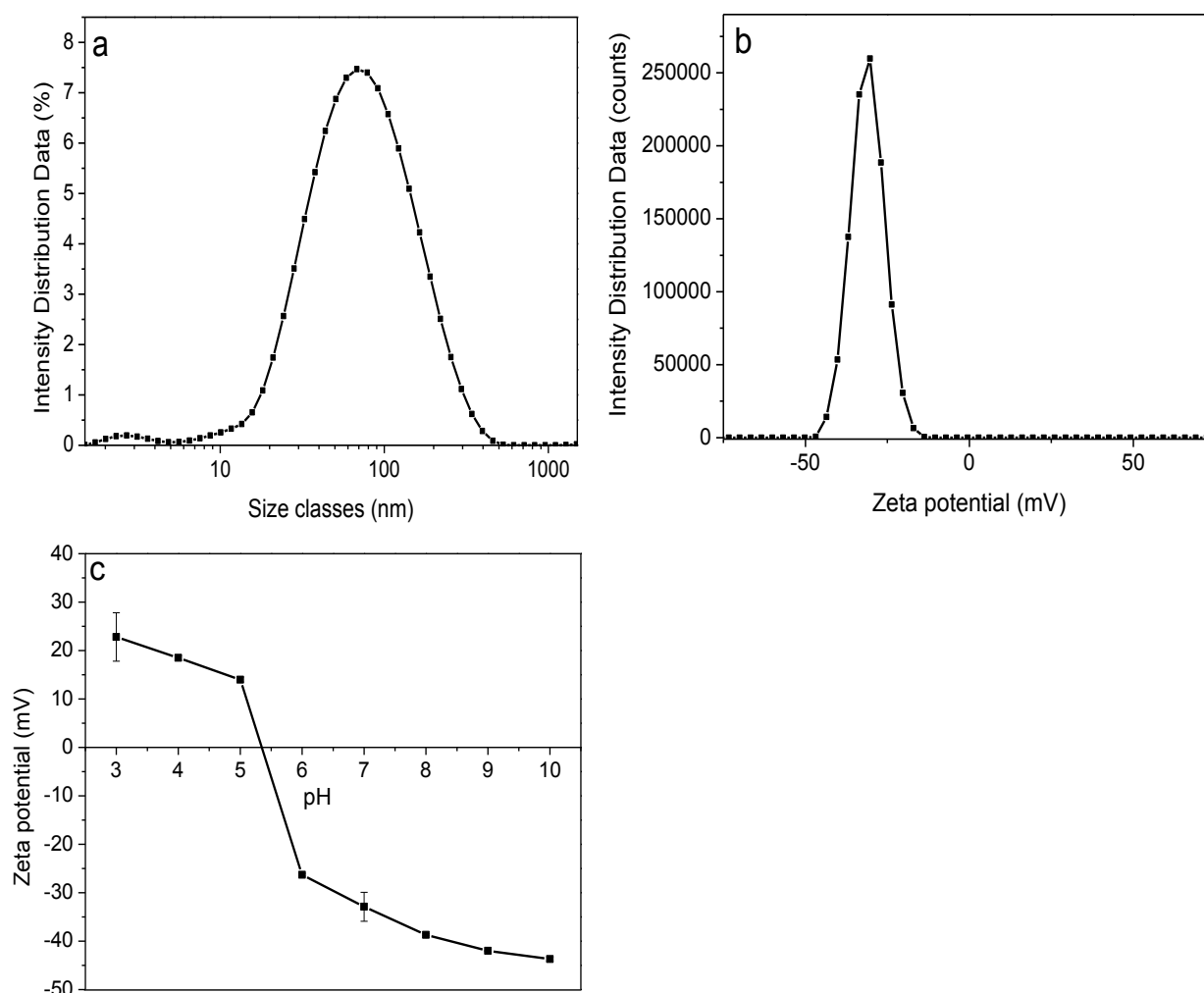
Figure 4: Dynamic light scattering (DLS) (a), Zeta potential (b) and pH dependent variation of zeta potential (c) of CuS-BSA nanocomposite.

CuS-BSA aqueous solution was stable for five months at a concentration ~10 mg/mL with no noticeable precipitates, which indicates the long-term colloidal stability and dispersibility of our nanocomposite. The long-term stability of CuS-BSA nanocomposite was also examined in different solvents (phosphate buffer saline (PBS), acetate buffer, DMSO, Dulbecco's modified Eagle's medium (DMEM)), where no apparent precipitation was observed at a concentration of 1 mg/mL (**Fig. 5**). Therefore, BSA proved to be an excellent capping agent to prevent aggregation of CuS NPs.

The chemical composition of BSA and CuS-BSA was further assessed by Fourier transform infrared spectroscopy (FTIR). **Figure 6** displays the FTIR spectrum of pure BSA, comprising the characteristic bands of amide I (C=O) and amide II (C-N stretching or N-H bending vibrations) at 1655 and 1539 cm^{-1}, respectively, OH at 3445-3296 cm^{-1} and amide A (-NH) at 3061 cm^{-1} [15]. The same bands appear in the FTIR spectrum of CuS-BSA, suggesting the presence of BSA in the nanocomposite [26]. However, by comparing both spectra, one can notice a slight decrease of the intensity of the characteristic -NH peak in CuS-BSA, most likely due to the coupling between NH in BSA and Cu^{2+}. Additionally, the OH peak in the FTIR spectrum of CuS-BSA is shifted by 49 cm^{-1} [27], confirming the interaction between BSA and CuS, as BSA can provide various binding sites such as -NH, -OH, -COOH, and -SH functionalities.
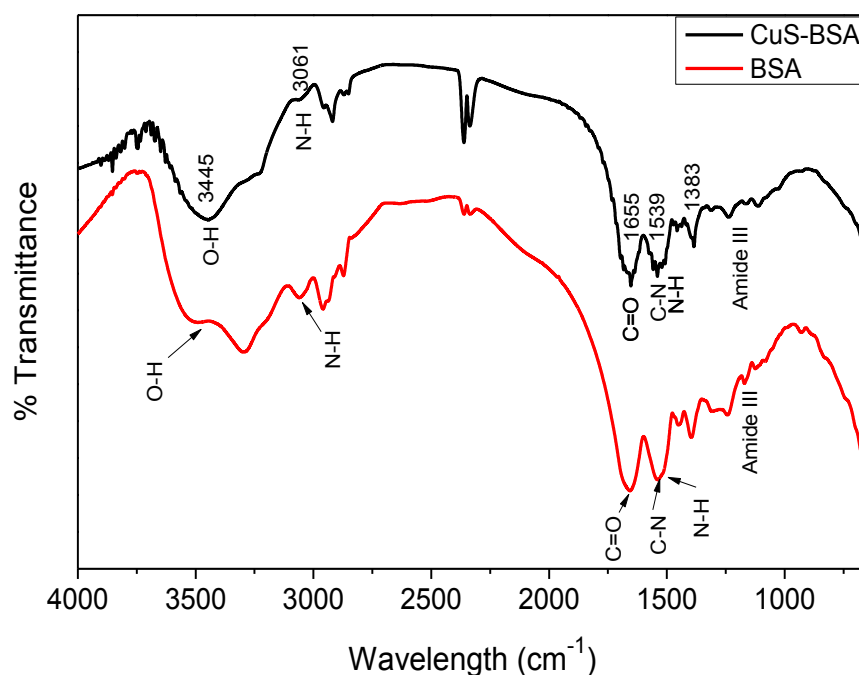
Figure 6: FTIR spectra of native BSA and CuS-BSA nanocomposite.

Thermogravimetric analysis (TGA) and derivative thermogravemetric (DTG) were conducted to confirm the interaction between CuS NPs and BSA and to study their thermal behavior. DTG is performed to detect the slight changes in weight that cannot be observed by TGA. The TGA curve of CuS-BSA exhibited a total weight loss ca. 78.88% from room temperature (RT) to 980 °C **(Fig. 7a)**, with 21.12 % of residual mass left at the end of heating, while the TGA curve of pure BSA showed a total weight loss ca 82.43% from RT to 980 °C

(Fig. 7b) with 17.57% of residual mass. This decrease in weight loss for CuS-BSA is attributed to the conjugation between BSA and CuS NPs. Pristine BSA showed 3 stages of weight loss observed by DTG, from 30 to 100 °C, 170 to 250 °C, and from 250 to 565 °C. The first stage of weight loss is due to evaporation of water molecules, while the second mass loss is assigned to BSA degradation (most likely oxygen containing groups). The last step corresponds to the decomposition of amino acid residues, which occurs at higher temperature range [27]. However, after conjugation of BSA with CuS NPs, the thermal curve displayed only two stages of weight loss, from RT to 100 °C, and from 160 to 480 °C. The decrease in decomposition temperature is attributed to the reduction of thermal stability of BSA after hybridization with the nanoparticles. BSA exhibited a steep curve at 320 °C, which is also displayed in CuS-BSA with a slight decrease in temperature. These results indicated the decrease in thermal stability of BSA could be ascribed to the physical adsorption of CuS on BSA rather than chemical interaction.
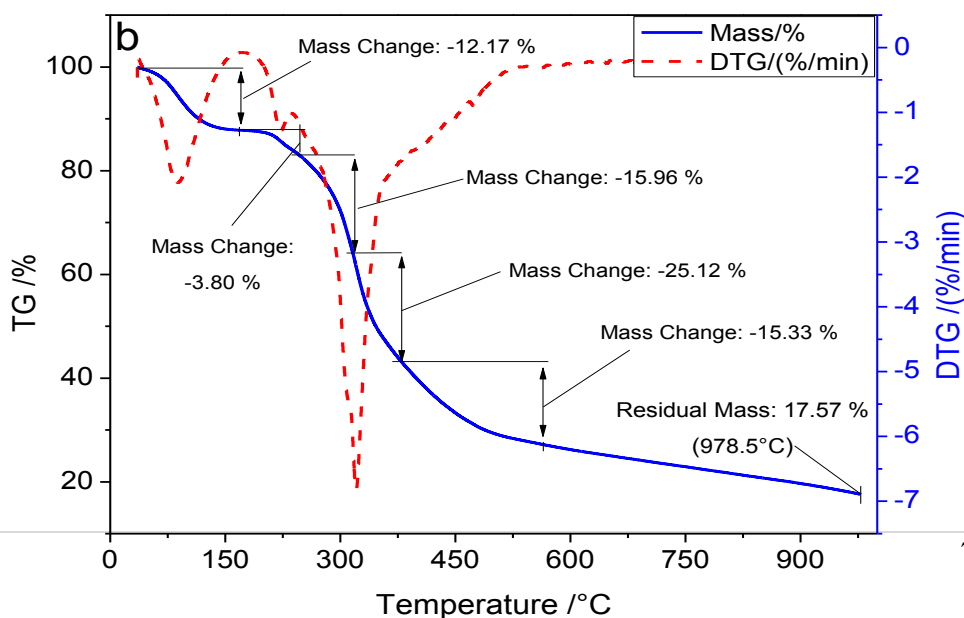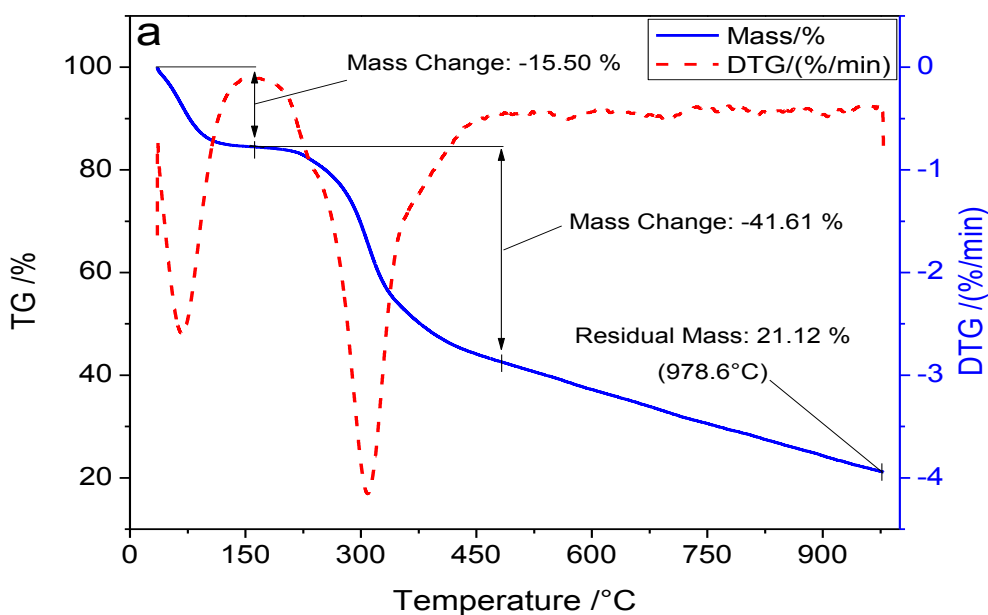
Figure 7: TGA and DTG curves of CuS-BSA nanocomposite (a) and pristine BSA (b).

2.3.2. Peroxidase-like catalytic activity of CuS-BSA nanocomposite

The peroxidase-like catalytic activity of CuS-BSA in mimicking the naturally occurring HRP enzyme was examined by studying the oxidation of the TMB molecule. As shown in **Figure 8**, the oxidation of TMB occurred within 30 s when H_2O_2 was added to CuS-BSA catalyst in acidic medium, confirmed by a visual color change from transparent to blue, and by dynamic increase of the absorbance peak at 654 nm. In order to confirm the catalytic nature of the process, control experiments were carried out in the absence of CuS-BSA and H_2O_2, respectively. Surprisingly, the experimental systems without H_2O_2 showed almost a negligible color change, while in absence of CuS-BSA, a slight blue color was observed **(Fig. 9)**, indicating that both CuS-BSA and H_2O_2 are responsible for the generation of blue colored oxTMB.
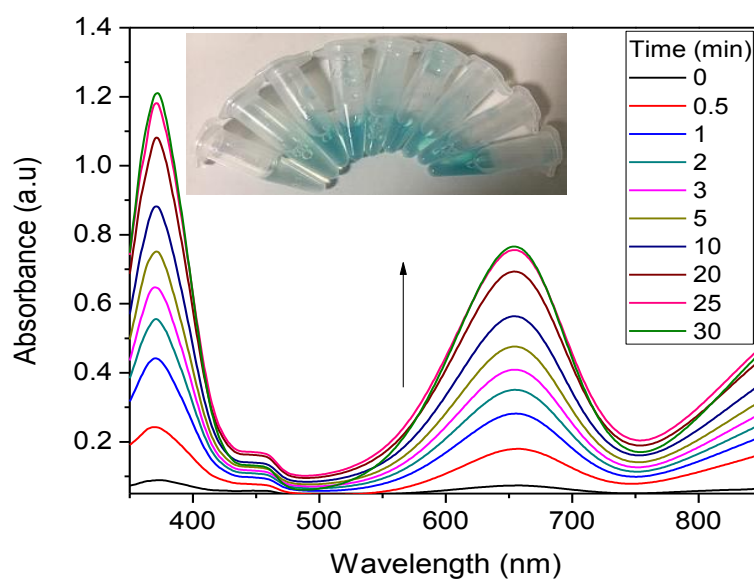
Figure 8: UV-Vis absorbance of TMB catalyzed by CuS-BSA in the presence of H_2O_2 in a time-scan mode. Reaction conditions: TMB (0.16 mM), H_2O_2 (20 mM), CuS-BSA (0.1 mg/mL), acetate buffer (pH = 3.9) at 25 °C. Inset: the color change at different time intervals.
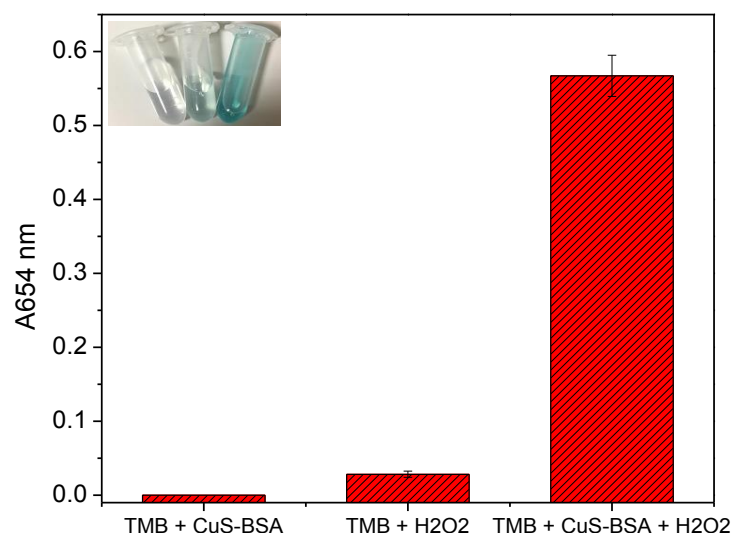
Figure 9: UV/vis absorption of TMB at 654 nm under different conditions. Inset: Typical photographs of TMB oxidation (from left to right: without H_2O_2 (colorless), without CuS-BSA (light blue), and with both H_2O_2 and CuS-BSA NPs (blue). Reaction conditions: CuS-BSA (0.1 mg/mL), TMB (0.16 mM), H_2O_2 (20 mM), acetate buffer (pH=3.9), T=25 °C, incubation time=25 min (error bars represent the STD of 3 repeated measurements).

It is worth to notice that the oxidation of TMB resulted from the hydroxyl radicals (HO$^{\bullet}$) generated from H_2O_2 decomposition in an acidic medium [28], which are catalyzed by Cu^{2+} ions on the CuS-BSA surface, similar to the Fenton reaction [29]. Basically, H_2O_2 degradation is catalytically mediated by Cu^{2+}, in which a reactive intermediate (Cu^{3+}) is formed through the process. Thereby, copper is being progressively cycled between two different oxidation forms (+2 and +3) (**Fig. 10**).

The mechanism of $^{\bullet}$OH formation can be summarized as follows:

$$Cu^{2+} + H_2O_2 \longrightarrow Cu^{3+} + HO^{\bullet} + HO^{-}$$

$$Cu^{3+} + H_2O_2 \longrightarrow Cu^{2+} + HOO^{\bullet} + H^{+}$$
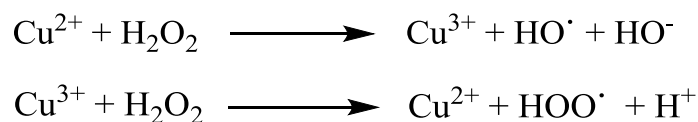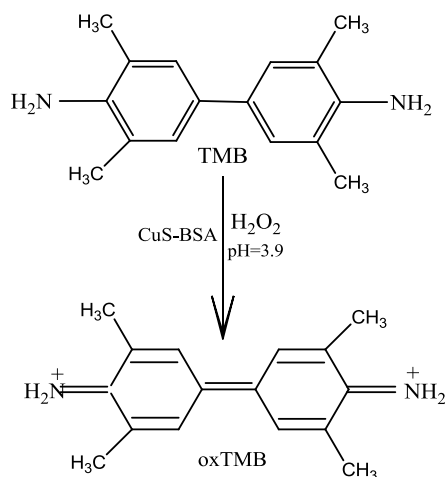
Figure 10: Schematic illustration of the oxidation of TMB.

2.3.3. Experimental conditions' optimization

To attain the optimal conditions for the catalytic reaction, TMB oxidation was performed by varying different parameters like the catalyst concentration, solution pH, and temperature of the reaction. The absorbance at 654 nm versus concentration of CuS-BSA response curve was plotted in **Figure 11a**. It is clear that the absorbance gradually increases with the increase of CuS-BSA concentration and saturates at almost 0.1 mg/mL, which is selected for the following experiments. Notably, the rate of the catalytic reaction is highly dependent on catalyst concentration due to the excessive amount of TMB [30].

The catalytic activity of CuS-BSA NPs, like natural enzymes, depends on pH and temperature. Changes of pH (2.5-10) and temperature (25-50 °C) were recorded to demonstrate their influence on the oxidation of TMB. As revealed in **Figure 11b**, the relative activity of CuS-BSA was plotted as a function of temperature, whereby the maximum absorbance intensity at 654 nm was set as 100%.

Relative activities were determined by the following equation (Eq. 1):

$$R.A = (A654 \text{ nm}/A654_{max}) \times 100\% \qquad (1)$$

Where R.A represents the relative activity, A654 is to the absorbance of oxTMB at 654 nm, and $A654_{max}$ is the maximum absorbance at 654 nm.

The catalytic oxidation of TMB was stable over a wide temperature range and reaches an optimum intensity at 40 °C, close to the physiological environment, due to the increase in the rate of the enzyme-like reaction at this value. A slight decrease in enzymatic activity takes

place at 50 °C, most probably due to partial decomposition of H_2O_2. This result indicates that CuS-BSA displayed better catalytic performance than natural enzymes, which lose their activity completely at high temperature. Similarly, CuS-BSA revealed higher activity at pH 3.9 **(Fig. 11c)** due to the enhanced solubility of TMB in acidic environment [30, 31]. Therefore, we performed the following assays in acidic medium and we selected 25 °C for the remaining experiments.

In order to evaluate the rate of the catalytic process, TMB oxidation was monitored at different incubation times in the presence of H_2O_2 (20 mM), CuS-BSA (0.1 mg/mL), and TMB (0.16 mM) in 1.5 mL acetate buffer (pH=3.9). As observed in **Figure 11d**, the catalytic activity of CuS-BSA increased upon increasing the incubation time to reach a maximum value after 25 min; this incubation time was adopted to complete the oxidation reaction in the following experiments.
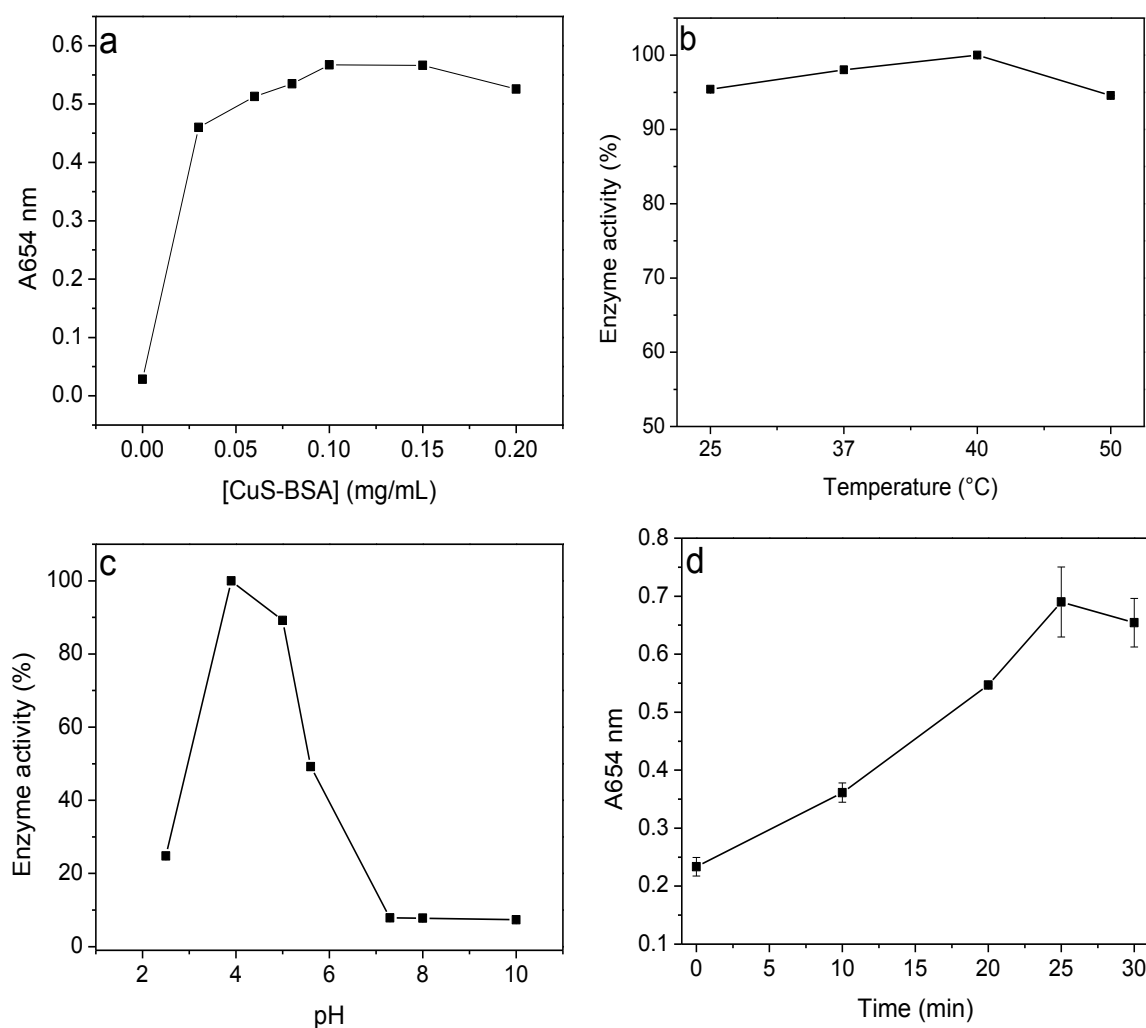
Figure 11: Influence of catalyst concentration (a), temperature (b), pH (c), and incubation time (d) on the catalytic oxidation of TMB. Conditions: TMB (0.16 mM), H_2O_2 (20 mM), CuS-BSA (0.1 mg/mL), incubation time=25 min.

2.3.4. Steady-state kinetic mechanism of CuS-BSA nanocomposite as a peroxidase-mimic and determining the Michaelis-Menten constant

The kinetic assay of CuS-BSA as a peroxidase mimic was carried out by determining the initial rate of each substrate, i.e. the slope of $\Delta A654$ per unit time (min). In order to determine the reaction rate of each substrate (TMB and H_2O_2), the UV/vis absorption spectra were recorded at 654 nm in a time-scan mode for different concentrations of substrate (**Fig. 12a, b**). Then the Beer-Lambert law (Eq. 2) was applied to convert the absorbance values to the corresponding concentrations:

$$A = \varepsilon \times c \times l \qquad (2)$$

Where A is the absorbance at 654 nm, ε is the molar absorptivity ($\varepsilon = 3.9 \times 10^4$ for oxTMB at 654 nm in $M^{-1}.cm^{-1}$), c represents the concentration of one substrate, and l corresponds to the optical path length (l=1 cm). **Figures 12c** and **12d** depict respectively typical Michaelis–Menten curves for TMB and H_2O_2, where the data are obtained by plotting the initial reaction rate versus concentration of one substrate and changing the concentration of the other. The catalytic parameters (K_m and V_{max}), determined from a Lineweaver–Burk plot, are listed in **Table 1**, where the y-intercept allows to determine the V_{max} and the x-intercept gives the K_m value.

Table 1: Michaelis-Menten constant and maximum velocity for typical TMB and H_2O_2 substrates in comparison with previously reported materials.

Catalyst	K_m (M)		V_{max} $(M.s^{-1})$	
	H_2O_2	TMB	H_2O_2	TMB
CuS-BSA (our work)	0.014	2×10^{-4}	2×10^{-8}	3.3×10^{-8}
HRP [32]	0.0037	4.34×10^{-4}	8.71×10^{-8}	10×10^{-8}
MoS_2 [28]	1.16×10^{-4}	3.87×10^{-4}	2.42×10^{-8}	7.23×10^{-8}
Cu-rGO [33]	0.0263	10.5×10^{-4}	5.385×10^{-8}	3.289×10^{-8}

It was found that the catalytic oxidation of TMB by CuS-BSA follows a typical Michaelis–Menten kinetics, and the low K_m value of CuS-BSA indicates a high affinity towards TMB.

The K_m value of CuS-BSA with TMB as the substrate was calculated to be 2×10^{-4} M, which is lower than that of HRP enzyme [34]. However, the K_m value of CuS-BSA with H_2O_2 as substrate is 0.014 M, suggesting a better binding affinity of CuS-BSA to TMB along with a good peroxidase-enzyme mimic behavior, compared to other previously reported nanomaterials (**Table 1**).
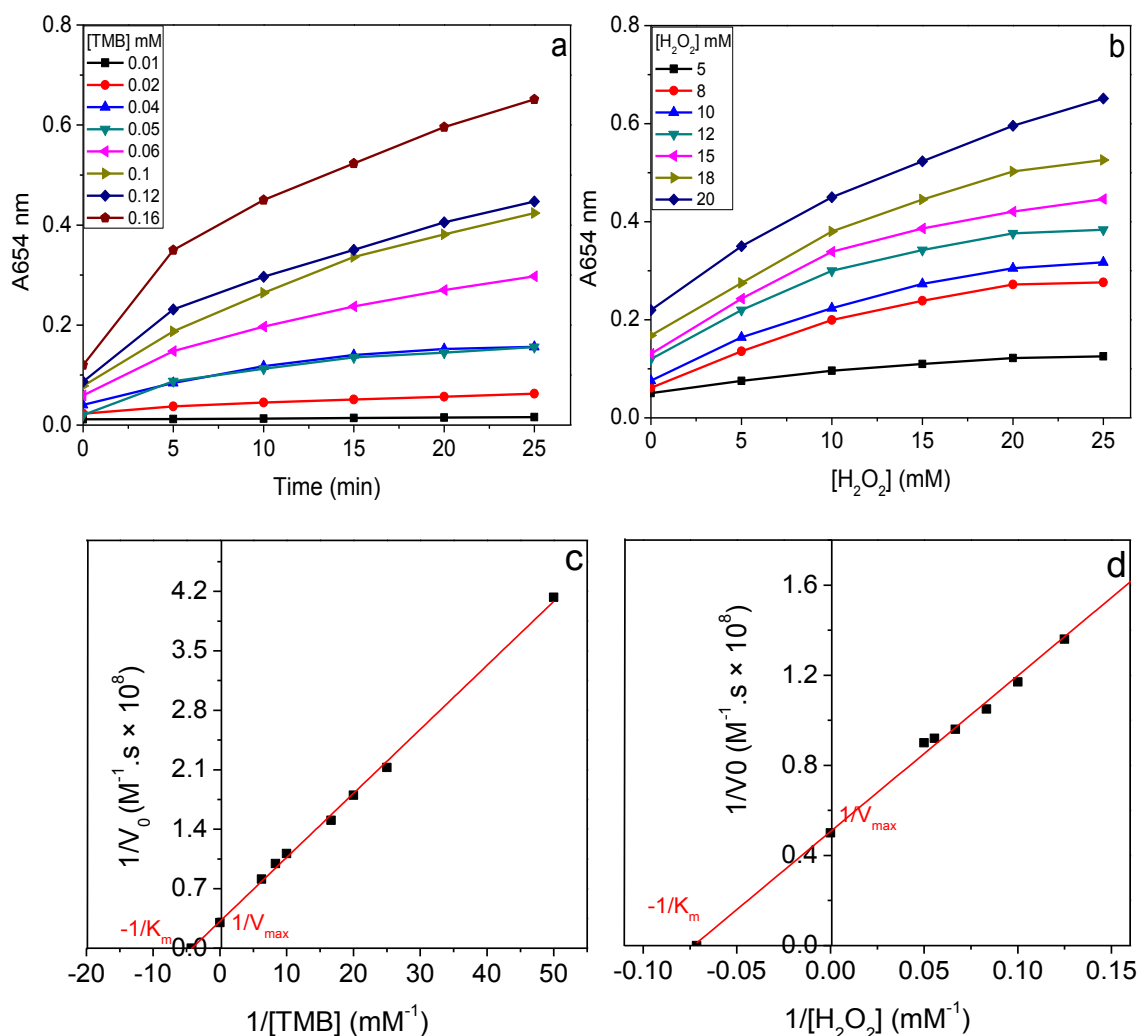
Figure 12: UV/vis absorption of different concentrations of TMB (a) and H_2O_2 (b) substrates in a time scan-mode; Steady-state kinetics using the Michaelis-Menten assay and Lineweaver-Burk plot for TMB (c) and H_2O_2 (d). Reaction conditions: CuS-BSA (0.1 mg/mL), acetate buffer (pH = 3.9), T=25 °C.

2.3.5. Colorimetric sensing of Cr(VI)

To further widen the scope of the CuS-BSA nanozyme, we have investigated the direct sensing of Cr(VI) using the optimized experimental conditions of TMB oxidation by H_2O_2.

Indeed, the catalytic activity of CuS-BSA towards TMB oxidation was enhanced in the presence of Cr(VI), whereby in a low pH medium (pH=3.9), Cr(VI) induces the decomposition of H_2O_2 into H_2O and O_2 [28], which can readily generate $HO^{\bullet}$ radicals when combined with Cu^{2+} on the surface of CuS-BSA nanocomposite; the reaction of Cr(VI) with H_2O_2 can also generate $HO^{\bullet}$ radicals (Haber Weiss-type reaction), which is favored in acidic medium [35, 36]. Cr(VI) sensing was recorded under various experimental conditions, i.e. in the absence and presence of H_2O_2 under the optimized reaction conditions.

A good linear relationship ($R^2 = 0.99372$) was obtained for Cr(VI) in the 80-200 μM concentration range in the absence of H_2O_2 **(inset of Fig. 13)**; the limit of detection (LOD) was determined using the following formula (Eq. 3):

LOD = (3× standard deviation of the blank)/slope of linear regression line   (3)

The LOD for Cr(VI) was determined to be 18 μM at a signal-to-noise ratio of 3.

Figure 13: A dose-responsive curve of Cr(VI) using CuS-BSA as a catalyst. Absorbance of oxTMB versus Cr(VI) concentration at 654 nm in the presence of CuS-BSA (0.1 mg/mL), TMB (0.16 mM), pH=3.9, T=25 °C, incubation time=25 min; inset: The linear calibration plot for the determination of Cr(VI).

Based on this result, the detection of Cr(VI) was examined in the presence of H_2O_2. **Figure 14** depicts the absorbance of oxTMB (A654 nm) at various H_2O_2 concentrations, where above 20 mM the catalytic activity of CuS-BSA was not much improved. Therefore, we fixed the concentration of H_2O_2 to 20 mM to determine the LOD of Cr(VI) within the 0.01-50 μM concentration range.
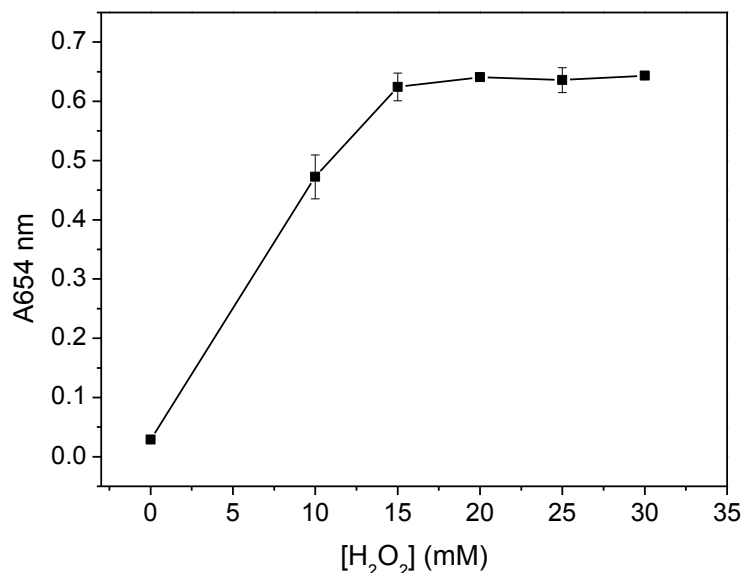
Figure 14: A dose-response curve of H_2O_2 during the oxidation of TMB (0.16 mM) catalyzed by CuS-BSA (0.1 mg/mL) in the presence of 20 μM Cr(VI) at 25 °C upon incubation for 25 min at pH=3.9.

Noticeably, the LOD of Cr(VI) was enhanced in the presence of H_2O_2, and a good linear relation (R^2= 0.9984) between the absorbance A654 nm and the concentration of Cr(VI) within the 0-100 nM and 1-20 μM ranges was observed **(Fig. 15 and inset of Fig. 16)**. The LOD was found to be 50 nM at a signal-to-noise ratio of 3 using the lower linear range, below the detectable level determined by the U.S EPA (1.9 μM) [37], demonstrating the sensitive detection of Cr(VI) using CuS-BSA nanocomposite.

The performance of the developed sensor is better than that reported for the same metal ion using colorimetric detection methods **(Table 2)**.
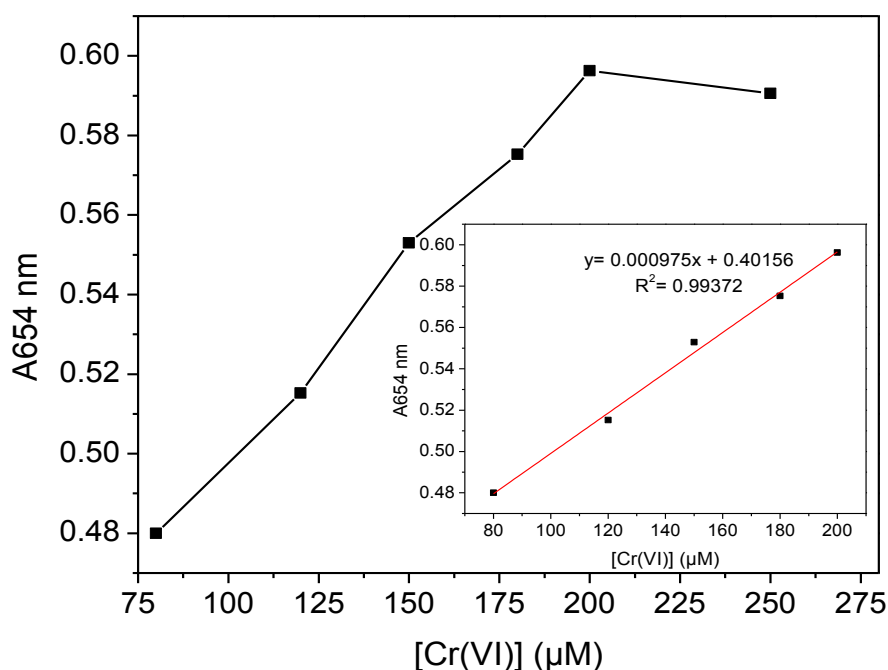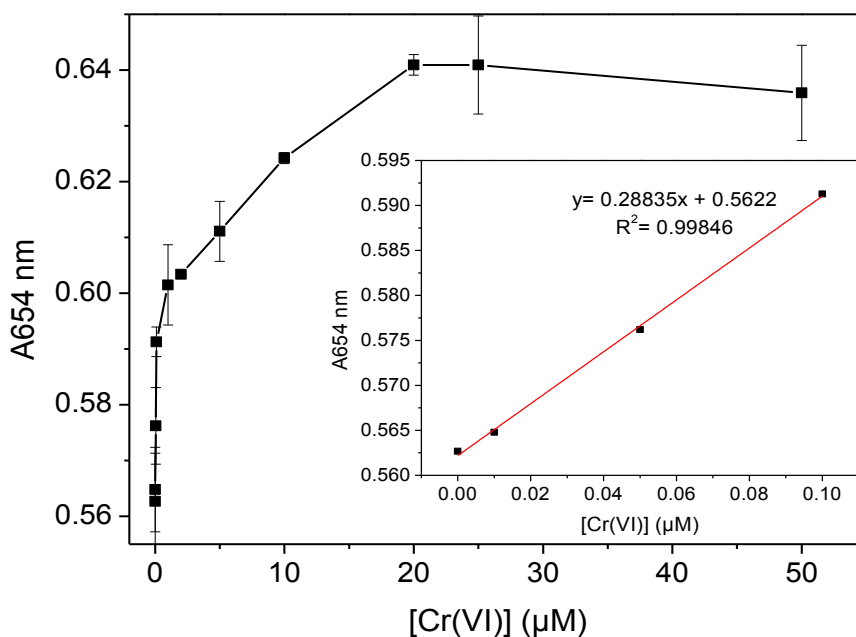
Figure 15: A dose-responsive curve of Cr(VI) using CuS-BSA as a catalyst. Absorbance of oxTMB versus Cr(VI) concentration at 654 nm in the presence of CuS-BSA (0.1 mg/mL), TMB (0.16 mM), H_2O_2 (20 mM), pH=3.9, T=25 °C, incubation time=25 min; inset: The calibration curve in the lower concentration range.
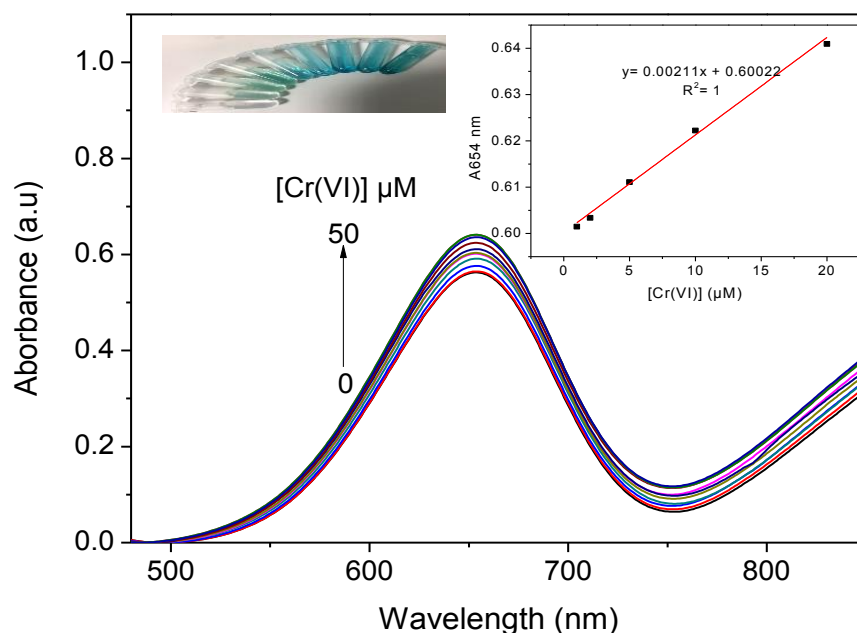
Figure 16: Cr(VI) concentration-dependent UV-Vis absorption spectra of oxTMB. Conditions: TMB (0.16 mM), CuS-BSA (0.1 mg/mL), H_2O_2 (20 mM), pH=3.9, T=25 °C, incubation time=25 min. Inset: from left to right: change in color for TMB oxidation with increasing concentration of Cr(VI), and the calibration curve in the higher Cr(VI) concentration range.

Table 2: Comparison of different nanomaterials for colorimetric sensing of Cr(VI).

Materials	LOD	Linear range	Ref.
GA-Au NPs	2 µM	1-20 µM	[37]
BSA-Au NPs/STCP	280 nM	0.5-50.0 µM	[38]
frGO-Cu	67.13 nM	0-200 nM	[39]
CuS-BSA	50 nM and 6.8 µM	0-100 nM and 1-20 µM	Our work

2.3.6. Analysis of hydroxyl radicals (HO$^{\bullet}$)

To better understand the mechanism of TMB oxidation, a probe molecule, terephthalic acid (TA), was used to confirm the generation of HO$^{\bullet}$ radicals; this molecule can react with HO$^{\bullet}$ radicals to produce a fluorescent molecule, 2-hydroxyterephthalic acid (HTA), which exhibits a fluorescence emission band with a maximum at 430 nm under an excitation at 315 nm. **Figure 17** depicts the evolution of fluorescence emission intensity under various experimental conditions, where the highest intensity was recorded for the reaction containing CuS-BSA, H_2O_2, Cr(VI) and TA, indicating that H_2O_2 decomposition was enhanced in the presence of Cr(VI).
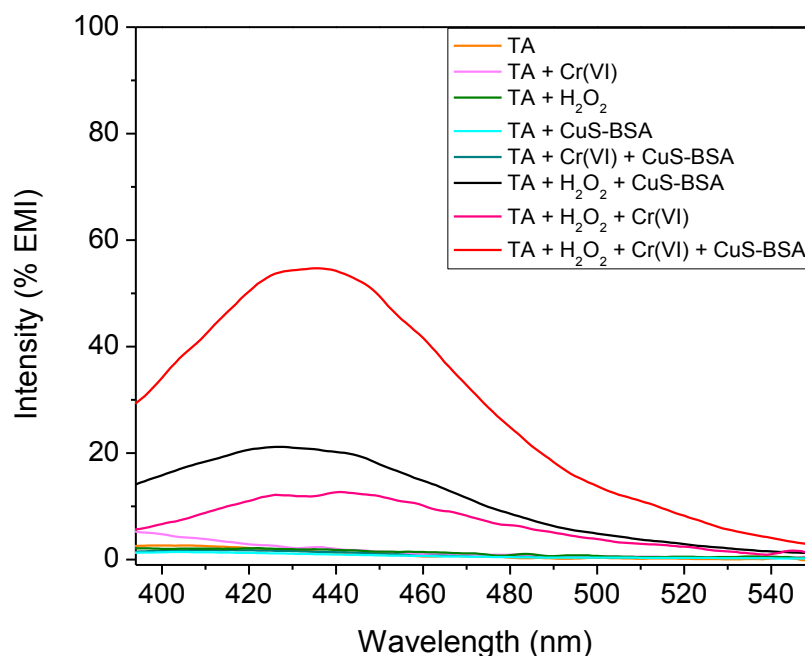
Figure 17: Fluorescence spectra to identify hydroxyl radicals' formation using terephthalic acid (TA) as a fluorescent probe. Reaction conditions: CuS-BSA (0.1 mg/mL), H_2O_2 (20 mM), Cr(VI) (20 µM), TA (0.15 mM) and 0.1 M acetate buffer (pH = 3.9) for 25 min at 25 °C.

2.3.7. Detection of Cr(VI) in real environmental water samples

To validate the practical application of our proposed nanozyme, Cr(VI) detection was tested in different environmental samples using the optimized conditions (CuS-BSA (0.1 mg/mL), H_2O_2 (20 mM), TMB (0.16 mM), T=25°C, t=25 min). In brief, various concentrations of Cr(VI) (10, 50, 100 nM) were spiked into real water samples collected from different areas in France. The Cr(VI) concentration present in real water samples was determined from a calibration curve, which was established at 654 nm using a series of Cr(VI) concentrations under the same procedure discussed above. The percentage recovery ($[Cr(VI)]_{found}/[Cr(VI)]_{added}$ × 100) and relative standard deviation (RSD %) in these water samples are listed in **Table 3** (n=3). As shown in **Table 3**, the CuS-BSA nanocomposite displayed good recovery percentage for Cr(VI) sensing in different environmental water samples.

Table 3: Detection of Cr(VI) in real environmental water samples (n=3).

Samples	Cr(VI) added (nM)	Cr(VI) found (nM)	Recovery (%)	RSD (%)
Tap water	10	9.95	99.5	0.71
	50	49.5	99	1.42
	100	96	96	2.94
Pond water (Parc du Héron, Lille-France)	10	9.6	96.3	5.79
	50	49.3	98.6	1.24
	100	97.6	97.6	0.59
Sea water (Wimereux)	10	9	90	15.7
	50	49.5	99	1.4
	100	92	92	3.07
Tube-well water	10	9.2	96.5	5.12
	50	49	98	5.7
	100	98.5	98.5	0.71

2.3.8. Selectivity and reproducibility of CuS-BSA enzyme-mimic for sensing heavy metal Cr(VI) ions

In order to evaluate the selectivity of CuS-BSA, the absorbance (A=654 nm) was monitored in presence of different interfering ions (Na^+, Hg^{2+}, Zn^{2+}, Co^{2+}, Ni^{2+}, Cr^{3+}) under the same

conditions using 5-times higher concentration than the optimized Cr(VI) concentration. The specificity of our sensor was tested with the same experimental procedure as mentioned above. As can be seen from **Figure 18a**, Cr(VI) showed the highest remarkable response, indicating the good selectivity of the developed sensor. Interestingly, the absorbance was not enhanced much, even when the concentration of the interfering ions was 5 times higher (100 µM) than that of Cr(VI) (**Fig. 18b**). Also, in the absence of H_2O_2, the interfering ions did not induce blue color change. Notably, due to the higher redox potential of Cr^{6+}/Cr^{3+} (E= +1.33 V) [40] among other interfering metal ions, Na^+/Na (-2.71 V), Co^{2+}/Co (-0.28 V), Zn^{2+}/Zn (-0.76 V), Ni^+/Ni (-0.36 V), Hg^{2+}/Hg (E= +0.92 V), Cr^{3+}/Cr (-0.74 V), it acts as a strong oxidizing agent in an acidic environment for the dismutation of H_2O_2 [7]. Therefore, the results demonstrated high specificity, sensitivity, selectivity, and colorimetric assay can be achieved using CuS-BSA nanocomposite for Cr(VI) detection.
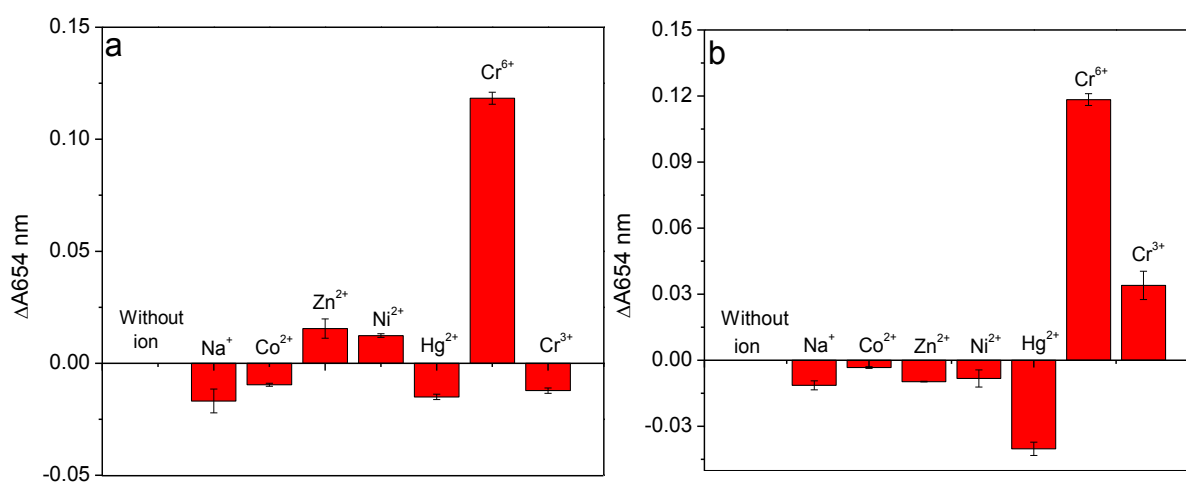
Figure 18: UV-vis absorption at 654 nm of oxTMB in the presence of different interfering ions of concentration 20 µM (a) and 100 µM (5-times higher than the concentration of Cr(VI)). Reaction conditions: CuS-BSA (0.1 mg/mL), H_2O_2 (20 mM), TMB (0.16 mM), Cr(VI) (20 µM) and 0.1 M acetate buffer (pH = 3.9), T=25 °C, incubation time=25 min.

The reusability of CuS-BSA as an enzyme-mimic for TMB oxidation was investigated by performing the reaction for four repeated cycles. As shown in **Figure 19**, the relative activity was approximately the same after four catalytic cycles with a relative STD of 2.8%. The result indicates that CuS-BSA nanocomposite is an enzyme-mimic with excellent catalytic activity and stability.
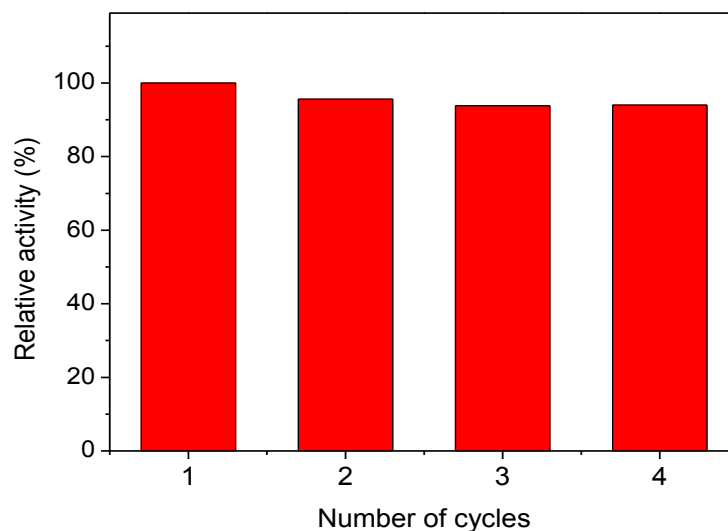
Figure 19: Catalytic activity of CuS-BSA nanocomposite for four successive repeated cycles.

2.4. Conclusion

In summary, this work presented a simple and cost-effective method for the synthesis of CuS-BSA nanocomposite with peroxidase-like activity towards the catalytic oxidation of TMB. The enhanced activity of the nanozyme was further applied for the sensitive and selective detection of hexavalent chromium ions. The proposed sensor showed that the catalytic reaction follows typical Michaelis–Menten kinetics in a pH-dependent manner. Under optimized experimental conditions, a good linear calibration plot was obtained in the concentration range of 0–100 nM and 1-20 μM of Cr(VI) with a detection limit of 50 nM using the lower linear range. Using terephthalic acid, it was possible to confirm the generation of HO$^{\bullet}$ radicals during the TMB catalytic oxidation by H_2O_2 in the presence of CuS-BSA, a process that has been enhanced in the presence of Cr(VI). The method was effectively tested for the determination of Cr(VI) content in spiked real environmental water samples. Based on these observations, the CuS-BSA nanocomposite showed better performance over natural enzymes which opened new promising applications in many fields.

2.5.   References

[1] R.A. Anderson, Chromium, glucose intolerance and diabetes, Am. J. Clin. Nutr. 17 (1998) 548-555.

[2] K.N. Jeejeebhoy, R. Chu, E. Marliss, G.R. Greenberg, A. Bruce-Robertson, Chromium deficiency, glucose intolerance, and neuropathy reversed by chromium supplementation, in a patient receiving long-term total parenteral nutrition, Am. J. Clin. Nutr. 30 (1977) 531-538.

[3] F.-M. Li, J.-M. Liu, X.-X. Wang, L.-P. Lin, W.-L. Cai, X. Lin, et al., Non-aggregation based label free colorimetric sensor for the detection of Cr (VI) based on selective etching of gold nanorods, Sens. Actuators B 155 (2011) 817-822.

[4] L. Blade, M.S. Yencken, M. Wallace, J. Catalano, A. Khan, J. Topmiller, et al., Hexavalent chromium exposures and exposure-control technologies in American enterprise: results of a NIOSH field research study, J. Occup. Environ. Hyg. 4 (2007) 596-618.

[5] U. EPA, Toxicological review of hexavalent chromium, Washington, DC: U, (1998).

[6] X. Shi, Y. Mao, A.D. Knapton, M. Ding, Y. Rojanasakul, P.M. Gannett, et al., Reaction of Cr (VI) with ascorbate and hydrogen peroxide generates hydroxyl radicals and causes DNA damage: role of a Cr (IV)-mediated Fenton-like reaction, Carcinogenesis 15 (1994) 2475-2478.

[7] J.F. Perez-Benito, C. Arias, A Kinetic Study of the Chromium (VI)− Hydrogen Peroxide Reaction. Role of the Diperoxochromate (VI) Intermediates, J. Phys. Chem. A. 101 (1997) 4726-4733.

[8] P.A. Glasser, Kinetics and Mechanisms of Cr 6+ Reduction by Structural Fe (II) in Clay Minerals: Miami University; 2014.

[9] U. EPA, Guidelines for Carcinogen Risk Assessment US Environmental Protection Agency, Washington, DC, EPA/630/P-03/001F, (2005).

[10] A.S. Trindade, A.F. Dantas, D.C. Lima, S.L. Ferreira, L.S. Teixeira, Multivariate optimization of ultrasound-assisted extraction for determination of Cu, Fe, Ni and Zn in vegetable oils by high-resolution continuum source atomic absorption spectrometry, Food Chem. 185 (2015) 145-150.

[11] V.N. Losev, O.V. Buyko, A.K. Trofimchuk, O.N. Zuy, Silica sequentially modified with polyhexamethylene guanidine and Arsenazo I for preconcentration and ICP–OES determination of metals in natural waters, Microchem. J. 123 (2015) 84-89.

[12] H. Wang, Z. Wu, B. Chen, M. He, B. Hu, Chip-based array magnetic solid phase microextraction on-line coupled with inductively coupled plasma mass spectrometry for the determination of trace heavy metals in cells, Analyst. 140 (2015) 5619-5626.

[13] C. Coughlan, M. Ibanez, O. Dobrozhan, A. Singh, A. Cabot, K.M. Ryan, Compound copper chalcogenide nanocrystals, Chem. Rev. 117 (2017) 5865-6109.

[14] Y. Zhao, L. Jiang, Hollow micro/nanomaterials with multilevel interior structures, Adv. Mater. 21 (2009) 3621-3638.

[15] P. Huang, Z. Li, H. Hu, D. Cui, Synthesis and characterization of bovine serum albumin-conjugated copper sulfide nanocomposites, J. Nanomater. 2010 (2010) 33.

[16] L. Yang, R. Xing, Q. Shen, K. Jiang, F. Ye, J. Wang, et al., Fabrication of protein-conjugated silver sulfide nanorods in the bovine serum albumin solution, J. Phys. Chem. B 110 (2006) 10534-10539.

[17] Y. Zhou, Y. Bai, H. Liu, X. Jiang, T. Tong, L. Fang, et al., Tellurium/Bovine Serum Albumin Nanocomposites Inducing the Formation of Stress Granules in a Protein Kinase R-Dependent Manner, ACS Appl. Mater. Interfaces 10 (2018) 25241-25251.

[18] E. Ieva, A. Trapani, N. Cioffi, N. Ditaranto, A. Monopoli, L. Sabbatini, Analytical characterization of chitosan nanoparticles for peptide drug delivery applications, Anal. BioanalChem. 393 (2009) 207-215.

[19] K. Jeon, Synthesis and Characterization of Thionated Reduced Graphene Oxides and Their Thin Films: Arizona State University; 2013.

[20] Z. Luo, S. Lim, Z. Tian, J. Shang, L. Lai, B. MacDonald, et al., Pyridinic N doped graphene: synthesis, electronic structure, and electrocatalytic property, J. Mater. Chem. 21 (2011) 8038-8044.

[21] S. Liu, J. Tian, L. Wang, Y. Zhang, X. Qin, Y. Luo, et al., Hydrothermal treatment of grass: a low-cost, green route to nitrogen-doped, carbon-rich, photoluminescent polymer

nanodots as an effective fluorescent sensing platform for label-free detection of Cu (II) ions, Adv. Mater. 24 (2012) 2037-2041.

[22] J. Zhang, J. Yu, Y. Zhang, Q. Li, J.R. Gong, Visible light photocatalytic H2-production activity of CuS/ZnS porous nanosheets based on photoinduced interfacial charge transfer, Nano Lett. 11 (2011) 4774-4779.

[23] J. Qian, K. Wang, Q. Guan, H. Li, H. Xu, Q. Liu, et al., Enhanced wet hydrogen peroxide catalytic oxidation performances based on CuS nanocrystals/reduced graphene oxide composites, Appl. Surf. Sci. 288 (2014) 633-640.

[24] I. Ancutiene, J.G. Navea, J. Baltrusaitis, Structural, chemical and optical properties of the polyethylene–copper sulfide composite thin films synthesized using polythionic acid as sulfur source, Appl. Surf. Sci. 347 (2015) 520-527.

[25] P. Borthakur, P.K. Boruah, G. Darabdhara, P. Sengupta, M.R. Das, A.I. Boronin, et al., Microwave assisted synthesis of CuS-reduced graphene oxide nanocomposite with efficient photocatalytic activity towards azo dye degradation, J. Environ. Chem. Eng. 4 (2016) 4600-4611.

[26] L. Liang, S. Peng, Z. Yuan, C. Wei, Y. He, J. Zheng, et al., Biocompatible tumor-targeting nanocomposites based on CuS for tumor imaging and photothermal therapy, RSC Adv. 8 (2018) 6013-6026.

[27] X. Chen, L. Ding, P. Liu, Q. Wang, Synthesis of protein-assisted aqueous Ag_2S quantum dots in the bovine serum albumin solution, Surf. Interface Anal. 46 (2014) 301-306.

[28] P. Borthakur, P.K. Boruah, M.R. Das, S.B. Artemkina, P.A. Poltarak, V.E. Fedorov, Metal free MoS_2 2D sheets as a peroxidase enzyme and visible-light-induced photocatalyst towards detection and reduction of Cr (VI) ions, New J. Chem. 42 (2018) 16919-16929.

[29] W. He, H. Jia, X. Li, Y. Lei, J. Li, H. Zhao, et al., Understanding the formation of CuS concave superstructures with peroxidase-like activity, Nanoscale 4 (2012) 3501-3506.

[30] H. Liu, M. Jiao, C. Gu, M. Zhang, Au@ CuxOS yolk-shell nanomaterials with porous shells act as a new peroxidase mimic for the colorimetric detection of H_2O_2, J. Alloys Compd. 741 (2018) 197-204.

[31] Q. Zhang, M. Li, C. Guo, Z. Jia, G. Wan, S. Wang, et al., Fe_3O_4 Nanoparticles Loaded on Lignin Nanoparticles Applied as a Peroxidase Mimic for the Sensitively Colorimetric Detection of H_2O_2, Nanomater. 9 (2019) 210.

[32] L. Gao, J. Zhuang, L. Nie, J. Zhang, Y. Zhang, N. Gu, et al., Intrinsic peroxidase-like activity of ferromagnetic nanoparticles, Nat. Nanotechnol. 2 (2007) 577.

[33] G. Darabdhara, B. Sharma, M.R. Das, R. Boukherroub, S. Szunerits, Cu-Ag bimetallic nanoparticles on reduced graphene oxide nanosheets as peroxidase mimic for glucose and ascorbic acid detection, Sens. Actuators B 238 (2017) 842-851.

[34] H.-F. Lu, J.-Y. Li, M.-M. Zhang, D. Wu, Q.-L. Zhang, A highly selective and sensitive colorimetric uric acid biosensor based on Cu (II)-catalyzed oxidation of 3,3′,5,5′-tetramethylbenzidine, Sens. Actuators B 244 (2017) 77-83.

[35] A.D. Bokare, W. Choi, Chromate-induced activation of hydrogen peroxide for oxidative degradation of aqueous organic pollutants, Environ. Sci. Technol. 44 (2010) 7232-7237.

[36] X. Shi, Reduction of chromium (VI) and its relationship to carcinogenesis, J Toxicol Environ Health Part B: Critical Reviews 2 (1999) 87-104.

[37] C. Dong, G. Wu, Z. Wang, W. Ren, Y. Zhang, Z. Shen, et al., Selective colorimetric detection of Cr (III) and Cr (VI) using gallic acid capped gold nanoparticles, Dalton Trans. 45 (2016) 8347-8354.

[38] J.-f. Guo, D.-q. Huo, M. Yang, C.-j. Hou, J.-j. Li, H.-b. Fa, et al., Colorimetric detection of Cr (VI) based on the leaching of gold nanoparticles using a paper-based sensor, Talanta 161 (2016) 819-825.

[39] P. Borthakur, P.K. Boruah, M.R. Das, S. Szunerits, R. Boukherroub, Cu (0) nanoparticle-decorated functionalized reduced graphene oxide sheets as artificial peroxidase enzymes: application for colorimetric detection of Cr (VI) ions, New J. Chem. 43 (2019) 1404-1414.

[40] M. Dehghani, B. Heibati, A. Asadi, I. Tyagi, S. Agarwal, V. Gupta, Reduction of noxious Cr (VI) ion to Cr (III) ion in aqueous solutions using H_2O_2 and UV/H_2O_2 systems, J. Ind. Eng. Chem. 33 (2016) 197-200.

CHAPTER 3

A. Ultrasmall CuS-BSA-Cu$_3$(PO$_4$)$_2$ nanozymes for highly efficient colorimetric sensing of H$_2$O$_2$ and glucose in contact lens care solutions and human serum

3.1.1. Introduction

Diabetes Mellitus (DM) is a serious metabolic disorder which causes chronic diseases, where more than 240 million individuals are affected by this disease and the amount of people who suffer from this disease is continuing to rise [1]. Diabetes is caused when the body cannot produce enough amount of insulin to meet its requirements, or when it cannot use the produced amount of insulin properly. This disease is considered as life threatening that can lead to various complications such as heart attack, vision loss, and kidney failure.

Biomolecules such as carbohydrates including glucose are considered as an essential source of energy for the survival of living organisms. In order to meet body health requirements, glucose in blood should be maintained in the appropriate range (3800 – 6900 μM) [2]. However, the typical cause of DM is the irregular raise of blood glucose concentration. Therefore, monitoring of blood glucose level constitutes a particular importance in the early diagnosis and to follow-up the treatment of this disease to maintain a balanced health state, as elevated or low levels of glucose can cause incurable health problems and many adverse side effects on the long term. Hydrogen peroxide (H$_2$O$_2$) as well, a naturally occurring end-product of glucose oxidation in cells, can lead to cell damage and represents a major threat to human health when it is overproduced in biological compartments, manifested by the generation of high levels of hydroxyl radicals (HO$^{\bullet}$) by the Fenton reaction mediated by active redox metals. Thus, cytotoxicity, hypoglycemia and hyperglycemia, and many serious health problems are related to high amount of H$_2$O$_2$ and unbalanced state of glucose, respectively. Therefore, quantitative determination of H$_2$O$_2$ and glucose contents in biological samples represents a very active research area for many decades. The first glucose monitoring sensor was utilized in 1962 [3], and since then considerable attempts have been made for the development of new affordable sensors.

In recent years, 2D materials and their composites have generated a huge attention in a wide scope of applications owing to their exceptional properties, such as their extreme small size, good electronic/optical properties and large surface area. Their potency to generate reactive oxygen species (ROS) such as $HO^•$ radicals is a key feature to imitate natural enzymes in their catalytic behavior, which can be used as an insight in sensing biomolecules. The utilization of nanomaterials in the field of sensing has gained tremendous interest over natural biological catalysts, which are sensitive to harsh environmental conditions and lose their catalytic performance when the conditions are not favorable. The low stability, denaturation ability and high cost of natural enzymes hampered their future applications in spite of their high selectivity and substrate specificity [4].

Up to the date, a plethora of nanoparticles (NPs) as enzyme-mimics have been reported for sensing H_2O_2 and glucose. However, stability, biocompatibility, and low detection limit remained a challenge. The first work illustrating the use of nanomaterials as horseradish peroxidase mimics (HRP) was described by Gao and co-workers [5]. This finding stimulated numerous efforts for the preparation of new enzyme-mimetic nanomaterials under the name of nanozymes [6-10], with particular importance in the field of sensors and catalysis for detecting glucose, H_2O_2 and other biologically-relevant molecules. Nanozymes with unexpected excellent catalytic behavior gained enormous interest over natural enzymes owing to their tunable properties, such as small size, large surface area and high stability; they have been utilized in a myriad of applications. Since H_2O_2 is implicated in the catalytic reaction of certain substrates mediated by peroxidases, its detection represents a particular importance. Meanwhile, the production of H_2O_2 in the catalytic oxidation process of glucose by the naturally occurring glucose oxidase (GOx) enzyme generated a great interest for glucose sensing in medical and food applications, which plays a critical role for recovering life quality.

Commonly, traditional methods such as chemiluminescence, fluorometry, electrochemical and spectrophotometric methods [11-15] have been devoted for blood glucose detection. However, the colorimetric determination of biological molecules is of uttermost importance in this field, due to its simplicity and fast detection response which can be easily visualized by the naked eyes or by UV-vis spectrophotometry. Additionally, this methodology can be applied for real time analysis without the requirement of expensive instrumentation.

Among a variety of nanozymes which are utilized for glucose sensing, the use of metal sulfides experienced a remarkable interest. Copper in its divalent form (Cu^{2+}) participates in the Fenton-like reaction and catalyzes the production of $HO^•$ radicals through the

decomposition of H_2O_2 [16]. He and coworkers pointed out that CuS with a specific morphology possesses enzyme-like behavior [17]. Dutta et al. [18] also investigated the use of CuS for glucose sensing in blood. Notably, copper sulfide (CuS) [19], an important chalcogenide semiconductor, was investigated in many fields like catalysis, sensing, solar cells, therapeutics and drug delivery [20]. Owing to its unique electrical, optical, and physico-chemical properties, CuS was chosen as a useful colorimetric tool to display a reliable assay for sensing of both H_2O_2 and glucose for biomedical applications.

In this chapter, we demonstrated the preparation of CuS-BSA stabilized $Cu_3(PO_4)_2$ nanoparticles (NPs) as intrinsic peroxidase mimics for H_2O_2 and glucose sensing. The use of metal sulfide nanoparticles coupled with metal phosphates, not only enhances the catalytic activity of the nanoparticles, but also produces nanoparticles with small size and become good alternatives for the preparation of enzymomimetic sensors. The peroxidase-like catalytic action of the proposed sensor is based on consuming hydrogen peroxide and in turn forming an oxidized substrate. Currently, by integrating the enzyme-like action of CuS-BSA-$Cu_3(PO_4)_2$ with the natural enzyme, glucose oxidase (GOx), a rapid, selective, and sensitive strategy of glucose detection was demonstrated. Thus, organic-inorganic hybrid nanomaterials can be added to the list of efficient artificial nanozymes to be utilized in a plethora of applications.

3.1.2. Synthesis of CuS-BSA-$Cu_3(PO_4)_2$ nanoparticles

The synthesis of CuS-BSA-$Cu_3(PO_4)_2$ nanoparticles was achieved in two steps using 0.1:0.0001 CuS/BSA Molar ratios.

In a typical procedure, 7 mL of MQ-water were placed in a two-neck round bottom flask and deoxygenated under continuous reflux for 1 h. After cooling down at room temperature, 70 mg of BSA (dissolved in 1 mL of previously degassed MQ-water) was added followed by the addition of 180 mg $Cu(Ac)_2$ dissolved in 1 mL of previously degassed MQ-water. After stirring for 5 min, 0.7 mL of NaOH (2 M) is then added to adjust the pH at ~12. Then 130 mg of $Na_2S.\times H_2O$ in 1 mL of degassed water were added under stirring. The mixture was heated at 90 °C for 5 h. The obtained CuS-BSA green-colored solution was dialyzed using a 12-14 kDa molecular mass cutoff dialysis membrane in Milli-Q water for 24 h to remove free copper ions and unreacted residues, by changing the water every 6 h.

CuS-BSA nanoparticles were also synthesized at 3 different temperatures (37, 55 and 90 °C), and using various CuS/BSA molar ratios with 1:1 Cu/S ratio to compare the catalytic activity using our previous optimal conditions from chapter 2 (0.1 mg/mL catalyst, 0.16 mM

TMB, and 20 mM H_2O_2 in 1.5 mL acetate buffer (0.1 M, pH 3.9) at 25 °C for 25 min incubation).

To the as-synthesized CuS-BSA nanoparticles of various concentrations (1-5 mg/mL) in 10 mL PBS (1X, pH 7.4) was added 50 µL of an aqueous $CuSO_4.5H_2O$ (160 mM) solution, followed by incubation at 4 °C for 3 days under continuous stirring. The obtained CuS-BSA-$Cu_3(PO_4)_2$ was purified by centrifugation at 8500 rpm at 4 °C for 20 min and washing five times with MQ-water; between each centrifugation step, the solution was sonicated in an ultrasonic ice bath for 10 min. A green powder of CuS-BSA-$Cu_3(PO_4)_2$ was obtained by lyophilization.

3.1.3. Results and discussion

3.1.3.1. Preparation and characterization of CuS-BSA-$Cu_3(PO_4)_2$ nanoparticles

Owing to its low cost, high stability and biocompatibility, BSA was used as a model protein in the preparation of CuS-BSA-$Cu_3(PO_4)_2$ nanoparticles (NPs). The strong binding affinity of free thiol group in the cysteine amino acid residue in BSA with CuS nanoparticles enhances their stabilization and prevents their precipitation in aqueous medium.

Notably, the preparation of nanoparticles was done in two separate steps, where CuS-BSA NPs were first synthesized under various conditions to yield the highest catalytic activity. Thus, different temperatures using different CuS/BSA molar ratios were performed to compare the catalytic activity towards the oxidation of TMB, according to our previous optimized conditions [21]. As can be seen in **Figures 1a** and **1b**, the highest absorbance intensity, corresponding to oxidized TMB, was observed using high CuS/BSA molar ratio and at higher preparation temperature (90 °C). High temperature is believed to facilitate the unfolding of BSA native structure and attachment of CuS NPs, enhancing the nucleation rate and crystal growth of CuS [22]. Therefore, the synthesis of CuS-BSA was accomplished at a temperature of 90 °C using 0.1/0.0001 CuS/BSA molar ratio. Meanwhile, $Cu_3(PO_4)_2$ were added to CuS-BSA for 3 days to enhance the nucleation and growth CuS-BSA-$Cu_3(PO_4)_2$.
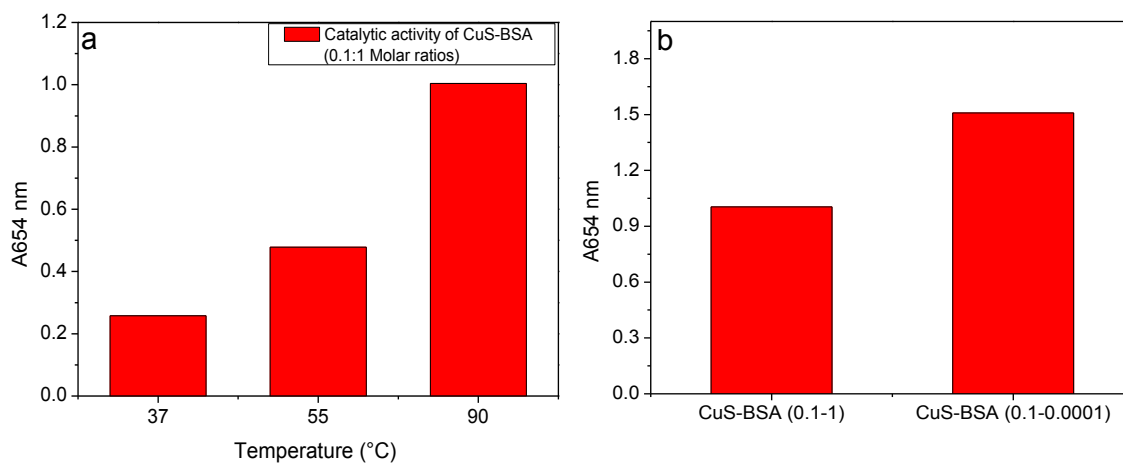
Figure 1: Comparison of CuS-BSA catalytic activity prepared at different temperatures (a) and using different CuS/BSA molar ratios (b), under our previous optimized conditions [21]. Reaction conditions: 0.1 mg/mL CuS-BSA, 0.16 mM TMB, 20 mM H_2O_2, acetate buffer (0.1 M, pH 3.9), T=25 °C, incubation time=25 min.

Zeta potential, which is a key indicator about the stability and surface charge of nanoparticles, was carried out by preparing diluted solutions of CuS-BSA and CuS-BSA-$Cu_3(PO_4)_2$ of 20 μg/mL in 1 mL MQ-water in a disposable folded capillary cell (DTS1070). As illustrated in **Figure 2a**, CuS-BSA displays a negative zeta potential value of -21.5 ± 7.9 mV, which is attributed to the electronegative nature of CuS in neutral medium [23], as well the existence of carboxyl groups in BSA [24]. Conjugation with $Cu_3(PO_4)_2$ resulted in a zeta potential value of -26.9 ± 4.9 mV, signifying the presence of $Cu_3(PO_4)_2$ on the nanoparticle's surface.

Figure 2: Comparison of Zeta potential (a) and average size (b) of CuS-BSA and CuS-BSA-$Cu_3(PO_4)_2$ nanoparticles in MQ-water.
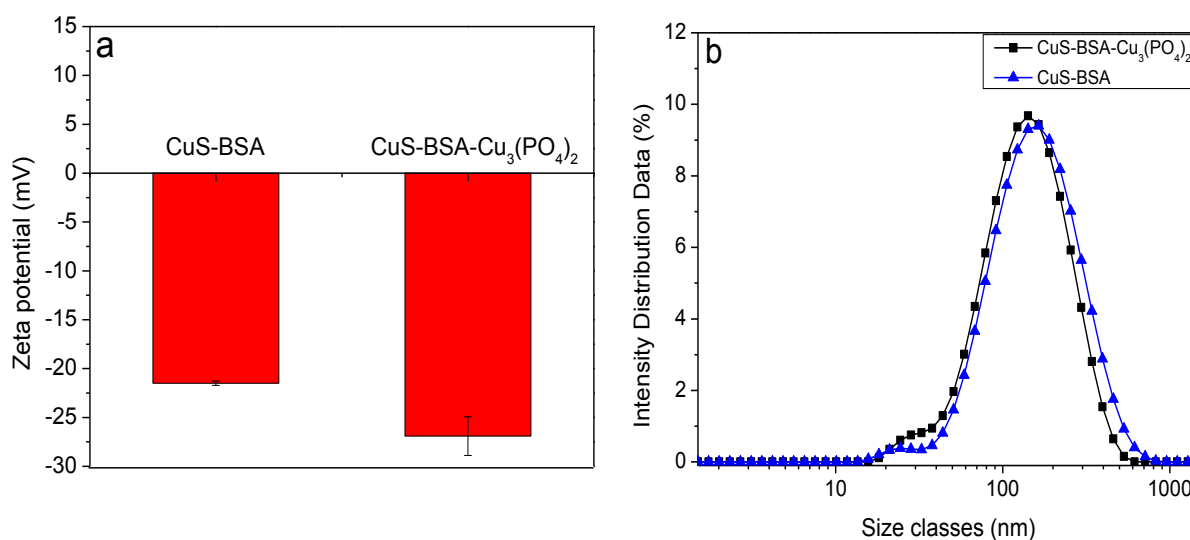
The hydrodynamic size of the nanoparticles was evaluated by dynamic light-scattering (DLS) measurements. As depicted in **Figure 2b**, the average diameters of CuS-BSA and CuS-BSA-$Cu_3(PO_4)_2$ are 134.5 ± 29.4 nm and 121.8 ± 34.5 nm, which are higher than TEM analysis due to the hydrodynamic water molecules on the nanoparticle's surface or slight aggregation.

The diffraction peaks in the XRD pattern of CuS-BSA-$Cu_3(PO_4)_2$ are indexed with the pure hexagonal covellite structure of the standard data in CuS (JCPDS No.06-0464) of space group 194, P63/ mmc (**Fig. 3a**). The characteristic peaks of CuS NPs located at 2θ values of 27.96^o, 29.56^o, 32.15^o, 33.08^o, 37.06^o, 42.05^o, 48.30^o, 53.02^o and 56.88^o are due to the (101), (102), (103), (006), (105), (106), (110), (114) and (202) crystalline planes with d-spacing values of 3.18, 3.01, 2.78, 2.70, 2.42, 2.14, 1.88, 1.72 and 1.61 Å, respectively [25-28]. The XRD pattern of CuS-BSA NPs (**Fig. 3b**) exhibits characteristic peaks located at 2θ values of 27.30^o, 29.36^o, 32.00^o, 33.44^o, 42.54^o, 48.20^o, 52.68^o and 59.50^o assigned to the (101), (102), (103), (006), (106), (110), (114) and (116) crystalline planes with d-spacing values of 3.26, 3.04, 2.79, 2.67, 2.12, 1.88, 1.74 and 1.55 Å (PDF Card No.: 00-002-0 820), respectively.
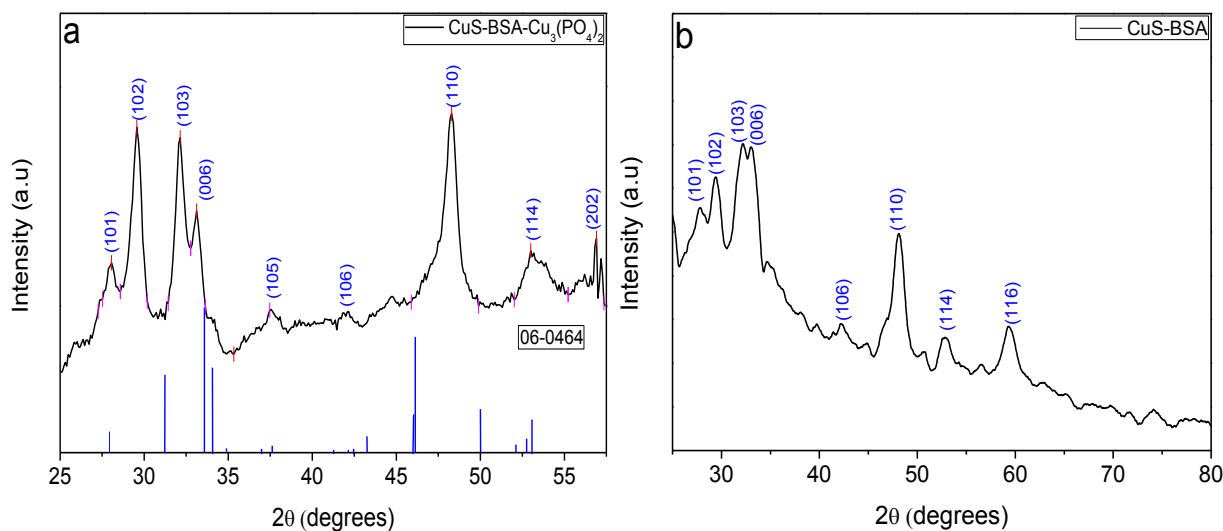
Figure 3: XRD pattern of CuS-BSA-$Cu_3(PO_4)_2$ and CuS-BSA nanoparticles.

TEM investigation of both CuS-BSA-$Cu_3(PO_4)_2$ (**Fig. 4**) and CuS-BSA (**Fig. 5**) nanoparticles revealed that the nanomaterials consist of nanoparticles with an average diameter of 10 ± 0.21 nm and 9.68 ± 0.602 nm, respectively. The lattice fringe of CuS-BSA-$Cu_3(PO_4)_2$ is 0.304 nm due to the (102) plane of the crystalline CuS NPs. The SAED pattern in **Figure 4a** (inset) confirms the presence of (101), (102), (103), (006) and (106) crystalline planes, in full

agreement with XRD analysis. Elemental mapping and EDX analysis reveals the presence of C, O, N, Cu, S, and P elements in CuS-BSA-$Cu_3(PO_4)_2$, consistent with the chemical composition of the material. Similarly, TEM images of CuS-BSA NPs (**Fig. 5**) illustrate the lattice fringes of 0.278 and 0.306 nm due to the (103) and (102) crystalline planes of CuS, respectively. The SAED pattern (inset of **Fig. 5d**) indicates the crystalline nature of CuS-BSA NPs by the presence of (101), (102), (103) and (106) crystalline planes. The elemental mapping and EDX pattern confirm the presence of C, N, O, Cu and S elements in CuS-BSA NPs, in agreement with the chemical nature of the material. From the TEM images we can ascertain that CuS-BSA and CuS-BSA-$Cu_3(PO_4)_2$ are of nano size with high crystallinity.
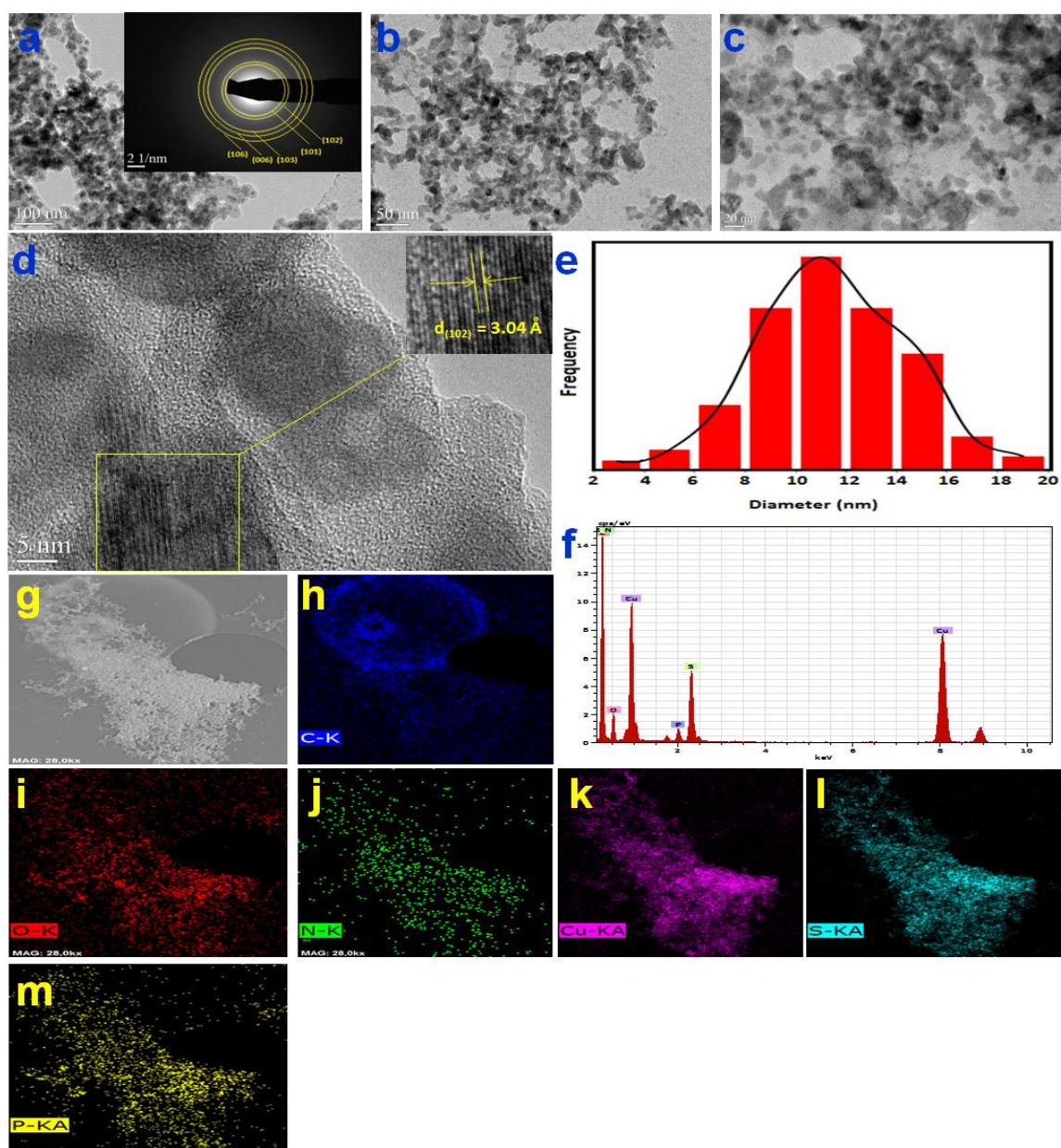
Figure 4: TEM images (a, b, c) and SAED pattern (inset a), HRTEM image (d), particle size distribution (e), EDX pattern (f), Dark Field-STEM image (g), elemental mapping for carbon (h), oxygen (i), nitrogen (j), copper (k), sulfur (l), phosphorus (m) of CuS-BSA-Cu$_3$(PO$_4$)$_2$ NPs.
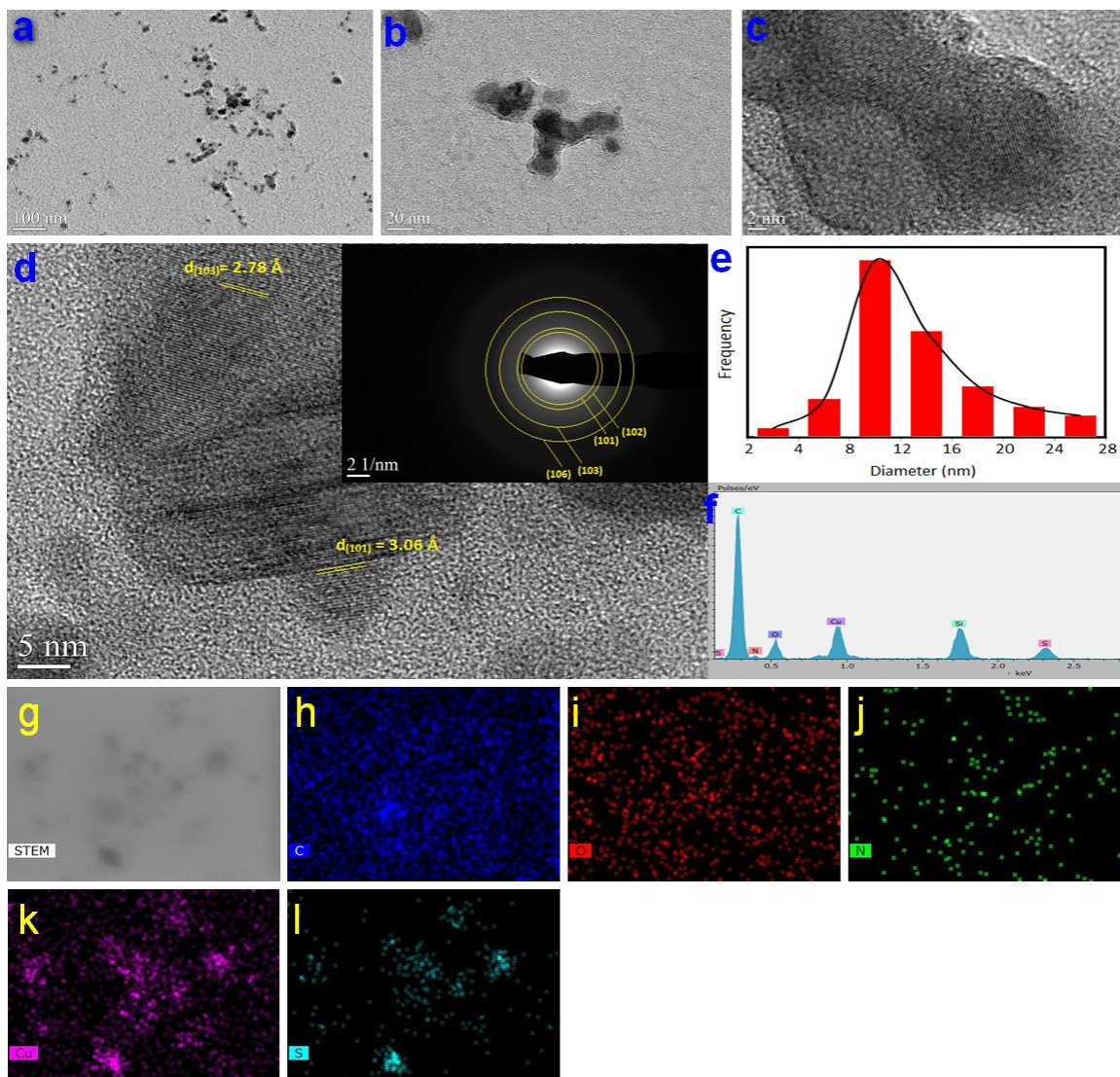
Figure 5: (a, b) TEM images, (c, d) HRTEM images and SAED pattern (inset d), (e) particle size distribution, (f) EDX pattern, (g) DF-STEM image, elemental mapping for (h) carbon, (i) oxygen, (j) nitrogen, (k) copper, (l) sulfur of CuS-BSA NPs.

The surface elemental composition of CuS-BSA-Cu$_3$(PO$_4$)$_2$ was examined by X-ray photoelectron spectroscopy (XPS). **Figure 6a** exhibits the XPS survey spectrum of CuS-BSA-Cu$_3$(PO$_4$)$_2$ and reveals the existence of C$_{1s}$ (284.6 eV), O$_{1s}$ (531 eV), N$_{1s}$ (400 eV), Cu$_{2p}$ (934 eV), S$_{2p}$ (162 eV), and P$_{2p}$ (133 eV) with respective atomic concentrations of 42.0%, 31.2%, 9.2%, 4.2%, 4.7% and 8.7%. The C$_{1s}$ high resolution XPS spectrum **(Fig. 6b)** can be fitted with characteristic peaks at 284.4, 285.6, and 287.5 eV ascribed to C=C, C-N/C-O and C=O,

respectively. The high resolution XPS spectrum of the O_{1s} **(Fig. 6c)** can be deconvoluted in two peaks due to O-H/C=O at 530.9 eV and C-O/P-O at 531.7 eV [29]. The N_{1s} spectrum **(Fig. 6d)** can be fitted with a single peak assigned to C-N at 399.6 eV. The Cu_{2p} displays two distinct peaks at 934.0 eV and 953.5 eV **(Fig. 6e)** ascribed to $Cu_{2p3/2}$ and $Cu_{2p1/2}$, respectively with a spin orbit separation of 19.5 eV, which is in accordance with literature data [30]. The existence of two shake-up satellite peaks at 941.7 and 961.6 eV confirms the presence of Cu^{2+} divalent state. S_{2p} XPS spectrum **(Fig. 6f)** comprises two peaks at 162.3 and 168.5 eV ascribed to S_{2p} in CuS and $CuSO_4$, respectively, which indicates the formation of CuS [31]. A strong characteristic peak corresponding to $Cu_3(PO_4)_2$ overlaps with $Cu_{2p3/2}$ [29]. The peak at 133.7 eV **(Fig. 6g)** in P_{2p} spectrum is assigned to $P_{2p1/2}$ of $Cu_3(PO_4)_2$ [32, 33].

To point out the complexation of $Cu_3(PO_4)_2$ with CuS-BSA, the XPS analysis of CuS-BSA is also carried out for comparison. **Figure 7a** depicts the XPS survey spectrum of CuS-BSA. It comprises peaks due to C_{1s} (284.6 eV), O_{1s} (531.8 eV), N_{1s} (400 eV), Cu_{2p} (932 eV) and S_{2p} (162.6 eV). Deconvolution of the C1s **(Fig. 7b)** also reveals the existence of C-C/C=C at 284.8 eV, C-N/C-O at 285.8 eV, and C=O at 287.8 eV, similar to the C_{1s} XPS spectrum of CuS-BSA-$Cu_3(PO_4)_2$. O_{1s} and N_{1s} deconvoluted XPS spectra confirm the presence of O-H/C=O (531.8 eV), C-N (399.8 eV) and C=N (402.2 eV), respectively **(Fig. 7c, d)**. The $Cu_{2p3/2}$ (934.2 eV), $Cu_{2p1/2}$ (954.1 eV), and two satellite peaks observed in the Cu_{2p} XPS spectrum **(Fig. 7e)**, indicate the existence of paramagnetic Cu(II) [34], in addition to the S_{2p} at 162.6 eV that can be deconvulated into two main peaks at 162.2 eV and 163.8 eV corresponding to the $S_{2p3/2}$ and $S_{2p1/2}$, respectively, indicating that the sulfur element exist as S^{2-} state. S^{6+} state also found according to the peaks at 167.9 eV and 169.2 eV, corresponding to oxidized sufur (CuSO4). The which confirms the successful synthesis of CuS **(Fig. 7f)**.
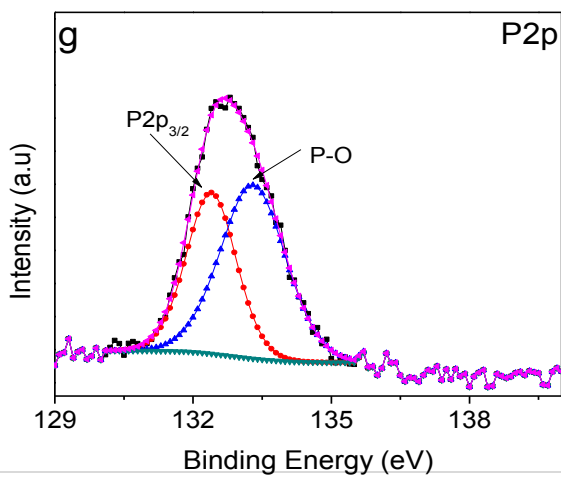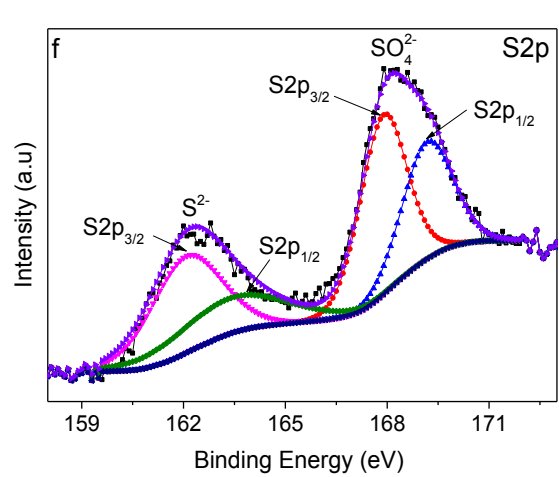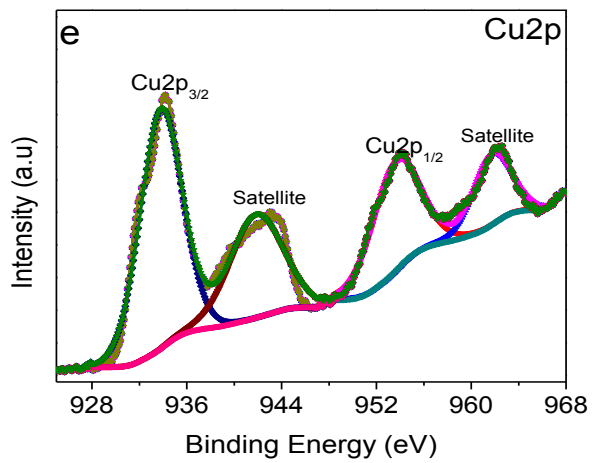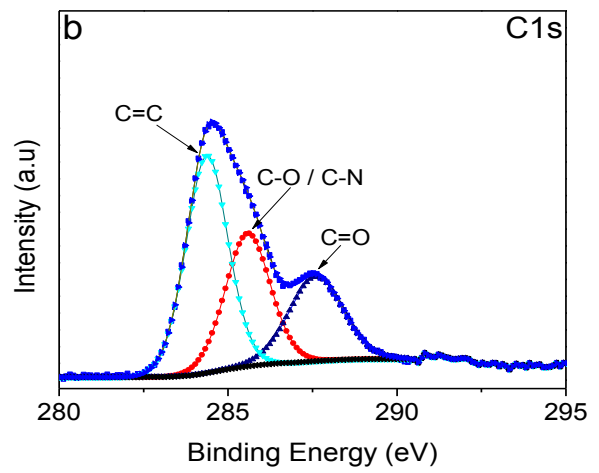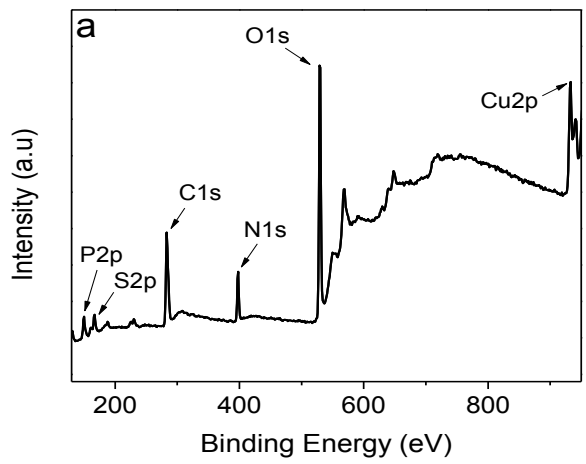
Figure 6: XPS survey spectrum (a), and high resolution XPS spectra of C_{1s} (b), O_{1S} (b), N_{1s} (d), Cu_{2p} (e), S_{2p} (f), and P_{2p} (g) of CuS-BSA-$Cu_3(PO_4)_2$ nanoparticles.
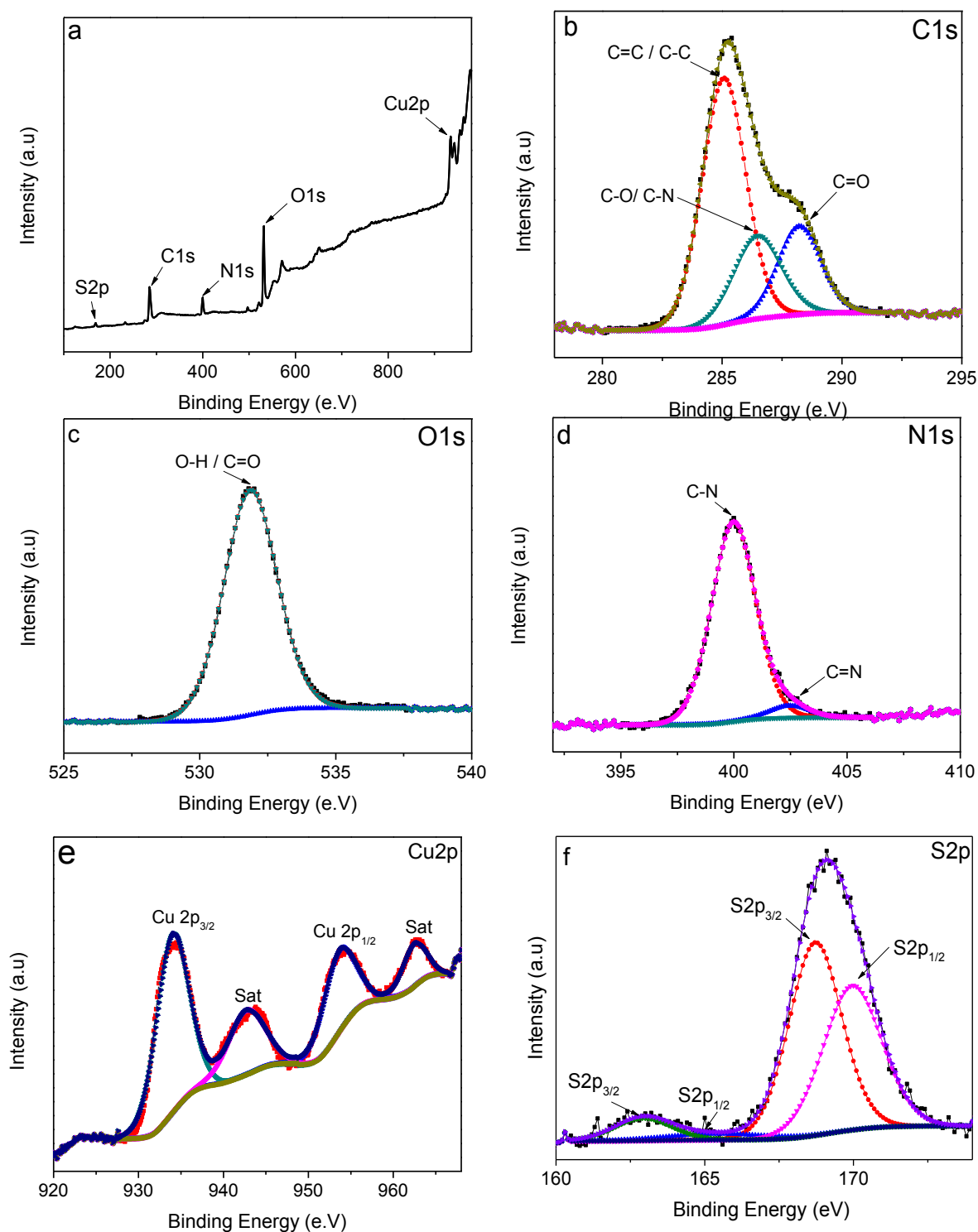
Figure 7: (a) XPS survey spectrum, and high resolution XPS spectra of C_{1s} (b), O_{1s} (c), N_{1s} (d), Cu_{2p} (e) and S_{2p} (f) of CuS-BSA nanoparticles.

Fourier transform infrared spectroscopy (FT-IR) was performed to provide evidence for the entrapment of CuS and $Cu_3(PO_4)_2$ in BSA. **Figure 8** depicts the FTIR spectra of CuS-BSA and CuS-BSA-$Cu_3(PO_4)_2$ nanoparticles showing the characteristic bands of BSA including OH stretching at 3445-3296 cm^{-1}, C-H stretching (2950-2860 cm^{-1}), amide I (C=O) at 1655 cm^{-1}, amide II (N-H bending and C-N stretching vibrations) [35] at 1539 cm^{-1}, and amide III at 1242 cm^{-1}. The FTIR spectrum of CuS-BSA displays two additional peaks at 780 and 1101 cm^{-1} due to Cu-O [26] and Cu-S [36], respectively. The new peak at 1051 cm^{-1} is ascribed to asymmetrical stretching of P=O [37, 38] in CuS-BSA-$Cu_3(PO_4)_2$, and another peak with a maximum at 1145 cm^{-1} is assigned to the symmetrical stretching of $[PO_4]^{3-}$. These data confirm the successful synthesis of CuS-BSA-$Cu_3(PO_4)_2$.
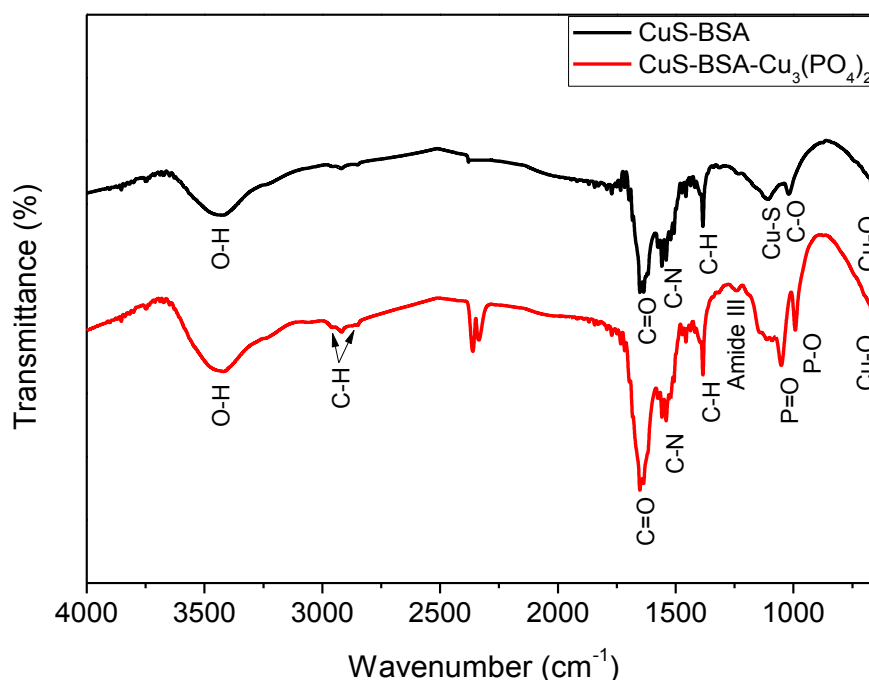
Figure 8: FTIR spectra of CuS-BSA and CuS-BSA-$Cu_3(PO_4)_2$ nanoparticles.

Figure 9 displays the UV-Vis absorption spectrum of pristine BSA, CuS-BSA and CuS-BSA-$Cu_3(PO_4)_2$ nanoparticles. The spectrum of BSA consists of an absorption peak at 280 nm [39], which can be observed in the UV-vi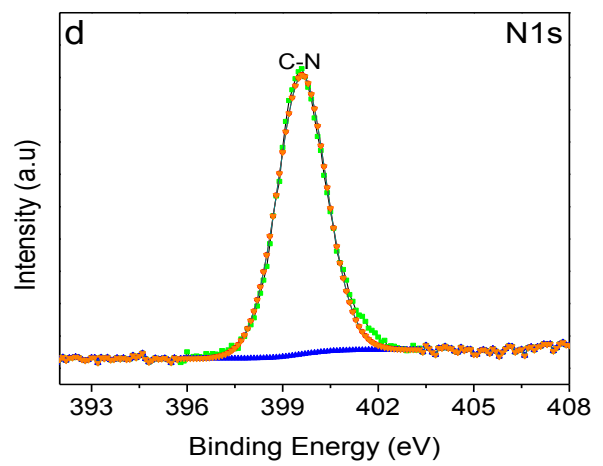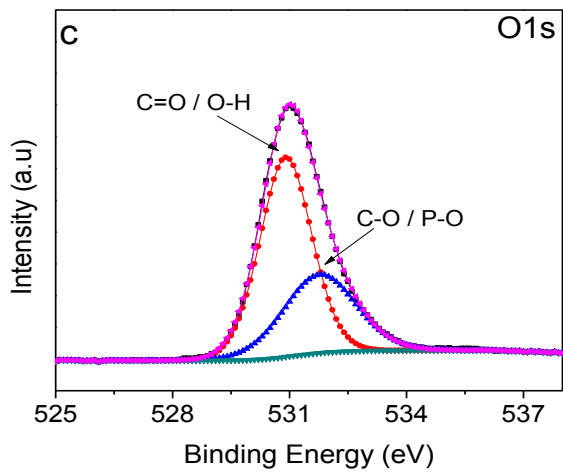s spectra of CuS-BSA and CuS-BSA-$Cu_3(PO_4)_2$ nanoparticles. The growth of covellite CuS in both CuS-BSA and CuS-BSA-$Cu_3(PO_4)_2$ is directly evidenced by the longitudinal absorption tail extending to the near infrared region (NIR) [40], due to the d-d band transition of Cu^{2+} and localized surface plasmon resonance of

CuS [41, 42], and a weak shoulder at 400 nm. These results suggest the conjugation of CuS and $Cu_3(PO_4)_2$ to BSA.
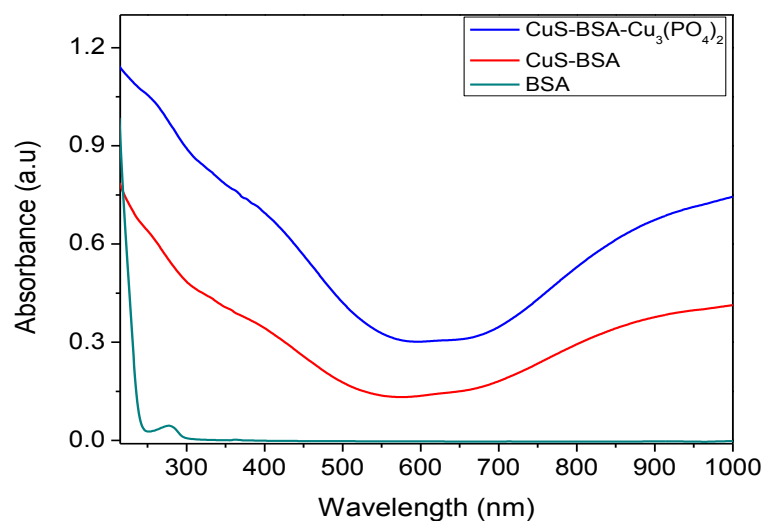
Figure 9: UV-vis absorption spectra of BSA (green), CuS-BSA (red), and CuS-BSA-$Cu_3(PO_4)_2$ (blue) nanoparticles.

3.1.3.2. Determination of CuS-BSA-$Cu_3(PO_4)_2$ enzyme-like catalytic activity

The peroxidase like-enzymatic action of CuS-BSA-$Cu_3(PO_4)_2$ is manifested through the oxidation of TMB molecule in acidic solution into a charge transferred product (oxTMB) in the presence of H_2O_2, confirmed by visual blue color formation, and by dynamic increase in the UV-vis absorption peak at 654 nm. As can be clearly observed in **Figure 10**, the catalytic oxidation of TMB substrate occurs rapidly in less than 30 s upon mixing the reagents.
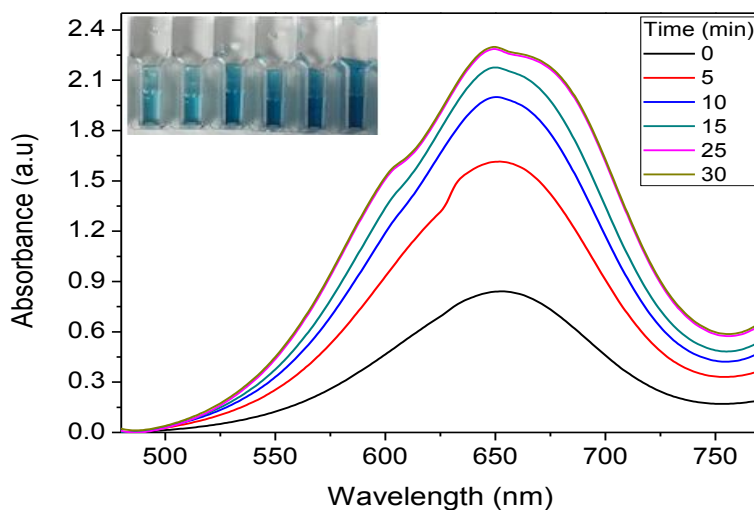
Figure 10: Time-dependent UV-vis absorbance of TMB catalyzed by CuS-BSA-Cu$_3$(PO$_4$)$_2$ in the presence of H$_2$O$_2$. Reaction conditions: 0.3 mg/mL CuS-BSA-Cu$_3$(PO$_4$)$_2$, 0.3 mM TMB, 1 mM H$_2$O$_2$, acetate buffer (0.1 M, pH 4) at 25 °C. Inset: the color change of oxTMB at different time intervals.

Several control experiments were carried to confirm the catalytic nature of this approach. Thus, TMB is mixed with H$_2$O$_2$ alone, or CuS-BSA-Cu$_3$(PO$_4$)$_2$, and with both H$_2$O$_2$ and CuS-BSA-Cu$_3$(PO$_4$)$_2$. **Figure 11** indicates that H$_2$O$_2$ alone was not able to generate an observable color change of TMB solution. Meanwhile, when both H$_2$O$_2$ and CuS-BSA-Cu$_3$(PO$_4$)$_2$ are present in solution, the catalytic oxidation rate is accelerated, as revealed by a great increase in the visible absorption peak at 654 nm and by the transformation of colorless TMB into blue oxTMB. This can be explained by the adsorption of TMB molecules on the surface of CuS-BSA-Cu$_3$(PO$_4$)$_2$ during the catalytic reaction, which facilitates the donation of amine group lone pair electrons in TMB [43] to CuS-BSA-Cu$_3$(PO$_4$)$_2$, which in turn enhances the electron transfer to H$_2$O$_2$ [44] and causes the generation of HO$^{\bullet}$ in a weakly acidic medium, that subsequently catalyzes the oxidation of TMB into a blue colored product, similar to the Fenton reaction. Notably, CuS-BSA-Cu$_3$(PO$_4$)$_2$ plays a key role in the transfer of electrons between TMB and H$_2$O$_2$.
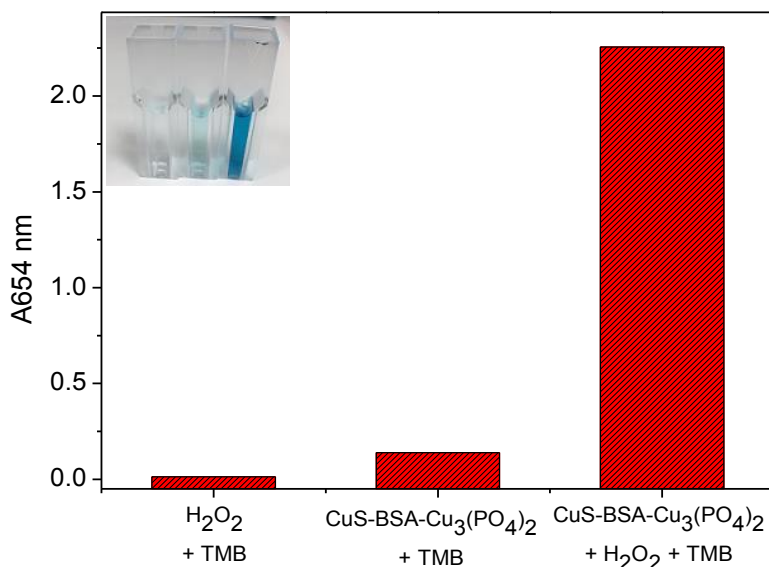
Figure 11: UV/vis absorption of TMB at 654 nm under different experimental conditions. Inset: Typical photographs of TMB oxidation (from left to right: without CuS-BSA-Cu$_3$(PO$_4$)$_2$ (colorless), without H$_2$O$_2$ (light blue), and with both H$_2$O$_2$ and CuS-BSA-Cu$_3$(PO$_4$)$_2$ (dark blue). Reaction conditions: 0.3 mg/mL CuS-BSA-Cu$_3$(PO$_4$)$_2$, 0.3 mM TMB, 1 mM H$_2$O$_2$, acetate buffer (0.1 M, pH 4), T=25 °C, incubation time=25 min.

3.1.3.3. Optimization of the experimental reaction conditions

To determine the optimal conditions for H_2O_2 detection and catalytic TMB oxidation, a set of different parameters are investigated, such as TMB and catalyst concentrations, pH, temperature, and incubation time. In each case, the absorbance for oxTMB is monitored and a plot of absorbance at 654 nm versus each variable is established. The experimental reaction conditions are initiated by choosing 0.16 mM TMB as the starting concentration to perform the optimization of catalyst concentration, where at this concentration, the oxidation of TMB is found to be catalyst-concentration dependent. TMB oxidation increases with the increase in CuS-BSA-Cu$_3$(PO$_4$)$_2$ concentration and saturates at 0.3 mg/mL (**Fig. 12a**). This is not surprising, as the catalytic reaction rate depends on the concentration of catalyst because of the high amount of TMB present in solution [45]. Thereby 0.3 mg/mL CuS-BSA-Cu$_3$(PO$_4$)$_2$ was chosen for the whole experimental procedure.
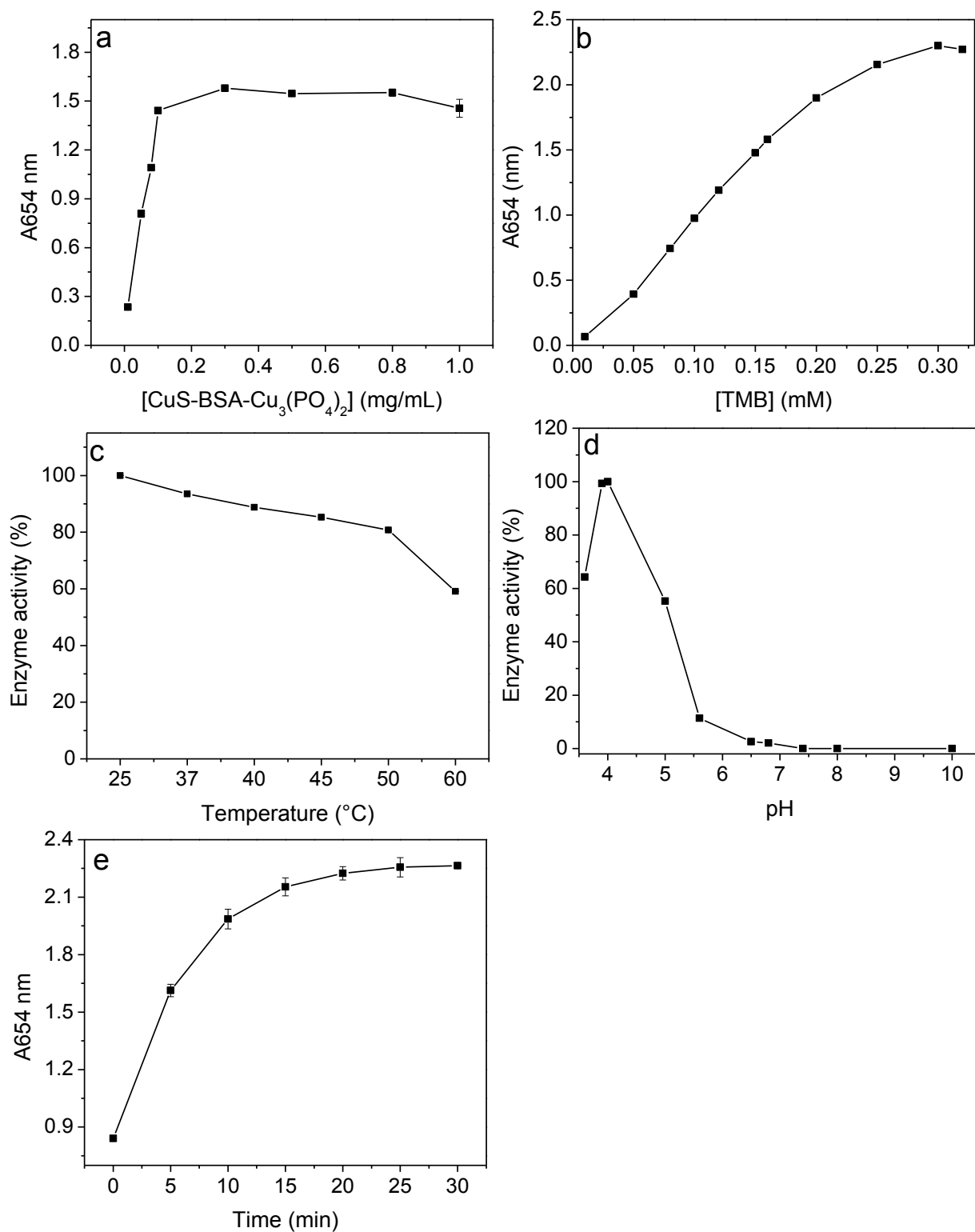
Figure 12: Influence of catalyst concentration (a), TMB concentration (b), temperature (c), pH (d), and incubation time (e) on the catalytic oxidation of TMB.

The optimization of TMB substrate is also monitored by recording the absorbance at 654 nm under various TMB concentrations **(Fig. 12b)**, using the optimized catalyst concentration (0.3 mg/mL), where the optimum TMB concentration was observed at 0.3 mM.

To gain a better insight about the performance of CuS-BSA-Cu$_3$(PO$_4$)$_2$ at a concentration of 0.3 mg/mL, the reaction was carried out in the 25-60 °C temperature range **(Fig. 12c)**. Unlike natural enzymes which tend to lose their activity at temperatures > 37 °C, CuS-BSA-Cu$_3$(PO$_4$)$_2$ displays superior catalytic activity at a temperature of 25°C, with a slight decrease at higher temperatures, due most likely to H$_2$O$_2$ decomposition. Also a maximum performance is evidenced at pH 4 **(Fig. 12d)**, whereby above this pH value, the catalytic action of CuS-BSA-Cu$_3$(PO$_4$)$_2$ exhibits an unexpected drop, until it is completely inhibited at pH close to 8. Therefore, room temperature and acidic medium are required to perform the following assay.

In the same context, the catalytic TMB oxidation rate is systematically analyzed at different incubation times under the following reaction conditions: CuS-BSA-Cu$_3$(PO$_4$)$_2$ (0.3 mg/mL), H$_2$O$_2$ (1 mM), and TMB (0.3 mM) in acetate buffer (0.1 M, pH 4) of total volume 1 mL. **Figure 12e** reveals that the oxidation response of CuS-BSA-Cu$_3$(PO$_4$)$_2$ towards TMB increases with time to attain a plateau after 25 min; thus, an incubation time of 25 min is employed to further perform the catalytic experiments.

3.1.3.4. Steady-state kinetic theory of CuS-BSA-Cu$_3$(PO$_4$)$_2$ and determination of Michaelis-Menten constant and maximum velocity

In order to get a clear understanding of the activity of CuS-BSA-Cu$_3$(PO$_4$)$_2$ nanozyme and compare its efficiency with natural enzymes towards TMB and H$_2$O$_2$ substrates, a kinetic theory was exploited by altering one substrate concentration and keeping the concentration of the other constant. Thus, to exploit the kinetic experiments, the initial rate of TMB and H$_2$O$_2$, which is the slope of ΔA654 per unit time (min), is obtained by applying the Beer-lambert law.
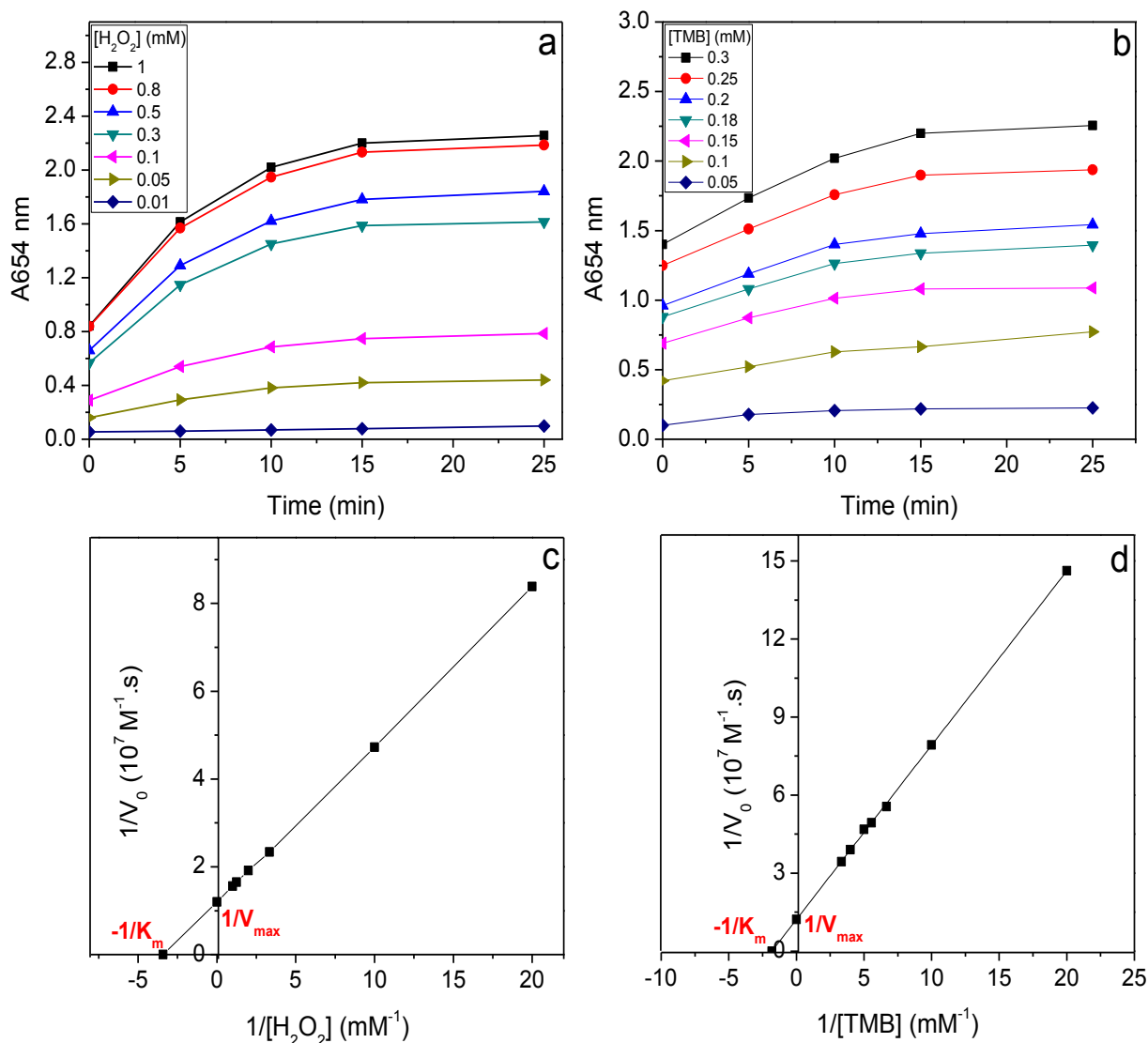
Figure 13: UV-vis absorption of different (a) H_2O_2 and (b) TMB concentrations in a time course-mode. Steady-state kinetics using the Michaelis-Menten method and Lineweaver-Burk plot for (c) H_2O_2 and (d) TMB as two different substrates. Reaction conditions: 0.3 mg/mL CuS-BSA-$Cu_3(PO_4)_2$, acetate buffer (0.1 M, pH 4), T=25 °C.

The catalytic parameters, K_m and V_{max} for TMB and H_2O_2 substrates, which are typical Michaelis-Menten constant and maximum velocity, respectively, are calculated by analyzing Lineweaver-Burk double reciprocal plot as depicted in **Figure 13c** and **13d**. **Table 1** summarizes the catalytic parameters (K_m and V_{max}) in comparison to the natural HRP enzyme and other previously reported nanomaterials as enzyme mimics. Achieving low K_m and high V_{max} values is important to ensure better catalytic performance. The catalytic action of CuS-BSA-$Cu_3(PO_4)_2$ for TMB oxidation displays a typical Michaelis–Menten model, under the

optimized experimental conditions, whereby the low K_m value (5.5×10^{-4}) obtained by Lineweaver-Burk plot is close to the naturally HRP enzyme [46], indicating a high affinity towards TMB [47]. Meanwhile, the obtained low K_m value for H_2O_2 as a substrate indicates that a small concentration of H_2O_2 is needed for achieving a high response of CuS-BSA-$Cu_3(PO_4)_2$ in the catalytic process. This reveals excellent substrate binding affinity towards both substrates compared to other well-known reported nanomaterials (**Table 1**), owing to high activity of CuS-BSA-$Cu_3(PO_4)_2$ and the enhancement of charge transfer between TMB and H_2O_2 with the high electron mobility provided by CuS-BSA-$Cu_3(PO_4)_2$ [48], as well to the enhancement in binding affinity between the negatively charged catalyst and positively charged TMB [49].

Table 1: Typical Michaelis-Menten constant and maximum velocity for TMB and H_2O_2 substrates in comparison with HRP and other previously reported nanomaterials.

Catalyst	$\underline{K_m}$ (M)		$\underline{V_{max}}$ (M.s^{-1})	
	H_2O_2	TMB	H_2O_2	TMB
HRP [5]	37×10^{-4}	4.34×10^{-4}	8.71×10^{-8}	10×10^{-8}
GO-COOH [44]	39.9×10^{-4}	0.237×10^{-4}	3.85×10^{-8}	3.45×10^{-8}
CuS-MMT [50]	22.7×10^{-4}	0.212×10^{-4}	0.971×10^{-8}	2.814×10^{-8}
MoS_2-GSSG [51]	3.3×10^{-4}	4.8×10^{-4}	2.63×10^{-8}	2.7×10^{-8}
Cu-Ag-rGO [52]	86.2×10^{-4}	6.34×10^{-4}	7.01×10^{-8}	4.25×10^{-8}
CuS-BSA-$Cu_3(PO_4)_2$ (this work)	2.9×10^{-4}	5.5×10^{-4}	8.31×10^{-8}	8.2×10^{-8}

3.1.3.5. Sensitivity of CuS-BSA-$Cu_3(PO_4)_2$ for detection of H_2O_2

The inherent catalytic activity of CuS-BSA-$Cu_3(PO_4)_2$ was thoroughly analyzed on detecting H_2O_2 under the optimized experimental conditions. Obviously, as can be clearly demonstrated from **Figure 14**, TMB oxidation is found to be H_2O_2-concentration dependent, which is in close agreement with the change in solution color (**inset Fig. 14**), where above 1

mM of H_2O_2, the catalytic efficiency is not enhanced. This can be explained by the decomposition of H_2O_2 into $HO^\bullet$ in weakly acidic environment (pH 4), enhanced by CuS-BSA-$Cu_3(PO_4)_2$, due to the existence of Cu^{2+} on the surface of the nanohybrid. This approach provides a convenient method for sensing H_2O_2 by the naked eyes at a concentration as low as 3 µM. A linear calibration plot is obtained in the 0-8 µM concentration range **(inset Fig. 14)** with a detection limit of 22 nM, obtained by 3*SD/a. This value is much better than those achieved by other nanomaterials described in literature **(Table 2)**.

Table 2: Comparison of various nanomaterials for colorimetric detection of H_2O_2.

Materials	LOD (µM)	Linear range (µM)	Ref.
MoS_2-GSSG	0.51	0-50	[51]
MoS_2 nanosheets	1.5	5-100	[53]
MoS_2 NFs	4.103	0-300	[49]
GO-Fe_3O_4	0.32	1-50	[54]
ZnO-CNTs	0.05	0.1-37.5	[55]
Pt NCs	0.46	0-200	[56]
CuS- BSA-$Cu_3(PO_4)_2$	0.022	0-8	Our work
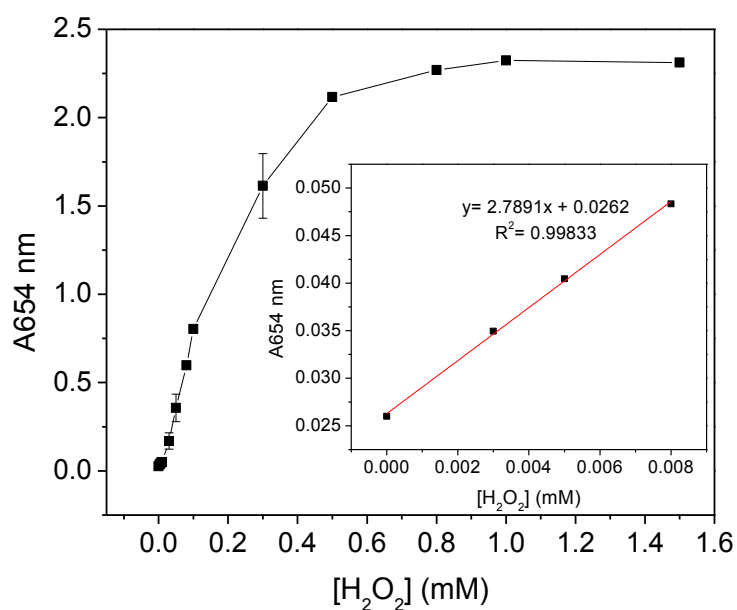
Figure 14: A dose-responsive curve of H_2O_2. oxTMB absorbance at 654 nm versus H_2O_2 concentration. Reaction conditions: 0.3 mM TMB, 0.3 mg/mL CuS-BSA-Cu$_3$(PO$_4$)$_2$, acetate buffer (0.1 M, pH 4), T=25 °C, incubation time=25 min. Inset: The linear calibration plot for the determination of H_2O_2.

3.1.3.6. Analysis of hydroxyl radicals (HO$^•$)

Artificial enzymes oxidize a set of substrates on the basis of reactive oxygen species (ROS) such as HO• radicals, generated from H_2O_2 decomposition. Thus, to confirm the catalytic oxidation of TMB by CuS-BSA-Cu$_3$(PO$_4$)$_2$ enzyme-mimic nanohybrid in the presence of H_2O_2 in acidic medium, a non-fluorescent probe molecule, terephthalic acid (TA) is used as a trap of HO• radicals. After TA reaction with the generated HO$^•$, 2-hydroxyterephthalic acid was formed, and an emission peak was observed by fluorescence spectroscopy at 435 nm. The fluorescence intensity was monitored under various experimental conditions, where the intensity was remarkably enhanced when both H_2O_2 and CuS-BSA-Cu$_3$(PO$_4$)$_2$ coexist in solution **(Fig. 15)**. As expected, no fluorescence emission peak was observed when TA was present alone or incubated with CuS-BSA-Cu$_3$(PO$_4$)$_2$ in the absence of H_2O_2. This reveals that H_2O_2 is effectively decomposed into HO$^•$ through the acceleration of electron transfer between H_2O_2 and TMB, whereby these free radicals oxidize TMB on the basis of the catalytic efficiency of CuS-BSA-Cu$_3$(PO$_4$)$_2$.
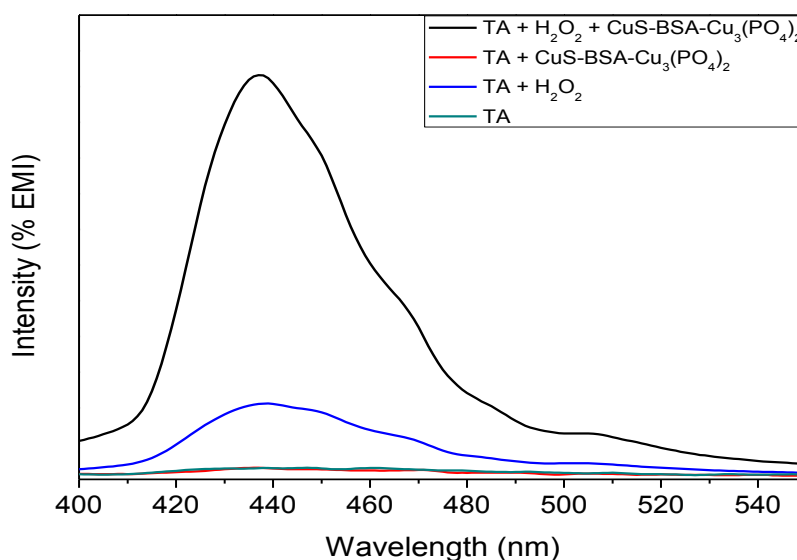
Figure 15: Fluorescence emission spectra recorded using terephthalic acid (TA) as a fluorescent probe molecule. Reaction conditions: 0.3 mM TMB, 0.3 mg/mL CuS-BSA-Cu$_3$(PO$_4$)$_2$, 1 mM H_2O_2, acetate buffer (0.1 M, pH 4), T=25 °C, incubation time=25 min.

3.1.3.7. Sensing of H_2O_2 in contact lens care solution

The excessive use of contact lens in modern society can cause corneal problems on the long term, associated with the disinfection process which is based on the use of lens care solutions that contain some traces of H_2O_2. As it is well known, H_2O_2 is used for disinfection due to its strong ability in microbial disruption, and becomes an alternative disinfecting system. Despite its progressive disinfection benefits, the use of H_2O_2 as a disinfectant is correlated to toxicity at a certain concentration. Therefore, it is highly desirable to detect the amount of H_2O_2 in contact lens care solutions.

In order to broaden the scope of H_2O_2 detection and confirm the practical applicability of the nanozyme, H_2O_2 detection is conducted in contact lens care solutions under our optimized experimental conditions. Typically, using a standard addition method, H_2O_2 at 20, 50, and 100 nM is spiked into contact lens care solution obtained from a pharmacy. The H_2O_2 content present in lens care solution was obtained from an already established calibration plot, adopted at 654 nm using a series of H_2O_2 concentrations under the same assay mentioned above. Percentage recovery was determined by the following equation (Eq. 1), and the results are listed in **Table 3** (n=3).

$$\text{Recovery (\%)} = \frac{[\text{H2O2}] \text{ found}}{[\text{H2O2}] \text{ added}} \times 100 \qquad (1)$$

As depicted in **Table 3**, there was no apparent difference between spiked values and those achieved by the established calibration curve. Thus, CuS-BSA-Cu$_3$(PO$_4$)$_2$ demonstrated good recovery percentage for H_2O_2 sensing, which provides a reliability to our nanozyme to be applied in clinical applications.

Table 3: Detection of H_2O_2 in contact lens care solution (n=3).

Samples	H_2O_2 added (nM)	H_2O_2 found (nM)	Recovery (%)	RSD (%)
	20	20.38	101.9	0.83
Lens care	50	49.06	98.12	1.66
solution	100	99.87	99.87	1.1

3.1.3.8. Selectivity and reproducibility of CuS-BSA-Cu$_3$(PO$_4$)$_2$ towards H$_2$O$_2$ sensing

An interference study was adopted to evaluate the selectivity of the proposed sensor. Thus, different ions (Fe^{3+}, Hg^{2+}, Co^{2+}, Na$^+$, Ni^{2+}, Zn^{2+}), and substances including galactose, ascorbic acid, uric acid, and citric acid, at a concentration 10-times higher than that of H$_2$O$_2$ concentration were tested at the same experimental procedure discussed above, and compared to H$_2$O$_2$. From the results in **Figure 16**, no apparent increase in the absorbance at 654 nm is recorded for the interfering ions or substances, while H$_2$O$_2$ achieved the highest remarkable response. These results indicate the enhanced specificity, high sensitivity, and good selectivity of the developed sensor.

The reproducibility of the catalytic action of CuS-BSA-Cu$_3$(PO$_4$)$_2$ nanozyme towards the oxidation of TMB is performed by investigating the reaction in four consecutive repeated cycles, where after each catalytic cycle, the developed sensor is separated by centrifugation for 5 min, washed repeatedly with MQ-water and reused in the following cycle. As depicted in **Figure 17**, the absorbance intensity for oxTMB remained approximately the same, indicating that the CuS-BSA-Cu$_3$(PO$_4$)$_2$ catalytic activity is not affected after four catalytic cycles with a relative standard deviation (STD) of 2.19%. The result reveals that CuS-BSA-Cu$_3$(PO$_4$)$_2$ nanoparticles are excellent enzyme-mimics with good catalytic activity, reusability and stability.
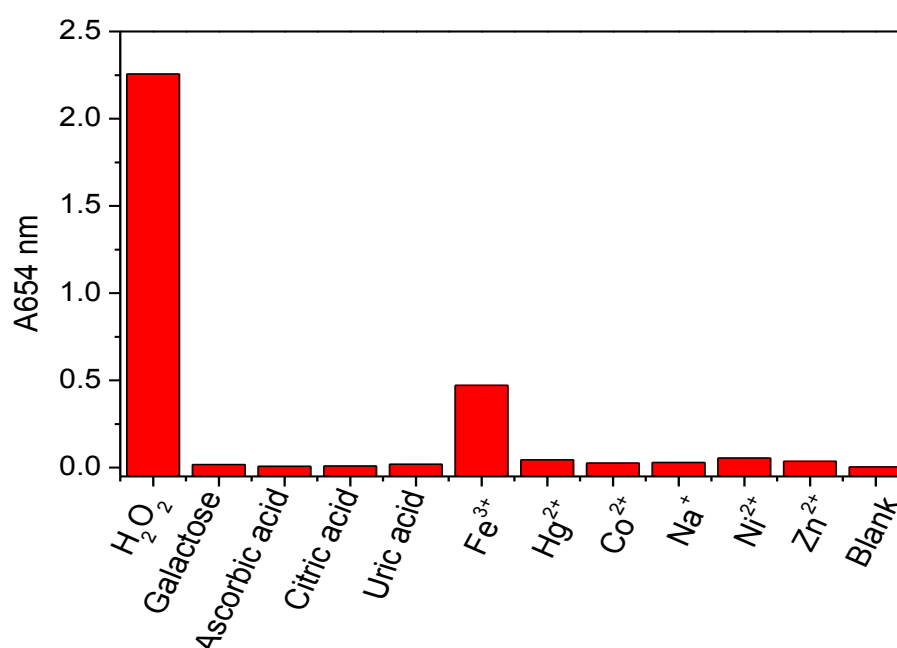
Figure 16 Absorbance of oxTMB in the presence of different interfering substances and ions at a concentration of 10 mM (10 times higher than the concentration of H_2O_2). Reaction conditions: 0.3 mg/mL CuS-BSA-$Cu_3(PO_4)_2$, 1 mM H_2O_2, 0.3 mM TMB, acetate buffer (0.1 M, pH 4), T=25 °C, incubation time=25 min.
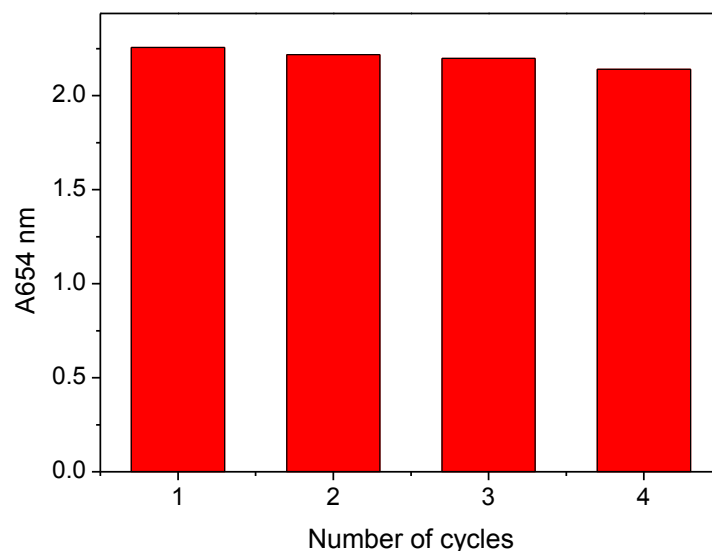
Figure 17: Absorbance of oxTMB in presence of different interfering substances and ions at a concentration of 10 mM (10 times higher than the concentration of H_2O_2). Reaction conditions: 0.3 mg/mL CuS-BSA-$Cu_3(PO_4)_2$, 1 mM H_2O_2, 0.3 mM TMB, acetate buffer (pH = 4), T=25 °C, incubation time=25 min.

3.1.3.9. Colorimetric sensing of glucose and detection in human serum samples

As a final end product in glucose oxidation catalyzed by glucose oxidase enzyme (GOx), and interested by the admirable high catalytic activity of CuS-BSA-$Cu_3(PO_4)_2$, we opted to widen our application in detecting glucose. Generally, in the presence of O_2, glucose is oxidized to gluconolactone and H_2O_2 by GOx at physiological pH. Subsequently, H_2O_2 was then decomposed by CuS-BSA-$Cu_3(PO_4)_2$ to initiate TMB oxidation in acidic solution. Thus, to take advantage of this property, the experiment is carried out in two independent steps, since natural enzymes can be denatured in acidic media and are pH sensitive. Thus, the reaction was initiated using 0.1 mg/mL GOx as the final concentration for the whole assay, which is sufficient to generate enough H_2O_2, based on the highest absorbance intensity observed at this amount **(Fig. 18)**. Incubation time was also critical for the generation of H_2O_2, where according to our results, 30 min were enough, after which longer time causes a slight depletion in

absorbance at 654 nm, which remains uncertain if it was due to H_2O_2 decomposition or evaporation [57].
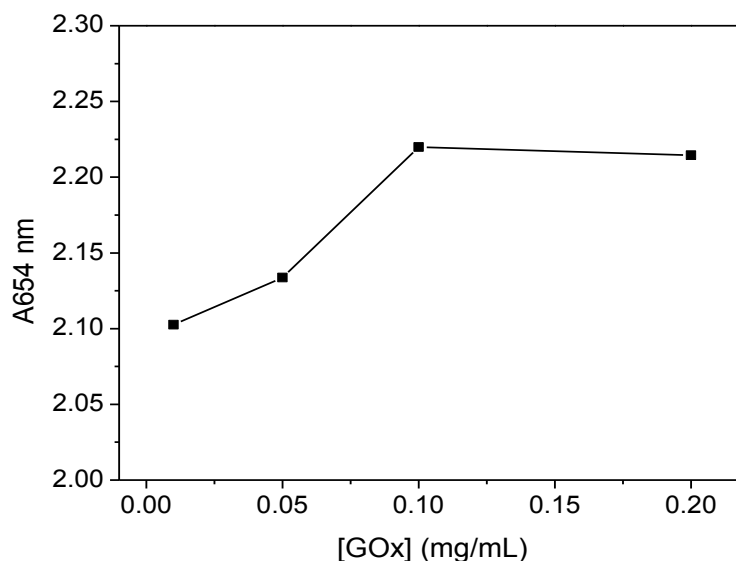
Figure 18: A dose-responsive curve of GOx. Reaction conditions: step 1: 1 mM glucose, PBS (0.1 mM, pH 7.4), T= 35°C, and 30 min incubation with different GOx concentrations; step 2: 0.3 mg/mL CuS-BSA-Cu$_3$(PO$_4$)$_2$, 0.3 mM TMB, acetate buffer (0.1 M, pH 4), T=25 °C, incubation time=25 min.

The nature of H_2O_2 production and catalytic oxidation of TMB can be summarized as follows:
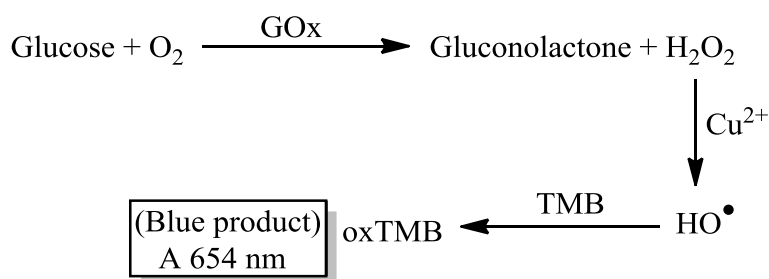
From **Figure 18**, one clearly sees a tremendous increase in absorbance at 654 nm with response to glucose concentration, where a plateau is reached at a glucose concentration of 1 mM. The change in color **(inset of Fig. 19)** further attests the capability of the proposed sensor for efficient colorimetric sensing of glucose in solution in an indirect way. A very low detection limit of 27.6 nM is achieved over a wide (0-1000 μM) concentration range, with a good linear relation (R^2 = 0.99267) between the oxTMB absorbance at 654 nm and glucose concentration. Compared to previous methods and reported materials for glucose sensing

(Table 4), a high sensitivity can be achieved by our method, and a simple visual detection can be easily qualified without the use of sophisticated instruments.
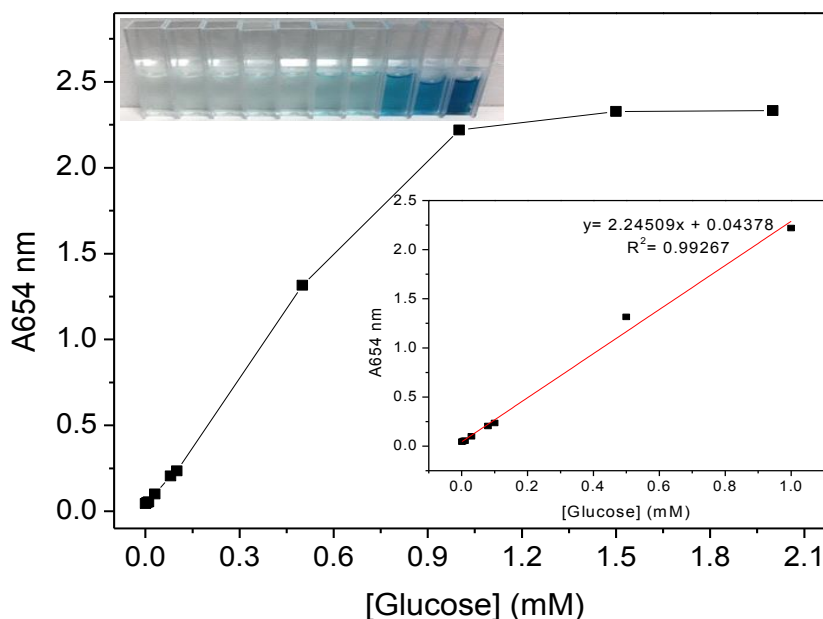
Figure 19: Increase trend in absorbance at 654 nm at various concentrations of glucose. Reaction conditions: step 1: 0.1 mg/mL GOx, PBS (0.1 mM, pH 7.4), T= 35°C, and 30 min incubation; step 2: 0.3 mg/mL CuS-BSA-Cu$_3$(PO$_4$)$_2$, 0.3 mM TMB, acetate buffer (0.1 M, pH 4), T=25 °C, incubation time=25 min. Inset: photographs of color changes during TMB oxidation using different concentrations of glucose.

Table 4: Quantitative analysis of glucose in comparison with reported materials using colorimetric method.

Materials	LOD (μM)	Linear range (μM)	Ref.
MoS$_2$ NFs	33.51	50-1000	[49]
GO-Fe$_3$O$_4$	0.74	2-200	[54]
CuS NPs	0.12	2-1800	[18]
Au-Ag NPs	3	5-70	[58]
Ficin	0.5	2-100	[59]
Cu-Ag-rGO	3.82	1-30	[52]
Pt NCs	0.28	0-200	[56]

CuS- BSA-Cu$_3$(PO$_4$)$_2$	0.0276	0-1000	Present study

Glucose level in blood is an important sign for human health. Thus, to estimate the feasibility of the colorimetric method for glucose determination, the assay was employed in sensing glucose in human blood samples. Following this purpose, freshly obtained blood solution from a healthy male volunteer was diluted 100 times after collecting the serum by centrifugation, and measured using a standard curve assay. **Table 5** summarizes the results achieved, with good recovery % obtained and very low relative standard deviation, whereby there was no marked difference observed among these methods. This indicated that the colorimetric method can be obviously applied in sensing glucose in human blood serum and potentially used in biomedical and clinical applications.

Table 5: Sensing of glucose in fresh human blood samples (n=3).

Samples	Glucose added (nM)	Glucose found (nM)	Recovery (%)	RSD (%)
	30	30.5	101.6	0.01
Human blood	80	84	105	0.0005
samples	130	131	100.76	0.004

3.1.3.10. Selectivity towards glucose sensing

Based on the acquired results, the selectivity for glucose detection was performed using other carbohydrates such as galactose, fructose and xylose, at a concentration 20 times higher than the optimal glucose concentration (1 mM), under the above aforementioned conditions. The results in **Figure 18** indicate that the highest absorbance intensity is recorded for glucose in comparison to other carbohydrate molecules, with an intense blue color solution, implying that the catalytic oxidation of TMB occurs rapidly in presence of glucose due to the excessive production of H$_2$O$_2$ from glucose oxidation by GOx. This suggests the high specificity and selectivity of our method for sensing glucose.
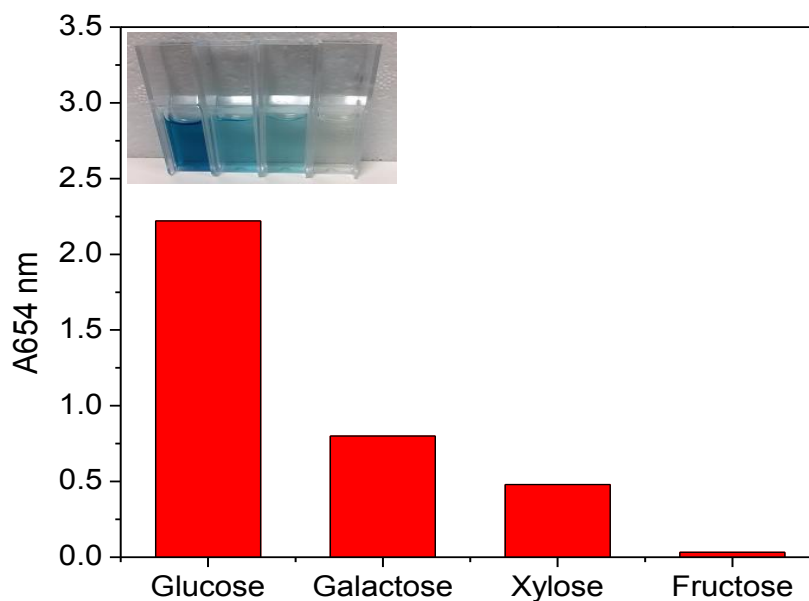
Figure 20: Selectivity of the colorimetric method using different glucose analogues. Reaction conditions: step 1: 1 mM glucose, 0.1 mg/mL GOx, PBS (0.1 mM, pH 7.4), T=35°C, incubation time=30 min; step 2: 0.3 mg/mL CuS-BSA-Cu$_3$(PO$_4$)$_2$, 0.3 mM TMB, acetate buffer (0.1 M, pH 4), T=25 °C, incubation time=25 min. Inset: photographs of color changes using interference substances of 20 times higher than glucose concentration (from left to right: with Glucose, Galactose, Xylose, and Fructose).

3.1.3.11. Hemolysis test

Nanomaterials can easily penetrate the cellular membrane by various ways, which causes damage to the model cell in accordance to nanoparticle's charge and size [60]. Thus, it is essential to test the hemolysis of the developed catalytic material on human red blood cells (RBC). Since nanoparticles can cause lysis to red blood cells, we opted to test the biocompatibility of CuS-BSA-Cu$_3$(PO$_4$)$_2$ on human erythrocytes. **Figure 21** shows the quantitative hemolysis percent of different concentrations of CuS-BSA-Cu$_3$(PO$_4$)$_2$ as compared to the positive control (PC). CuS-BSA-Cu$_3$(PO$_4$)$_2$ in the 37.5-300 µg/mL concentration range did not show hemolysis. However, at 600 µg/mL, hemolysis occurred obviously with 8.4% compared to PC.
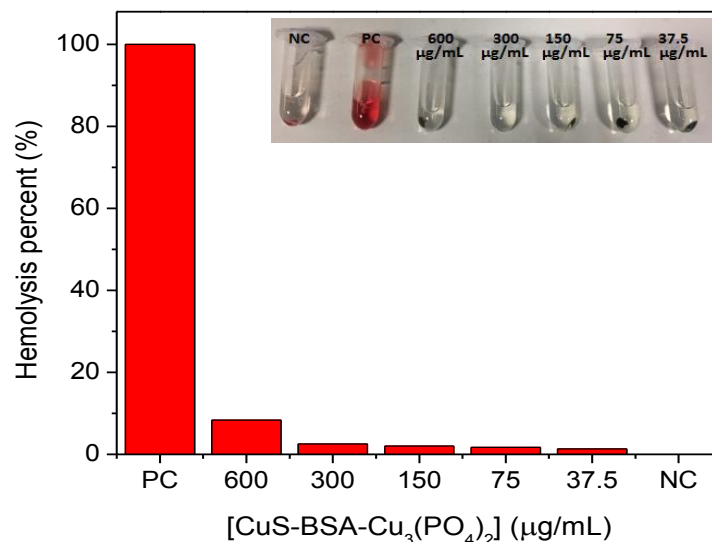
Figure 21: Hemolysis assay of different concentrations of CuS-BSA-Cu$_3$(PO$_4$)$_2$ on human erythrocytes for 2 h at 37 °C. Inset: photographs of visual hemolysis of CuS-BSA-Cu$_3$(PO$_4$)$_2$ incubated with RBCs.

3.1.4. Conclusion

We have developed an eco-friendly enzyme-like hybrid catalyst, CuS-BSA-Cu$_3$(PO$_4$)$_2$, for sensing glucose in human blood samples using TMB as a probe substrate. Surface modification with Cu$_3$(PO$_4$)$_2$ forms nanoparticles with small size, responsible for the efficient catalytic action of the nanocomposite material. Simplicity, selectivity and sensitivity are some interesting features offered by CuS-BSA-Cu$_3$(PO$_4$)$_2$ nanozyme for glucose detection through direct sensing of H$_2$O$_2$, which is the final product in the enzymatic reaction mediated by GOx. The nanozyme adopted typical Michaelis-Menten model. Under optimized experimental conditions, a good linear calibration curve was obtained for H$_2$O$_2$ detection in the linear concentration range of 0-8 μM with a detection limit of 22 nM. Similarly, the proposed sensor offered good sensitivity and selectivity for glucose detection with a detection limit as low as 27.6 nM and linearity in the 0-1000 μM range. The nanohybrid exhibited great catalytic action and better performance than natural enzymes, which allowed detecting both H$_2$O$_2$ and glucose at very low concentrations. All these advantages permitted the use of CuS-BSA-Cu$_3$(PO$_4$)$_2$ in widespread applications such as clinical diagnosis and environmental applications.

B. Colorimetric sensing of dopamine in beef meat using CuS-based nanoparticles

3.2.1. Introduction

Dopamine (DA) is a biogenic amine that forms as a result of amino acid decarboxylation, and is a proven anti-oxidant against the damaging effect of free radicals [1]. DA is also considered an essential endogenous catecholamine neurotransmitter that can transmit specific signals in the peripheral and central nervous systems, and an important contributor in human metabolism [2]. It is also involved in the blood pressure regulation and can be used for the treatment of several diseases, especially the hydrochloride salt, such as kidney failure, heart attack, as well blood infections caused by bacteria [3]. However, abnormal release of dopamine in the human body can cause Alzheimer, Huntington, Parkinson, Schizophrenia and many neuronal diseases [4, 5]. In certain cases, DA is added to animal feed in order to lower the amount of fat in animal species and help build muscles [6, 7]. Thereby dopamine residues are susceptible to accumulate in tissues which represents a major hazard to animal species even if they are exposed to a low level of DA. Thus, the detection of DA represents an indispensable need to achieve early disease diagnosis with high degree of sensitivity, selectivity, and fast response.

Due to the significant importance of this molecule, researchers in the medicinal field focused on various methods to determine DA concentration such as HPLC [8], electrophoresis [9], chemiluminescence [10], capillary electrophoresis [11], and particularly electrochemical methods [12-14] were shown to be more promising due to the electroactive nature of this molecule.

Recently, optical spectroscopic methods based on colorimetric assays gained much attention for DA sensing due to their simple analysis. Additionally, given that the detection of DA should be highly sensitive due to the low amount of this molecule in physiological media that represents only few nanomolar to lower micromolar (0.01-0.1 μm) [15], this method seems to be more suitable for DA sensing. In addition, dopamine coexists with various analogous in biological fluids; particularly ascorbic acid (AA) and uric acid (UA) [16, 17] co-exist with DA

at a concentration 100 times higher than that of dopamine [14], thus DA can interfere with these molecules which might influence the specificity of detection.

Generally, since the successful utilization of nanomaterials as new members of artificial enzymes, an enormous array of enzymomimetics or nanozymes have been developed as novel colorimetric sensors for the detection of a wide variety of chemical and biological species [18]. In this context, nanozymes occupy a central place and have been extensively investigated in the field of sensing and proved to be promising alternatives to analytical sensing devices due to their exceptional properties [18, 19]. Shiyun and colleagues reported a colorimetric assay for DA determination based on the aggregation of gold NPs mediated by Cu^{2+} ions [20]. Wang *et al.* investigated the use of a composite material of reduced graphene oxide (rGO) conjugated with $NiCo_2S_4$ for colorimetric DA sensing [21], and many other reported materials have been utilized for DA sensing using colorimetric assays [4, 5, 22-24]. In these circumstances, colorimetric sensing provided highly sensitive and selective monitoring of biological molecules, in addition to rapid time response that can monitor concentration changes which occur at a sub-second time scale.

In recent years, a tremendous attention has been devoted to transition metals mainly Cu-based nanomaterials such as copper oxides (CuO), copper-containing metal organic frameworks (Cu-MOFs) and copper phosphates ($Cu_3(PO_4)_2$), etc. [25-27] as a result of their interesting properties, which have been investigated in many different applications, particularly in sensing and catalysis-related applications [28]. In this regard, the promising features of copper sulfide (CuS) nanomaterials make them ideal candidates as nanozymes for the detection of biological molecules, such as glucose, cholesterol, uric acid, and heavy metal ions, among others [29-32], based on the enzymatic-like behavior of CuS which can effectively catalyze the oxidation of peroxidase substrates in the presence of H_2O_2. A CuS-based sensor has been reported previously by Tarasankar and co-workers in combination with rGO [24] for sensing dopamine. However, the nanocomposite showed low sensitivity and selectivity.

Herein, we demonstrated a rapid sensing platform for dopamine using CuS-BSACu$_3$(PO$_4$)$_2$ nanoparticles, in which an immense reduction of HO$^\bullet$ radical generation and an inhibition of the catalytic oxidization action towards TMB have been achieved in the presence of DA. The technique achieved high sensitivity and selectivity of sensing and was successfully applied for DA sensing in meat samples.

3.2.2. Preparation of CuS-BSA-Cu₃(PO₄)₂ enzymomimetic nanoparticles

The synthetic route of CuS-BSA-Cu$_3$(PO$_4$)$_2$ followed the same procedure described in chapter 3 (part A) with some modifications. In brief, 63 mg of BSA lyophilized powder were dissolved in 9 mL Milli-Q water in a 50 mL round bottom flask. Then, 162 mg of copper acetate [Cu(Ac)$_2$] were added to the BSA solution, followed by the addition of 0.5 mL NaOH (2.0 M) under continuous magnetic stirring to ensure homogeneous dispersion. 117 mg of Na$_2$S.xH$_2$O were successively added to the above mixture, and the reaction continued for 5 h at 90 °C in an oil bath. The resulted CuS-BSA product was purified by using a 12000-14000 Da molecular mass cutoff dialysis membrane against Milli-Q water for 24 h.

10 mg of the as-synthesized CuS-BSA were mixed with 0.1 mL aqueous solution of CuSO$_4$.5H$_2$O (80 mM) in 9.9 mL PBS (0.01 M, pH 7.4), and incubated at 4 °C for 72 h under magnetic agitation. The obtained CuS-BSA-Cu$_3$(PO$_4$)$_2$ product was purified by dialysis using a 12000-14000 Da molecular mass cutoff dialysis membrane in Milli-Q water for 24 h, after which it is lyophilized to obtain a CuS-BSA-Cu$_3$(PO$_4$)$_2$ green powder.

3.2.3. Results and discussion

3.2.3.1. Characterization of CuS-BSA-Cu₃(PO₄)₂ nanoparticles

The CuS-BSA-Cu$_3$(PO$_4$)$_2$ nanoparticles were synthesized using a simple assay and characterized using different techniques.

The surface charge and hydrodynamic size of CuS-BSA-Cu$_3$(PO$_4$)$_2$ were evaluated by ζ potential and dynamic light scattering (DLS), respectively. As illustrated in **Figure 1** and **2**, conjugation of Cu$_3$(PO$_4$)$_2$ with CuS-BSA demonstrates a noticeable slight increase in both the negative surface charge and diameter which increased up to -29 ± 2.6 nm and 142.7 nm, from -26 ± 2.8 mV and 54 nm, respectively.
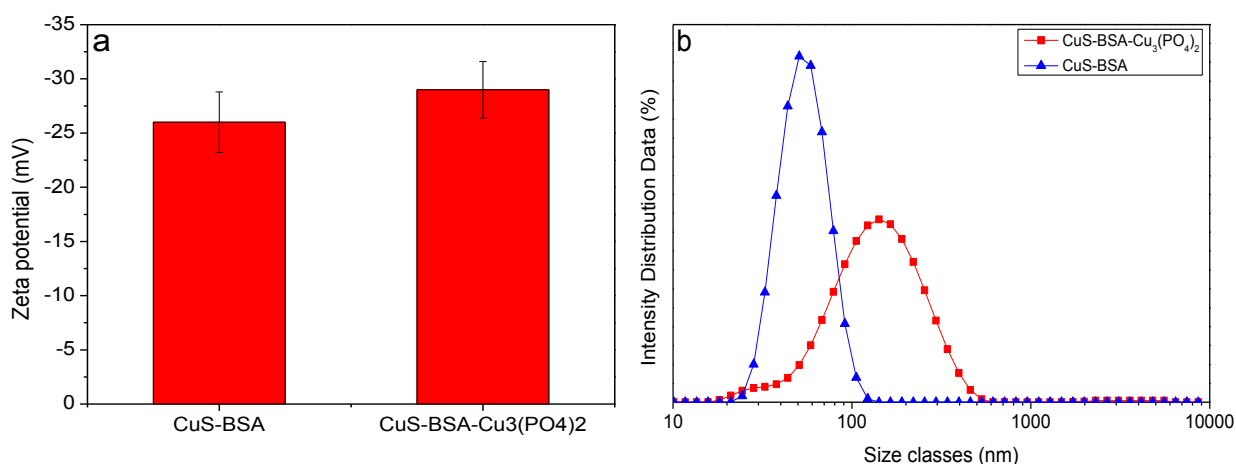
Figure 1: Comparison of zeta potential (a) and hydrodynamic size (b) of CuS-BSA and CuS-BSA-Cu$_3$(PO$_4$)$_2$ nanoparticles in MQ-water.

The successful synthesis of the nanoparticles and the presence of diverse functional groups were confirmed by FTIR analysis. **Figure 2** reveals the existence of characteristic absorption bands at 1046 and 981 cm^{-1} ascribed to asymmetrical P=O and symmetrical P-O stretching [33, 34], respectively, in CuS-BSA-Cu$_3$(PO$_4$)$_2$ spectrum. The characteristic peak at 1115 cm^{-1} corresponds to CuS [35] in the CuS-BSA spectrum. Additional peaks at 3433, 1652, 1543, 1381 cm^{-1} correspond to O-H, C=O (amide I), N-H (amide II), and C-H stretching modes in BSA, respectively [36].
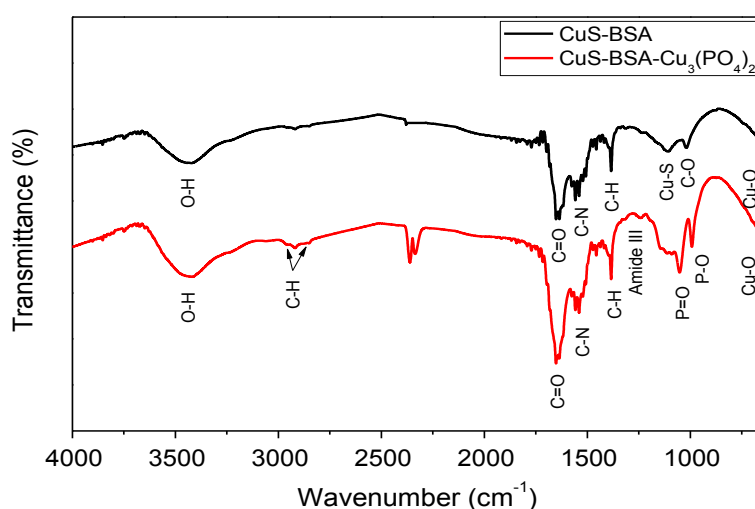
Figure 2: FTIR spectra of CuS-BSA and CuS-BSA-Cu$_3$(PO$_4$)$_2$ nanoparticles.

X-ray photoelectron spectroscopy (XPS) was performed in addition on CuS-BSA-Cu$_3$(PO$_4$)$_2$ nanoparticles. As shown in **Figure 3a**, the wide-survey XPS spectrum confirms the presence of C$_{1s}$ (284.7 eV), O$_{1s}$ (531.2 eV), and N$_{1s}$ (399.6 eV) of BSA molecules, in addition to Cu$_{2p}$ (932.4 eV), S$_{2p}$ (162.3 eV), and P$_{2p}$ (133.1 eV) which derive from CuS and Cu$_3$(PO$_4$)$_2$, with atomic concentrations of 62.69%, 21.75%, 12.91%, 1.28%, 0.59% and 0.75%, respectively. To get better detailed information and inspect the various chemical groups, the deconvolution of C$_{1s}$ spectrum with peak fitting was given in **Figure 3b**. It shows the existence of C-C/C=C (284.5 eV), C-N/C-O (285.7 eV), and C=O (287.7 eV) bonds. The O$_{1s}$ spectrum **(Fig. 3c)** can be curve-fitted with two separate peaks due to C=O/O-H (531.1 eV) and C-O/P-O (532.5 eV). The N$_{1s}$ wide spectrum **(Fig. 3d)** can be separated into two peaks due to C-N (399.6 eV) and C=N (401.8 eV) [25]. The Cu$_{2p}$ high resolution spectrum **(Fig. 3e)** shows two peaks corresponding to Cu$_{2p3/2}$ (932.8 eV) and Cu$_{2p1/2}$ (952.5 eV) [37] separated by a spin orbit of 19.7 eV, which fully agrees with literature data [38]. In addition two "shakeup" satellite

peaks are observed at 942.6 and 962.9 eV [39], which confirms the partially filled d-orbital of divalent copper (Cu^{2+}). The S_{2p} wide spectrum **(Fig. 3f)** encompasses two main peaks deconvulated into $S_{2p3/2}$ (162.39 eV) and $S_{2p1/2}$ (164.3 eV) of CuS and $S_{2p3/2}$ (168.3 eV) with $S_{2p1/2}$ (170 eV) due to $CuSO_4$ which arises from the vulnerable oxidation of CuS [40]. The peak located at 133.18 eV is severally ascribed to P-O bond in $Cu_3(PO_4)_2$ [41]
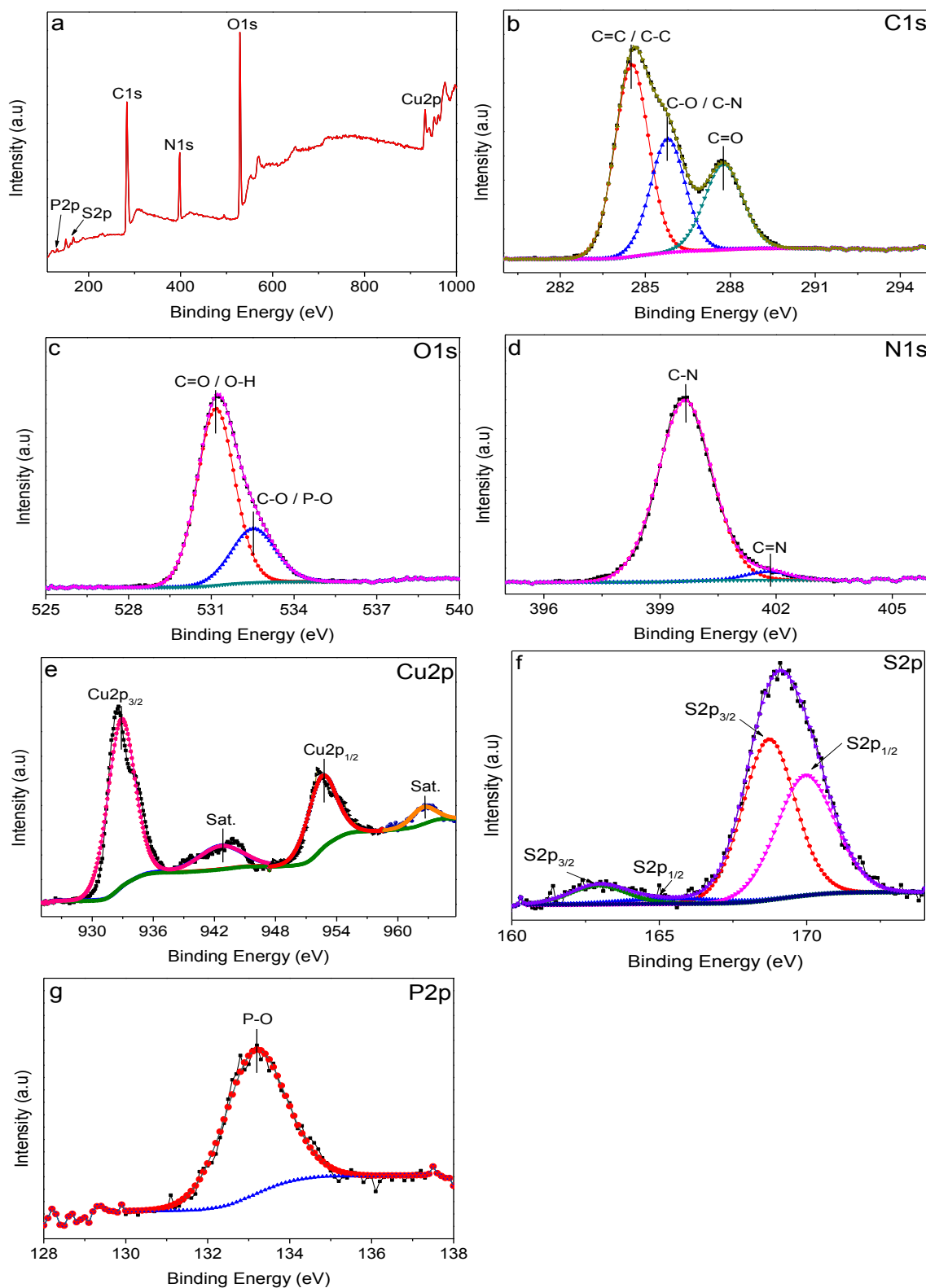
Figure 3: XPS survey of CuS-BSA-Cu$_3$(PO$_4$)$_2$ nanoparticles (a), and the high resolution XPS spectra of C$_{1s}$ (b), O$_{1s}$ (c), N$_{1s}$ (d), Cu$_{2p}$ (e), S$_{2p}$ (f), and P$_{2p}$ (g).

3.2.3.2. Enzymomimetic activity of CuS-BSA-Cu$_3$(PO$_4$)$_2$ nanoparticles

The enzymomimetic activity of CuS-BSA-Cu$_3$(PO$_4$)$_2$ was evaluated for the catalytic oxidation of a chromogenic peroxidase substrate ''TMB'' for 20 min in presence of H$_2$O$_2$ in an acidic buffered medium. On the basis of this assay, the enzyme-like catalytic reaction was carried out under different parameters to optimize the conditions and achieve the highest catalytic response. **Figure 4** shows that the highest catalytic activity was observed in the presence of CuS-BSA-Cu$_3$(PO$_4$)$_2$ and H$_2$O$_2$, however the oxidation of TMB was not achieved when CuS-BSA-Cu$_3$(PO$_4$)$_2$ or H$_2$O$_2$ was absent. This indicates that both catalyst and H$_2$O$_2$ are required to obtain an enzyme-like catalytic reaction.
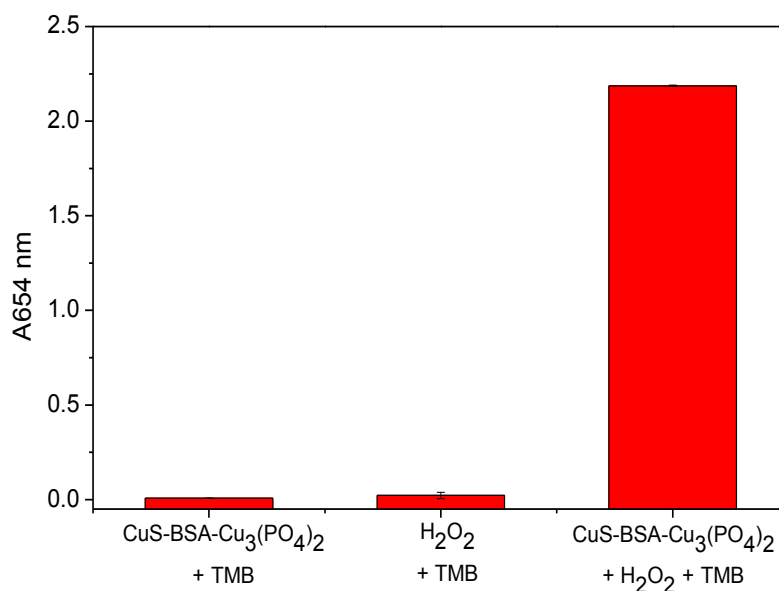
Figure 4: UV-vis absorption spectra of oxTMB under different experimental conditions. Reaction conditions: 0.1 mg/mL CuS-BSA-Cu$_3$(PO$_4$)$_2$, 0.3 mM TMB, 1 mM H$_2$O$_2$, acetate buffer (0.1 M, pH 4), RT, 20 min incubation.

To optimize the experimental conditions for the enzyme-like catalyzed reaction, various parameters were tested. As depicted in **Figure 5**, the oxidation reaction of TMB was shown to be catalyst concentration-dependent, and saturates at 0.1 mg/mL of CuS-BSA-Cu$_3$(PO$_4$)$_2$. Thus, this concentration was adopted to initiate the subsequent experiments. At this value (0.3 mM), TMB oxidation gives the highest absorption intensity, as clearly observed in **Figure 6**. Thereby, 0.3 mM of TMB was selected for the rest of the catalytic experiments.
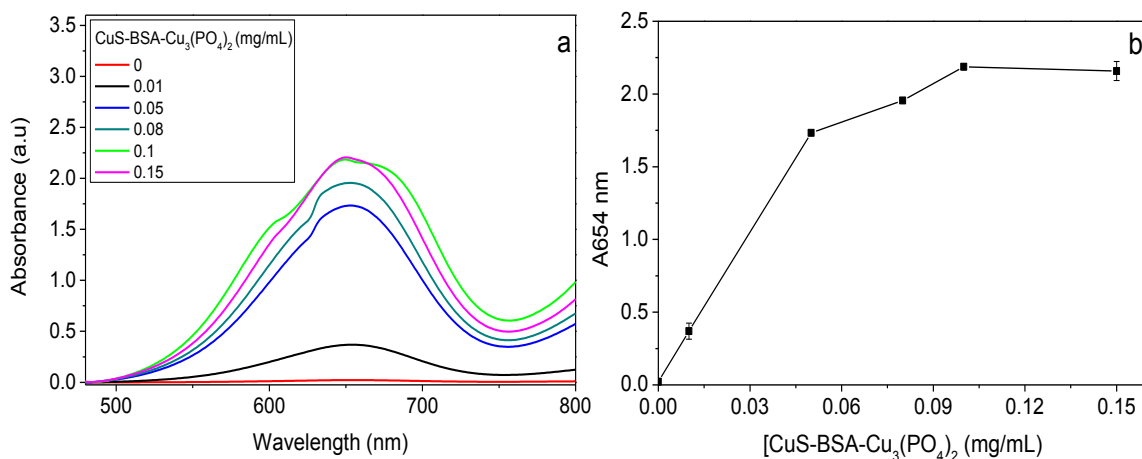
Figure 5: UV-vis absorption spectra of oxTMB at different concentrations of CuS-BSA-Cu$_3$(PO$_4$)$_2$ (a) and a dose-responsive curve of CuS-BSA-Cu$_3$(PO$_4$)$_2$ under various concentrations (b). Reaction conditions: 0.3 mM TMB, 1 mM H$_2$O$_2$, acetate buffer (0.1 M, pH 4), RT, 20 min incubation.
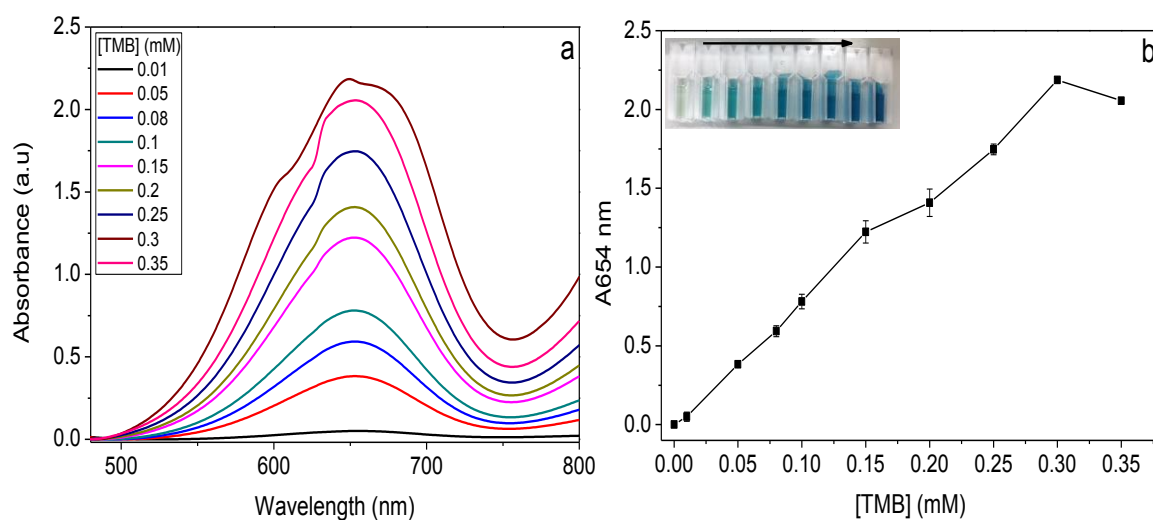
Figure 6: The UV-vis absorption spectra of different concentrations of TMB (a), and a dose-responsive curve of TMB (b). Reaction conditions: 0.1 mg/mL CuS-BSA-Cu$_3$(PO$_4$)$_2$, 1 mM H$_2$O$_2$, acetate buffer (0.1 M, pH 4), RT, 20 min incubation. Inset (b) the color changes at different TMB concentrations.

The nanozyme-catalyzed reaction can be influenced by several parameters such as, temperature, pH and time. Thus, the catalytic performance of CuS-BSA-Cu$_3$(PO$_4$)$_2$ was examined at four different temperatures **(Fig. 7a)**, and under a set of various pH values **(Fig. 7b)**. Surprisingly, the nanozyme exhibited a better catalytic action than native enzymes, where

the catalytic activity was not affected by temperature changes. However, a slight acidic medium (pH 4) is required to achieve excellent catalytic behavior, as explained previously. Under these conditions, the reaction was completed within 20 min **(Fig. 8)**.
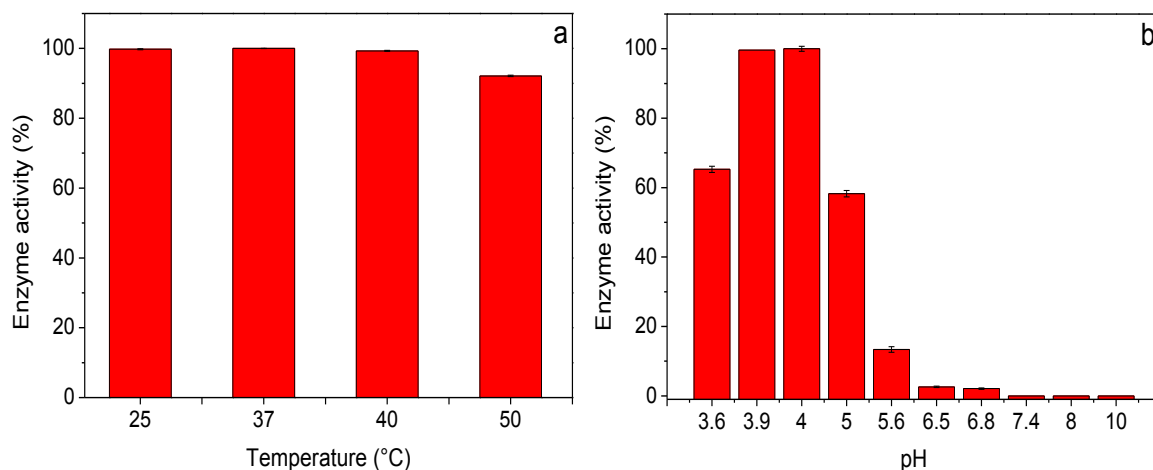
Figure 7: Influence of temperature (a) and pH (b) on the catalytic oxidation of TMB. Reaction conditions: 0.3 mM TMB, 1 mM H_2O_2, 0.1 mg/mL CuS-BSA-$Cu_3(PO_4)_2$, 20 min incubation.
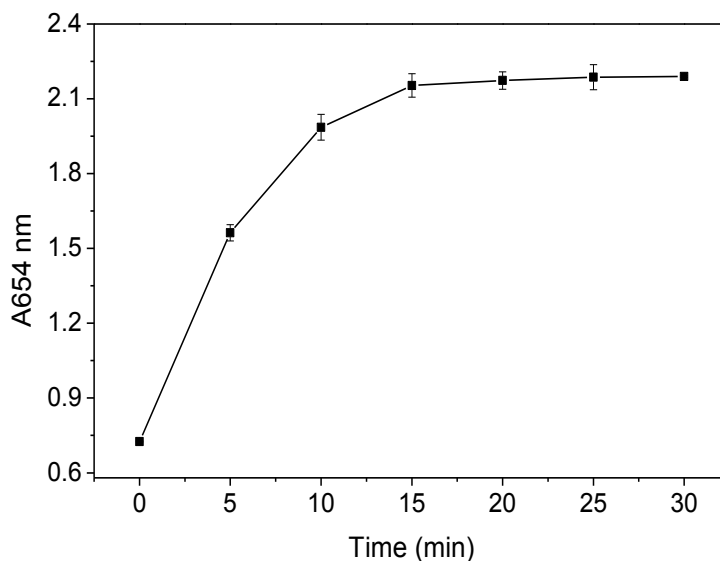
Figure 8: Time-course responsive curve of oxTMB. Reaction conditions: 0.3 mM TMB, 1 mM H_2O_2, 0.1 mg/mL CuS-BSA-$Cu_3(PO_4)_2$, acetate buffer (0.1 M, pH 4), RT.

Based on the obtained results, the kinetic study was conducted for determining the limit of H_2O_2 concentration needed to accomplish the catalytic reaction. Thereby, upon addition of various concentrations of H_2O_2 **(Fig. 9a and b)**, the absorbance maximum at 654 nm, which corresponds to the oxidized product of TMB, increased rapidly to reach a steady state at 1 mM.

This was also confirmed by an intense color change **(inset of Fig. 9b)** achieved at this higher H_2O_2 concentration.

A good linear calibration curve for H_2O_2 can be obtained within the 0-0.1 mM range with a linear relation ($R^2 = 0.99815$), and a low detection limit of 10.8 nM.
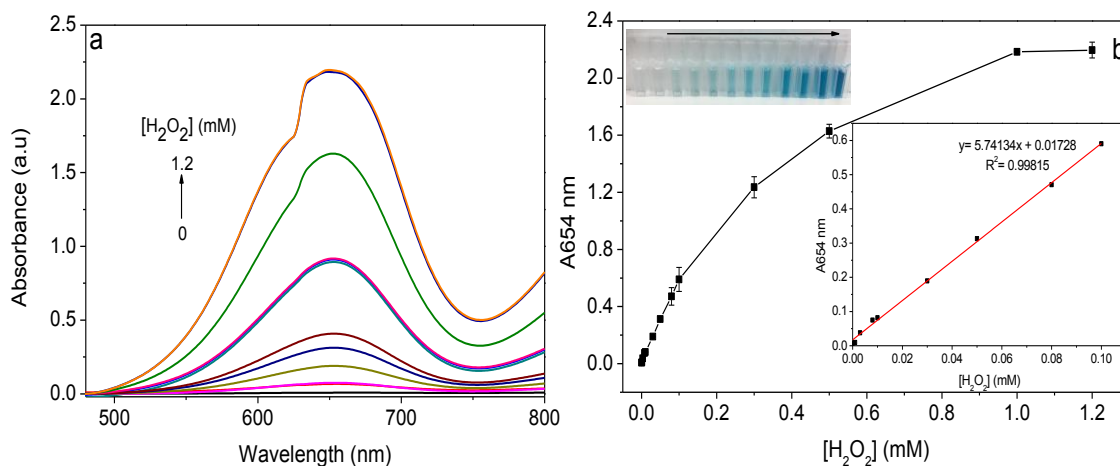
Figure 9: UV-vis absorbance spectra of oxTMB at different H_2O_2 concentrations (a), and a dose-responsive curve of H_2O_2 (b). Reaction conditions: 0.3 mM TMB, 0.1 mg/mL CuS-BSA-$Cu_3(PO_4)_2$, acetate buffer (0.1 M, pH 4), RT, 20 min incubation. Inset (b): the linear calibration curve for the determination of H_2O_2 and the photographs of TMB oxidation at low (left) to high (right) H_2O_2 concentrations.

3.2.3.3.   Nanozyme-mediated colorimetric determination of dopamine

Considering the enzymomimetic property of CuS-BSA-$Cu_3(PO_4)_2$ at the optimized conditions, a colorimetric sensor was designed for dopamine (DA) sensing. **Figure 10** depicts the effect of DA concentration on the catalytic behavior of CuS-BSA-$Cu_3(PO_4)_2$ nanoparticles. Noticeably, the absorption intensity at 654 nm decreases gradually upon successive addition of DA, and a huge decline can be observed at an elevated amount of DA (0.5 mM), causing the blue oxTMB product to fade. This indicates that dopamine induces an inhibitory action of the Fenton mediated reaction catalyzed by Cu(II) divalent ions of CuS-BSA-$Cu_3(PO_4)_2$ nanozyme as a result of $HO^{\bullet}$ quenching by DA, which results in the depletion of available $HO^{\bullet}$ in solution [22, 42]. DA sensing displays a linear equation y= -11.883x (mM) + 1.9602 with a good linear relation ($R^2 = 0.9916$) in the 0-0.1 mM concentration range **(inset of Fig. 4)** with a LOD as low as 5.2 nM, which has not achieved to date by colorimetric assays based on nanozymes. **Table 1**

shows the LOD of DA obtained by various nanomaterials using colorimetric approaches, where CuS-BSA-Cu$_3$(PO$_4$)$_2$ displayed the highest sensitivity among all.
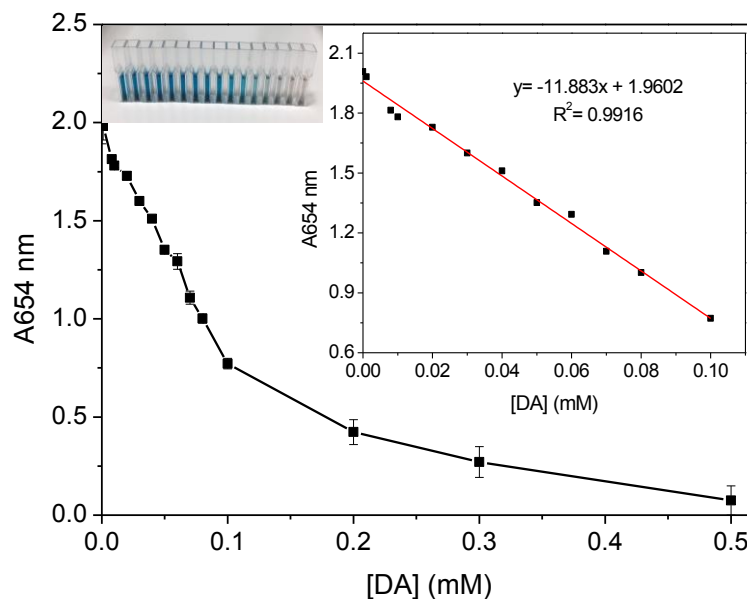
Figure 10: Absorbance spectrum of oxTMB at different DA concentrations. Inset: the linear calibration curve for the determination of DA and typical photographs of oxTMB at increasing concentrations of DA. Reaction conditions: 0.3 mM TMB, 0.1 mg/mL CuS-BSA-Cu$_3$(PO$_4$)$_2$, 1 mM H$_2$O$_2$, acetate buffer (0.1 M, pH 4), RT, 20 min incubation.

Table 1: Comparison of different colorimetric methods for dopamine sensing.

Sensor	Linear range (µM)	LOD (nM)	References
MOFs	0.05-30	50	[4]
GNPs	0.5-10	200	[20]
NiCo$_2$S$_4$-rGO	0.5-100	420	[21]
CuS-rGO	2-100	480	[24]
CuS-BSA-Cu$_3$(PO$_4$)$_2$	0-0.1	5.2	Present study

3.2.3.4. Nanozyme-mediated colorimetric determination of dopamine

kinetics was manifested using TMB and H_2O_2 as two different substrates at the optimal conditions, that is at 0.1 mg/mL CuS-BSA-$Cu_3(PO_4)_2$, pH 4, and RT. Thus, a set of catalytic experiments were executed by changing the concentration of one substrate while retaining the other constant, in a time-course mode, in order to evaluate the catalytic performance of the proposed nanozyme. The Beer-Lambert law was used to estimate the initial rate of each substrate.

A plot of the initial catalytic reaction rate as a function of each substrate concentration was illustrated in **Figure 11a** and **12a**, which also enables to draw a Lineweaver–Burk plot (**Fig. 11b and 12b**), to calculate the kinetic parameters, where the slope determines the K_m and the intercept gives the V_{max} for TMB and H_2O_2. **Table 2** summarizes the kinetic parameters displayed by CuS-BSA-$Cu_3(PO_4)_2$ in comparison with reported literature. The K_m values for TMB and H_2O_2 exhibited by the proposed nanozyme were found to be lower than the natural horseradish peroxidase, elucidating a high affinity towards both substrates.
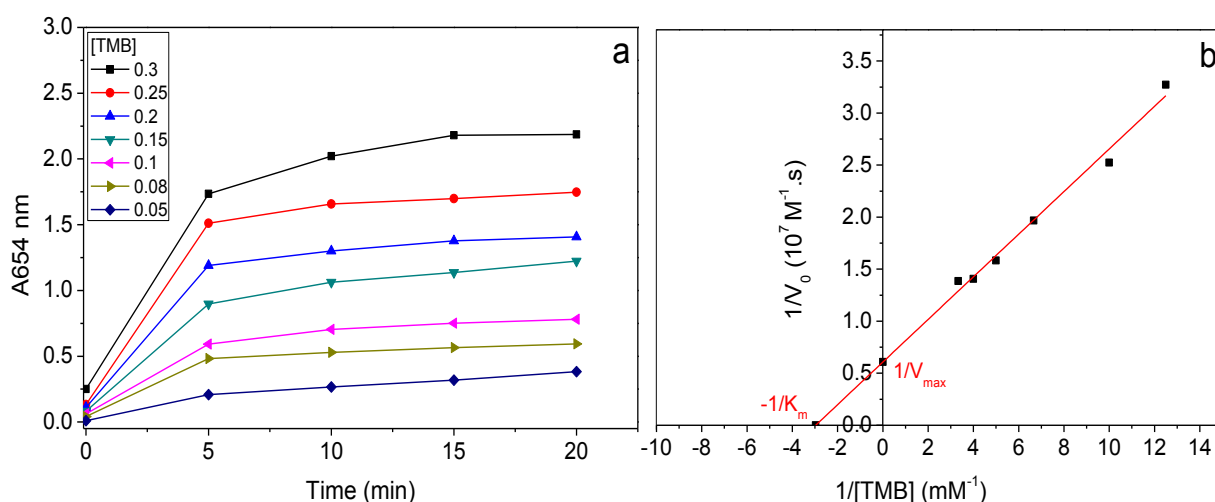
Figure 11: UV/vis absorption spectra of different concentrations of TMB as a substrate under fixed concentration of H_2O_2 in a time course-mode (a); Steady-state kinetics using the Michaelis-Menten method and Lineweaver-Burk plot for TMB as a substrate (b). Reaction conditions: 0.1 mg/mL CuS-BSA-$Cu_3(PO_4)_2$, 1 mM H_2O_2, acetate buffer (0.1 M, pH 4), RT.
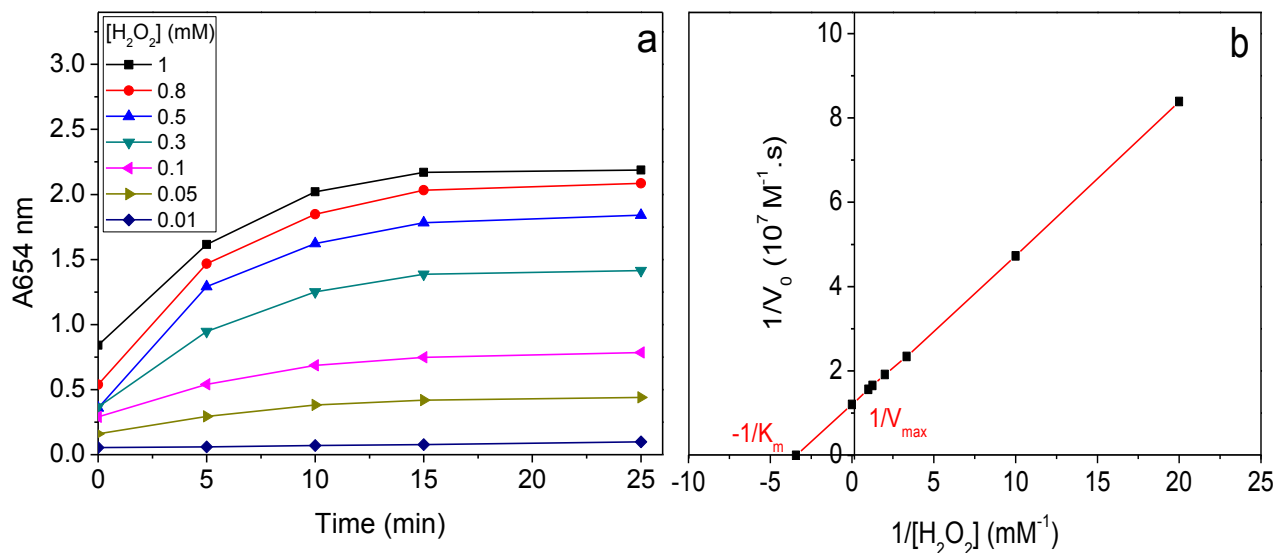
Figure 12: UV/vis absorption spectra of different concentrations of H_2O_2 as a substrate at a fixed concentration of TMB in a time course-mode (a); Steady-state kinetics using the Michaelis-Menten method and Lineweaver-Burk plot for H_2O_2 as a substrate (b). Reaction conditions: 0.3 mM TMB, 0.1 mg/mL CuS-BSA-Cu$_3$(PO$_4$)$_2$, acetate buffer (0.1 M, pH 4), RT.

Table 2: Comparison of K_m and V_{max} kinetic parameters of H_2O_2 and TMB substrates with different reported sensing studies.

Catalyst	$\underline{K_m}$ (mM)		$\underline{V_{max}}$ (mM.s^{-1})		Ref.
	H$_2$O$_2$	TMB	H$_2$O$_2$	TMB	
HRP	3.7	0.434	8.71×10^{-5}	10×10^{-5}	[44]
Ceria nanorods	293	0.417	3.8×10^{-2}	6.2×10^{-2}	[45]
Magnetic nanocomposite	2.05	5.7	6.08×10^{-3}	1.43×10^{-4}	[46]
CuS-BSA-Cu$_3$(PO$_4$)$_2$	0.29	0.33	8.31×10^{-5}	1.6×10^{-4}	Present study

3.2.3.5. CuS-BSA-Cu$_3$(PO$_4$)$_2$ nanozyme recyclability and selectivity

The reusability of the nanozyme was examined for 4 successive catalytic cycles. Before each repeated cycle, the CuS-BSA-Cu$_3$(PO$_4$)$_2$ nanosensor was separated from the reaction mixture by centrifugation and washed with Milli-Q water, followed by adding fresh solutions of TMB and H$_2$O$_2$ in acetate buffer to initiate the redox reaction. **Figure 13** indicates that the

absorption intensity of oxTMB (654 nm) was slightly reduced with every cycle, which could be ascribed to the washing steps that causes loss of some amount of the catalyst, even though, the catalyst can be reused efficiently.
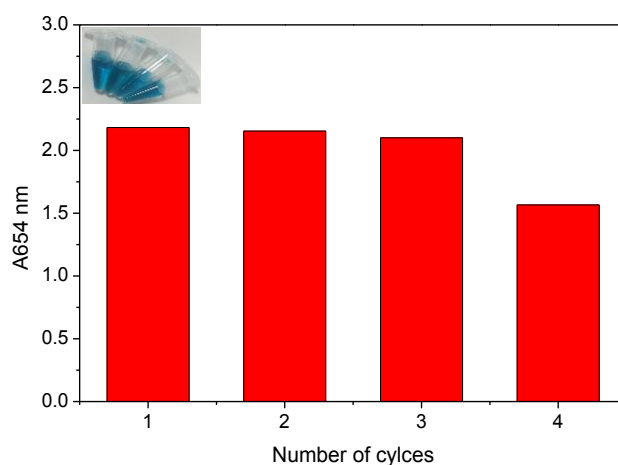
Figure 13: Catalytic cycles of TMB oxidation. Reaction conditions: 0.3 mM TMB, 0.1 mg/mL CuS-BSA-Cu$_3$(PO$_4$)$_2$, 1 mM H$_2$O$_2$, acetate buffer (0.1 M, pH 4), RT, 20 min incubation.

Furthermore, the nanozyme selectivity towards dopamine sensing was evaluated in the presence of diverse biological molecules, and their absorption intensity difference ($\Delta A_{654}= A_{H2O2} - A_{interfering\ molecule}$) was compared with that of DA. **Figure 14** indicates that interference molecules even at a concentration of 0.6 mM (2-times higher than DA) showed a very low reduction of the absorbance at 654 nm, which indicates the outstanding selectivity towards DA. The inhibited catalytic oxidation of TMB in the presence of DA is attributed to the attachment of hydroxyl radicals on the phenolic ring of DA [1].
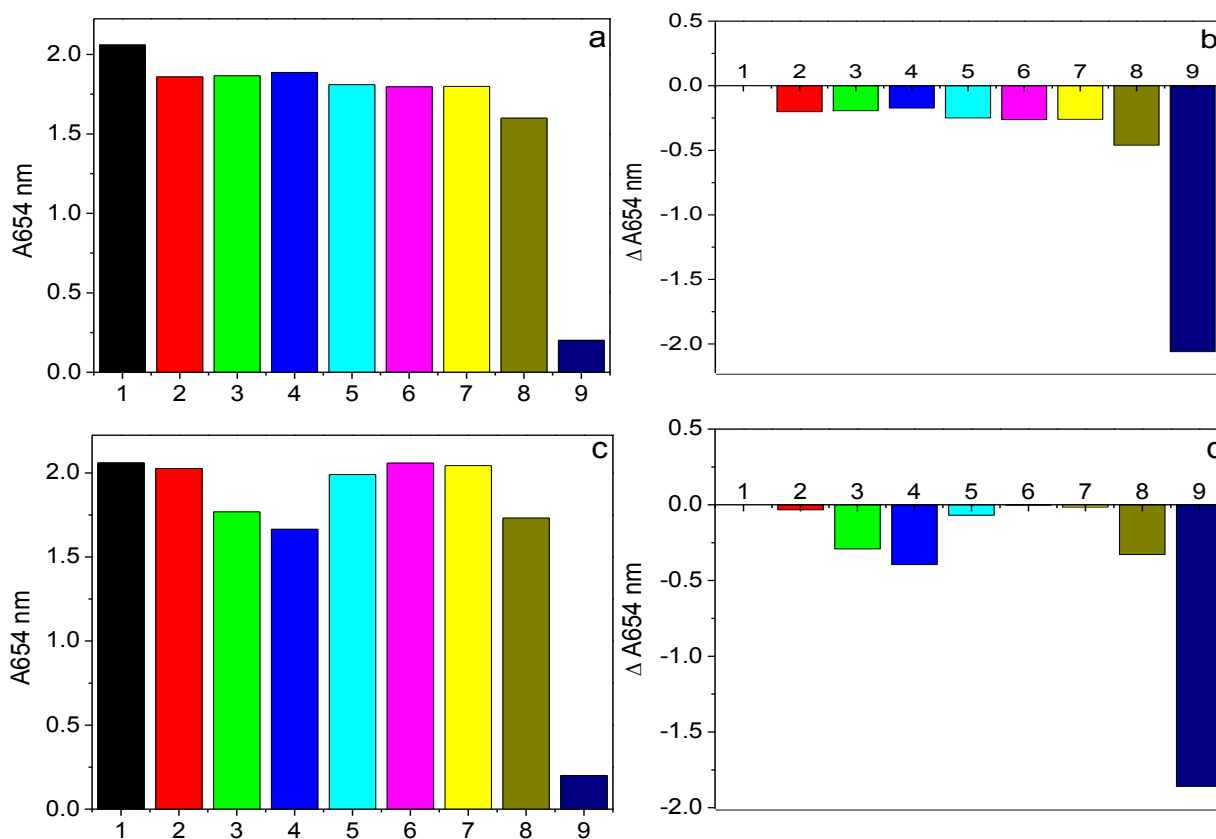
Figure 14: Comparison of oxTMB absorption in the presence of different interfering biological molecules (1: Control, 2: Lactose, 3: Glutathione, 4: Uric acid, 5: Cholesterol, 6: Glucose, 7: Fructose, 8: Ascorbic acid, 9: Dopamine) at a concentration of 0.3 mM (a,b) (same as DA) and 0.6 mM (c,d) (2 times higher than the concentration of DA). Reaction conditions: 0.1 mg/mL CuS-BSA-Cu$_3$(PO$_4$)$_2$, 1 mM H$_2$O$_2$, 0.3 mM TMB, acetate buffer (0.1 M, pH 4), RT, 20 min incubation.

3.2.3.6. Hydroxyl radicals generation mechanism

In order to understand the effective enhancement of the catalytic action of CuS-BSA-Cu$_3$(PO$_4$)$_2$ towards the generation of HO$^\bullet$, fluorescence (FL) spectroscopy was carried out using a hydroxyl radical trapping molecule named ''Terephthalic acid'' (TA). FL spectra of different reaction mixtures were monitored in the 393-530 nm range after 20 min incubation. It is worth to notice that TMB oxidation was closely correlated to the HO$^\bullet$ production by the CuS-BSA-Cu$_3$(PO$_4$)$_2$-stimulated decomposition of H$_2$O$_2$. TA can track the generated HO$^\bullet$ to yield a fluorescent molecule ''HTA'' that can be easily monitored by FL spectroscopy through an emission peak at 410 nm. **Figure 15** shows that TA alone could not display any fluorescent signal, however the presence of both H$_2$O$_2$ and CuS-BSA-Cu$_3$(PO$_4$)$_2$ in the reaction mixture

greatly enhances TA oxidation and resulted in emission maxima at 410 nm. On the other hand, the presence of dopamine in the reaction mixture causes depletion in the amount of the generated hydroxyl radicals, explained by an immense reduction in the FL intensity. This indicates that $CuS\text{-}BSA\text{-}Cu_3(PO_4)_2$ are promising peroxidase mimetics and TMB oxidation was proceeded due to the generation of $HO^•$ in the presence of H_2O_2.
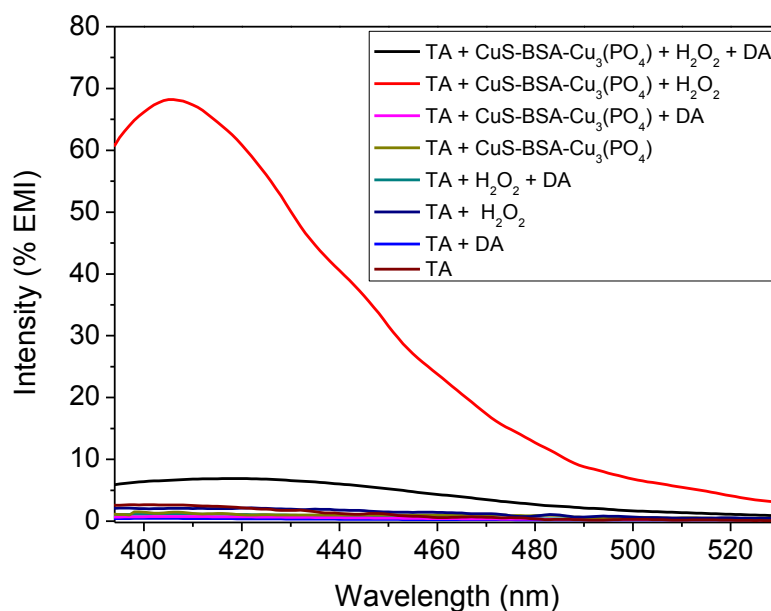
Figure 15: Comparison of fluorescence spectra using TA fluorescent probe. Reaction conditions: 0.2 mM TA, 0.1 mg/mL $CuS\text{-}BSA\text{-}Cu_3(PO_4)_2$, 1 mM H_2O_2, 0.2 mM DA, acetate buffer (0.1 M, pH 4), RT, 20 min incubation.

3.2.3.7. Detection of DA in beef meat samples

To evaluate the sensing performance of $CuS\text{-}BSA\text{-}Cu_3(PO_4)_2$, we widen the scope of our investigation towards dopamine sensing in beef meat samples. By comparing the absorbance intensity of oxTMB at 654 nm, using the calibration curve (**inset of Figure 10**), in the presence of 0.4 µM DA solution with the diluted meat sample resulted in DA concentration of 0.43 µM. HPLC analysis of meat samples was used to validate the results, which resulted in DA concentration of 0.4 µM using the calibration plot in **Figure 16**, in agreement with the colorimetric results.
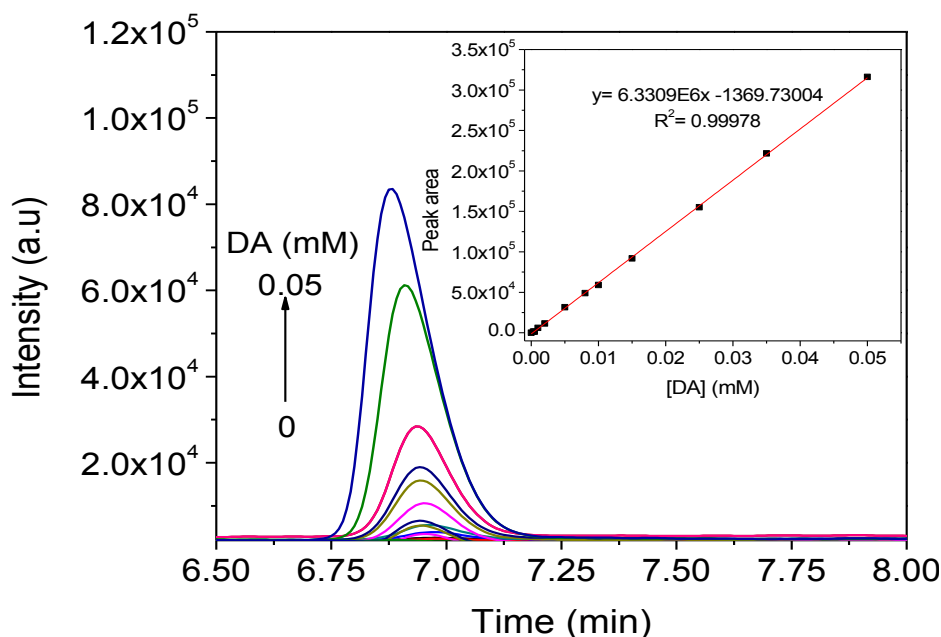
Figure 16: HPLC intensity of DA at various concentrations. Inset: the linear calibration plot of DA.

Table 3: UV-vis and HPLC analysis of dopamine in beef meat samples.

Sample	Colorimetry		HPLC	
	Absorbance (a.u)	[DA] (µM)	Peak area	[DA] (µM)
Beef meat	1.955	0.43	1386	0.4

3.2.4. Conclusion

In summary, we successfully developed an efficient CuS-BSA-Cu$_3$(PO$_4$)$_2$ nanosensor following a simple, low cost and eco-friendly method. The CuS-BSA-Cu$_3$(PO$_4$)$_2$ effectively catalyzes the oxidation of a chromogenic peroxidase substrate "TMB" with H$_2$O$_2$, due to its potential generation of HO$^\bullet$ in an acidic medium. The CuS-BSA-Cu$_3$(PO$_4$)$_2$ nanoparticles were also utilized as excellent candidates for sensing an important biological molecule "dopamine", which acts as an inhibitor to the peroxidase-like action of the nanozyme. In fact, upon addition of increasing DA amounts to the mixture, an obvious stepwise decrease in A654 nm has been detected. Dopamine sensing was achieved in a selective and sensitive way by the proposed nanosensor, where in the existence of different interfering compounds such as uric acid and ascorbic acid, DA showed the highest inhibition of TMB oxidation. Meanwhile, the nanosensor displayed a detection limit as low as 5.2 nM for DA with good linearity over a wide linear

range of 0-100 µM. The practical applicability of the designed nanosensor for dopamine sensing was successfully evaluated in beef meat. Hence, this method provided further insights for utilizing metal-based nanomaterials in biomedical and clinical diagnostic applications.

3.2.5. References:

[1] G.-C. Yen, C.-L. Hsieh, Antioxidant effects of dopamine and related compounds, Biosci. Biotechnol. Biochem. 61 (1997) 1646-1649.

[2] S.K. Kailasa, J.R. Koduru, M.L. Desai, T.J. Park, R.K. Singhal, H. Basu, Recent progress on surface chemistry of plasmonic metal nanoparticles for colorimetric assay of drugs in pharmaceutical and biological samples, TrAC, Trends Anal. Chem. 105 (2018) 106-120.

[3] J. Liu, L. Yuan, X. Dong, Recent advances in analytical techniques for the determination of dopamine, Int. J. Chem. Stud. 3 (2015) 39-45.

[4] C. Zhao, Y. Liu, Y. Li, Colorimetric and Fluorometric Assays for Dopamine with a Wide Concentration Range Based on Fe-MIL-88NH$_2$ Metal-organic Framework, Anal. Sci. 31 (2015) 1035-1039.

[5] Y. Tao, Y. Lin, J. Ren, X. Qu, A dual fluorometric and colorimetric sensor for dopamine based on BSA-stabilized Aunanoclusters, Biosens. Bioelectron. 42 (2013) 41-46.

[6] L. Zhihua, Z. Xucheng, W. Kun, Z. Xiaobo, S. Jiyong, H. Xiaowei, et al., A novel sensor for determination of dopamine in meat based on ZnO-decorated reduced graphene oxide composites, Innovative Food Sci. Emerg. Technol. 31 (2015) 196-203.

[7] H.-X. Zhao, H. Mu, Y.-H. Bai, H. Yu, Y.-M. Hu, A rapid method for the determination of dopamine in porcine muscle by pre-column derivatization and HPLC with fluorescence detection, J. Pharm. Anal. 1 (2011) 208-212.

[8] G.E. De Benedetto, D. Fico, A. Pennetta, C. Malitesta, G. Nicolardi, D.D. Lofrumento, et al., A rapid and simple method for the determination of 3,4-dihydroxyphenylacetic acid, norepinephrine, dopamine, and serotonin in mouse brain homogenate by HPLC with fluorimetric detection, J. Pharm. Biomed. Anal. 98 (2014) 266-270.

[9] X. Wang, Y. Ma, X. Yao, J. Wang, M. Yin, Determination of dopamine in rat less differentiated pheochromocytoma cells by capillary electrophoresis with a palladium nanoparticles microdisk electrode, RSC Adv. 3 (2013) 24605-24611.

[10] R. Cui, Y.-P. Gu, L. Bao, J.-Y. Zhao, B.-P. Qi, Z.-L. Zhang, et al., Near-infrared electrogenerated chemiluminescence of ultrasmall Ag2Se quantum dots for the detection of dopamine, Anal. Chem. 84 (2012) 8932-8935.

[11] H. Fang, M.L. Pajski, A.E. Ross, B.J. Venton, Quantitation of dopamine, serotonin and adenosine content in a tissue punch from a brain slice using capillary electrophoresis with fast-scan cyclic voltammetry detection, Anal. Methods 5 (2013) 2704-2711.

[12] Y. Zhou, M. He, C. Huang, S. Dong, J. Zheng, A novel and simple biosensor based on poly (indoleacetic acid) film and its application for simultaneous electrochemical determination of dopamine and epinephrine in the presence of ascorbic acid, J. Solid State Electrochem. 16 (2012) 2203-2210.

[13] B. Li, Y. Zhou, W. Wu, M. Liu, S. Mei, Y. Zhou, et al., Highly selective and sensitive determination of dopamine by the novel molecularly imprinted poly (nicotinamide)/CuO nanoparticles modified electrode, Biosens. Bioelectron. 67 (2015) 121-128.

[14] Y.-R. Kim, S. Bong, Y.-J. Kang, Y. Yang, R.K. Mahajan, J.S. Kim, et al., Electrochemical detection of dopamine in the presence of ascorbic acid using graphene modified electrodes, Biosens. Bioelectron. 25 (2010) 2366-2369.

[15] A. Hermans, Fabrication and applications of dopamine-sensitive electrodes: The University of North Carolina at Chapel Hill; 2007.

[16] G.-C. Yen, P.-D. Duh, H.-L. Tsai, Antioxidant and pro-oxidant properties of ascorbic acid and gallic acid, Food Chem. 79 (2002) 307-313.

[17] J. Yang, J.R. Strickler, S. Gunasekaran, Indium tin oxide-coated glass modified with reduced graphene oxide sheets and gold nanoparticles as disposable working electrodes for dopamine sensing in meat samples, Nanoscale 4 (2012) 4594-4602.

[18] Y. Lin, J. Ren, X. Qu, Catalytically active nanomaterials: a promising candidate for artificial enzymes, Acc. Chem. Res. 47 (2014) 1097-1105.

[19] X. Wang, Y. Hu, H. Wei, Nanozymes in bionanotechnology: from sensing to therapeutics and beyond, Inorg. Chem. Front. 3 (2016) 41-60.

[20] H. Su, B. Sun, L. Chen, Z. Xu, S. Ai, Colorimetric sensing of dopamine based on the aggregation of gold nanoparticles induced by copper ions, Anal. Methods 4 (2012) 3981-3986.

[21] Y. Wang, L. Yang, Y. Liu, Q. Zhao, F. Ding, P. Zou, et al., Colorimetric determination of dopamine by exploiting the enhanced oxidase mimicking activity of hierarchical $NiCo_2S_4$-rGO composites, Microchim. Acta 185 (2018) 496.

[22] M. Ivanova, E.D. Grayfer, E.E. Plotnikova, L.S. Kibis, G. Darabdhara, P.K. Boruah, et al., Pt-Decorated Boron Nitride Nanosheets as Artificial Nanozymes for Detection of Dopamine, ACS Appl. Mater. Interfaces 11 (2019) 22102-22112.

[23] J.-J. Feng, H. Guo, Y.-F. Li, Y.-H. Wang, W.-Y. Chen, A.-J. Wang, Single molecular functionalized gold nanoparticles for hydrogen-bonding recognition and colorimetric detection of dopamine with high sensitivity and selectivity, ACS Appl. Mater. Interfaces 5 (2013) 1226-1231.

[24] S. Dutta, C. Ray, S. Mallick, S. Sarkar, R. Sahoo, Y. Negishi, et al., A gel-based approach to design hierarchical CuS decorated reduced graphene oxide nanosheets for enhanced peroxidase-like activity leading to colorimetric detection of dopamine, J. Phys. Chem. C 119 (2015) 23790-23800.

[25] J. Gao, H. Liu, L. Pang, K. Guo, J. Li, Biocatalyst and Colorimetric/Fluorescent Dual Biosensors of H_2O_2 Constructed via Hemoglobin–$Cu_3(PO_4)_2$ Organic/Inorganic Hybrid Nanoflowers, ACS Appl. Mater. Interfaces 10 (2018) 30441-30450.

[26] C. Wang, J. Gao, Y. Cao, H. Tan, Colorimetric logic gate for alkaline phosphatase based on copper (II)-based metal-organic frameworks with peroxidase-like activity, Anal. Chim. Acta. 1004 (2018) 74-81.

[27] Q. Wu, L. He, Z.W. Jiang, Y. Li, Z.M. Cao, C.Z. Huang, et al., CuO nanoparticles derived from metal-organic gel with excellent electrocatalytic and peroxidase-mimicking activities for glucose and cholesterol detection, Biosens. Bioelectron. (2019) 111704.

[28] S. Goel, F. Chen, W. Cai, Synthesis and biomedical applications of copper sulfide nanoparticles: from sensors to theranostics, Small 10 (2014) 631-645.

[29] Y. Zhang, Y.-N. Wang, X.-T. Sun, L. Chen, Z.-R. Xu, Boron nitride nanosheet/CuS nanocomposites as mimetic peroxidase for sensitive colorimetric detection of cholesterol, Sens. Actuators, B 246 (2017) 118-126.

[30] A. Swaidan, P. Borthakur, P.K. Boruah, M.R. Das, A. Barras, S. Hamieh, et al., A facile preparation of CuS-BSA nanocomposite as enzyme mimics: Application for selective and sensitive sensing of Cr (VI) ions, Sens. Actuators, B 294 (2019) 253-262.

[31] A.K. Dutta, S. Das, S. Samanta, P.K. Samanta, B. Adhikary, P. Biswas, CuS nanoparticles as a mimic peroxidase for colorimetric estimation of human blood glucose level, Talanta 107 (2013) 361-367.

[32] W. Xue, T. Cheng-Ling, L. Jia-Jun, H.-Z. Zhang, W. Jian, Ultra-small CuS nanoparticles as peroxidase mimetics for sensitive and colorimetric detection of uric acid in human serum, Chin. J. Anal. Chem. 46 (2018) e1825-e1831.

[33] X. Yu, C. Qian, X. Wang, Microbiological precipitation, morphology and thermal behavior of barium hydrogen phosphate, J. Chil. Chem. Soc. 60 (2015) 2885-2887.

[34] L. Liang, X. Fei, Y. Li, J. Tian, L. Xu, X. Wang, et al., Hierarchical assembly of enzyme-inorganic composite materials with extremely high enzyme activity, RSC Adv. 5 (2015) 96997-97002.

[35] X. Wen, H. Zhang, Photoelectrochemical Properties of $CuS-GeO_2-TiO_2$ Composite Coating Electrode, PloS one 11 (2016) e0152862.

[36] J. Grdadolnik, Y. Maréchal, Bovine serum albumin observed by infrared spectrometry. I. Methodology, structural investigation, and water uptake, Biopolymers: Original Research on Biomolecules 62 (2001) 40-53.

[37] H. Yan, J. Chen, Y. Li, Y. Bai, Y. Wu, Z. Sheng, et al., Ultrasmall hybrid protein–copper sulfide nanoparticles for targeted photoacoustic imaging of orthotopic hepatocellular carcinoma with a high signal-to-noise ratio, Biomater. Sci. 7 (2019) 92-103.

[38] A.C. Poulose, S. Veeranarayanan, M.S. Mohamed, R.R. Aburto, T. Mitcham, R.R. Bouchard, et al., Multifunctional Cu_2-x Te Nanocubes Mediated Combination Therapy for Multi-Drug Resistant MDA MB 453, Sci. Rep. 6 (2016) 35961.

[39] C. Ye, M.Q. Wang, L.J. Li, H.Q. Luo, N.B. Li, Fabrication of Pt/Cu 3 (PO 4) 2 ultrathin nanosheet heterostructure for photoelectrochemical microRNA sensing using novel G-wire-enhanced strategy, Nanoscale 9 (2017) 7526-7532.

[40] C.-J. Chang, Y.-H. Wei, W.-S. Kuo, Free-standing CuS–ZnS decorated carbon nanotube films as immobilized photocatalysts for hydrogen production, Int. J. Hydrogen Energy (2018). DOI: 10.1016/j.ijhydene.2018.04.229

[41] S. Hu, Z. Chen, X. Guo, Inhibition Effect of Three-Dimensional (3D) Nanostructures on the Corrosion Resistance of 1-Dodecanethiol Self-Assembled Monolayer on Copper in NaCl Solution, Materials 11 (2018) 1225.

[42] A. Slivka, G. Cohen, Hydroxyl radical attack on dopamine, J. Biol. Chem. 260 (1985) 15466-15472.

[44] L. Gao, J. Zhuang, L. Nie, J. Zhang, Y. Zhang, N. Gu, et al., Intrinsic peroxidase-like activity of ferromagnetic nanoparticles, Nature Nanotechnol. 2 (2007) 577.

[45] Z. Tian, J. Li, Z. Zhang, W. Gao, X. Zhou, Y. Qu, Highly sensitive and robust peroxidase-like activity of porous nanorods of ceria and their application for breast cancer detection, Biomaterials 59 (2015) 116-124.

[46] S. Luo, Y. Liu, H. Rao, Y. Wang, X. Wang, Fluorescence and magnetic nanocomposite $Fe_3O_4@SiO_2@Au$ MNPs as peroxidase mimetics for glucose detection, Anal. Biochem. 538 (2017) 26-33.

CHAPTER 4

Enhanced antibacterial activity of CuS-BSA/Lysozyme under NIR irradiation

4.1.   Introduction

Infection by pathogenic bacteria represents a serious threat to human health. Currently, the use of antibacterial agents such as antibiotics remained the choice of interest, where mortality and morbidity have been reduced since the 1940s due to the commercial use of antibiotics [1]. Antibiotics could be bactericidal or bacteriostatic, where the former means they can induce a killing effect, and the latter means they can slow down the growth of pathogens. Although antibiotics showed a key role in fighting bacterial infections, yet, their maltreatment, as well their excessive and improper use have promoted the development of multidrug resistant bacteria, which causes many adverse side effects on the long term [2]. Furthermore, most bacteria form clusters of cells by producing a protective polysaccharide matrix and acidic microbial environment in addition to a variety of enzymes [3-5]. These densely packed microbial communities are referred to as biofilms, and compared to planktonic bacteria, biofilms are more resistant to antibiotics and hard to eradicate [6, 7].

Biofilm formation started when planktonic bacterial cells attach and adhere to surfaces, as illustrated in **Figure 1**, followed by bacterial aggregation and subsequent growth and division. The last step is characterized by the development of biofilm environment; however, a new biofilm population can be formed in regard to the detachment of micro-colonies. Biofilm formation or ''biofouling'' become a major problem in food processing, biomedicine, and water purification systems.

The emergence of antibiotic resistant bacteria and biofilm formation coupled with low rate development of new antibiotics have inspired the development of effective antibacterial treatment methodologies, which become more and more interesting over the years, under which bacteria lose the ability to develop resistance.
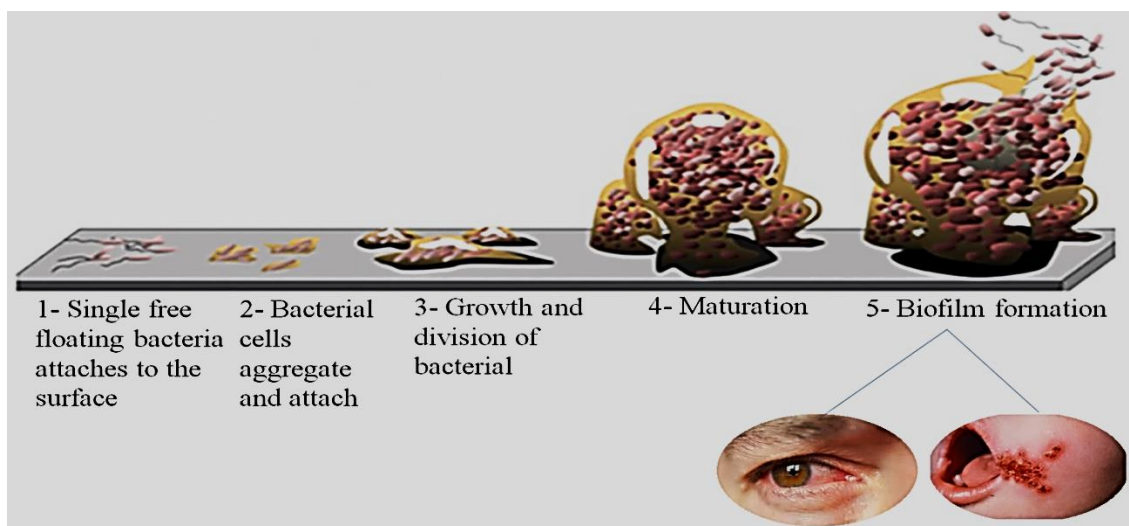
Figure 1: Biofilm formation and development of infection [8].

Compared to synthetic antibiotics [9], natural antibacterial agents such as lysozyme, have gained much more attention due to their biocompatibility and biodegradability [10]. Lysozyme, a glycoside hydrolase enzyme, is an antibacterial enzyme against food poisoning bacteria [11]. The wide spectrum of lysozyme makes it a promising platform in pharmaceuticals, food preservation and biomedical applications [12]. Lysozyme, often named as "body's own antibiotic" and reported in 1992, was well-known in inhibiting Gram positive bacterial strains by damaging the peptidoglycan in bacterial cell wall through hydrolyzing the 1,4-β-linkage between *N*-acetyl- muramic acid and *N*-acetyl-d-glucosamine [13, 14]. In contrast, lysozyme was shown to be less effective towards Gram negative strains due to the protective lipopolysaccharide (LPS) layer on the cell wall of such bacteria [15]. Despite the myriad applications of this antibiotic, natural enzymes are prone to various drawbacks, thus the low stability of lysozyme and its weak binding affinity to bacterial membrane, as well its denaturation ability restrict its research interest [16].

To address these issues, recent advances in nanotechnology and materials science have contributed to the expansion of nanomaterials as antibacterial agents or antibiotic carriers. However, the synthesis of such nanomaterials may require tedious methodologies or involve the use of toxic chemical compounds. Thus, the search for effective, safe and robust nanomaterials as alternatives to traditional antibiotic therapy becomes a growing research interest worldwide. In this regard, lysozyme can be prepared in microcapsule forms or integrated with other antibiotics to enhance its activity [17-19]; these approaches are very promising to ensure the efficacy of the enzyme. It has been also reported that coating of lysozyme with polymers or polysaccharides such as sucrose, poly-γ-glutamic acid and chitosan

improves lysozyme quality, and its long-term stability, but also enhances its bactericidal activity [20-22]. Lysozyme immobilization or loading on nanoparticles such as carbon nanotubes [23] and ZnO nanoparticles [24] represents another strategy which broadens the antimicrobial spectrum of lysozyme, and becomes a promising releasing vehicle for bacterial treatment. Moreover, mesoporous silica nanoparticles with their tunable structures, good biocompatibility and high loading capacity have been considered as promising drug carriers [25] for bacterial treatment [15]. These approaches have witnessed a huge development of nanomaterials for bacterial ablation and biofilm disruption.

Recent studies reported a plethora of nanomaterials with photothermal capacities as a new class of therapeutic nanoagents for selective targeting of bacteria. Among them, CuS-based nanomaterials which have emerged as a novel platform in various fields, due to their low cost, low toxicity, and unique optical, physical and chemical properties [26], were employed as antiseptic agents [25]. The most intriguing feature behind, is the strong optical absorption of CuS nanomaterials in the near-infrared (NIR) region, which makes them effective photothermal agents for antimicrobial therapy by means of local hyperthermia that minimizes the therapeutic issues of conventional antibiotics [25]. Ming-Yong et al. [27] reported the use of CuS-BSA nanoparticles as novel antibacterial agents under near infrared (NIR) irradiation. Baocheng and colleagues [28] also demonstrated the successful use of CuS-BSA NPs for *in vitro* photothermal treatment of bacterial infections. Moreover, Khan *et al.* [29] investigated the therapeutic capability of CuS NPs for antibacterial purposes through the generation of reactive oxygen species.

Encouraged by the photothermal capability of CuS nanomaterials, these nanostructures have been selected as the material of choice and utilized as smart antibiotic carriers to induce a chemical or physical damage to antibiotic resistant strains influenced by NIR light as an external stimulus, which offered new perspectives for treatment of *in vivo* microbial infections [28]. Although targeted antibiotic delivery at infected sites, good biocompatibility, low cytotoxicity, high photothermal conversion efficiency, high antibiotic loading capacity, delivery of high antibiotic doses, enhanced therapeutic efficacy of antibiotics and prevention of their inactivation by alteration with biological environment are the key issues to achieve desirable treatment of microbial infections, photothermal therapy (PTT) as a non-invasive tool, has emerged as an interesting approach for this purpose [30]. Thus, the fabrication of a desirable nanocarrier based on CuS nanomaterials with the aforementioned multifunctional

properties can achieve a synergistic therapy for microbial infections and demonstrate excellent therapeutic efficacy over traditional antibiotics.

Based on these advantages, and to extend the antibacterial action of lysozyme, enhance its stability, and minimize drug resistance behavior of bacteria, we opted to develop a PPT agent loaded with an antibacterial lysozyme enzyme. To the best of our knowledge, there has no work reported yet on the antibacterial activity of lysozyme integrated into the negatively charged CuS-BSA NPs for complete elimination of both Gram-negative and Gram-positive bacteria using a 980 nm-NIR laser as an external physical stimulus to enhance the controlled release of lysozyme. Meanwhile, the release of lysozyme can be controlled by adjusting the laser power and duration of irradiation, where under NIR irradiation lysozyme can be detached from the nanocomposite to induce complete eradication of bacteria. These fascinating highlights are encouraging for particular treatment of infectious diseases caused by bacteria, and the use of multifunctional nanomaterials in drug delivery and biomedical applications by offering outstanding benefits over classical antibiotics.

4.2. Synthesis of CuS-BSA nanoparticles

CuS-BSA nanoparticles were prepared *via* bio-mineralization assay similar to our previously reported method with modifications. In typical experiment, 70.0 mg of BSA were dissolved in 9.0 mL MQ-water. A blue cloudy solution is observed after adding 180.0 mg of $Cu(Ac)_2$ under magnetic stirring. The solution pH was adjusted to 12 by adding 0.7 mL of an aqueous NaOH (2.0 M) solution. Then 130.0 mg of $Na_2S.xH_2O$ were added, resulting in a brown colored solution and the reaction mixture was continued for 4 h at 90 °C. CuS-BSA nanoparticles were further purified by dialysis against a 12-14 kDa molecular mass cut off dialysis membrane in MQ-water for 24 h and stored at 4 °C for later use.

4.3. Results and discussion

4.3.1. Characterization of CuS-BSA nanoparticles

The CuS-BSA NPs inspected in this study were synthesized using a facile method with 0.1:0.0001 CuS/BSA molar ratio and characterized by various techniques.

The Raman spectrum of CuS-BSA (**Fig. 1**) shows a pronounced peak at 480 cm^{-1}, attributed to stretching mode of Cu-S bond [31, 32] and a weak peak at ~ 270 cm^{-1} assigned to the S–S bond vibration [33]. The additional peaks correspond to amide I (1500-1800 cm^{-1}) which arises from C=O stretching, amide III (1380 cm^{-1}) ascribed to C-N stretching and N-H bending

vibrations, and amide A (3520 cm^{-1}) ascribed to N-H stretching in BSA, in addition to OH and C-O stretching modes at 2890 and 981 cm^{-1}, respectively [34]. The peak at 520 cm^{-1} corresponds to Si reference which comes from the silicon wafer onto which the CuS-BSA was deposited for Raman measurements [35].
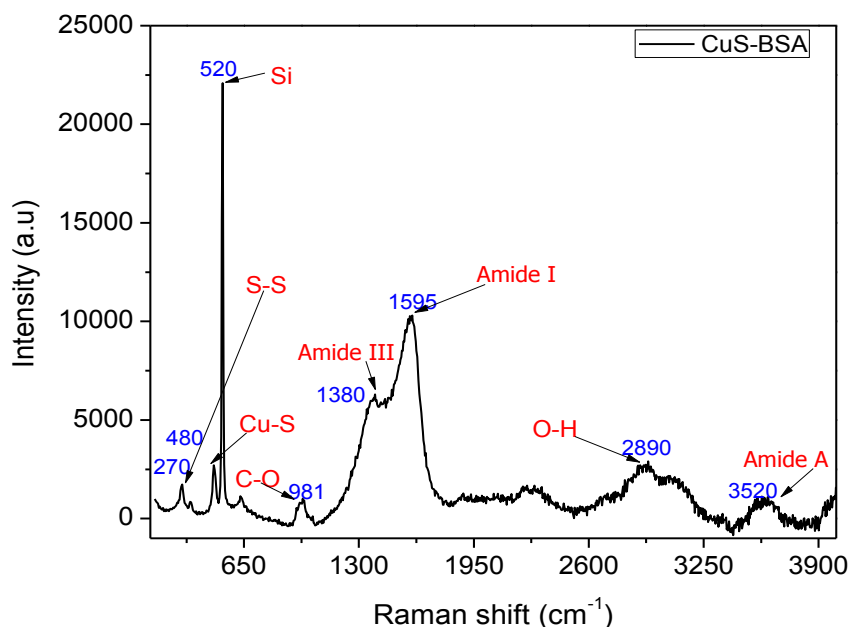

Figure 1: Raman spectrum of CuS-BSA NPs.

The chemical composition and structure of CuS-BSA NPs were analyzed by X-ray diffraction (XRD). As shown in **Figure 2**, the diffraction peaks in the XRD pattern of CuS-BSA matches well the JCPDS No.06-0464 of covellite CuS (space group 194, P63/ mmc). The characteristic peaks of CuS NPs located at 2θ value of 27.96^{o}, 29.56^{o}, 32.13^{o}, 33.02^{o}, 39.12^{o}, 48.29^{o}, and 53.00^{o} [36-39] corresponding to the crystalline planes (101), (102), (103), (006), (106), (110), and (114) with d-spacing value 3.18, 3.01, 2.78, 2.71, 2.30, 1.88, 1.72 Å, respectively.

The average crystallite size was calculated by the Debye-Scherrer equation [40]:

$$D = \frac{k\lambda}{\beta \, Cos\theta} \qquad (1)$$

Where *D* corresponds to the crystallite size, *k* is the geometrical factor (0.9 for spherical crystals), λ represents the wavelength of incident radiation (1.54), β illustrates the full width at half maximum (FWHM in radians), and θ is the Bragg angle (radians). By utilizing the FWHM of the (110) crystalline plane, D was calculated to be 9.59 nm.
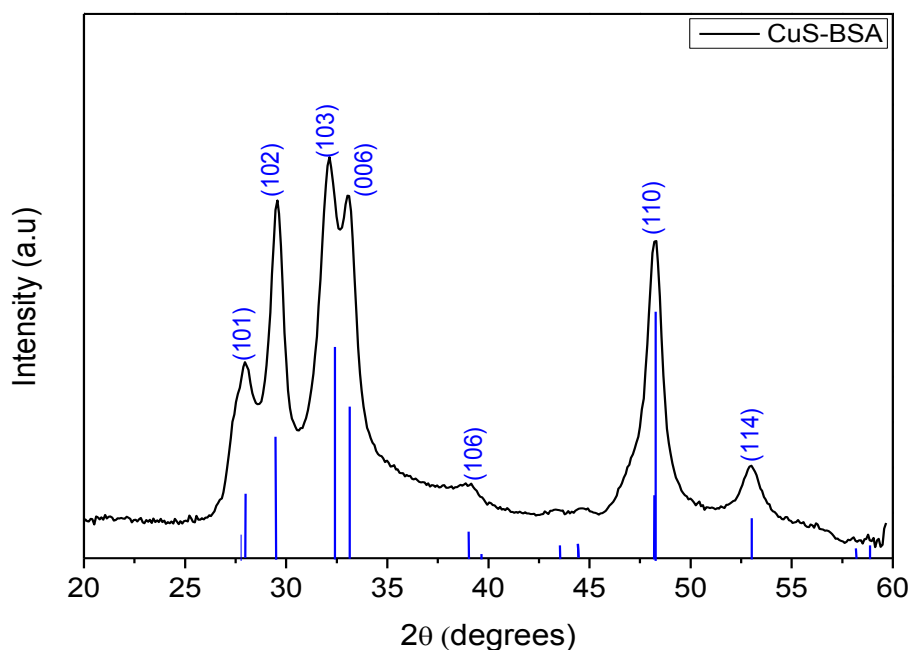
Figure 2: High resolution XRD pattern of CuS-BSA NPs.

X-ray photoelectron spectroscopy (XPS) was used to determine the chemical composition, purity and valence states of CuS-BSA NPs. The XPS wide scan of CuS-BSA **(Fig. 3a)** indicates the presence of C_{1s} (284.6 eV), N_{1s} (399.2 eV), O_{1s} (531.1 eV), Cu_{2p} (933 eV and 952.8 eV) and S_{2p} (162.34 eV) with atomic concentrations 50.48%, 10.7%, 30.22%, 6.75% and 1.84%, respectively, in full accordance with the composition of the material. The high resolution C_{1s} XPS spectrum **(Fig. 3b)** can be fitted with several components at binding energies of 284.27, 285.5 and 287.5 eV corresponding to C-C/C=C, C-N/C-O and C=O groups, respectively [41, 42]. The O_{1s} high resolution spectrum **(Fig. 3c)** can be fitted with one component at 531.1 eV assigned to oxygen in C=O and O-H groups. The high resolution N_{1s} spectrum **(Fig. 3d)** can be deconvoluted into C-N (399.2 eV) and C=N (401.6eV) of BSA [43, 44]. Cu_{2p} high resolution XPS spectrum (**Fig. 3e)** illustrates the deconvoluted peaks at 9334 and 952.8 eV corresponding to $Cu_{2p3/2}$ and $Cu_{2p1/2}$, respectively. The characteristic satellite peaks observed at ~942.8 and 962.0 eV indicate the presence of Cu^{2+} oxidation state of CuS [45]. The binding energy peaks at 162.3 and 168.4 eV in the S_{2p} spectrum **(Fig. 3f)** correspond to $S_{2p3/2}$ and $S_{2p1/2}$, respectively [46].
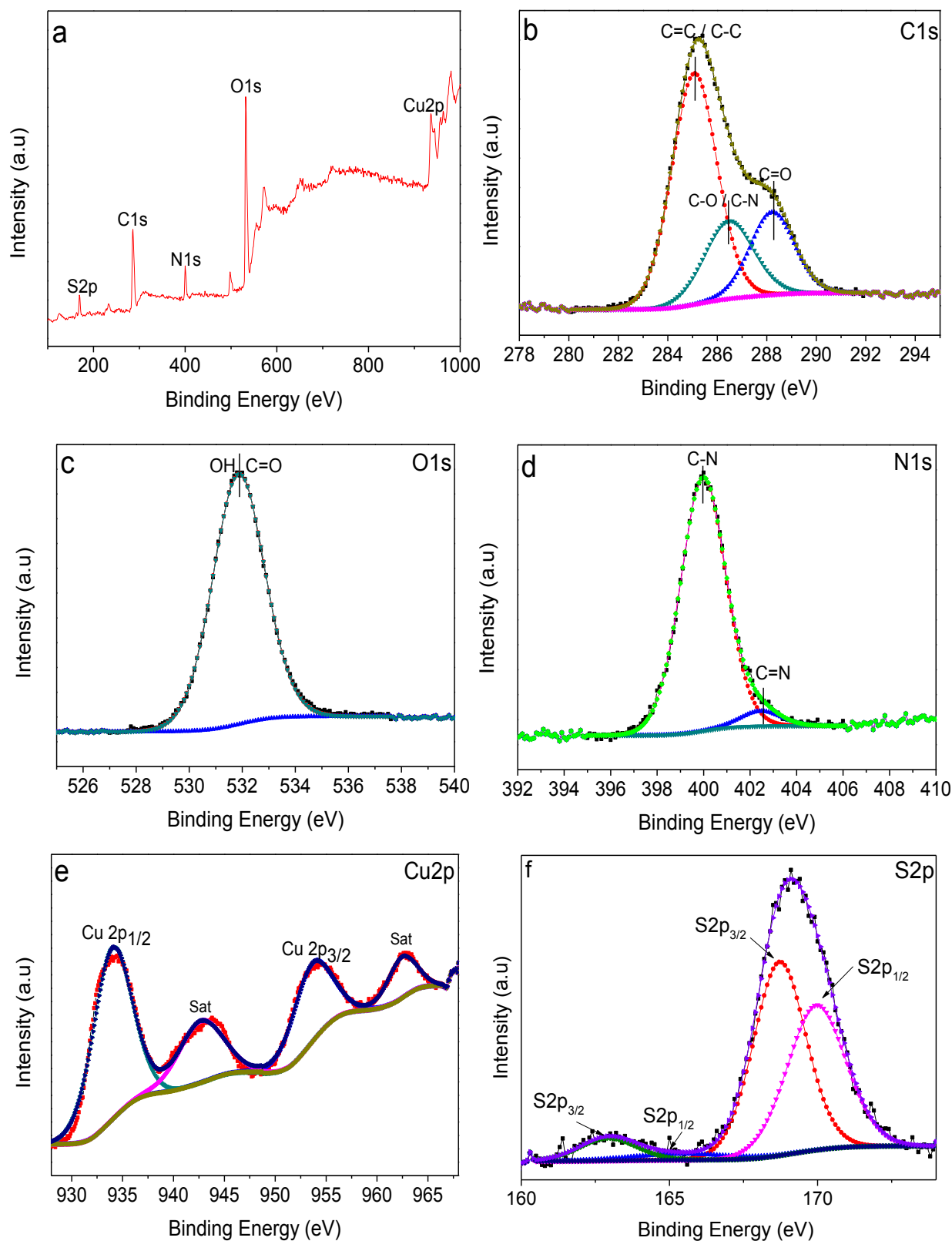
Figure 3: XPS survey spectrum (a), and high resolution XPS spectra of C_{1s} (b), O_{1s} (c), N_{1s} (d), Cu_{2p} (e) and S_{2p} (f) of CuS-BSA NPs.

To qualitatively confirm the loading of lysozyme to CuS-BSA, UV-vis absorption spectra of CuS-BSA/Lysozyme were recorded along with those of CuS-BSA and lysozyme, for

comparison **(Fig. 4)**. The UV-vis absorption spectrum of CuS-BSA shows absorption in the visible region (400-600 nm) with an increase in the absorption tail in the near infrared (NIR) region, which are characteristics of CuS NPs [47]. Meanwhile, lysozyme shows a typical absorption band at 279 nm [21]. In the UV-vis absorption spectrum of CuS-BSA/Lysozyme, an absorption peak at 279 nm and an NIR absorption tail are the clear fingerprints of the successful loading of lysozyme on CuS-BSA NPs.
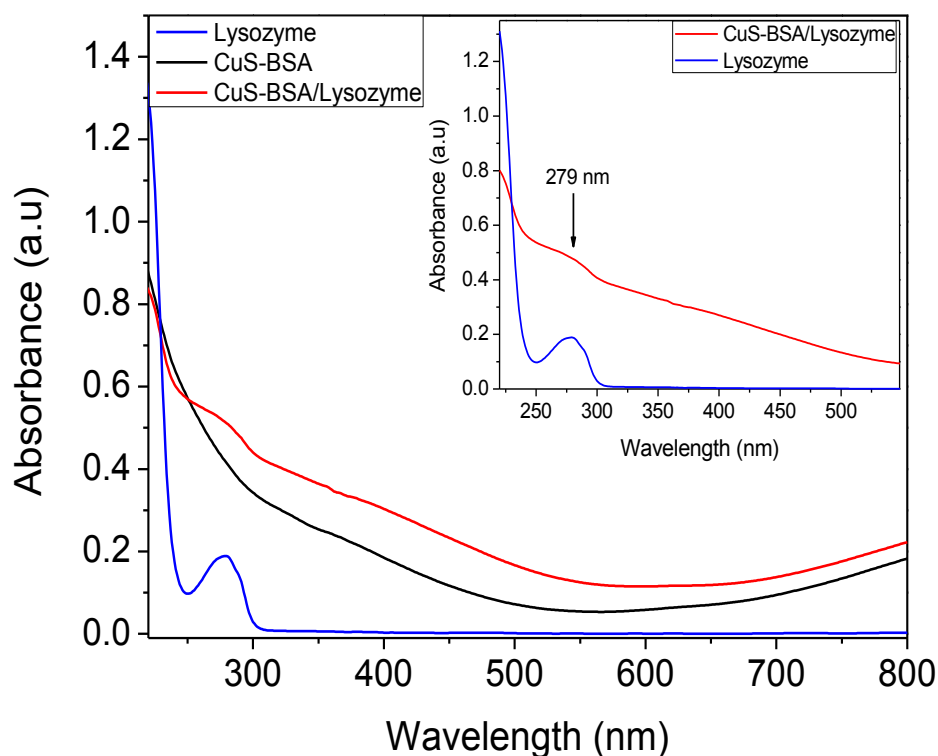
Figure 4: UV-vis absorption spectra of Lysozyme, CuS-BSA, and CuS-BSA/Lysozyme.

Lysozyme with an isoelectric point of 11.35 [20] is considered to be positively charged at physiological pH. Thus, the use of negatively charged CuS-BSA NPs can enhance its adsorption through electrostatic interaction. Thereby, the successful loading of lysozyme on CuS-BSA NPs was also confirmed through hydrodynamic size and surface charge measurements by dynamic light-scattering (DLS) and zeta potential measurements, respectively. The mean hydrodynamic average diameter of bare CuS-BSA NPs was determined to be 122 ± 8.8 nm **(Fig. 5a)** and a surface charge of -18.6 ± 2.4 mV **(Fig. 5b)**, due to the presence of hydroxyl and carboxyl groups in BSA [48]. After lysozyme loading, a surface charge of $+7.13 \pm 3.28$ mV and an average size of 158.2 nm were obtained, which indicates the adsorption of positively charged lysozyme onto negatively charged CuS-BSA surface; the

positive charge of CuS-BSA/Lysozyme is favorable for attachment to the negatively charged bacterial membrane [49].
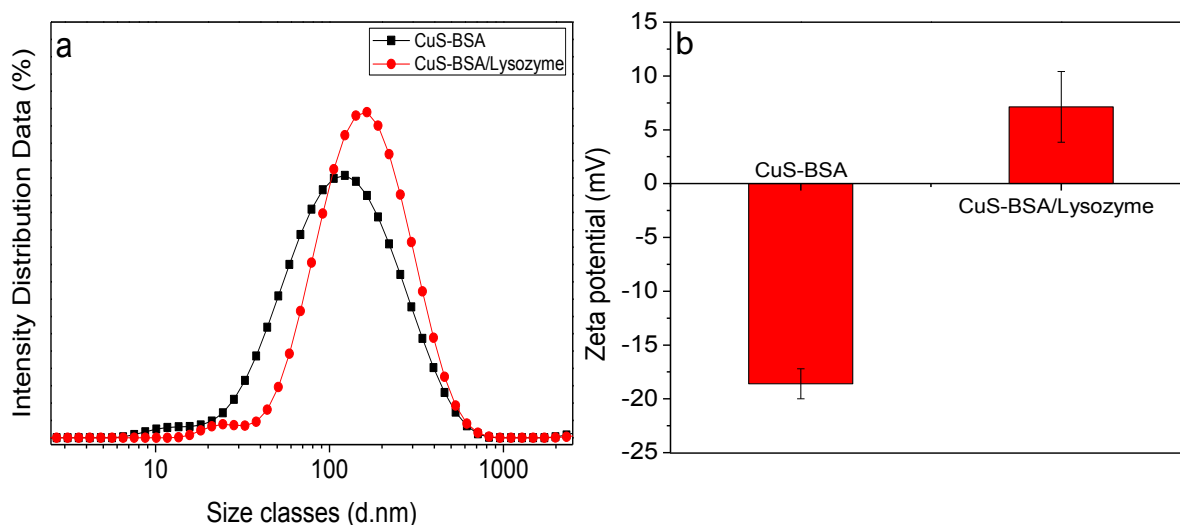
Figure 5: Dynamic light scattering (DLS) (a) and Zeta potential curves (b) of CuS-BSA and CuS-BSA/Lysozyme.

4.3.2. Lysozyme loading efficiency

Lysozyme loading onto CuS-BSA was evaluated by UV-vis absorption spectroscopy at 279 nm using an established calibration plot **(Fig. 6)**, under physiological neutral conditions in PBS (0.01 M, pH 7.4), with a maximum amount loaded of 0.76 mg/mL for 1 mg/mL CuS-BSA at 4 °C. The loading efficiency (L.E %) significantly increased with the increase of lysozyme concentration from 0.1 (L.E 43 %) to 1 mg/mL (L.E 76 %) **(Fig. 7)**. The loading efficiency was also tested at RT. As can be seen in **Figure 8**, 63.4 % of lysozyme was loaded using 1 mg/mL CuS-BSA.

Figure 6: UV-vis absorption spectra of lysozyme in PBS (0.01 M, pH 7.4) at various concentrations. Inset: The corresponding calibration curve.

Figure 7: Lysozyme loading efficiency (L.E %) by CuS-BSA in PBS (0.01 M, pH 7.4).
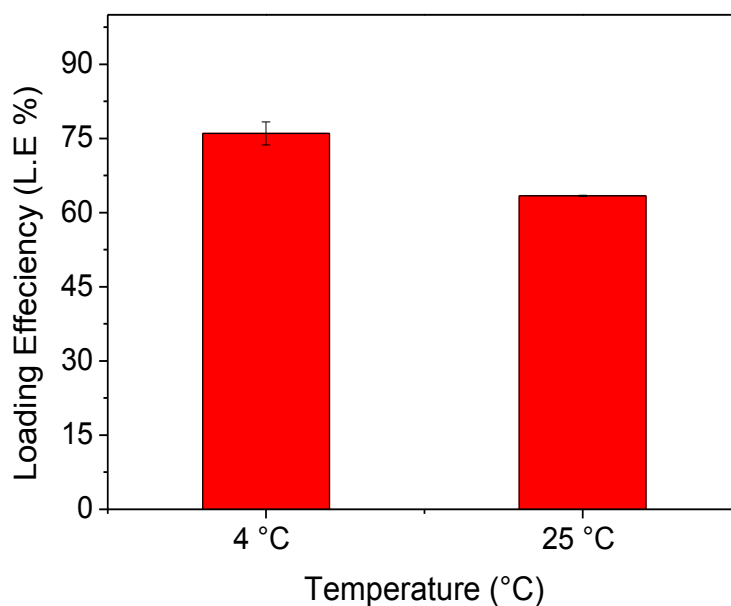
Figure 8: Lysozyme loading efficiency (L.E %) by CuS-BSA in PBS (0.01 M, pH 7.4) at different temperatures.

4.3.3. Photothermal heating performance of CuS-BSA NPs

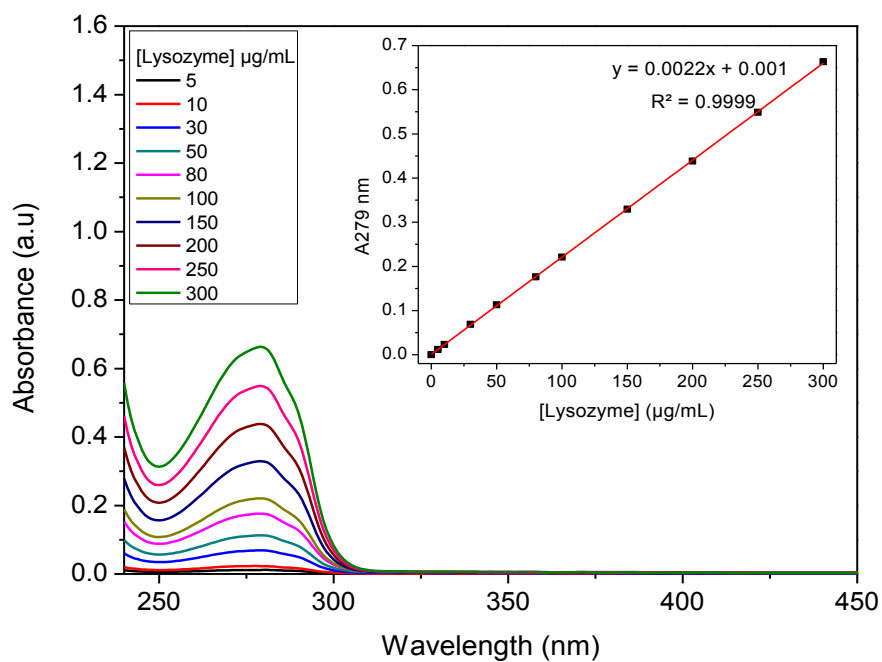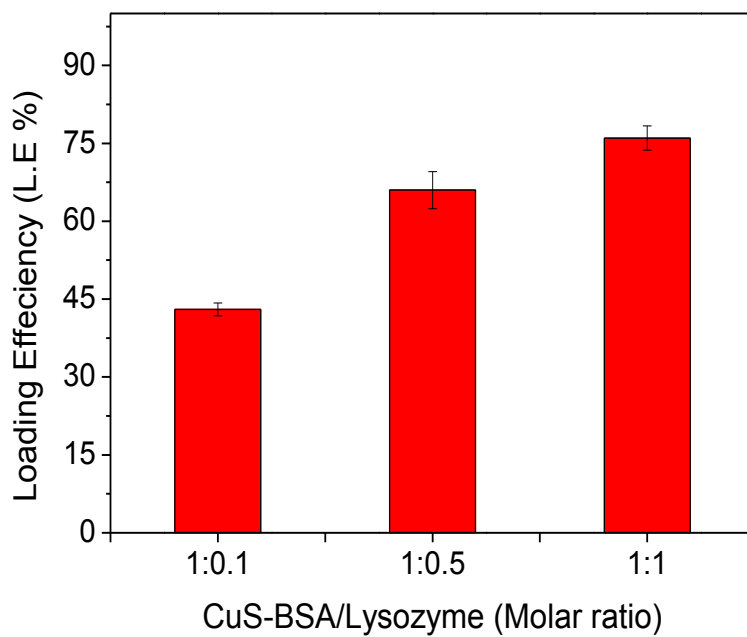CuS-BSA NPs are recognized as a strong absorping photothermal agent in the near infrared (NIR) region. Thus, the photothermal behavior of CuS-BSA and CuS-BSA/Lysozyme at various concentrations of (0-200 µg/mL in PBS) was investigated by monitoring the temperature elevation induced upon a 980 nm continuous wave NIR laser irradiation at different power densities for 3 min. Under these experimental conditions, the temperature of CuS-BSA and CuS-BSA/Lysozyme solutions increases rapidly within 3 min. **Figure 9** shows a remarkable increase in temperature with the increase of sample concentration. The highest temperatures reached are about 57 and 47 °C at the highest concentration of 200 µg/mL of CuS-BSA **(Fig. 9b)** and CuS-BSA/Lysozyme **(Fig. 9d)**, respectively, under a laser power density of 0.7 W.cm^{-2}, suggesting that the absorbed energy is rapidly converted to thermal energy. The heating rate was significantly enhanced when the laser power density was increased to 1 W.cm^{-2}, to reach 67 °C **(Fig. 9a)** and 58 °C **(Fig. 9c)** for CuS-BSA and CuS-BSA/Lysozyme, respectively.

As a control, 1 mL of PBS was subjected to irradiation under the same conditions mentioned above, where no noticeable increase in temperature was observed in the absence of nanoparticles.
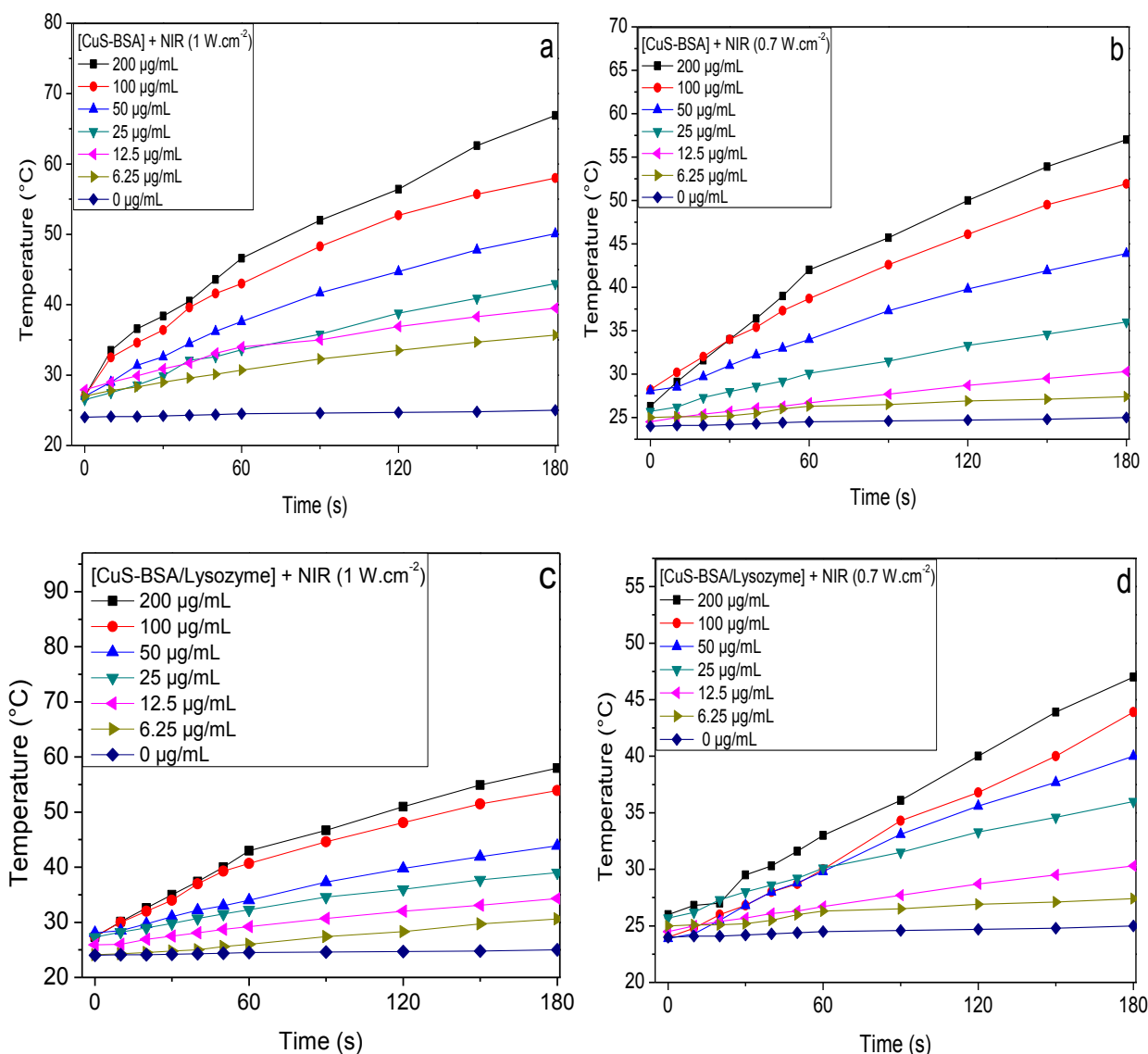
Figure 9: Photothermal heating curves of CuS-BSA and CuS-BSA/Lysozyme at various concentrations in PBS (0.01 M, pH 7.4) under NIR illumination (980 nm) using a continuous wave laser at different power densities for 3 min.

Additionally, the photothermal behavior of CuS-BSA induced by NIR-laser irradiation at 980 nm was assessed for several ON/OFF cycles. Thus, we recorded the time-dependent temperature of CuS-BSA upon NIR irradiation for 3 min (Laser on) at 0.7 W.cm^{-2}, followed by cooling at room temperature when the laser is switched off for another 3 min. This cycle was repeated four times in order to investigate the photothermal stability of the CuS-BSA nanoparticles. The results in **Figure 10** clearly indicate that the photothermal properties of CuS-BSA are not affected after 4 cycles, suggesting that the nanocarrier exhibits stable photothermal heating performance.
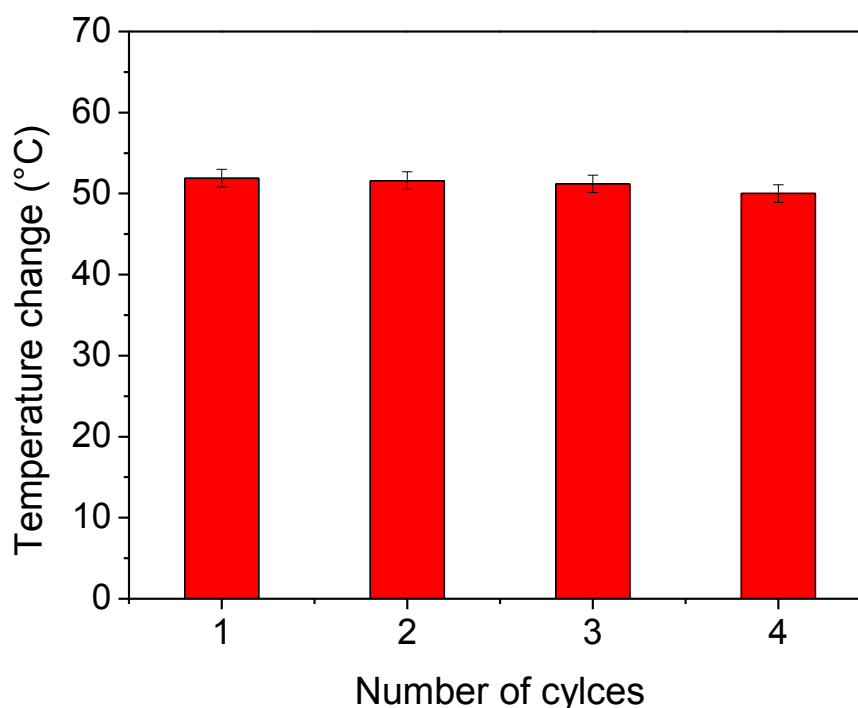
Figure 10: Temperature elevation of CuS-BSA (100 µg/mL) over four laser on/off cycles under 980-NIR laser irradiation at a power density 0.7 W.cm^{-2} for 3 min.

4.3.4. *In vitro* photothermal lysozyme release

As an efficient drug delivery carrier, CuS-BSA should acquire a release property. Therefore, lysozyme release from CuS-BSA was investigated by dispersing 0.1 mL of CuS BSA/Lysozyme (1 mg/mL with 0.76 mg/mL Lysozyme loaded concentration) in 1 mL PBS (0.01 M, pH 7.4) under NIR illumination at two different laser power densities (1 or 0.7 W.cm^{-2}) for 3 min. Under these conditions, 37.2 µg/mL of lysozyme are released at 0.7 W.cm^{-2} (48.98 %). Meanwhile, the release of lysozyme can be controlled by adjusting the laser power. Thus, with the increase of the laser power density to 1 W.cm^{-2}, lysozyme release rate is slightly enhanced to reach 39.7 µg/mL (52.36 %) within 3 min irradiation (**Fig. 11**). These results suggest that lysozyme exhibits a temperature responsive release profile, where at a higher laser power density, CuS-BSA achieved better heating performance, which enhances the detachment of lysozyme due to the change in binding energy by NIR-mediated local heat that reduces the interaction between lysozyme and CuS-BSA.
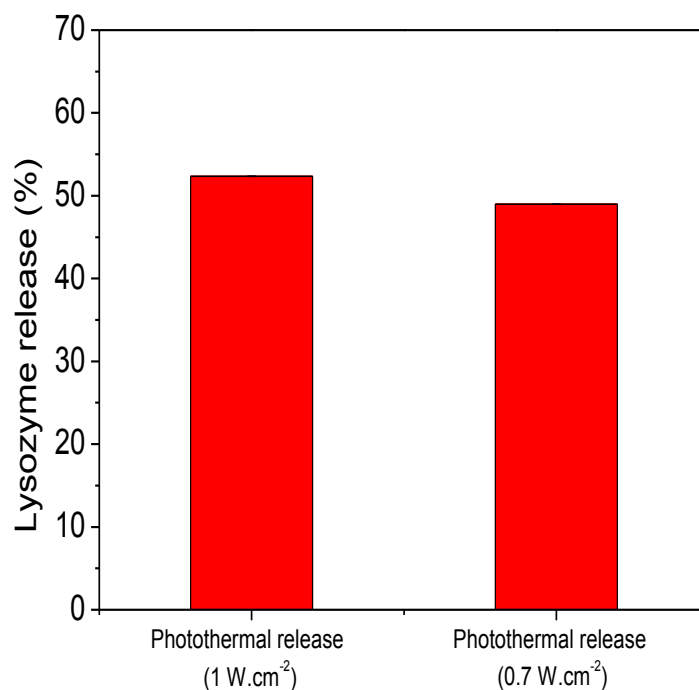
Figure 11: Photothermal release of lysozyme (%) from CuS-BSA (100 µg/mL) within 3 min irradiation. Experiments were performed in triplicate.

Furthermore, the passive release of lysozyme from CuS-BSA NPs was assessed by immersing 0.1 mL CuS BSA/Lysozyme (1 mg/mL with 0.76 mg/mL Lysozyme) in PBS solution (0.01 M, pH 7.4) under moderate shaking (150 rpm) at different temperatures and incubation times. Under the aforementioned conditions, only a small fraction of lysozyme detached from CuS-BSA during the first 4 h at room temperature **(Fig. 12)**. Lysozyme leakage was shown to be influenced by temperature and time of incubation, where it reaches 13.9 % and 41.6 % at RT and 37 °C, respectively. However, the passive release of lysozyme after 12 h incubation was shown to be less than the photothermal release under NIR irradiation for 3 min. This indicates that CuS-BSA NPs represent a promising therapeutic agent for drug loading and release.
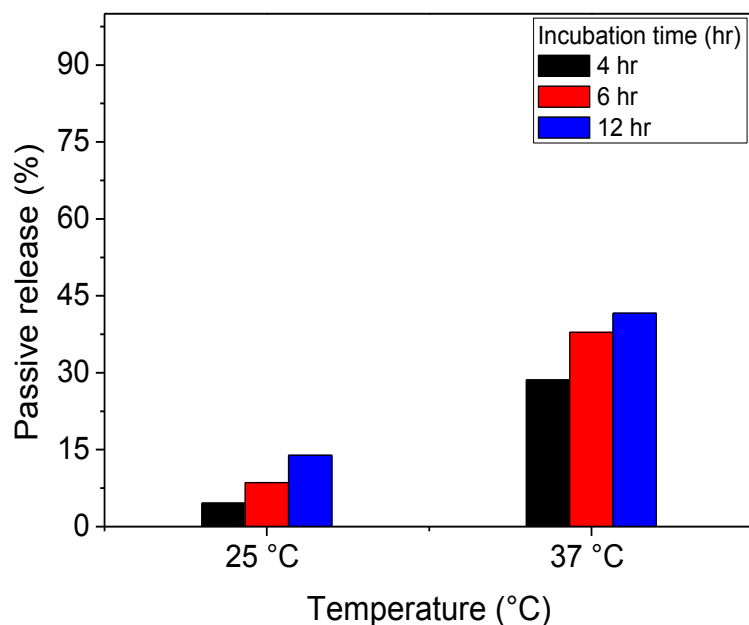
Figure 12: Passive release of lysozyme (%) from CuS-BSA (100 μg/mL) at different temperatures and incubation times.

4.3.5. Cellular toxicity and viability studies

The cell toxicity studies of CuS-BSA and CuS-BSA/Lysozyme were conducted on Hela and U87MG cells by using Uptiblue assay. The results revealed that the cell viability remained above 80% **(Fig. 13)** even at a high concentration of CuS-BSA or CuS-BSA/Lysozyme (100 μg/mL), which indicates the biocompatibility of the synthesized nanoparticles.

The cytotoxicity was also assessed under NIR irradiation. Cells were incubated with CuS-BSA and CuS-BSA/Lysozyme at increasing concentrations and subjected to irradiation at 0.7 W.cm^{-2} for 3 min. A dose-dependent toxicity was observed at 200 μg/mL, however, the cellular viability remained above 80% even at 100 μg/mL. The higher killing efficiency at 200 μg/mL was attributed to the strongest photothermal heating effect at this concentration. As a control, Hela cells were irradiated under the same conditions, where no significant decrease in viability was observed.

Similarly, CuS-BSA and CuS-BSA/Lysozyme showed significant cell growth inhibition on U87MG cells at the highest concentration (200 μg/mL) **(Fig. 14a, b)**. However, one can notice that lysozyme has a protecting effect, as the cell viability at 200 μg/mL was higher when lysozyme integrated onto CuS-BSA than CuS-BSA alone. Thus, lysozyme can be also used to enhance the biocompatibility of the nanoparticles and reduce their cytotoxicity. On the other

hand, incubation of U87MG cells with CuS-BSA and CuS-BSA/Lysozyme of various concentrations followed by irradiation (1 W.cm^{-2} and 0.7 W.cm^{-2}) for 3 min, the cellular viability decreased due to the excellent photothermal heating performance of the nanoparticles. In order to preclude the cell killing efficiency under the influence of NIR irradiation, U87MG cells were also illuminated at 0.7 W.cm^{-2} and 1 W.cm^{-2} in the absence of nanoparticles. Under both laser power densities, the cell viability remained 100 %, indicating that the tested cancer cell lines are not sensitive to NIR laser irradiation, and the obtained cell killing was attributed to the photothermal heating effect of the nanoparticles.
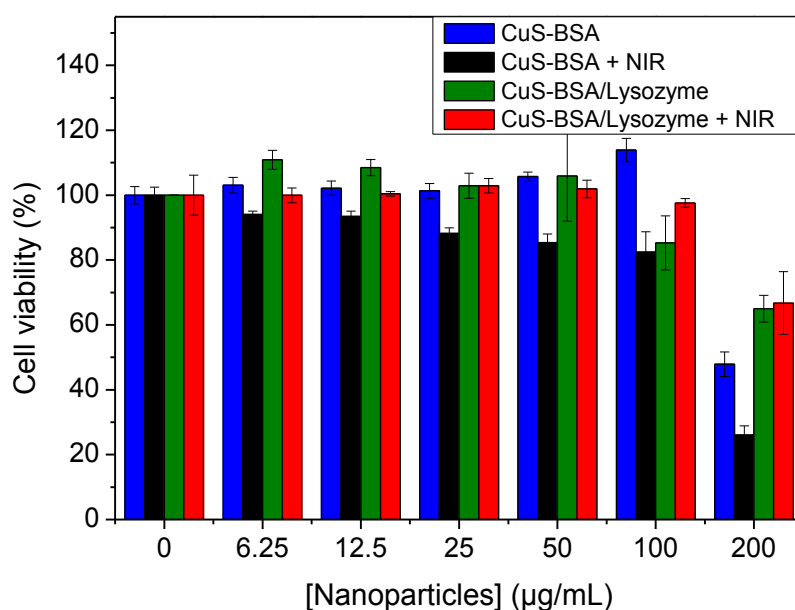
Figure 13: Cellular viability of CuS-BSA and CuS-BSA/Lysozyme at various concentrations (0-200 µg/mL) with and without irradiation (980 nm, 0.7 W.cm^{-2}, 3 min) on Hela cells.
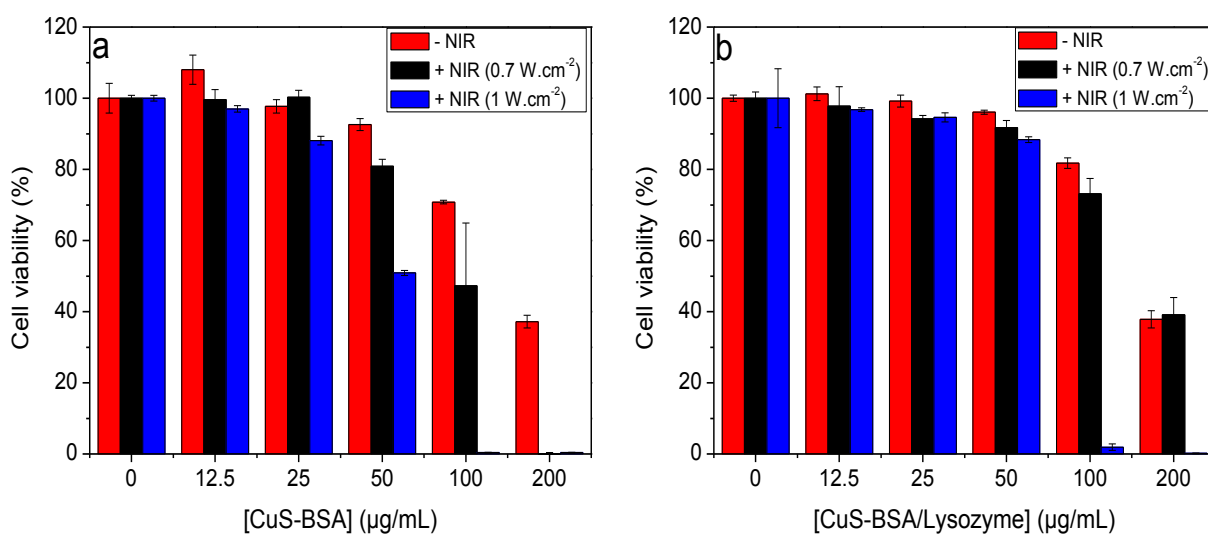
Figure 14: Cellular viability of CuS-BSA and CuS-BSA/Lysozyme at various concentrations (0-200 µg/mL) without and with NIR irradiation at various power densities (980 nm, 3 min) on U87MG cells.

4.3.6. Singlet oxygen generation under NIR illumination

CuS NPs have been reported as antibacterial agents under NIR light irradiation which can generate singlet oxygen and behave as PDT nanoagents [25]. Thereby we examined the singlet oxygen generation ability of CuS-BSA NPs under NIR illumination by 980 nm NIR laser at a power density 0.7 $W.cm^{-2}$ through monitoring the variation of 1,3-Diphenyl isobenzofuran DPBF UV-vis absorbance at 415 nm.

The reaction of DPBF with singlet oxygen generates an oxidized DPBF product (endoperoxide) [49, 50], and therefore the absorbance at 415 nm is reduced. **Figure 15** shows the variation of absorbance at 415 nm (A415 nm) as a function of irradiation time of CuS-BSA + DPBF, CuS-BSA/Lysozyme + DPBF and DPBF alone. The results revealed that in the absence of CuS-BSA, there is only a slight decrease in DPBF absorbance due to the low stability of DPBF in water. However, in the presence of CuS-BSA and CuS-BSA/Lysozyme, there is a significant decrease in absorbance due to the generation of singlet oxygen under NIR irradiation, which causes an oxidation of DPBF. With further increase in irradiation time, there is an enhanced bleach of DPBF, as witnessed by a considerable decrease of A415 nm. This indicates that CuS-BSA can be used as a potential PDT agent for the generation of $^1O_2$ under NIR illumination.
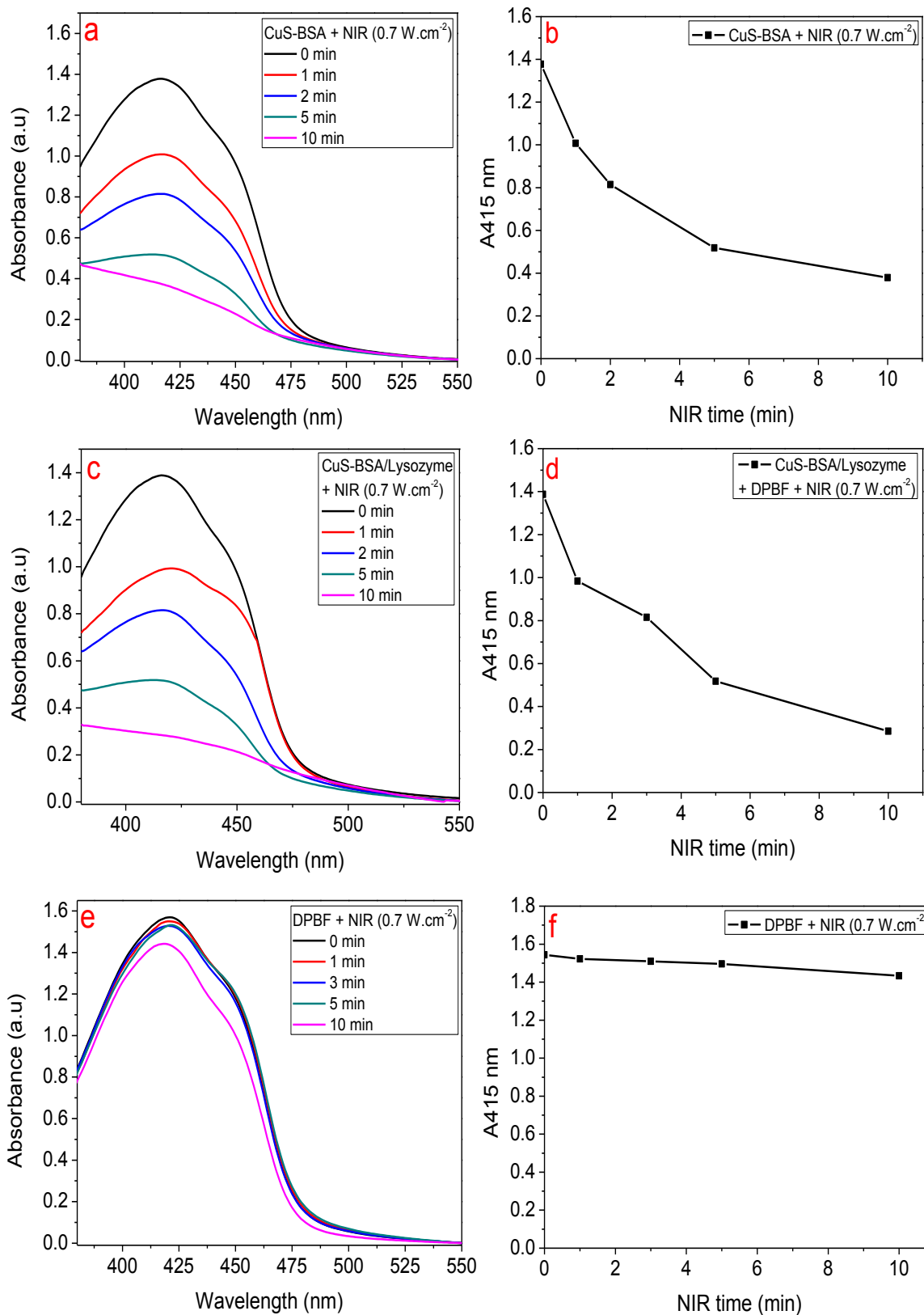
Figure 15: Time dependent DPBF quenching experiment, (a) CuS-BSA + DPBF + NIR (0.7 W.cm^{-2}), (b) DPBF + NIR (0.7 W.cm^{-2}), (c) and (d) $^1O_2$ generation efficiency upon NIR laser irradiation.

4.3.7. Antibacterial activity

The antibacterial properties of lysozyme, CuS-BSA, and CuS-BSA/Lysozyme with and without NIR irradiation were assessed on *E. coli* and *B. subtilis* as model bacterial strains.

Lysozyme is proved to be effective in inhibiting the growth of bacteria. Thus, on the basis of the optical density at 600 nm (O.D$_{600}$) **(Fig. 16)** and plating method **(Fig. 17)**, lysozyme exhibits a decrease in the viable bacterial cells on both strains with a more pronounced toxicity to Gram positive *B. subtilis* than *E. coli*. However, one can notice that illumination using NIR light does not induce any observable change in the number of viable cells, even at higher irradiation power density (1 W.cm^{-2}). This indicates that lysozyme does not possess any photothermal heating capacity, and the decrease in the number of bacterial colonies with increasing concentrations of lysozyme is attributed to the bactericidal action of this antibiotic.

The toxicity of CuS-BSA and CuS-BSA/Lysozyme NPs was also examined on *B. subtilis* and *E. coli* under various concentrations with and without NIR irradiation. As can be seen in **Fig. 18a**, CuS-BSA shows negligible toxicity to *B. subtilis* without irradiation. In contrast, upon 3 min irradiation at 0.7 W.cm^{-2}, a slight toxicity is observed at a concentration of 50 µg/mL and above, which can be explained by the photothermal heating capacity at this concentration under laser treatment (46.6°C). On the contrary, CuS-BSA/Lysozyme **(Fig. 18b)** resulted in a considerable reduction in bacterial viability. The illumination of *B. subtilis* at 0.7 W.cm^{-2} NIR laser causes complete destruction of the bacterial strain in the presence of CuS-BSA/Lysozyme at 200 µg/mL. The enhanced antibacterial action of CuS-BSA/Lysozyme can be attributed to the strongest binding affinity to the bacterial surfaces, and the use of NIR light source promoted the release of lysozyme from CuS-BSA and exposes the bacteria to large amount of lysozyme [51]. This also demonstrated that the released lysozyme can still maintain good bioactivity at higher temperature, which can effectively decompose the bacterial membrane to induce its killing efficiency. Under the aforementioned conditions, CuS-BSA NPs were less toxic to *E. coli* even under irradiation at 0.7 W.cm^{-2}. **Figures 18b** and **19b** clearly demonstrate that CuS-BSA/Lysozyme possesses stronger bacterial killing efficiency to *B. subtilis* than *E. coli* due to the difference in bacterial cell wall surfaces, as most Gram positive bacteria secretes a protein that enhances its cell wall surface viscosity and increases the adsorption of nanoparticles [27].

Furthermore, we evaluated the influence of increasing laser power density on bacterial viability. Interestingly, both *E. coli* and *B. subtilis* are completely eradicated after 3 min

irradiation at 1 W.cm^{-2} using low concentration of CuS-BSA/Lysozyme of 50 µg/mL on *B. subtilis* (**Fig. 18b**) and 100 µg/mL on *E. coli* (**Fig. 19b**) due to efficient heating effect achieved at higher laser power and enhanced lysozyme release at 1 W.cm^{-2}.

To rule out the effect of irradiation on bacteria without NPs, *E. coli* and *B. subtilis* were subjected to NIR laser treatment for 3 min at two different laser power densities, where no observable decrease in viability was detected even at a high laser power density (1 W.cm^{-2}). This indicates that the killing efficiency was ascribed to the combined effect of lysozyme antibacterial action and the heating effect of CuS-BSA under irradiation. Comparing both bacterial strains, *B. subtilis* was more sensitive under the same conditions, and the antibacterial action was found to be nanoparticle's concentration-dependent ranging from 12.5 µg/mL to 200 µg/mL.
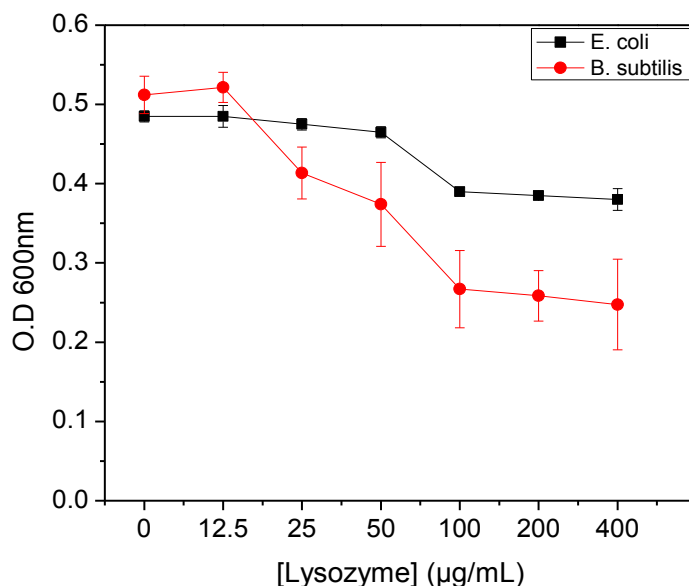
Figure 16: Change of O.D$_{600}$ in the presence of various concentrations of lysozyme (µg/mL) on *E. coli* and *B. subtilis.*
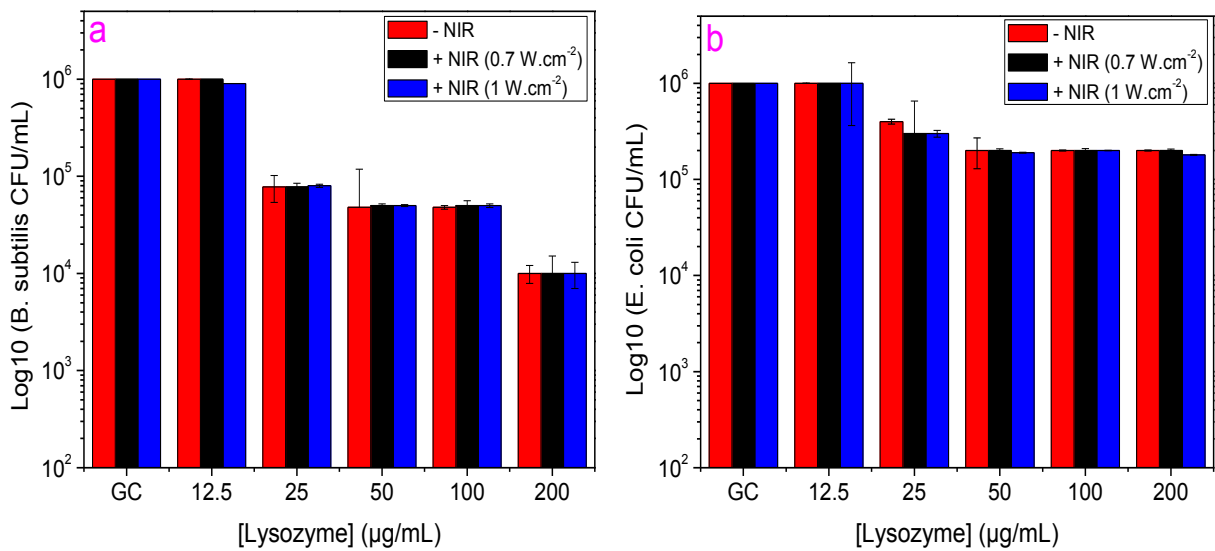
Figure 17: Antibacterial activity of Lysozyme on *B. subtilis* (a) and *E. coli* (b) using various concentrations without and with NIR irradiation (980 nm) at different laser power densities for 3 min.
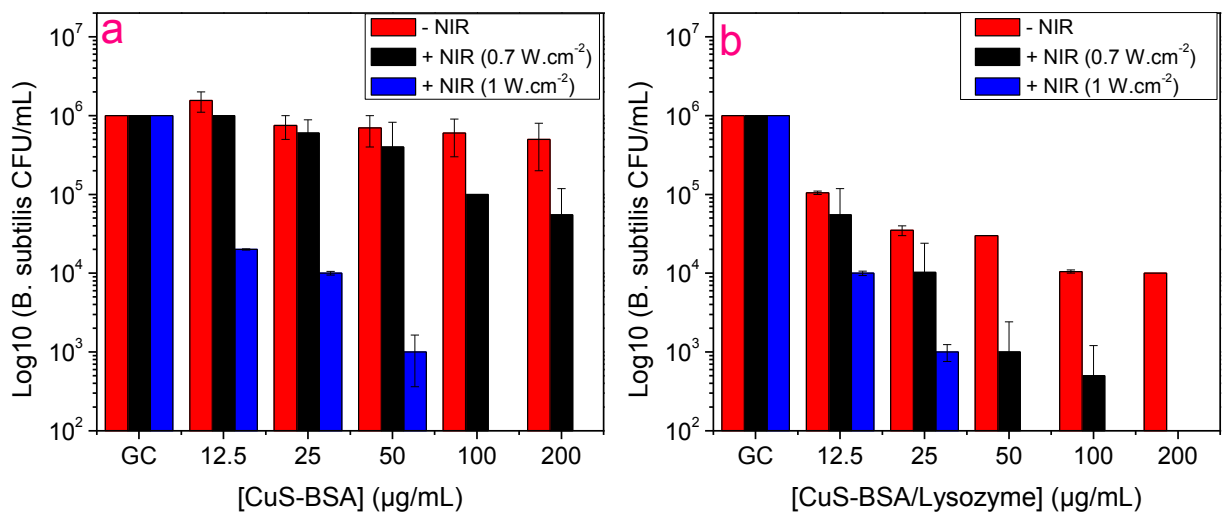
Figure 18: Antibacterial activity of CuS-BSA (a) and CuS-BSA/Lysozyme (b) on *B. subtilis* using various concentrations with and without NIR irradiation (980 nm, 3 min).
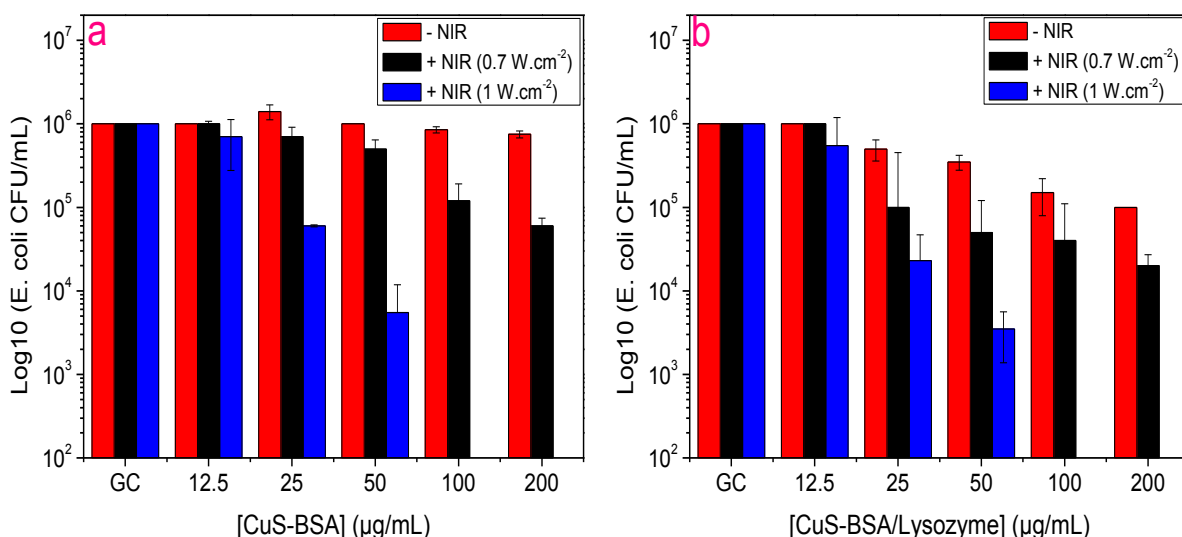
Figure 19: Antibacterial activity of CuS-BSA (a) and CuS-BSA/Lysozyme (b) on *E. coli* using various concentrations with and without NIR irradiation (980 nm, 0.7 W.cm^{-2}, 3 min).

4.4.　Conclusion

Among all the challenges regarding antibiotics resistance development and their delivery, CuS-BSA NPs, prepared *via* a simple method, proved to be a novel photothermal nanoagent and antibiotic carrier for a natural enzyme ''lysozyme''. The CuS-BSA loaded with lysozyme exhibited a rapid temperature increase under NIR irradiation at low laser power density of 0.7 W.cm^{-2} within a few min. The photothermally-triggered released enzyme demonstrated an efficient antibacterial activity against two bacterial strains (*E. coli* and *B. subtilis*) with no noticeable toxicity to mammalian cells at a high concentration (100 µg/mL), where cytotoxicity studies demonstrated that the prepared CuS-BSA/Lysozyme conjugate exhibited reduced mammalian cell inhibition for both U87MG and Hela cells, indicating that lysozyme enhances the biocompatibility of the nanoparticles. The excellent photothermal heating performance, high stability, efficient antibiotic loading capacity and release property suggested that CuS-BSA can be applied as a promising alternative for pharmaceutical and biomedical applications.

4.5. References:

[1] S. Szunerits, R. Boukherroub, Antibacterial activity of graphene-based materials, J. Mater. Chem. B 4 (2016) 6892-6912.

[2] L.-L. Li, J.-H. Xu, G.-B. Qi, X. Zhao, F. Yu, H. Wang, Core–shell supramolecular gelatin nanoparticles for adaptive and "on-demand" antibiotic delivery, ACS Nano 8 (2014) 4975-4983.

[3] H. Koo, J. Xiao, M. Klein, J. Jeon, Exopolysaccharides produced by Streptococcus mutans glucosyltransferases modulate the establishment of microcolonies within multispecies biofilms, J. Bacteriol. 192 (2010) 3024-3032.

[4] H.-C. Flemming, J. Wingender, The biofilm matrix, Nat. Rev. Microbiol. 8 (2010) 623.

[5] D. Beighton, The complex oral microflora of high-risk individuals and groups and its role in the caries process, Community Dent. Oral Epidemiol. 33 (2005) 248-255.

[6] E. Teirlinck, A. Barras, J. Liu, J.C. Fraire, T. Lajunen, R. Xiong, et al., Exploring Light-Sensitive Nanocarriers for Simultaneous Triggered Antibiotic Release and Disruption of Biofilms Upon Generation of Laser-Induced Vapor Nanobubbles, Pharmaceutics 11 (2019) 201.

[7] J. Del Pozo, R. Patel, The challenge of treating biofilm-associated bacterial infections, Clin. Pharmacol. Ther. 82 (2007) 204-209.

[8] R. Jijie, Synthesis and characterization of complex nano-structures at the interface with biological medium: Department of chemistry, University of Lille 1, France 2016.

[9] Y. Liu, J. Li, X. Cheng, X. Ren, T. Huang, Self-assembled antibacterial coating by N-halamine polyelectrolytes on a cellulose substrate, J. Mater. Chem. B 3 (2015) 1446-1454.

[10] X. Wang, W. Cao, Q. Xiang, F. Jin, X. Peng, Q. Li, et al., Silver nanoparticle and lysozyme/tannic acid layer-by-layer assembly antimicrobial multilayer on magnetic nanoparticle by an eco-friendly route, Mater. Sci. Eng. C 76 (2017) 886-896.

[11] V. Hughey, E. Johnson, Antimicrobial activity of lysozyme against bacteria involved in food spoilage and food-borne disease, Appl. Environ. Microbiol. 53 (1987) 2165-2170.

[12] L. Zheng, Y. Wan, L. Yu, D. Zhang, Lysozyme as a recognition element for monitoring of bacterial population, Talanta 146 (2016) 299-302.

[13] P. Jolles, Recent developments in the study of lysozymes, Angew. Chem. Int. Ed. 3 (1964) 28-36.

[14] S. Yuan, J. Yin, W. Jiang, B. Liang, S. Pehkonen, C. Choong, Enhancing antibacterial activity of surface-grafted chitosan with immobilized lysozyme on bioinspired stainless steel substrates, Colloids Surf. B 106 (2013) 11-21.

[15] Y. Wang, Y.A. Nor, H. Song, Y. Yang, C. Xu, M. Yu, et al., Small-sized and large-pore dendritic mesoporous silica nanoparticles enhance antimicrobial enzyme delivery, J. Mater. Chem. B 4 (2016) 2646-2653.

[16] T. Zhang, P. Zhou, Y. Zhan, X. Shi, J. Lin, Y. Du, et al., Pectin/lysozyme bilayers layer-by-layer deposited cellulose nanofibrous mats for antibacterial application, Carbohydr. Polym. 117 (2015) 687-693.

[17] C.B. Amara, N. Eghbal, P. Degraeve, A. Gharsallaoui, Using complex coacervation for lysozyme encapsulation by spray-drying, J. Food Eng. 183 (2016) 50-57.

[18] J. Jiang, C. Zhang, G.-M. Zeng, J.-L. Gong, Y.-N. Chang, B. Song, et al., The disinfection performance and mechanisms of Ag/lysozyme nanoparticles supported with montmorillonite clay, J. Hazard. Mater. 317 (2016) 416-429.

[19] M. Jing, W. Song, R. Liu, Binding of copper to lysozyme: spectroscopic, isothermal titration calorimetry and molecular docking studies, Spectrochim. Acta Part A 164 (2016) 103-109.

[20] Y. Liu, Y. Sun, Y. Xu, H. Feng, S. Fu, J. Tang, et al., Preparation and evaluation of lysozyme-loaded nanoparticles coated with poly-γ-glutamic acid and chitosan, Int. J. Biol. Macromol. 59 (2013) 201-207.

[21] T. Wu, C. Wu, S. Fu, L. Wang, C. Yuan, S. Chen, et al., Integration of lysozyme into chitosan nanoparticles for improving antibacterial activity, Carbohydr. Polym. 155 (2017) 192-200.

[22] A.K. Muszanska, H.J. Busscher, A. Herrmann, H.C. van der Mei, W. Norde, Pluronic–lysozyme conjugates as anti-adhesive and antibacterial bifunctional polymers for surface coating, Biomaterials 32 (2011) 6333-6341.

[23] D.W. Horn, G. Ao, M. Maugey, C. Zakri, P. Poulin, V.A. Davis, Dispersion State and Fiber Toughness: Antibacterial Lysozyme-Single Walled Carbon Nanotubes, Adv. Funct. Mater. 23 (2013) 6082-6090.

[24] S. Chakraborti, T. Chatterjee, P. Joshi, A. Poddar, B. Bhattacharyya, S.P. Singh, et al., Structure and activity of lysozyme on binding to ZnO nanoparticles, Langmuir 26 (2009) 3506-3513.

[25] Y. Qiao, Y. Ping, H. Zhang, B. Zhou, F. Liu, Y. Yu, et al., Laser-Activatable CuS Nanodots to Treat Multidrug-Resistant Bacteria and Release Copper Ion to Accelerate Healing of Infected Chronic Nonhealing Wounds, ACS Appl. Mater. Interfaces 11 (2019) 3809-3822.

[26] A. Prodi, F.L. Filon, F.O.E. Assessment, An Integrated Approach from Air Sampling to Skin and Surface Contamination, Nano. Biomed. Eng. 8 (2016) 91-104.

[27] J. Huang, J. Zhou, J. Zhuang, H. Gao, D. Huang, L. Wang, et al., Strong near-infrared absorbing and biocompatible CuS nanoparticles for rapid and efficient photothermal ablation of gram-positive and-negative bacteria, ACS Appl. Mater. Interfaces 9 (2017) 36606-36614.

[28] Y. Zhao, Q. Cai, W. Qi, Y. Jia, T. Xiong, Z. Fan, et al., BSA-CuS Nanoparticles for Photothermal Therapy of Diabetic Wound Infection *In Vivo*, ChemistrySelect 3 (2018) 9510-9516.

[29] K.B.A. Ahmed, V. Anbazhagan, Synthesis of copper sulfide nanoparticles and evaluation of in vitro antibacterial activity and in vivo therapeutic effect in bacteria-infected zebrafish, RSC Adv. 7 (2017) 36644-36652.

[30] J.-W. Xu, K. Yao, Z.-K. Xu, Nanomaterials with a photothermal effect for antibacterial activities: an overview, Nanoscale 11 (2019) 8680-8691.

[31] H. Yang, H. Liang, Y. Xie, Q. Chen, A cancer cell turn-on protein-CuSMn nanoparticle as the sensor of breast cancer cell and CH_3O-PEG-phosphatide, Chin. Chem. Lett. 29 (2018) 1528-1532.

[32] T. Safrani, J. Jopp, Y. Golan, A comparative study of the structure and optical properties of copper sulfide thin films chemically deposited on various substrates, RSC Adv. 3 (2013) 23066-23074.

[33] A.G. Milekhin, N.A. Yeryukov, L.L. Sveshnikova, T.A. Duda, E.E. Rodyakina, V.A. Gridchin, et al., Combination of surface-and interference-enhanced Raman scattering by CuS nanocrystals on nanopatterned Au structures, Beilstein J. Nanotechnol. 6 (2015) 749-754.

[34] N. Kuhar, S. Sil, T. Verma, S. Umapathy, Challenges in application of Raman spectroscopy to biology and materials, RSC Adv. 8 (2018) 25888-25908.

[35] D. Ratnayake, M.D. Martin, U.R. Gowrishetty, D.A. Porter, T.A. Berfield, S.P. McNamara, et al., Engineering stress in thin films for the field of bistable MEMS, J. Micromech. Microeng. 25 (2015) 125025.

[36] Z. Cheng, S. Wang, Q. Wang, B. Geng, A facile solution chemical route to self-assembly of CuS ball-flowers and their application as an efficient photocatalyst, CrystEngComm. 12 (2010) 144-149.

[37] S. Riyaz, A. Parveen, A. Azam, Microstructural and optical properties of CuS nanoparticles prepared by sol–gel route, Perspect. Sci. 8 (2016) 632-635.

[38] Z. Li, L. Mi, W. Chen, H. Hou, C. Liu, H. Wang, et al., Three-dimensional CuS hierarchical architectures as recyclable catalysts for dye decolorization, CrystEngComm. 14 (2012) 3965-3971.

[39] M. Tanveer, C. Cao, Z. Ali, I. Aslam, F. Idrees, W.S. Khan, et al., Template free synthesis of CuS nanosheet-based hierarchical microspheres: an efficient natural light driven photocatalyst, CrystEngComm. 16 (2014) 5290-5300.

[40] M. Pal, N. Mathews, E. Sanchez-Mora, U. Pal, F. Paraguay-Delgado, X. Mathew, Synthesis of CuS nanoparticles by a wet chemical route and their photocatalytic activity, J. Nanopart. Res. 17 (2015) 301.

[41] Y. Zhou, Y. Bai, H. Liu, X. Jiang, T. Tong, L. Fang, et al., Tellurium/Bovine Serum Albumin Nanocomposites Inducing the Formation of Stress Granules in a Protein Kinase R-Dependent Manner, ACS Appl. Mater. Interfaces 10 (2018) 25241-25251.

[42] E. Ieva, A. Trapani, N. Cioffi, N. Ditaranto, A. Monopoli, L. Sabbatini, Analytical characterization of chitosan nanoparticles for peptide drug delivery applications, Anal. BioanalChem. 393 (2009) 207-215.

[43] Z. Luo, S. Lim, Z. Tian, J. Shang, L. Lai, B. MacDonald, et al., Pyridinic N doped graphene: synthesis, electronic structure, and electrocatalytic property, J. Mater. Chem. 21 (2011) 8038-8044.

[44] S. Liu, J. Tian, L. Wang, Y. Zhang, X. Qin, Y. Luo, et al., Hydrothermal treatment of grass: a low-cost, green route to nitrogen-doped, carbon-rich, photoluminescent polymer nanodots as an effective fluorescent sensing platform for label-free detection of Cu (II) ions, Adv. Mater. 24 (2012) 2037-2041.

[45] J. Zhang, J. Yu, Y. Zhang, Q. Li, J.R. Gong, Visible light photocatalytic H2-production activity of CuS/ZnS porous nanosheets based on photoinduced interfacial charge transfer, Nano Lett. 11 (2011) 4774-4779.

[46] L. An, P. Zhou, J. Yin, H. Liu, F. Chen, H. Liu, et al., Phase transformation fabrication of a Cu2S nanoplate as an efficient catalyst for water oxidation with glycine, Inorg. Chem. 54 (2015) 3281-3289.

[47] S. Yadav, P. Bajpai, Synthesis of copper sulfide nanoparticles: pH dependent phase stabilization, Nano-Structures & Nano-Objects, 10 (2017) 151-158.

[48] Y. Zhao, Q. Cai, W. Qi, Y. Jia, T. Xiong, Z. Fan, et al., BSA-CuS Nanoparticles for Photothermal Therapy of Diabetic Wound Infection *In Vivo*, Chem. Select 3 (2018) 9510-9516.

[49] G. Gorle, A. Bathinapatla, Y.-Z. Chen, Y.-C. Ling, Near infrared light activatable PEI-wrapped bismuth selenide nanocomposites for photothermal/photodynamic therapy induced bacterial inactivation and dye degradation, RSC Adv. 8 (2018) 19827-19834.

[50] P. Carloni, E. Damiani, L. Greci, P. Stipa, F. Tanfani, E. Tartaglini, et al., On the use of 1, 3-diphenylisobenzofuran (DPBF). Reactions with carbon and oxygen centered radicals in model and natural systems, Res. Chem. Intermed. 19 (1993) 395-405.

[51] R. Jijie, A. Barras, J. Bouckaert, N. Dumitrascu, S. Szunerits, R. Boukherroub, Enhanced antibacterial activity of carbon dots functionalized with ampicillin combined with visible light triggered photodynamic effects, Colloids Surf. B 170 (2018) 347-354.

CONCLUSIONS

The rapid evolution of nanotechnology worldwide has created enormous interest for designing catalytically smart and active nanomaterials. The interest of designing environmentally friendly CuS-based nanoparticles for colorimetric sensing and photothermal therapy has been investigated in this thesis.

A general review on the utilization of peroxidase enzyme mimics designated under the name ''nanozymes'' for colorimetric detection applications was presented in **chapter 1**. This work attempts to investigate the catalytic efficiency of various nanomaterials which are investigated for sensing purposes. A modulation of enzyme kinetics was also discussed in this chapter showing that the enzyme catalyzed reaction is strongly dependent on specific parameters. Considering that nanozymes are free-enzyme nanoparticles that mimic natural enzymes, the catalytic parameters including the maximum velocity (V_{max}) and Michaelis-Menten constant (K_m) of natural enzymes can be also used for nanozymes. This investigation provided new insights for designing novel nanomaterials with high efficient enzymatic-like behavior with multifunctional properties and widespread applications. The importance of nanozymes in the field of nanomedicine as well as their recent development was also described in the last part of this chapter, particularly when associated with nanotechnology for photothermal therapy *via* drug delivery mediated by NIR light.

Chapter 2 presents the potential of CuS nanoparticles modified with BSA protein via bio-mineralization assay for colorimetric sensing assay. Surface functionalization with BSA accelerates the kinetic mechanism by enhancing the stability of CuS and producing nanoparticles with small size, thus providing large number of active sites to achieve high catalytic efficiency. The catalytic action was based on a remarkable color conversion of colorless TMB into the blue oxidized product (oxTMB) with absorption maximum at 654 nm. The enzymomimetic activity of the nanoparticles is believed to occur through hydroxyl radical (HO•) generation when H_2O_2 is present. The developed sensor was applied for colorimetric sensing of hexavalent chromium ions, where under optimized experimental conditions, a good linear calibration plot of Cr(VI) was obtained in the concentration range of 0–100 nM and 1-20 μM with a detection limit of 50 nM using the lower linear range. Using terephthalic acid, it was possible to confirm the generation of HO• radicals during the TMB catalytic oxidation by

H_2O_2 in the presence of CuS-BSA, a process that has been enhanced in the presence of Cr(VI). The development of this enzyme-free sensor displayed a rapid, sensitive, and selective platform which offers a reliable assay for sensing of Cr(VI) ions in environmental water samples.

A non-enzymatic glucose and H_2O_2 sensor was also accomplished in this work (**Chapter 3, part A**). Ultra-small nanoparticles with crystalline morphology and high catalytic activity were achieved after conjugation of copper phosphate to the as-synthesized CuS-BSA nanocomposite designated as CuS-BSA-$Cu_3(PO_4)_2$. The sensing assay was performed for the detection of glucose due to the enhanced generation of hydroxyl radicals, and showed selective and sensitive determination of H_2O_2 and glucose with detection limits as low as 7.4 and 27.6 nM, respectively. The excellent analytical performance of the hybrid nanoparticles allowed for sensing glucose in real human serum samples, and H_2O_2 in contact lens care solutions. The sensor also exhibited high selectivity for glucose and H_2O_2 in the presence of different interference molecules.

The CuS-BSA-$Cu_3(PO_4)_2$ engineered nanoparticles with excellent stability, solubility and enhanced catalytic activity were also demonstrated as promising platform for colorimetric sensing of dopamine using TMB as a substrate in the presence of H_2O_2 (**Chapter 3, part A**). Under optimized conditions, the oxidation of TMB molecule was impeded in the presence of dopamine. This property was successfully applied for dopamine sensing with good sensitivity and selectivity. The good sensitivity of the developed nanosensor with a detection limit of 5.2 nM allows testing its robustness in meat samples. This method proved to be promising for diagnostic and biomedical applications without the requirement of complex and expensive instrumentations.

The promising optical properties of the designed nanozymes have inspired the fabrication of photoactive agents that uses light, mainly NIR light, to alter bacterial activity. Thus, the work outlined in **chapter 4** shows the strong photothermal properties of the proposed CuS-based nanoparticles modulated as a photothermal nanoagent to inhibit bacterial growth. A natural antibacterial drug model named ''lysozyme'' was loaded on CuS-BSA nanoparticles under physiological conditions and investigated as effective means for eradication of gram negative *E. coli* and gram positive *B. subtilis*. Besides the photothermal properties, CuS-BSA/Lysozyme nanocomposite possesses photodynamic activity, in which effective generation of singlet oxygen was also achieved under NIR illumination at low laser power

density (0.7 W.cm^{-2}), that participates in another way to inhibit bacterial growth. The biocompatibility of CuS-BSA and CuS-BSA/Lysozyme was elicited *in vitro* on two cancer cell lines, Hela and U87-MG cells. Considering these advantages, CuS-BSA NPs can be used as an ideal drug carrier, which opens new ways to overcome the traditional antibiotic therapy.

PERSPECTIVES

This work showed a great progress in the synthesis of nanozymes that possess enhanced catalytic activity for colorimetric sensing of heavy metal ions and biomolecules in real samples. The current assay of nanozymes was mostly relying on the use of specific chromogenic peroxidase substrate such as TMB, thus it will be interesting to examine other potential substances of different charges to improve the sensing performance of nanozymes. Also, there are still many challenges remained to be tackled. So far most of the studied nanomaterials mimic peroxidase enzyme, thus it is of paramount interest to discover other enzymatic activities.

In addition, the fabricated nanoparticles were applied for antibacterial applications. However, much effort should be devoted to perform the potential of such nanomaterials for *in vivo* applications. After examining the cytotoxic effect of our nanoparticles on mammalian cells, it is highly desirable to test their impact on mice animal model, as well to identify their interaction with biological compartments, and to understand their metabolism, biocompatibility, and clearance.

ANNEX

Experimental Part

5.1. Chemicals

Bovine serum albumin (BSA, $\geq$ 96%), copper(II) acetate [$Cu(Ac)_2$, 98.0%], sodium sulfide hydrate ($Na_2S.xH_2O$, $\geq$ 97.0%), sodium hydroxide pellets (NaOH, $\geq$ 97.0%), 3,3',5,5'-tetramethylbenzidine (TMB, $\geq$ 95.0%), sodium acetate (anhydrous) [CH_3COONa, $\geq$ 99.0%], chromium(III) chloride hexahydrate ($CrCl_3 \cdot 6H_2O$, 96.0%), chromium trioxide (CrO_3, $\geq$ 99.0%), nickel(II) chloride hexahydrate ($NiCl_2.6H_2O$, $\geq$ 98.0%), cobalt(II) nitrate hexahydrate ($CoN_2O_6.6H_2O$, $\geq$ 98.0%), mercury(II) nitrate monohydrate ($HgN_2O_6.H_2O$, $\geq$ 99.99%), sodium sulfite (Na_2SO_3, $\geq$ 98.0%), zinc chloride ($ZnCl_2$, $\geq$ 98.0%), iron(III) chloride ($FeCl_3$, $\geq$ 99.99%), copper (II) sulfate pentahydrate ($CuSO_4.5H_2O$, $\geq$ 98.0%), glucose oxidase (GOx, Aspergillus niger), nickel (II) nitrate hexahydrate ($Ni(NO_3)_2.6H_2O$, $\geq$ 98.5 %), sodium chloride (NaCl, $\geq$ 99.5%), zinc nitrate hexahydrate ($Zn(NO_3)_2.6H_2O$, 98.0%), iron(III) chloride hexahydrate ($FeCl_3.6H_2O$, $\geq$ 99.0 %), barium chloride ($BaCl_2$, 99.99 %), citric acid ($\geq$ 99.5%), uric acid ($C_5H_4N_4O_3$, $\geq$ 99.0%), L-Ascorbic acid ($\geq$ 99.0 %), D(-)-Fructose ($\geq$ 99.0%), D(+)-Galactose ($\geq$ 99.0%), D(+)-Glucose ($\geq$ 99.5%), D(+)-Xylose ($\geq$ 99.0%), dopamine hydrochloride ($C_8H_{11}NO_2 \cdot HCl$), β-Lactose minimum ($C_{12}H_{22}O_{11}$, $\geq$ 99.0 %), L-Glutathione reduced ($C_{10}H_{17}N_3O_6S$, $\geq$ 98%), cholesterol ($C_6H_{12}O_6$, $\geq$ 99.0%), phosphate buffered saline pellets (PBS), terephthalic acid (C_6H_4-1,4-$(CO_2H)_2$, 98.0 %), Lysozyme form chicken egg white (protein $\geq$ 90 %, $\geq$ 40,000 units/mg protein), Dulbecco's modified Eagle's medium (DMEM), Mueller Hinton Agar, Muller Hinton Broth, and 1,3-Diphenyl isobenzofuran (DPBF, 97 %) were purchased from Sigma-Aldrich.

Ethanol (95% v/v), hydrochloric acid (HCl, ~37%), dimethyl sulfoxide (DMSO, $\geq$ 99.9%), glacial acetic acid (99.0 %), hydrogen peroxide (30 wt%, H_2O_2), LB (Luria-Bertani) Broth Miller, LB Agar Miller, and sterile PBS (1X, 7.4) were purchased from fisher scientific. UptiBlue was purchased from Interchim. Human blood samples for glucose sensing were provided by Prof. Amar Abderrahmani (Faculty of Medicine, Université du Droit et de la Santé Lille 2, France). Hela cells (Human cervical adenocarcinoma cell line) [ATCC® CCL-2™, ECACC], and U87MG cells (Uppsala 87 Malignant Glioma cell line) were purchased from

Sigma Aldrich, Saint-Quentin Fallavier, France. Water was used throughout the whole experiments which was purified with a Milli-Q system from Millipore Co. (resistivity = 18 MΩ.cm).

5.2. Experimental conditions based on CuS-BSA nanocomposite for Cr(VI) sensing

5.2.1. Peroxidase-mimic activity of CuS-BSA

The catalytic activity of CuS-BSA as a peroxidase-mimic was assessed *via* the oxidization of TMB substrate in presence of H_2O_2. In brief, the reaction was carried out first by mixing 150 µL of each TMB (1.6 mM dissolved in 96% ethanol), H_2O_2 (200 mM), and the as-prepared CuS-BSA nanocomposite (1 mg/mL) at a temperature of 25 °C for 25 min. 0.1 M acetate buffer (pH 3.9) was used to adjust the reaction volume to 1.5 mL. Absorption spectra were recorded by UV/vis absorption spectrophotometer in the 350-850 nm range to follow the changes of the oxidized TMB (oxTMB) peak at 654 nm.

The effect of CuS-BSA concentration over the range 0.03-0.20 mg/mL, pH (2.5-10.0), temperature (25-50 °C), and incubation time (0-30 min) were performed to investigate their influence on the catalytic oxidation reaction.

A set of control experiments were also conducted to highlight the catalytic activity of CuS-BSA towards the oxidation of TMB.

5.2.2. Catalytic mechanism of CuS-BSA and steady-state kinetics

Enzyme affinity to its substrate can be assessed by the determination of the Michaelis–Menten constant (K_m), where smaller K_m value indicates a high affinity.

A Lineweaver-Burk double reciprocal plot is used to determine the enzyme affinity using the following relation (1):

$$\frac{1}{V} = \frac{Km}{V\max} \times \frac{1}{[S]} + \frac{1}{Vmax} \qquad \textbf{(1)}$$

Where *V* corresponds to the initial rate of the reaction, V_{max} represents the maximum rate, K_m is the Michaelis–Menten constant, and [*S*] is the concentration of the substrate.

The kinetic measurements were recorded at 654 nm in a time-scan mode at different concentrations of one substrate (TMB or H_2O_2) and at a fixed concentration of the other. The experiments were performed by mixing different concentrations of TMB (0.01-0.16 mM) with

H_2O_2 (20 mM) and CuS-BSA (0.1 mg/mL) catalyst in 1.5 mL acetate buffer (0.1 M) at pH 3.9. Similarly, using H_2O_2 as a substrate, the reaction was executed by mixing different concentrations of H_2O_2 (5-20 mM) with TMB (0.16 mM) and CuS-BSA (0.1 mg/mL) in 1.5 mL of 0.1 M acetate buffer (pH 3.9).

5.2.3. Colorimetric sensing of Cr(VI) in aqueous medium

The colorimetric detection of Cr(VI) ion was carried out by adding various concentrations of CrO_3 (dissolved in water) to a mixture of CuS-BSA (0.1 mg/mL), TMB (0.16 mM), and H_2O_2 (20 mM). The reaction volume was adjusted by 0.1 M acetate buffer (pH = 3.9) to 1.5 mL. The resulting mixture was incubated for 25 min at 25 °C, and the absorption spectra were measured by monitoring the absorbance at 654 nm.

Cr(VI) detection was also recorded in the absence of H_2O_2 under the same conditions mentioned above.

In order to evaluate the validation of the method, the limit of detection (LOD) was determined using equation 2:

$$LOD = \frac{3*SD}{a} \qquad (2)$$

Where LOD is the limit of detection, *SD* corresponds to the standard deviation of the blank, and *a* represents the slope of the linear calibration plot.

5.2.4. Selectivity and reproducibility of CuS-BSA

The selectivity of CuS-BSA nanocomposite was investigated for speciation of Cr(VI). The credibility of this assay was studied by determining the absorbance at 654 nm in presence of different potentially co-existing ions. Thus, 20 μM and 100 μM of different ions (Na^+, Hg^{2+}, Zn^{2+}, Co^{2+}, Ni^{2+}, Cr^{3+}) were mixed with CuS-BSA (0.1 mg/mL), TMB (0.16 mM), and H_2O_2 (20 mM) in 0.1 M acetate buffer (pH 3.9) to examine the response of the proposed sensor for the colorimetric detection of Cr(VI) ion using other ions at same and five-times higher than the concentration of Cr(VI). The reusability of the nanocomposite was also determined for several repeated cycles under the optimized experimental conditions.

5.2.5. Mechanism of HO˙ generation

In order to confirm the catalytic activity of CuS-BSA towards TMB oxidation through the formation of hydroxyl radicals from H_2O_2 decomposition in acidic medium, terephthalic acid

(TA) was used as a probe molecule that can readily react with $^{\bullet}$OH radicals to produce 2-hydroxyterephthalic acid (HTA). The HTA exhibits a fluorescence emission peak at 430 nm under excitation wavelength of 315 nm. In brief, TA (0.15 mM in DMSO) was subsequently treated with (a) H_2O_2 (20 mM), (b) Cr (VI) (20 µM), (c) CuS-BSA (0.1 mg/mL), (d) H_2O_2 (20 mM) + CuS-BSA (0.1 mg/mL), (e) H_2O_2 (20 mM) + Cr(VI) (20 µM), (f) Cr(VI) (20 µM) + CuS-BSA (0.1 mg/mL), (g) H_2O_2 (20 mM) + Cr(VI) (20 µM) + CuS-BSA (0.1 mg/mL) in 1.5 mL acetate buffer (pH 3.9) and incubated for 25 min at 25 °C. The fluorescence emission spectra were then collected in the range of 325-550 nm using a Safas Xenius XC fluorescence spectrophotometer (Monaco) under excitation wavelength of 315 nm.

5.2.6. Sensing of Cr(VI) ion in real environmental water samples

To investigate the practical application of CuS-BSA as a colorimetric sensor, concentration of Cr(VI) ions were determined in various real environmental water samples (sea, pond, tap and tube well water) spiked with different concentrations of Cr(VI) ions. The tube well water samples were taken from local area of Lille city, Rihour, France. The pond water samples were collected from the Parc du Héron, Villeneuve d'Ascq (France). The tap water samples were obtained from our laboratory (IEMN, Villeneuve d'Ascq), and the sea water samples were from the North Sea (marginal sea of Atlantic Ocean). The collected water samples were purified by centrifugation at 13,500 rpm for 10 min and the supernatant was then collected and filtered through 0.2 µm pore size membrane, before standard solutions of Cr(VI) ions (10, 50, 100 nM) were added separately.

The sensing experiments were conducted as follows: 150 µL of the as-prepared CuS-BSA suspension (1 mg/mL), 150 µL of TMB (1.6 mM in ethanol) and 150 µL of H_2O_2 (200 mM) were added successively to 150 µL of each water sample containing different concentrations of Cr(VI) (10, 50, 100 nM), and the total volume was adjusted to 1.5 mL by adding acetate buffer (pH = 3.9). The reaction mixture was kept at 25 °C for 25 min, and the absorbance was monitored at 654 nm by UV/vis absorbance spectrophotometry.

5.3. Optimization of the experimental conditions based on CuS-BSA-Cu₃(PO₄)₂ nanozymes for glucose sensing

5.3.1. Peroxidase-mimic activity of CuS-BSA-Cu₃(PO₄)₂

Based on the excellent solubility, stability and dispersibility of CuS-BSA-Cu₃(PO₄)₂, the peroxidase-mimic activity was investigated for the catalytic oxidization of TMB. Typically, the

catalytic reaction was carried out by adding 30 μL of TMB (10 mM stock solution dissolved in DMSO), and 100 μL H_2O_2 (10 mM) to 130 μL of aqueous CuS-BSA-$Cu_3(PO_4)_2$ solution (2.3 mg/mL) for 25 min at 25 °C, and the volume was adjusted to 1 mL by adding 740 μL sodium acetate buffer (0.1 M, pH 4); the acetate buffer was prepared by mixing 19 mg of sodium acetate anhydrous with 43.8 μL of glacial acetic acid in MQ-water of 10 mL total volume. The formation of oxidized TMB (oxTMB) was monitored by UV-vis absorption at 654 nm.

The influence of CuS-BSA-$Cu_3(PO_4)_2$ concentration (0.01-1 mg/mL), TMB concentration (0.1-0.32 mM), incubation time (0-30 min), pH (3.6-10) and temperature (25-60 °C) on the oxidation reaction was assessed to determine the optimal conditions.

Control experiments were run in the absence of catalyst or H_2O_2, and with both CuS-BSA-$Cu_3(PO_4)_2$ catalyst and H_2O_2 for comparison.

5.3.2. Colorimetric sensing of H_2O_2

Given that the intensity of the produced color from oxTMB is highly dependent on the catalyst concentration as well as various parameters, the standard curve determination of H_2O_2 was constructed under the optimized experimental conditions, using different concentrations of H_2O_2 (0.003-1.5 mM), CuS-BSA-$Cu_3(PO_4)_2$ (0.3 mg/mL), TMB (0.3 mM) at 25 °C in acetate buffer (0.1 M, pH 4); the reaction time was 25 min.

5.3.3. Catalytic mechanism of CuS-BSA-$Cu_3(PO_4)_2$ and steady-state kinetics

The reaction kinetics were investigated by incubating TMB as a substrate over a concentration range (0.05-0.3 mM) with 1 mM H_2O_2, or H_2O_2 (0.01-1 mM) as a substrate with 0.3 mM TMB. Both substrates were subsequently mixed with CuS-BSA-$Cu_3(PO_4)_2$ (0.3 mg/mL) catalyst in 1 mL sodium acetate buffer (0.1 M, pH 4) at 25 °C.

Thus, for the enzyme-like catalytic activity of CuSBSA-$Cu_3(PO_4)_2$, a plot of Lineweaver-Burk is used to investigate the enzyme affinity using Eq. 1.

5.3.4. Sensing of H_2O_2 in contact lens care solution

The colorimetric sensing method of H_2O_2 in lens care solution was evaluated using CuS-BSA-$Cu_3(PO_4)_2$ enzyme-like nanohybrid based on a standard addition method performed in triplicate. 130 μL of CuS-BSA-$Cu_3(PO_4)_2$ (2.3 mg/mL), 100 μL of H_2O_2 at different concentrations (20, 50, and 100 nM), and 30 μL of TMB (10 mM in DMSO) were successively added to 100 μL of lens care solution. Acetate buffer (0.1 M, pH 4) was used to adjust the total

reaction volume up to 1 mL. The resulting mixture was incubated at 25 °C for 25 min, followed by monitoring the oxTMB absorbance at 654 nm.

5.3.5. Selectivity towards H_2O_2 sensing and catalyst reusability

The selective monitoring of H_2O_2 based on the enzymatic activity of CuS-BSA-Cu$_3$(PO$_4$)$_2$ was examined against different ions (Fe^{3+}, Hg^{2+}, Co^{2+}, Na$^+$, Ni^{2+}, Zn^{2+}) and substances (galactose, ascorbic acid, uric acid, and citric acid) in a relatively 10 times higher concentration than the optimal H_2O_2 concentration (1 mM). The selectivity test was modulated by mixing 10 mM of these ions and interfering substances with CuS-BSA-Cu$_3$(PO$_4$)$_2$ (0.3 mg/mL), TMB (0.3 mM), in acetate buffer (pH 4) for 25 min at 25 °C.

The reproducibility of the designed nanohybrid was studied for four successive cycles at the optimal experimental conditions.

5.3.6. Mechanism of HO$^•$ generation

In a typical experiment, terephthalic acid (TA, 0.15 mM dissolved in DMSO) was mixed separately with (a) CuS-BSA-Cu$_3$(PO$_4$)$_2$ (0.3 mg/mL), (b) H_2O_2 (1 mM), (c) CuS-BSA-Cu$_3$(PO$_4$)$_2$ (0.3 mg/mL) and H_2O_2 (1 mM) in 1 mL acetate buffer (0.1 M, pH 4). After 25 min incubation at 25 °C, fluorescence emission spectra (λ_{ex}=318 nm) were recorded in the 400-550 nm range.

5.3.7. Quantitative detection of glucose

Based on the high sensitivity of CuS-BSA-Cu$_3$(PO$_4$)$_2$ for H_2O_2 detection, the nanocomposite was applied for glucose sensing. The quantitative determination of glucose in solution was achieved as following: 50 µL of aqueous GOx (0.6 mg/mL stock concentration) was mixed with 50 µL of glucose (final concentration in the range of 0.001-1.5 mM) in 0.3 mL of PBS (0.1 mM, pH 7.4). The reaction mixture was incubated for 30 min at 37 °C in the dark, for the successive production of H_2O_2. Afterwards, 130 µL of CuS-BSA-Cu$_3$(PO$_4$)$_2$ (2.3 mg/mL) and 30 µL TMB (10 mM) were added to the glucose solution, followed by 540 µL acetate buffer (0.1 M, pH 4). The total reaction volume was 1 mL. After 25 min incubation at room temperature, glucose sensing was analyzed by recording the UV-vis absorption spectra of oxTMB at 654 nm.

5.3.8. Glucose sensing in real human serum samples

The validity of the proposed sensor was extended by analyzing glucose in human serum samples. Blood samples were taken from a male volunteer at CHU Lille, France. The blood samples were first centrifuged at 13,500 rpm for 10 min. The supernatant, which is the serum, was collected and diluted 100 times with PBS (0.1 mM, pH 7.4) to ensure that the glucose content is within our established calibration plot. 10 μL of serum solution was spiked with glucose at different concentrations (30, 80, 130 nM). 50 μL of GOx (0.6 mg/mL) was then added, and the volume was adjusted to 0.3 mL using PBS (0.1 mM, pH= 7.4). After 30 min incubation at 35 °C, 30 μL of TMB (10 mM), 130 μL of CuS-BSA-Cu$_3$(PO$_4$)$_2$ (2.3 mg/mL), and acetate buffer (0.1 M, pH 4) were added successively (total volume=1 mL). The oxTMB absorbance at 654 nm was recorded using UV-vis spectrophotometry.

5.3.9. Selectivity test towards glucose sensing

On the basis of glucose determination, the selectivity of CuS-BSA-Cu$_3$(PO$_4$)$_2$ was conducted in the presence of different glucose analogues (galactose, fructose, and xylose) at a concentration 20 times higher than the optimal glucose concentration (1 mM) using the optimized experimental conditions for CuS-BSA-Cu$_3$(PO$_4$)$_2$ nanozymes.

5.3.10. Hemolysis assay

The hemolysis test of CuS-BSA-Cu$_3$(PO$_4$)$_2$ was performed on human erythrocytes after being freshly obtained from a male volunteer. Typically, 0.5 mL blood solution was centrifuged (13,500 rpm) for 15 min to remove the plasma, and the precipitate containing the red blood cells (RBC) was washed repeatedly with PBS (1X, pH 7.4), followed by dilution with 9 mL PBS. 0.4 mL out of this solution was mixed with 0.6 mL PBS (negative control, NC), or MQ-water (positive control, PC). Simultaneously, CuS-BSA-Cu$_3$(PO$_4$)$_2$ of various concentrations (37.5-600 μg/mL prepared in PBS) were mixed with 0.4 mL of the diluted blood samples, and the volume was adjusted to 1 mL by PBS. Concurrently, the solutions were incubated at 37 °C for 3 h with gentle shaking every 20 min. The supernatant was then collected by centrifugation (13,500 rpm) for 5 min, and the absorbance was monitored at 540 nm, that is correlated to the released hemoglobin caused by cell rupture, which gives evidence of hemolysis.

The percentage hemolysis was calculated using the Eq. 3:

$$Hemolysis\ (\%) = \frac{As - An}{Ap - An} \qquad (3)$$

Where A_s is the absorbance of solution containing the nanomaterial, A_p and A_n are the absorbance of positive and negative controls, respectively.

5.4. Optimization of the experimental conditions based on CuS-BSA-Cu₃(PO₄)₂ nanozymes for dopamine sensing

5.4.1. Enzymomimetic activity of CuS-BSA-Cu₃(PO₄)₂ nanoparticles

In a typical procedure, the reaction achieved by mixing 0.1 mL of CuS-BSA-Cu₃(PO₄)₂ (1 mg/mL) as a catalyst, 0.1 mL of H_2O_2 (10 mM) and 10 µL TMB (30 mM in DMSO) in 0.79 mL of acetate buffer (0.1 M, pH 4). After 20 min incubation at room temperature (RT), the solution was measured by ultraviolet-visible absorption spectroscopy in the range of 380-800 nm, to monitor the absorbance variation at 654 nm which corresponds to the oxidized product of TMB (oxTMB).

The influence of different concentrations of CuS-BSA-Cu₃(PO₄)₂ (0-0.15 mg/mL), TMB (0.01-0.35 mM), H_2O_2 (0-1.2 mM), temperature (0-50 °C), pH (3.6-10) and incubation time (0-30 min) on the enzyme-like reaction were also recorded for comparison

Control experiments were also postulated to compare the effect of both CuS-BSA-Cu₃(PO₄)₂ catalyst and H_2O_2 on the oxidation reaction towards TMB. Thus, three different reactions were carried out, in the absence of H_2O_2, in the absence of CuS-BSA-Cu₃(PO₄)₂, and in the presence of both H_2O_2 and CuS-BSA-Cu₃(PO₄)₂ under the optimized reaction parameters.

5.4.2. Michaelis-Menten model of CuS-BSA-Cu₃(PO₄)₂

Kinetic experiments were achieved by mixing various concentrations of H_2O_2 as a substrate (0-1.2 mM) with 0.3 mM TMB and 0.1 mg/mL (CuS-BSA-Cu₃(PO₄)₂) in 1 mL acetate buffer (0.1 M, pH 4). Similarly, by mixing TMB as substrate (0.01-0.35 mM) with 1 mM H_2O_2 and 0.1 mg/mL (CuS-BSA-Cu₃(PO₄)₂) in 1 mL acetate buffer (0.1 M, pH 4). All the kinetic reactions were done in a time-scan mode.

5.4.3. Colorimetric assays based on sensing H₂O₂ and DA

The feasibility of the enzymomimetic activity of CuS-BSA-Cu₃(PO₄)₂ was evaluated for determining H_2O_2 in an acidic environment, achieved by mixing different H_2O_2 concentrations (0-1.2 mM) with 0.1 mg/mL CuS-BSA-Cu₃(PO₄)₂ and 0.3 mM TMB in 1 mL of acetate buffer

(0.1 M, pH 4) for 20 min incubation at RT. The absorption spectra at 654 nm were then monitored which enable to achieve a linear calibration plot of H_2O_2 for determining the limit of detection.

Similarly, DA detection was carried out by adding freshly prepared dopamine.HCl aqueous solutions of different concentrations (0-0.5 mM) to a mixture of CuS-BSA-$Cu_3(PO_4)_2$ (0.1 mg/mL), TMB (0.3 mM), and H_2O_2 (1 mM) in acetate buffer solution (0.1 M, pH 4) of total volume 1 mL. The entire mixture was then incubated for 20 min at RT, followed by monitoring the sequential change in the absorption spectra (A654 nm) of oxTMB at variable DA concentrations.

A calibration curve was further established and the LOD was determined from Eq. 2.

5.4.4. Selectivity towards DA sensing

The enzymatic selectivity of CuS-BSA-$Cu_3(PO_4)_2$ was performed for speciation of DA in aqueous solutions. Thus, in order to confirm the selective determination of our proposed nanosensor towards DA sensing, different biological molecules (lactose, glutathione, uric acid, cholesterol, glucose, fructose, and ascorbic acid) at concentrations 0.3 mM (same as optimum DA concentration) and 0.6 mM (2x higher than DA concentration) were mixed separately with CuS-BSA-$Cu_3(PO_4)_2$ (0.1 mg/mL), TMB (0.3 mM), and H_2O_2 (1 mM) in 1 mL acetate buffer (0.1 M, pH 4) for 20 min at RT.

The reproducibility of the nanosensor was also examined under the optimum reaction parameters for 4 successive cycles, where before each cycle, the mixture was centrifuged at 13500 rpm for 3 min to collect the catalyst which was then washed with MQ-water to remove any traces of H_2O_2 or oxTMB, to be ready for the next cycle.

5.4.5. Generation of hydroxyl radicals (HO$^{\bullet}$)

Briefly, 10 µL of TA (20 mM dissolved in DMSO) was separately mixed with 100 µL of (a) H_2O_2 (10 mM), (b) CuS-BSA-$Cu_3(PO_4)_2$ (1 mg/mL), (c) DA (2 mM), (d) DA (2 mM) + H_2O_2 (10 mM), (e) DA (2 mM) + CuS-BSA-$Cu_3(PO_4)_2$ (1 mg/mL), (f) DA (2 mM) + CuS-BSA-$Cu_3(PO_4)_2$ (1 mg/mL) + H_2O_2 (10 mM), (g) H_2O_2 (10 mM) + CuS-BSA-$Cu_3(PO_4)_2$ (1 mg/mL) for 20 min at RT, and the volume was adjusted to 1 mL by acetate buffer (0.1 M, pH 4). Fluorescence emission was then collected within the range of 393-530 nm using a fluorescence spectroscopy at a 318 nm excitation wavelength.

5.4.6. DA sensing in meat samples

To achieve an excellent colorimetric practicality, selectivity is highly crucial in real samples, thus, DA sensing was evaluated in meat samples collected from a local market in Lille, France and prepared according to previous procedure [1]. Typically, 3.989 g of beef meat was cut into small pieces and grinded well using a mortar and pestle, after which 10 mL of PBS buffer solution (0.1 M, pH 7.4) was then added, followed by the addition of another 10 mL of $ZnCl_2$ solution (1 M) to induce protein precipitation. The mixture was moderately agitated for 20 min at 100 rpm, centrifuged for 15 min at 4 °C with a speed of 4000 rpm, and filtered 2x using a Minisart filter of 0.2 μm pore size. The obtained samples were then used for dopamine sensing.

In brief, 20 μL of meat solution were mixed with 100 μL of CuS-BSA-$Cu_3(PO_4)_2$ (1 mg/mL), 10 μL of TMB (30 mM), and 100 μL of H_2O_2 (10 mM) in 1 mL acetate buffer (0.1 M, pH 4) for 20 min at RT. The absorbance at 654 nm was then recorded to determine the amount of dopamine in meat samples.

High performance liquid chromatography (HPLC) analysis was used to confirm the results for determining the concentration of DA in meat samples.

5.5. CuS-BSA with 0.1:0.0001 Molar ratio for lysozyme loading and release

5.5.1. Lysozyme loading into CuS-BSA nanoparticles

Loading of lysozyme onto CuS-BSA NPs was achieved by simple mixing of 1 mg/mL aqueous CuS-BSA solution with 1 mg/mL lysozyme in 1 mL PBS buffer (0.01 M, pH 7.4) for 24 h at different temperatures (4 °C and 25 °C) under moderate shaking at 150 rpm. CuS-BSA NPs mixed with various lysozyme concentrations under the aforementioned conditions were also performed to determine the highest loading efficiency of lysozyme.

The resulting solution mixture was centrifuged (8,500 rpm at 4 °C) for 10 min and the supernatant was collected after several washing steps with MQ-water, and filtered twice using 0.2 μm Ge-Whatman filter to determine the amount of lysozyme integrated in CuS-BSA, which was evaluated by measuring the concentration of lysozyme in solution before and after loading using UV/Vis spectrometric measurements at 279 nm and calculated as below (Eq. 4). At this wavelength, lysozyme displays a well-defined absorption band which mostly scales linearly with its concentration in solution.

$$[\text{Lysozyme}]_{loaded} = [\text{Lysozyme}]_{initial} - [\text{Lysozyme}]_{supernatant} \ (\mu g/mL) \qquad \textbf{(4)}$$

Where [Lysozyme]$_{loaded}$ is the concentration of lysozyme loaded on CuS-BSA, [Lysozyme]$_{initial}$ is the initial concentration of lysozyme in solution, and [Lysozyme]$_{supernatant}$ is the concentration of free lysozyme in the supernatant.

A calibration curve was established at 279 nm using a series of lysozyme solutions of different concentrations to determine the amount of loaded lysozyme.

To evaluate the loading efficiency, the content of lysozyme in the supernatant was determined by UV-Vis measurements at 279 nm using the following equation (Eq. 5):

$$L.E \% = \frac{I(lysozyme) - S(lysozyme)}{I(lysozyme)} \times 100 \qquad (5)$$

Where L.E is the loading efficiency of lysozyme, I$_{lysozyme}$ and S$_{lysozyme}$ are the contents of initial and free lysozyme in the supernatant, respectively.

The pellet which corresponds to CuS-BSA/Lysozyme nanocomposite was re-dispersed in 1 mL of fresh PBS solution for subsequent lysozyme release.

5.5.2. NIR light induced photothermal heating of CuS-BSA nanoparticles

The photothermal heating performance of different CuS-BSA and CuS-BSA/Lysozyme concentrations (0-200 µg/mL) were examined in PBS solution (0.01 M, pH 7.4) of total volume 1.0 mL, in 24 polystyrene well-plates under NIR irradiation with a continuous wave Lens laser (Gbox model, Fournier Medical Solution) of an output light at 980 nm at different power densities (0.7 or 1 W.cm^{-2}) for 3 min. Thermal images were captured by using an Infrared Camera (Thermovision A40) and treated by ThermaCam Researcher Pro 2.9 software.

5.5.3. *In vitro* photothermal release of Lysozyme

Release experiments were investigated by mixing 0.1 mL of CuS-BSA/Lysozyme nanocomposites (1 mg/mL) in 0.9 mL PBS (0.01 M, pH 7.4), and subjecting the solution to 980 nm-NIR light at different laser power densities (0.7 or 1 W.cm^{-2}) for 3 min. After irradiation, the solution was centrifuged at 13,500 rpm for 5 min, and the supernatant was collected, filtered using 0.2 µm Ge-Whatman filter, and its absorbance at 279 nm was monitored by UV-vis spectrometry.

We also tested the passive release of lysozyme from CuS-BSA in 1.0 mL of PBS at different temperatures (4, 25, and 37 °C) and for various time intervals (4, 6, and 12 h).

5.5.4. Cell culture and cytotoxicity assay

The cytotoxicity of CuS-BSA and CuS-BSA/Lysozyme was assessed on two cancer cell lines; Hela cells (Human cervical adenocarcinoma cell line) derived from a 31 years old female with cervical carcinoma [ATCC® CCL-2™, ECACC, Sigma Aldrich, Saint-Quentin Fallavier, France] and U87MG (Human glioblastoma cell line) with and without NIR irradiation, using UptiBlue assay (Interchim).

Cells were cultured in Dulbecco's Modified Eagle's medium (DMEM, Gibco®) which is supplemented with 10% fetal bovine serum (FBS), 1% penicillin-streptomycin, and maintained in a humidified incubator at 37 °C under 5% CO_2.
Cells were then plated into 96-well plates at a density of 1×10^4 cells/well with 100 μL DMEM medium and incubated for 24 h before assay. After removing the old media, the cells were exposed to a fresh medium with various concentrations of CuS-BSA and CuS-BSA/Lysozyme (0-200 μg/mL) for another 24 hrs. The old medium was then aspirated, cells were washed 3x with PBS and replaced with a new medium.

Prior to laser treatment, cells were incubated with CuS-BSA and CuS-BSA/Lysozyme for 4 h before irradiation at 37 °C. After incubation, cells were irradiated with 980 nm continuous mode laser at different laser power densities (1 and 0.7 $W.cm^{-2}$) for 3 min and incubated for another 20 hrs. After that, the old medium was aspirated, cells were then washed 3x with PBS and replaced with a new medium.
Cellular viability was measured using Uptiblue (Interchim) method. In brief, 10 μL of the Uptiblue solution (11 mg/mL) was added to the wells containing 100 μL of DMEM with 10% FBS and the plate was incubated for 4 h in the incubator, then the fluorescence of each well (excitation wavelength= 540 nm / emission wavelength= 590 nm) was obtained with a plate reader. Experimental runs were repeated three times, and the average absorbance of untreated cells was considered as 100% viability. Cells without treatment were considered as positive control.
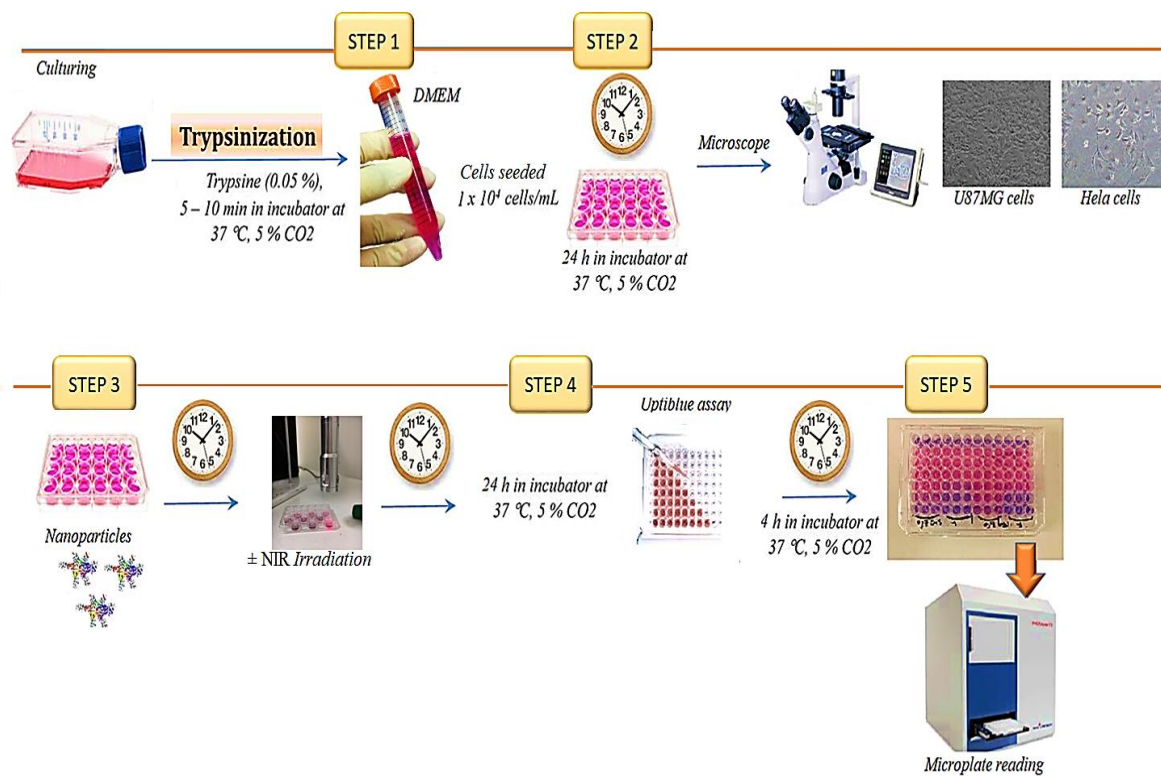
Figure 1: Schematic illustration of the experimental setup for cytotoxicity assay.

5.5.5. Bacterial culture and enzyme activity assay

Gram positive *Bacillus subtilis* (*B. subtilis* 168) and gram negative *E. coli* K12 bacteria were selected to evaluate the antibiotic activity of the photothermally released lysozyme from CuS-BSA NPs.

In typical procedure, a single isolated colony of E. coli K-12 and B. subtilis from LB/MHB agar plates was inoculated in 8 mL of LB/MHB medium. After incubation for 12 h at 37 °C under moderate shaking (150 rpm), the pre-culture was diluted by 50–folds and incubated for another 4-6 h to reach $O.D_{600}$ 0.5 – 1.0 [2]. 1.0 mL of nutrient medium (LB/MHB) was used as the blank for calibrating the spectrophotometer. The bacterial culture was then diluted to 10^6 CFU/mL in the desired medium. 100 µL out of the diluted bacterial culture was then mixed with 100 µL of lysozyme, CuS-BSA, and CuS-BSA/Lysozyme with various concentrations (0-200 µg/mL in PBS) in 96-well plates, and incubated for 18-24 h at 37 °C. Bacterial culture in the absence of NPs was considered as a growth control (GC) and treated as above.

Prior to photothermal ablation of bacterial strains, 0.5 mL of the bacterial culture (10^6 CFU/mL) was incubated at 37 °C with 0.5 mL CuS-BSA or CuS-BSA/Lysozyme (0-200 µg/mL in PBS) in 24-well plates for 30 min before irradiation. As a control, 0.5 mL of bacterial culture was mixed with 0.5 mL lysozyme (0-200 µg/mL), and sterile PBS (0.01 M,

pH 7.4), respectively. Afterwards, the solutions were subjected to NIR-laser (980 nm) at different laser power densities (0.7 or 1 W.cm^{-2}) for 3 min.

The turbidimetric and micro-dilution methods were applied to test the minimal inhibitory concentration (MIC) and minimal bactericidal concentration (MBC) of the samples, respectively. Thus, a plating method was used to count the number of viable bacterial cells, through diluting the bacterial/NPs solution by 10-fold in PBS in 96-well plates, followed by depositing 10 µL out of the diluted solution on LB/MHB agar plate, and incubation for 18-24 h at 37 °C. The number of visual colonies was counted, which allowed determining the final concentrations of E. coli and B. subtilis strains. The bacterial growth rates were measured using a microplate reader by determining the absorbance at 600 nm (PHERAstar FS, BMG LABTECH GmbH, Germany).

$$\text{Number of Colonies/mL} = \frac{\text{Number of colonies}}{\text{Volume plated} \times \text{total dilution used}} \quad \text{(CFU/mL)} \quad (6)$$
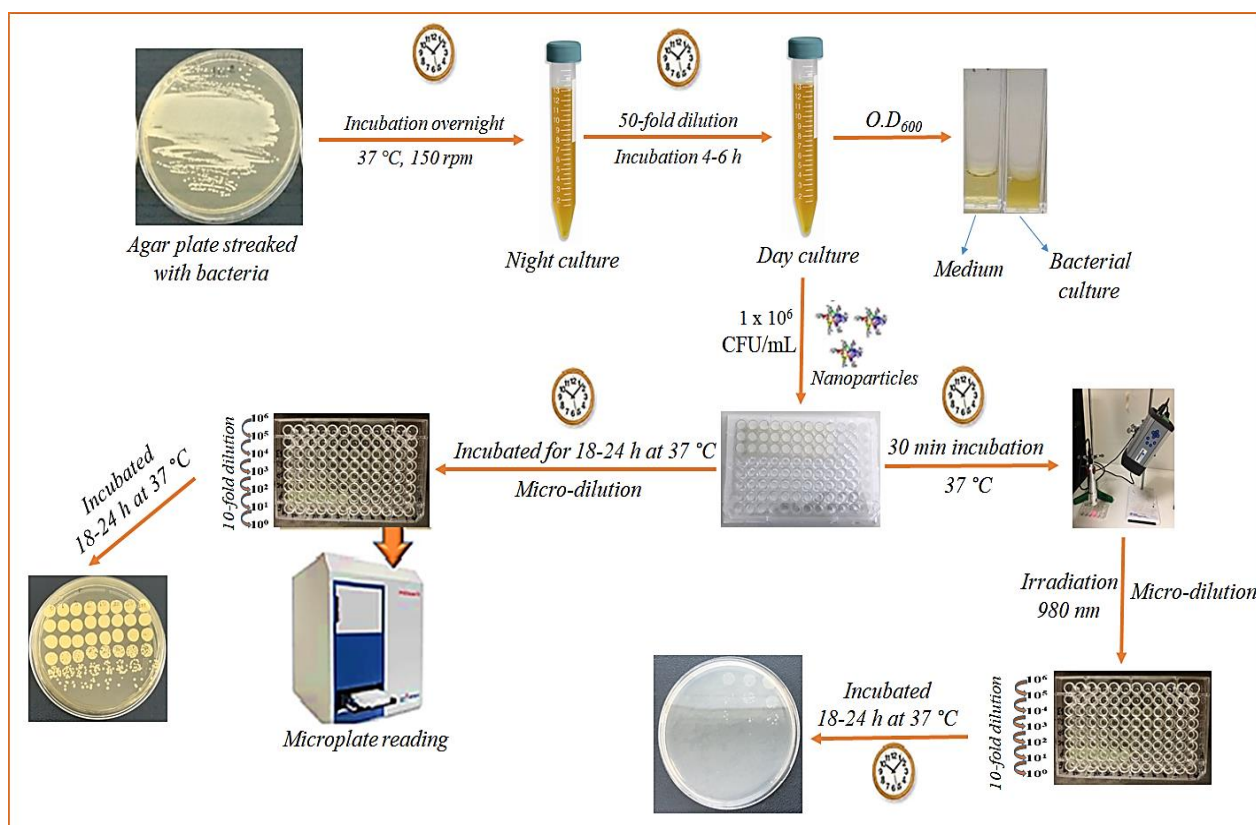

Figure 2: Schematic illustration of the experimental setup for the antibacterial activity of CuS-BSA/Lysozyme.

5.5.6. Photodynamic properties of CuS-BSA nanoparticles under NIR light irradiation

UV-vis absorption spectroscopy was used to estimate the singlet oxygen ($^1O_2$) generation by CuS-BSA NPs under NIR irradiation, through monitoring the decrease of absorbance intensity at 415 nm of 1,3-diphenyl isobenzofuran (DPBF) [3]. DPBF is well-known as a singlet oxygen trapping agent that forms a bleached adduct when it reacts with $^1O_2$.

Typically, 0.1 mL of DPBF (0.8 mM in ethanol) was mixed with 0.1 mL of (a) CuS-BSA (1 mg/mL), or (b) CuS-BSA/Lysozyme (1 mg/mL), and the total volume was adjusted to 1.0 mL using MQ-water. The samples were then irradiated for different time intervals at 0.7 W.cm^{-2}, and the decrease in absorbance at 415 nm was then recorded by UV-vis spectroscopy. As a control, DPBF absorbance intensity was also recorded after irradiation under the same conditions mentioned above.

5.6. INSTRUMENTATION

5.6.1. UV-Vis absorption spectroscopy

The UV-vis absorbance spectra were recorded in the 200-1000 nm wavelength range using a Perkin Elmer Lambda UV/vis 950 spectrophotometer with an optical path of 10 mm in a 1 cm quartz cuvette.
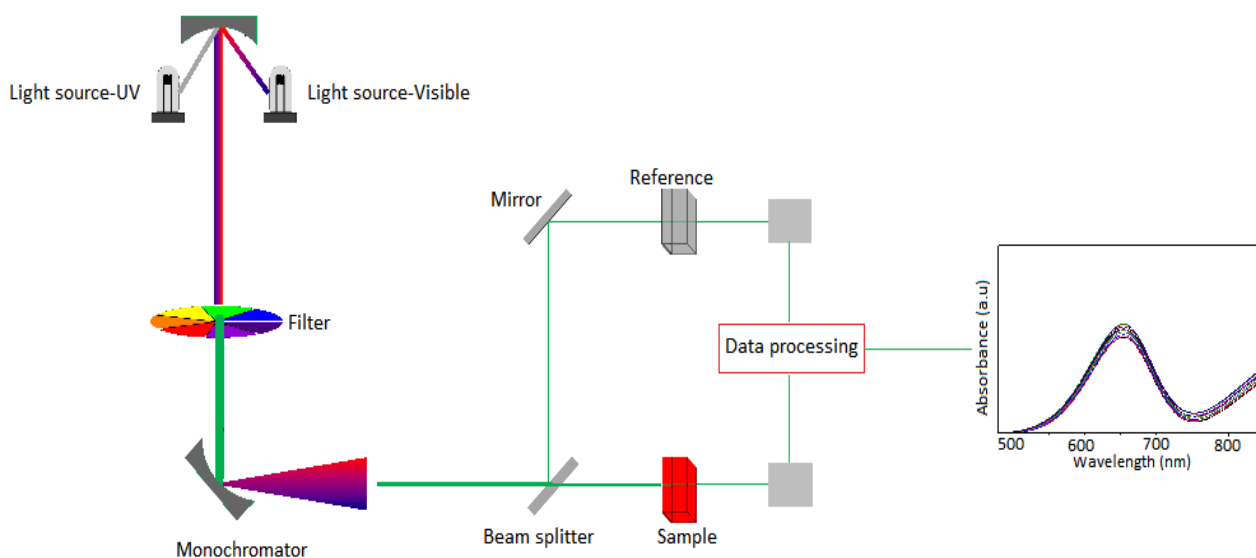

Figure 4: Schematic diagram of a UV-Vis spectrophotometer.

5.6.2. Transmission electron microscopy (TEM)

Morphology and particle size of the synthesized nanoparticles were investigated by transmission electron microscopy (TEM) and High resolution TEM (HRTEM) recorded on FEI TECNAI G2-20 operated at an accelerating voltage of 200 kV with a resolution of 1.9 Å and equipped with EDS detector. Analysis was carried out by depositing ~ 10 µL of each sample (0.1 mg/mL) on carbon 200 mesh grid and left to dry at room temperature.

5.6.3. X-ray photoelectron spectroscopy (XPS)

XPS experiments were performed on a PHI 5000 VersaProbe-Scanning ESCA Microprobe (ULVAC-PHI, Japan/USA) instrument at a base pressure below 5×10^{-9} mbar. Monochromatic AlK_α radiation was used and the X-ray beam, focused to a diameter of 100 µm, was scanned on a 250×250 µm surface, at an operating power of 25 W (15 kV). Photoelectron survey spectra were acquired using a hemispherical analyzer at pass energy of 117.4 eV with a 0.4 eV energy step. Core-level spectra were recorded at pass energy of 23.5 eV with a 0.1 eV energy step. All spectra were obtained with 90° between X-ray source and analyzer and with the use of low energy electrons and low energy argon ions for charge neutralization. After subtraction of the linear-type background, the core-level spectra were decomposed into their components with mixed Gaussian-Lorentzian (30:70) shape lines using the CasaXPS software. Quantification calculations were performed using sensitivity factors supplied by PHI.

Sample preparation was done by depositing ~ 50 µL of an aqueous solution of nanoparticles (0.1 mg/mL) on silicon wafer and left dry at room temperature before analysis.

5.6.4. Fourier transform infrared spectroscopy (FTIR)

FTIR was performed on a Thermo Fisher Inc, Nicolet 380. The nanoparticles were analyzed in the IR radiation in a pallet form, which is made by mixing ~ 1 mg of each sample with 175 mg of potassium bromide (KBr). The mixture was then grinded properly in agar mortar to ensure uniform distribution in the KBr base. Finally, the grinded mixture was pressed in a hydraulic press by applying a pressure of ~7 to 9 tons for ~ 2 min, and the spectra were recorded immediately.

5.6.5. Fluorescence spectroscopy (FL)

Emission Fluorescence spectra were recorded using Safas Xenius XC fluorescence spectrophotometer (Monaco). The excitation wavelength was set at 315 or 318 nm and the

emission spectra were recorded in the range of 393-550 nm using 10 mm quartz cuvette, where the excitation and emission slit widths were adjusted at 10 nm.
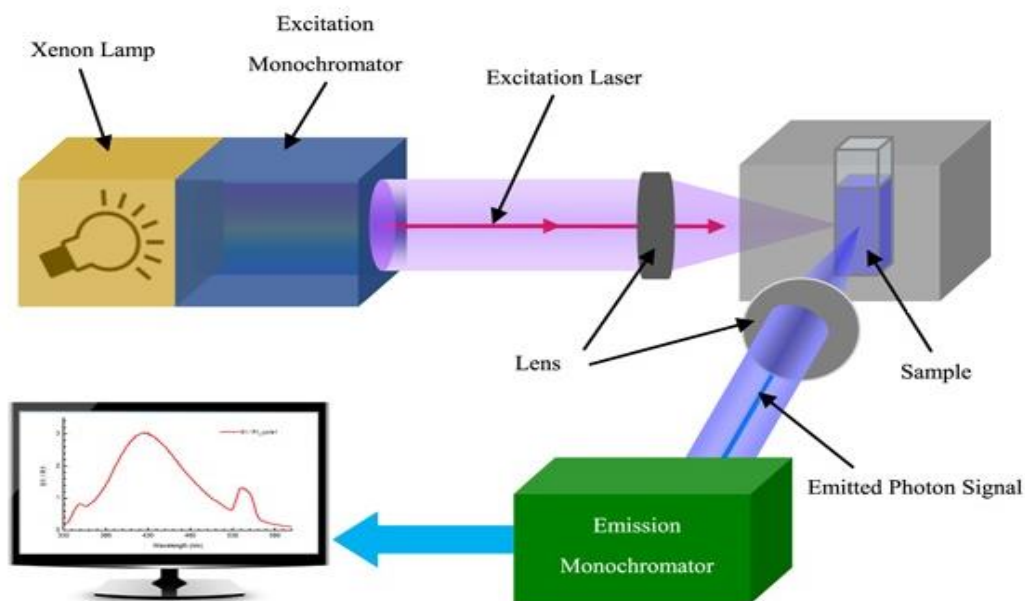

Figure 5: Schematic representation of fluorescent spectroscopy [4].

5.6.6. Raman spectroscopy

Raman spectroscopy measurements were made by depositing 30 µL of aqueous solution of the nanoparticles (0.1 mg/mL) on silicon wafer and left to dry at room temperature (Silicon wafer was cleaned separately with acetone, ethanol, and water and sonicated for 10 min between each washing step). Analysis were performed on a LabRam HR Micro-Raman system (Horiba Jobin Yvon) using a 473-nm laser diode as excitation source. Visible light is focused by a 100× objective. The scattered light is collected by the same objective in backscattering configuration, dispersed by a 300 mm focal length monochromator and detected by a CCD camera.

5.6.7. X-ray diffraction (XRD)

The crystallinity of the synthesized nanoparticles was performed on a Xeuss 2.0 SAXS/WAXS system (Xenocs) operating under vacuum with a GeniX3D microsource ($\lambda = 1.54189$ Å) at a generator voltage of 50 kV and a current of 0.6 mA with a 2D Pilatus 3R 200K detector.

5.6.8. Zeta-potential and Dynamic Light Scattering (DLS) measurements

The hydrodynamic size and surface charge of the synthesized nanoparticles were determined using dynamic light scattering principle (Malvern Zetasizer, NanoZS) at 25 °C. Solutions were freshly prepared before analysis, and the reported data are means for three independent measurements. Typically, 1 mL of an aqueous solution of nanoparticles (~ 10-50 µg/mL) were inserted into a disposable folded capillary cell (DTS1070) using a Terumo syringe to run the analysis.

5.6.9. Thermogravemetric analysis (TGA)

Thermogravimetric analysis (TGA/DTG) was carried out on a TG/DTG NETZSCH TG 209 F3 instrument. Thermograms were recorded by loading ~ 3-15 mg of lyophilized nanoparticles and subjecting the samples to a heating rate of 10 °C/min from 30 °C to 980 °C under nitrogen atmosphere.

5.6.10. High performance liquid chromatography

 HPLC analysis was carried out on a Shimadzu LC2010-HT (Shimadzu, Tokyo, Japan) equipped with a 5 µm C18AQ Uptisphere® X-serie 300 Å, 250 mm × 4.6 mm column (Interchim, Montluçon, France) heated to 30 °C. The mobile phase consisted of a mixture of eluent A (formic acid 0.1% in H_2O) and eluent B (formic acid 0.1% in CH_3CN) at a flow rate of 1 mL min^{-1}. The isocratic flow (eluent 1) was for 5 min, the linear gradient was 0 to 80% of eluent B in 6 min and further 80% of eluent B for 4 min. The detection was performed at 215/280 nm. Solutions were analyzed directly by injecting of 40 µL into the HPLC column.

5.7. References

[1] K. Kahlouche, R. Jijie, I. Hosu, A. Barras, T. Gharbi, R. Yahiaoui, et al., Controlled modification of electrochemical microsystems with polyethylenimine/reduced graphene oxide using electrophoretic deposition: Sensing of dopamine levels in meat samples, Talanta 178 (2018) 432-440.

[2] A.K. Al Atya, K. Drider-Hadiouche, A. Vachee, D. Drider, Potentialization of β-lactams with colistin: in case of extended spectrum β-lactamase producing Escherichia coli strains isolated from children with urinary infections, Res. Microbiol. 167 (2016) 215-221.

[3] G. Gollavelli, Y.-C. Ling, Magnetic and fluorescent graphene for dual modal imaging and single light induced photothermal and photodynamic therapy of cancer cells, Biomaterials 35 (2014) 4499-4507.

[4] S.K. Kailasa, J.R. Koduru, M.L. Desai, T.J. Park, R.K. Singhal, H. Basu, Recent progress on surface chemistry of plasmonic metal nanoparticles for colorimetric assay of drugs in pharmaceutical and biological samples, TrAC, Trends Anal. Chem. 105 (2018) 106-120.